Quantum transport of Dirac fermions in single and bilayer graphene: Chiral tunneling and quantum interference

Grzegorz Rut

Rozprawa doktorska
Promotor: dr hab. Adam Rycerz

Uniwersytet Jagielloński
Instytut Fizyki im. Mariana Smoluchowskiego
Zakład Teorii Materii Skondensowanej i Nanofizyki

Kraków, luty 2016

Wydział Fizyki, Astronomii
i Informatyki Stosowanej
Uniwersytet Jagielloński

Oświadczenie

Ja niżej podpisany Grzegorz Rut (nr indeksu: 1015903), doktorant Wydziału Fizyki, Astronomii i Informatyki Stosowanej Uniwersytetu Jagiellońskiego kierunku fizyka, oświadczam, że przedłożona przeze mnie rozprawa doktorska pt. *Quantum transport of Dirac fermions in single and bilayer graphene: Chiral tunneling and quantum interference* jest oryginalna i przedstawia wyniki badań wykonanych przeze mnie osobiście, pod kierunkiem dr. hab. Adama Rycerza. Pracę napisałem samodzielnie.

Oświadczam, że moja rozprawa doktorska została opracowana zgodnie z Ustawą o prawie autorskim i prawach pokrewnych z dnia 4 lutego 1994 r. (Dziennik Ustaw 1994 nr 24 poz. 83 wraz z późniejszymi zmianami). Jestem świadom, że niezgodność niniejszego oświadczenia z prawdą ujawniona w dowolnym czasie, niezależnie od skutków prawnych wynikajacych z ww. ustawy, może spowodować unieważnienie stopnia nabytego na podstawie tej rozprawy.

Kraków, dnia

podpis doktoranta

Contents

Acknowledgments **1**

Abstract **3**

Streszczenie **5**

List of publications **7**

List of abbreviations **8**

1 Introduction **9**
1.1 Pseudodiffusive charge-transport regime 10
1.2 Aim and scope of the thesis 12

2 Methodology **15**
2.1 Effective low-energy Hamiltonian 15
2.2 Derivation of quantum transport properties 16
2.2.1 Charge transfer cumulants at finite source-drain voltage 18
2.2.2 Transfer matrix approach 19

3 Conductance scaling for ballistic bilayer graphene **23**
3.1 Conductance of disordered systems and the scaling function 23
3.2 Conductivity dependence on the system size: single parameter scaling for BLG 25
3.2.1 Shot noise characteristics 26
3.2.2 Impact of electrostatic bias between the layers 26

4 Magnetoconductance of bilayer graphene **28**
4.1 Overview 28
4.2 Method of approach 28
4.3 High magnetic field limit for $t' = 0$ 29
4.4 Finite voltage effect 29
4.5 Effect of trigonal warping 30

5 Quantum relativistic Corbino effect (QRCE) **32**
5.1 Introduction 32

5.2 QRCE in bilayer graphene 34
5.2.1 High magnetic field limit; $t' = 0$ 35
5.2.2 Impact of trigonal warping 35
5.3 Beyond the linear response regime 36
5.4 QRCE in 2DEG 36

6 Conditions for conductance quantization in graphene nanostructures 38
6.1 Overview 38
6.2 Conductance of MLG disk section 39

Conclusions and perspectives 41

Bibliography 43

Acknowledgments

I would like to express my deepest gratitude to my supervisor, Dr. Adam Rycerz for his scientific guidance. Working under his supervision during the last few years has been a great privilage and honor. Apart from that, I am very grateful for his critical reading of this Thesis.

I would like to thank the people associated with the Department of Condensed Matter Theory and Nanophysics, Marcin Abram, Dr. Olga Howczak, Dr. Danuta Goc-Jagło, Dr. Jakub Jędrak, Dr. Jan Kaczmarczyk, Dr. Andrzej Kapanowski, Dr. Andrzej Kądzielawa, Ewa Kądzielawa-Major, Patryk Kubiczek, Prof. Józef Spałek, Prof. Włodzimierz Wójcik, Dr. Marcin Wysokiński, and Dr. Michał Zegrodnik for good working atmosphere and their help in so many different ways.

Many sincere thanks are due to Karol Dąbrowski, Dawid Dul, Dr. Krzysztof Głowiński, Przemysław Witaszczyk and Jacek Grela for the time spent on many fruitful conversations not only limited to physics.

Finally, I would like to thank my family for their love and support.

The work was partly supported by the National Science Centre of Poland (NCN) via grants No. N-N202-031440, 2014/14/E/ST3/00256 and 2014/15/N/ST3/03761. I would also like to acknowledge the partial finantial support from the Foundation for Polish Science (FNP) within project TEAM/2010-6/7 carried out within the TEAM programme, cofinanced from the European Union under the European Regional Development Fund. Computations were partly performed using the PL-Grid infrastructure.

Abstract

This thesis is concerned with the quantum transport properties of ballistic systems based on mono and bilayer graphene. Within the Landauer-Büttiker formalism, the Dirac systems have been investigated in terms of electrical conductivity and related quantum effects. The main subject of our research is connected with the so-called pseudodiffusive transport regime which appears (at zero temperature and zero field) when the Fermi energy is close to the Dirac point. At high magnetic field, the pseudodiffusive transport appears also in close vicinity to the Landau levels. Physical discussion, carried out mostly in analytical terms, is based on the effective low-energy Hamiltonian.

The first part of the thesis is devoted to the ballistic conductance of bilayer graphene within the pseudodiffusive regime. We have shown that conductivity of this material, contrary to the monolayer case, is not universal but depends on the system size. The scaling function, based on this dependence, reproduces the behavior of disordered Dirac systems with Coulomb interaction included. Higher charge transfer cumulants, the Fano factor $\mathcal{F}$ and the $\mathcal{R}$ factor, approach with increasing system size their pseudodiffusive values (1/3 and 1/15, respectively). This suggests that the pseudodiffusive behavior is connected with shot noise characteristics rather than a constant value of the conductivity.

An external magnetic field, perpendicular to the sample surface, leads to a suppression of conductivity outside the pseudodiffusive regime. The pseudodiffusive value of the conductivity strongly depends on the coupling between the layers, quantified by interlayer hopping integrals between nearest ($t_\perp$) and next nearest neighbors (t'). The conductivity increases with the magnetic field, reaching its maximal value near a crossover field B_{res}, depending both on t' and $t_\perp$. Above the field B_{res}, conductivity decreases with the magnetic field, approaching the value $\sigma = \sigma_{BLG} = 8e^2/(\pi h)$ at the Dirac point and $\sigma = \sigma_{MLG} = 4e^2/(\pi h)$, identically as in a monolayer, at other Landau levels. An external, perpendicular electric field decreases the conductivity of bilayer graphene up to a value twice as small than in a single layer. This is due to the fact that such a field lifts the valley degeneracy.

The next section describes the magnetoconductance of graphene based systems in the Corbino geometry. The *quantum relativistic Corbino effect* (QRCE), in which charge transfer cumulants oscillate with magnetic flux piercing the disk area, is manifested in bilayer graphene by pronounced beating patterns with a period proportional to the square root of magnetic field. In contrast to mean conductance enhancement due to $t' \neq 0$, beating patterns remain visible even for large magnetic fields. Similar analysis of a system based on 2DEG proves that QRCE does not appear in standard Schrödinger systems.

For the sake of completeness, magnetoconductance of graphene based systems as well as QRCE have been analyzed outside of the linear response regime. For finite source-drain voltages as well as for fluctuating doping, charge transfer cumulants drastically diverge from their pseudodiffusive values. We have shown that for such a setup, although the conductance is suppressed, the Fano factor $\mathcal{F}$ as well as the factor $\mathcal{R}$ approach the finite high-voltage limits $\mathcal{F} \simeq 0.74$ and $\mathcal{R} \simeq 0.51$.

In the last part of this thesis we have investigated conductance quantization in graphene on the example of a section of the Corbino disk. For a proper ratio of outer and inner radii, such a geometry leads to a suppression of Fabry-Perot resonances present in a rectangular system. By adapting the neutrino billiards theory by Berry and Mondragon to open graphene nanosystems, we have shown that the conductance can emerge for disk sections with an opening angle $\theta \lesssim \pi/3$. An emergence of n-th quantization step requires a condition $\sqrt{n}\theta/\pi \gg 1$, which suggest a smearing of conductance with increasing n.

Streszczenie

Niniejsza rozprawa dotyczy badań nad balistycznymi układami na bazie monowarstwowego i dwuwarstwowego grafenu. W oparciu o formułę Landauera-Büttikera zbadano zachowanie układów dirakowskich w kontekście przewodnictwa elektrycznego oraz efektów kwantowych bezpośrednio z nim związanych. Główna tematyka badań dotyczy tak zwanego pseudodyfuzyjnego reżimu przewodnictwa. Reżim ten, w przypadku zerowej temeratury i zrowych pól, pojawia się w sąsiedztwie punktu Diraca. W przypadku wysokich pól magnetycznych, reżim ten rozszerza się również na bliskie otoczenie poziomów Landaua. Przeprowadzone obliczenia, w przeważającej części analityczne, zostały oparte o hamiltonian efektywny dla niskoenergetycznych kwazicząstek.

Pierwsza część pracy dotyczy przewodności balistycznej dwuwarstwy grafenowej w reżimie transportu pseudodyfuzyjnego. Wykazaliśmy, iż przewodność właściwa tego materiału zależy od rozmiaru układu. Zależność ta pozwoliła na wyznaczenie uniwersalnej funkcji skalującej, która odtwarza zachowanie układu fermionów dirakowskich z domieszkami. Wyższe kumulanty transferu ładunku, czynnik Fano $\mathcal{F}$ oraz trzecia kumulanta $\mathcal{R}$, zbliżają się do swych wartości pseudodyfuzyjnych (odpowiednio 1/3 i 1/15) wraz ze wzrostem rozmiaru układu. Wynik ten sugeruje, iż zachowanie pseudodyfuzyjne jest nie tyle związane ze stałą wartością przewodnictwa, co z charakterystyką szumu śrutowego układu.

Przyłożenie do dwuwarstwy prostopadłego, zewnętrznego pola magnetycznego prowadzi do wygaszenia przewodnictwa poza reżimem pseudodyfuzyjnym. W obszarze tym przewodność silnie zależy od sprzężenia między warstwami, które definiują międzywarstwowe hoppingi między najbliższymi ($t_\perp$) oraz drugimi sąsiadami (t'). W reżimie niskich pól, w punkcie Diraca, przewodnictwo rośnie monotonicznie aż do wartości maksymalnej osiągniętej dla pola magnetycznego B_{res}. Powyżej B_{res} przewodnictwo maleje odwrotnie proporcjonalnie do pola, zbliżając się do wartości asymptotycznej $\sigma = \sigma_{BLG} = 8e^2/h$. Na wyższych poziomach Landaua przewodność w granicy wysokich pól osiąga wartość $\sigma{=}\sigma_{MLG} = 4e^2/h$, identycznie jak w monowarstwie. Co więcej, po przyłożeniu do układu prostopadłego pola elektrycznego, przewodność dwuwarstwy w reżimie pseudodyfuzyjnym może być dwukrotnie niższa niż w monowarstwie, co jest wynikiem zniesienia degeneracji dolinowej.

Kolejna część pracy dotyczy tzw. *kwantowego relatywistycznego efektu Corbino* - periodycznych oscylacji przewodnictwa i wyższych kumulant transferu ładunku jako funkcji pola magnetycznego w układach grafenowych o geometrii dysku Corbino. W dwuwarstwowym grafenie efekt ten przejawia się w postaci dudnień o okresie proporcjonalnym do pierwiastka z pola magnetycznego. W porównaniu ze wzmocnieniem średniej wartości przewodności w obecności niezerowych hoppingów skośnych,

częstość dudnień zanika znacznie wolniej ze wzrostem pola magnetycznego. Analogiczna analiza przeprowadzona dla standardowego dwuwymiarowego gazu elektronowego sugeruje, iż efekt Corbino nie występuje w układach schrödingerowskich.

Magnetoprzewodnictwo dwuwarstwy grafenowej jak i efekt Corbino były badane również poza obszarem liniowej odpowiedzi. Wykazaliśmy, iż wartość kumulant transferu ładunku w przypadku niezerowej różnicy potencjałów źródło-dren ulega znacznej zmianie. Choć przewodność w takim układzie szybko ulega wygaszeniu przez pole magnetyczne, czynniki Fano $\mathcal{F}$ i $\mathcal{R}$ osiągają w granicy wysokich napięć wartości $\mathcal{F} \simeq 0.74$ oraz $\mathcal{R} \simeq 0.51$. Analogiczne zachowanie spodziewane jest w układach o fluktuującym wypełnieniu.

Ostatnia część pracy dotyczy zagadnienia kwantowania przewodnictwa w grafenie na przykładzie sekcji dysku Corbino oraz dla próbki prostokątnej. Geometria tego typu, przy odpowiednim stosunku promieni, pozwala na wygaszenie oscylacji Fabry Perota obecnych w prostokątnych układach. Adaptując teorię bilardów neutrinowych Berrego i Mondragona do otwartych nanoukładów grafenowych, określiliśmy analitycznie warunki, dla których schodki przewodnictwa są dobrze widoczne. Wykazaliśmy, iż kwantyzacja pojawia się już dla sekcji o kącie rozwarcia $\theta = \pi/3$. Obserwacja n-tego schodka w rozważanym układzie grafenowym wymaga spełnienia warunku $\sqrt{n}\theta/\pi \gg 1$, co przewiduje rozmycie przewodnictwa wraz ze wzrostem n.

List of publications

1. G. Rut and A. Rycerz, *Pseudodiffusive conductance, quantum-limited shot noise, and Landau-level hierarchy in biased graphene bilayer*, **Physical Review B 89, 045421 (2014)**.
   http://arxiv.org/abs/1307.7093 DOI: 10.1103/PhysRevB.89.045421

2. G. Rut and A. Rycerz, *Conditions for conductance quantization in mesoscopic Dirac systems on the examples of graphene nanoconstrictions*, **Acta Physica Polonica A 126, A-114 (2014)**.
   http://arxiv.org/abs/1312.7601 DOI: 10.12693/APhysPolA.126.A-114

3. G. Rut and A. Rycerz, *Quantum-limited shot noise and quantum interference in graphene based Corbino disk*, **Philosophical Magazine 95, 599-608, (2015)**.
   http://arxiv.org/abs/1401.7247 DOI: 10.1080/14786435.2014.974712

4. G. Rut and A. Rycerz, *Magnetoconductance of the Corbino disk in graphene: Chiral tunneling and quantum interference in the bilayer case,* **Journal of Physics: Condensed Matter 26, 485301 (2014)**.
   http://arxiv.org/abs/1405.4908 DOI: 10.1088/0953-8984/26/48/485301

5. G. Rut and A. Rycerz, *Minimal conductivity and signatures of quantum criticality in ballistic graphene bilayer*, **Europhysics Letters 107, 47005 (2014)**.
   http://arxiv.org/abs/1407.1684 DOI: 10.1209/0295-5075/107/47005

Submitted:

6. G. Rut and A. Rycerz, *Trigonal warping, pseudodiffusive transport, and finite-system version of the Lifshitz transition in magnetoconductance of bilayer-graphene Corbino disks*, accepted to **Physical Review B**.
   http://arxiv.org/abs/1511.04705

List of abbreviations and symbols

Frequently used abbreviations

2DEG	Two dimensional electron gas
BLG	Bilayer graphene
LL(s)	Landau level(s)
MLG	Monolayer graphene
QRCE	Quantum relativistic Corbino effect

Frequently used symbols

t_0	intralayer hopping integral, $t_0 \approx 3.16$ eV [1–3]
$t_\perp$	interlayer nearest neighbor hopping integral, $t_\perp \approx 0.38$ eV [1–3]
t'	skew interlayer hopping integral (unknown precisely), $t' \approx 0.1 - 0.38$ eV [1–3]
a	lattice constant in a single layer, $a = 0.246$ nm
v_F	Fermi velocity, $v_F = \sqrt{3} t_0 a / (2\hbar) \approx 10^6$ m/s
V	potential difference between layers
V_{sd}	source drain voltage
E_L	Lifshitz energy, $E_L = t_\perp t'^2 / (2t_0)^2 \approx 0.095 - 1.374$ meV
G	Landauer-Büttiker conductance
$\mathcal{F}$	Fano factor (a dimensionless quantifier of the shot-noise power)
$\mathcal{R}$	dimensionless quantifier of the third charge transfer cumulant
g_0	conductance quantum, e^2/h
σ	conductivity
σ_{MLG}	pseudodiffusive conductivity of MLG, $\sigma_{MLG} = 4e^2/(\pi h)$
σ_{BLG}	pseudodiffusive conductivity of BLG, $\sigma_{BLG} = 8e^2/(\pi h)$
$\sigma_\star$	asymptotic conductivity of BLG in $L \to \infty$ limit, $\sigma_\star = 3\sigma_{BLG}$
$\beta(\sigma)$	scaling function, $\beta(\sigma) = d\log(\sigma)/d\log(L)$
$R_i (R_o)$	inner (outer) radius of the Corbino disk
$\mathcal{L}$	$\ln(R_o/R_i)$
l_B	magnetic length, $l_B = \sqrt{\hbar/(e\lvert B\rvert)}$
r_c	cyclotron radius, $r_c = \lvert \hbar k/(eB) \rvert$
Φ_D	magnetic flux piercing the Corbino disk, $\Phi_D = B\pi(R_o^2 - R_i^2)$
Φ_0	basic oscillation period in QRCE, $\Phi_0 = (2h/e)\mathcal{L}$

1 Introduction

The whole field of electronic materials is driven by the discovery of new phases, which provide the playgrounds in which to search for new macroscopic physical properties. These words, while said in a recent interview by David Hsieh in context of superconductivity [4], greatly depict graphene's impact on condensed matter physics. It is remarkable that more than seventy years[1] of studies over an abstract two dimensional material, turned out to be something much more than just an intellectual challenge.

Before graphene's discovery in 2004 [6], it had been believed that free standing two dimensional systems should not exist. Landau and others argued that, due to divergent thermal fluctuations, displacements of atoms would be so large that the material would be unstable [7–10]. These theoretical predictions seemed bulletproof. Investigation of thin films proved that the fewer the layers, the more fragile the material becomes and breaks into small islands [10–12]. Graphene has been the first two dimensional material being able to persevere the expected breakdown [10, 13]. As it turns out, the thermal fluctuations can be suppressed by ripples stabilizing the two dimensional material at a price of large height fluctuations. This feature, next to the absence of the band gap, makes graphene exceptional in the group of novel 2D materials such as silicene, hexagonal boron nitride, black phosphorus, or molybdenum disulfide [14], which usually require to be sustained by a three-dimensional substrate.

A lot of attention brought on graphene was due to its linear dispersion relation. Low energy quasiparticles are massless and thus their behavior is far from the expected from Schrödinger equation. This new type of emergent particles, Dirac fermions, introduced a variety of new phenomena to condensed matter physics, the most prominent of which is the Klein effect [15]. It is also worth to mention that graphene is the first material which allows to observe a purely quantum mechanical effect at room temperatures - the quantum Hall effect [6, 16].

Although monolayer graphene (MLG) is considered as a material for multiple applications - from transistors to gas sensors and water filters [17–19] - its lack of an energy gap limits its potential in the field of electronics. This is not the case of bilayer graphene (BLG). While maintaining graphene's treats such as mechanical durability and high mobility of charge carriers, it allows one to control the energy gap through external electric field [20]. BLG is also interesting from the fundamental science

[1] It is known that the band structure theory of graphite and its single layer was formulated by Wallace [5] during his work for National Research Council of Canada in the Montréal Lab, 1943-1946 in the group lead by George Placzek.

point of view since it hosts *massive* chiral fermions, another type of dual-natured quasiparticles.

1.1 Pseudodiffusive charge-transport regime

One of the most prominent examples of new physical phenomena discovered in graphene-based materials is the pseudodiffusive charge-transport. Ideal samples of undoped graphene have the same shot-noise characteristics, quantified by the Fano factor $\mathcal{F} = 1/3$, as a diffusive wire [21–27], albeit a current passing through a normal ballistic sample is expected to show no fluctuations ($\mathcal{F} = 0$) [28, 29]. The pseudodiffusive transport is expected to emerge in mono- and bilayer graphene close to the Dirac (charge-neutrality) point, as well as in the vicinity of each Landau level (LL) in case the nonzero magnetic field is applied (see Fig. 1.1) [22, 30–32].

The unexpected shot-noise in the pseudodiffusive regime is attributed to the so-called *Zitterbewegung* (eng. trembling motion), already considered by Schrödinger in 1930 [33–36]. This quantum-relativistic effect, described as a jittering motion of charge carriers (even in absence of external fields or interactions), emerges in Dirac systems in which the current operator does not commute with the Hamiltonian [37, 38]. A physical view on this phenomenon links it with the position uncertainty of the relativistic particles due to creation of virtual particle-antiparticle pairs during the measurement [34, 39, 40].

Zitterbewegung leads to an interesting conductivity behavior in the pseudodiffusive regime. First experimental papers on transport properties of graphene revealed that, though the density of states at the Dirac point is zero, conductivity of monolayer graphene is finite [6, 16]. Numerous theoretical groups claimed to explain this result, though for some time there has been an argument about the actual value of minimal conductivity.

In particular, an inconsistency occurred between different theoretical predictions and early experimental results [6, 16]. The Landauer-Büttiker formalism suggested the minimal conductivity was $\sigma = 4e^2/(\pi h) \equiv \sigma_{MLG}$ [2] [22, 34]. Results based on the Kubo formula, from $\sigma = 4e^2/(\pi h)$ to even $\sigma = \pi e^2/h$, depending on order in which certain limits are taken [41–44]. More recent experimental results [23, 24, 45] seem to favor σ_{MLG} as the minimal value. Further theoretical investigations proved that σ_{MLG} is expected to appear in presence of magnetic field at the Landau levels as well [30].

Similarly as in the monolayer case, there have been several attempts to derive minimal conductivity of bilayer graphene (BLG). Based on the approximate low-energy dispersion relation as well as different formalisms (either the Kubo or Landauer-Büttiker), several results have been obtained [46–50]. If the coupling between the layers is defined solely by the interlayer nearest-neighbor hopping integral $t_\perp$, the dispersion relation is close to paraboloidal. Papers based on this approximation suggested that the BLG minimal conductivity is simply twice as large as the MLG

[2] The prefactor 4 originates from both spin and valley degeneracy.

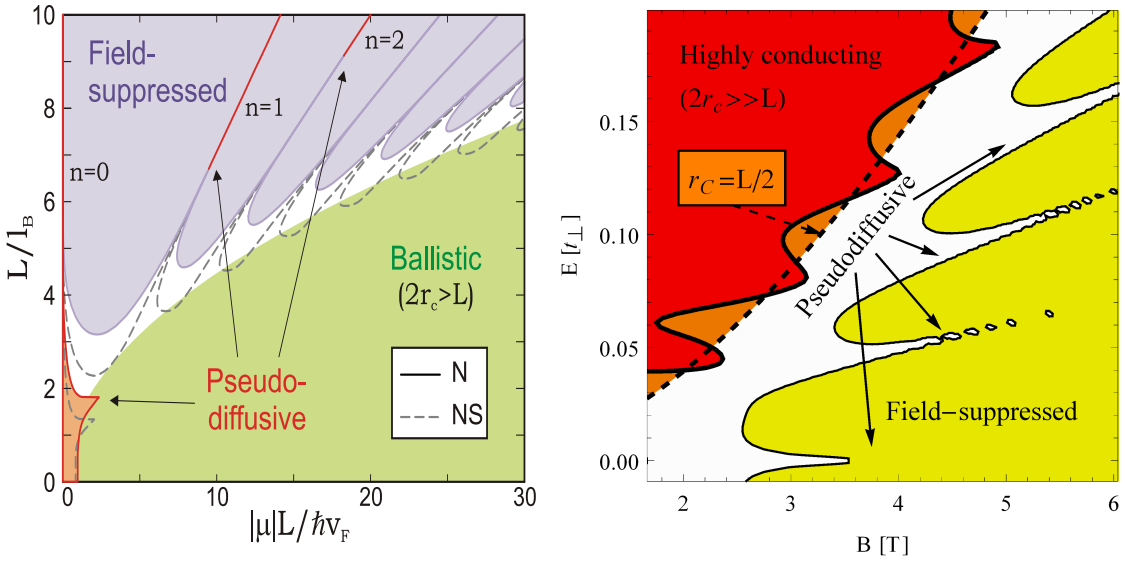

Figure 1.1: Pseudodiffusive transport regimes in MLG (left) and BLG (right) in presence of the magnetic field B. E stands for the Fermi energy, μ is the electrochemical potential ($\mu = E$ at zero temperature), $l_B = \sqrt{\hbar/(e|B|)}$ is the magnetic length, $v_F \approx 10^6$ m/s is the Fermi velocity and $t_\perp$ is the interlayer nearest-neighbor hopping integral. In case the cyclotron diameter is smaller than the system's length $2r_c < L$, the conductance at each Landau level remains finite while at other energies it is suppressed by magnetic field. Figures adapted from Refs. [30, 32].

minimal conductivity, $\sigma_{BLG} = 2\sigma_{MLG}$ [47, 48]. Moreover, it has been shown that the pseudodiffusive shot-noise characteristics ($\mathcal{F} = 1/3$) are the same as in MLG[3].

Inclusion of the skew-interlayer hopping integrals t' has triggered a very nontrivial effect - an enhancement of minimal conductivity up to $\sigma = 3\sigma_{BLG}$ (six times larger than minimal conductivity of a single layer) [49]. This dramatic change is attributed to the Lifshitz transition of the Fermi surface in which three additional Dirac cones emerge for $t' \neq 0$ (see Fig. 1.2). Further analysis proved that this result can be obtained only for asymptotically large samples. Also, since $t' \neq 0$ breaks the cylindrical symmetry of the dispersion relation, charge-transport is no longer isotropic. Depending on the orientation of the sample, the asymptotic conductivity may take values from $\sigma = (7/3)\,\sigma_{BLG}$ to $\sigma = 3\sigma_{BLG}$ [50].

If we neglect the edge channels in a sample, classical trajectories of charge carries would not allow to pass the current further than the cyclotron diameter $2r_c$. Such

[3] An interesting result, $\sigma = 2e^2/h$ and $\mathcal{F} = 1 - 2/\pi$, has been obtained by Katsnelson by utilizing the two-band effective mass Hamiltonian corresponding to the limit $t_\perp \to \infty$ [46, 51]. Snyman and Beenakker have proved that such an approximation usually fails to reproduce quantum-transport properties of BLG sample attached to heavily-doped BLG leads, apart from the case the doping in leads is set to approximately $0.2t_\perp$ [48].

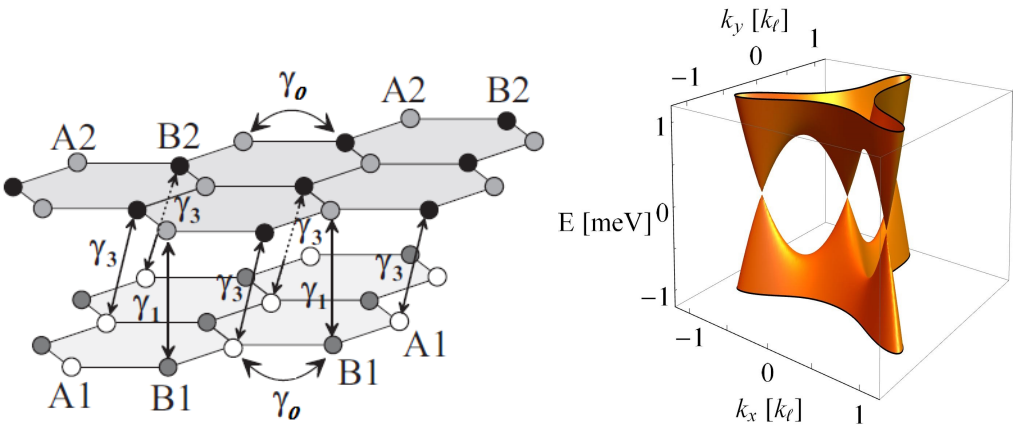

Figure 1.2: Left: Two honeycomb lattices in the AB Bernal stacking. The arrows depict connections between distinct nodes through hopping integrals ($t_0 \equiv \gamma_0$, $t_\perp \equiv \gamma_1$, $t' \equiv \gamma_3$). Picture adapted from Refs. [51]. Right: Dispersion relation in vicinity of the Dirac point with the skew interlayer hopping integral set to $t' = 0.3$ eV. The satellite Dirac cones are shifted in the momentum space from the central one by $k_\ell = \nu t_\perp / (\hbar v_F)$ with $\nu = t'/t_0$.

an effect would not occur in both undoped MLG and BLG. The wavefunctions of quasiparticles at the Dirac point are of an evanescent nature and do not follow the classical picture. Nonzero conductivity at the Dirac point is preserved in both single and bilayer graphene in applied external magnetic field[4]. The Dirac point in both these materials coincides with the lowest Landau level (in case we disregard the Zeeman effect and the electrostatic bias between the layers in BLG case) [16, 52–55]. Quantum-transport properties characteristic for the Dirac (charge-neutrality) point appear on higher Landau levels as well[5]. Nonzero conductance in high magnetic field allows a novel type of quantum effect to appear - the *quantum relativistic Corbino effect* (QRCE) [56–58]. This interference-related effect manifests itself in oscillations of charge transfer cumulants with magnetic field. Contrary to a similar Aharonov Bohm effect [59–61], QRCE seems not to have a counterpart for Schrödinger electron systems [62].

1.2 Aim and scope of the thesis

The rich physics of the pseudodiffusive regime was mainly explored in the context of a single layer of graphene. We have tried to fill this gap by investigating bilayer

[4]In contrast to the Landau levels (LLs) in standard two-dimensional electron gas (2DEG), the Dirac point is a peculiar case in which the position of LL does not depend on magnetic field (as long as one neglects the Zeeman effect and the bias between the layers in BLG case). In fact, the Dirac point in bilayer graphene hosts two degenerate Landau levels, see Ref. [52].

[5]In the case of BLG, many of these properties may be altered due to interlayer coupling.

graphene-based systems. The coupling between its layers not only leads to more complex quantum effects than in a single layer, but also introduces a novel class of effective quasiparticles, massive chiral fermions, which are introduced via low-energy excitation in the vicinity of the Dirac point.

Several suppositions have been taken into account in our discussion. All types of disorder as well as the edge states are disregarded[6]. While the impact of impurities on the physics of relativistic quasiparticles is an important and ever-growing subject [63–67], we focus here on perfect ballistic samples. Most of the topics tackled in this thesis have not been considered in the literature earlier thus it is natural to deal with impurity free samples first and treat the results as reference points for future, more complete discussions.

Another important point is the description of wavefunctions in the leads. In our investigations we suppose that the doping in the contacts is infinite. In a general situation, analytical results show some dependence on the doping at the leads [48]. In order to limit the number physical parameters, it is a common practice to consider the limit of heavily-doped graphene leads in which measurable quantities become insensitive to this doping. Such an approximation seems to reasonably reproduce typical experimental situations with graphene samples overlapped by metallic leads.

Since we are dealing with energies in the vicinity of the Dirac (charge-neutrality) point, our methodology is based on the effective low-energy Hamiltonians. Employing the Landauer-Büttiker formalism along with the Levitov formula [29, 68], we were able to produce analytical results, supplemented by numerical simulations in more complex situations.

The pseudodiffusive transport regime is limited to the Dirac point or to the vicinity of the Landau levels in case of nonzero magnetic field. As this regime rapidly shrinks with increasing magnetic field [30], the role of a finite source-drain voltage on both the magnetoconductance and higher charge-transfer cumulants is considered.

Several problems regarding bilayer graphene have been tackled:

- The conductivity dependence on the system size.
- Influence of magnetic field on the charge transfer cumulants (G, $\mathcal{F}$ and $\mathcal{R}$) in the pseudodiffusive limit.
- The quantum relativistic Corbino effect in the opposite, quantum-tunneling limit.

Additionally, the above tasks have been supplemented by investigation of other closely related issues on the example of single layer graphene:

- The finite source-drain voltage on magnetoconductance and other charge-transfer cumulants.

[6]For instance, we have considered periodic boundary conditions in rectangular samples. The pseudodiffusive transport regime requires a large number of transmission channels thus the edge currents should not have a considerable impact on the quantum transport. These boundary conditions also can model carbon nanotubes.

- Conductance quantization in a section of the Corbino disk.

While this list does not reflect the chronological order of problems tackled, it includes the most important tasks undertaken in this thesis.

2 Methodology

2.1 Effective low-energy Hamiltonian

Since we are dealing with charge transport in the linear-response regime, it is sufficient to take into account only the energies in a close vicinity of the Fermi level E. While in free-standing MLG and BLG samples the Fermi energy is localized at the Dirac (charge-neutrality) point, in existing transistor-like devices, the back gate voltage allows one to tune the doping in the range of $|E| < 0.1$ eV $\ll t_0$ [38]. The dispersion relation in such a range can be approximated by valleys placed at two inequivalent points in the Brillouin zone - K and K' (see Fig. 2.1).

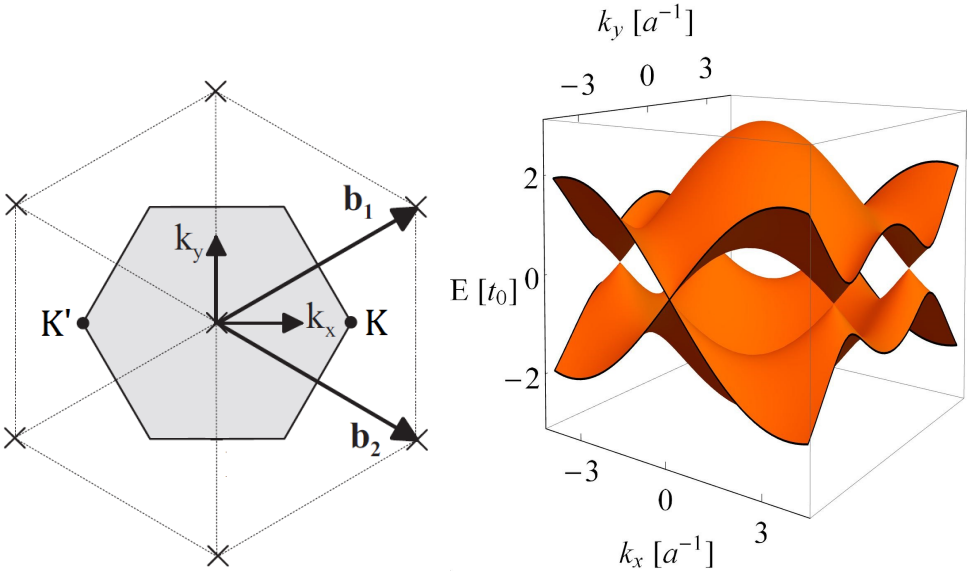

Figure 2.1: Left: Reciprocal space (same for both MLG and BLG) spanned by primitive vectors $\mathbf{b}_1 = \left[2\pi/a, 2\pi/\left(\sqrt{3}a\right)\right]$ and $\mathbf{b}_2 = \left[2\pi/a, -2\pi/\left(\sqrt{3}a\right)\right]$. Points $K = \left[4\pi/\left(3a\right), 0\right]$ and $K' = \left[-4\pi/\left(3a\right), 0\right]$ mark two independent corners of the first Brillouin zone (shaded area). Picture adapted from Ref. [69]. Right: Dispersion relation of MLG. Note the approximately linear energy dependence on the wavevector near $E = 0$.

The dynamics of charge carriers with energies close to the Fermi energy can be described within effective low energy Hamiltonians. At valleys K and K', in the

MLG case we have

$$H_K = v_F \vec{\sigma} \cdot \vec{p} = -H_{K'}^T, \tag{2.1}$$

where $\vec{\sigma} = (\sigma_x, \sigma_y)$ is an operator built of Pauli matrices, $\vec{p} = -i\hbar\,(\partial_x, \partial_y)$ is the in-plane momentum, and $v_F = \sqrt{3}at_0/2 \approx 10^6$ m/s is the Fermi velocity, with the lattice parameter $a \approx 2.46$ nm and $t_0 \approx 3.16$ eV the intralayer nearest neighbor hopping integral. Since the effective Hamiltonian is a 2×2 matrix operator, the wavefunctions take the form of 2-element spinors.

Contrary to high energy particles, the pseudospin index of graphene's quasiparticles does not refer to an actual spin but to the contribution from sublattices A and B (see Fig. 1.2). Projection of this pseudospin on the direction of momentum is referred as pseudochirality [70], which is further related to an intrinsic symmetry between electrons and holes [15]. Electrons with energy E have the same pseudochirality as holes with energy $-E$ and opposite momentum. The term *chiral particles* applies generically to Dirac fermions, including also massive quasiparticles in bilayer graphene.

In case of bilayer graphene, since there are four atoms in the basic cell of the lattice, the effective low energy Hamiltonian is given by a 4×4 operator of the form

$$H_\xi = \xi \begin{pmatrix} -V/2 & \pi\nu & 0 & \pi^\dagger \\ \nu\pi^\dagger & -V/2 & \pi & 0 \\ 0 & \pi^\dagger & V/2 & t_\perp \xi \\ \pi & 0 & t_\perp \xi & V/2 \end{pmatrix}, \tag{2.2}$$

where $\pi = v_F\,(p_x + ip_y)$, V is the difference between electrochemical potentials on the layers[1], and the $\xi = 1\,(-1)$ describes the case of K (K') valley. Moreover, $t_\perp \approx 0.38$ eV is the nearest neighbor interlayer hopping integral and $\nu = t'/t_0$ is the ratio between next nearest neighbor hopping integral $t' \approx 0.1 - 0.38$ eV [1–3] (the directions of these hopping integrals as well as low energy dispersion relation of BLG are presented in Fig. 1.2). The skew interlayer hopping integral t' has been so far measured with a very limited accuracy thus a novel approach of estimating this parameter is very desired.

2.2 Derivation of quantum transport properties

In our analysis we have employed the Landauer-Büttiker formalism which allows one to describe quantum transport in terms of the scattering properties of the system. In this picture, the analyzed graphene sample is treated as a scattering region connected

[1] This bias potential can be in principle induced by an external, perpendicular to the plane, electric field [20]. Some experimental results suggest that an intrinsic bias potential may appear in BLG due to electron-electron interaction [71, 72].

by ideal waveguides to two reservoirs (metallic leads) of charge carriers between which the current is passed. It is assumed that the electrons or holes exit and enter the leads with negligible probability of reflection, i.e., the scattering takes place only in the sample region [29, 73].

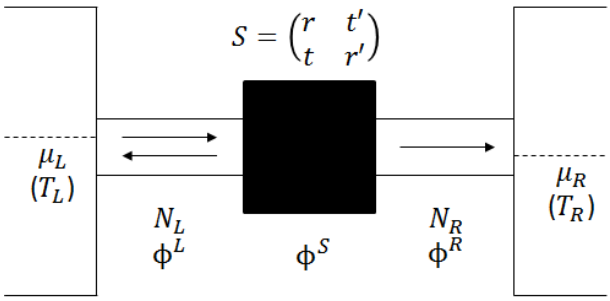

Figure 2.2: Schematic picture of the analyzed system. Charge carries are transfered between two reservoirs, source (L) and drain (R), characterized by the chemical potential μ_L (μ_R) and temperature T_L (T_R), through a scatterer (the analysed sample). The reservoirs are connected with the scattering area through ideal waveguides (with N_L and N_R opened transmission channels, respectively). The wavefunctions in the waveguides, ϕ^L (consisting of both incoming and reflected waves) and ϕ^R (the transmitted wave), are mode matched with the wavefunction of the scaterrer ϕ^S at the borders of the scattering area.

Here we focus on the linear-response regime applicable for systems with approximately constant transmission properties in the vicinity of the Fermi energy, in which the transport occurs [29, 73]. We disregard both effects of finite temperature and impurities, thus the only noise in the system is connected with discrete nature of charge carriers (see chapter 1).

We have restricted our attention to first three charge transfer cumulants. The first cumulant is quantified by the conductance G, which is given by the ratio between current passed through a system and voltage between the leads. The second one, quantified by the Fano factor $\mathcal{F}$, is a measure of the shot noise in the system (its two limiting values, $\mathcal{F} = 0$ and $\mathcal{F} = 1$, correspond to zero and Poisson noise, respectively). Last one, the $\mathcal{R}$ factor, connected with the third moment, expresses the asymmetry of current fluctuations [68, 74]. An interest in these higher moments of charge transfer is motivated by the complementary character of the information they carry.

In brief, the Landauer-Büttiker formalism in the linear-response transport regime [29, 73] allows one to express the conductance G, the Fano factor $\mathcal{F}$ and the factor

$\mathcal{R}$ as

$$G = \frac{e^2}{h}\mathrm{Tr}\boldsymbol{T}, \tag{2.3}$$

$$\mathcal{F} = \frac{\mathrm{Tr}\left[\boldsymbol{T}\left(\mathbf{1}-\boldsymbol{T}\right)\right]}{\mathrm{Tr}\boldsymbol{T}}, \tag{2.4}$$

$$\mathcal{R} = \frac{\mathrm{Tr}\left[\boldsymbol{T}\left(\mathbf{1}-\boldsymbol{T}\right)\left(\mathbf{1}-2\boldsymbol{T}\right)\right]}{\mathrm{Tr}\boldsymbol{T}}, \tag{2.5}$$

where $\boldsymbol{T} = \boldsymbol{t}^{\dagger}\boldsymbol{t}$ and $\boldsymbol{t}$ is a matrix of transmission amplitudes t_{mn} between channels m and n.

Scattering properties of the system are obtained by mode matching of wavefunctions at the boundary of the leads and the sample. Contrary to the wavefunctions of nonrelativistic charge carriers described by the Schrödinger equation, in case of both MLG and BLG it is enough to match only the wavefunctions and disregard their derivatives. This is due to the fact that the Dirac equation is equivalent to a system of first order differential equations.

The mode matching between wavefunctions (which in principle can be expressed as vectors, see sec. 2.2.2) in the leads $\boldsymbol{\phi}^L$ and in the sample area $\boldsymbol{\phi}^S$ for the Corbino disk, with the inner radius R_i and outer radius R_o, can be expressed as

$$\begin{aligned} \boldsymbol{\phi}^L_+\left(R_i\right) + \mathbf{r}\boldsymbol{\phi}^L_-\left(R_i\right) &= \boldsymbol{\phi}^S\left(R_i\right), \\ \boldsymbol{\phi}^S\left(R_o\right) &= \mathbf{t}\boldsymbol{\phi}^L_+\left(R_o\right), \end{aligned} \tag{2.6}$$

where the lower index refers to waves propagating from $r = 0$ $(+)$ or from $r = \infty$ $(-)$, and $\boldsymbol{r}$ is a matrix of reflection amplitudes r_{mn} between channels m and n.

In most of the cases we have disregarded mode mixing, i.e., $t_{mn} = t_m$. This is justified since the subject of our investigation is an ideal, impurity-free system in which quantum channels are protected by the symmetry. Mode mixing is naturally introduced in case the system has a random-like position dependent potential, which is usually employed to model disordered systems. The important exception is the Corbino disk in bilayer graphene. In our investigation of trigonal warping's impact on the quantum transport, we have treated the skew interlayer hopping integrals as a peculiar type of symmetry-breaking potential, introducing the mixing between the channels.

2.2.1 Charge transfer cumulants at finite source-drain voltage

In order to take into account the finite source drain voltage, we have employed the Levitov formula [68]. This formalism concerns a random charge Q passing through the system in a time interval Δt in presence of a bias voltage V_{sd}. The statistical distribution of the random variable Q/e has a characteristic function

$$\begin{aligned}\Lambda(\chi) &= \langle \exp\left(i\chi Q/e\right)\rangle \\ &= (\Delta t/h) \times \int_{E_0-eV_{sd}/2}^{E_0+eV_{sd}/2} dE' \, \ln\left\{\det\left[\boldsymbol{I} + \left(e^{i\chi}-1\right)\boldsymbol{T}(E')\right]\right\},\end{aligned} \tag{2.7}$$

where E_0 is the mean doping. The m-th moment of the transmitted charge $\langle\langle Q^m\rangle\rangle \equiv \langle Q^m - \langle Q\rangle^m\rangle$ is expressed through $\Lambda(\chi)$ as its m-th derivative over $i\chi$ at $\chi = 0$, i.e.,

$$\langle\langle Q^m\rangle\rangle = \left.\frac{\partial^m \ln\Lambda}{\partial(i\chi)^m}\right|_{\chi=0}. \tag{2.8}$$

Within this formalism, the conductance G, the Fano factor $\mathcal{F}$, and the factor $\mathcal{R}$ can be quantified as follows

$$G(V_{sd}) = \frac{\langle Q\rangle}{V_{sd}\Delta t} = \frac{e}{V_{sd}\Delta t}\left.\frac{\partial \ln\Lambda}{\partial(i\chi)}\right|_{\chi=0} \equiv G_0\Big\langle \operatorname{Tr}\boldsymbol{T}\Big\rangle_{|E-E_0|\leqslant eV_{sd}/2}, \tag{2.9}$$

$$\mathcal{F}(V_{sd}) = \frac{\langle\langle Q^2\rangle\rangle}{\langle\langle Q^2\rangle\rangle_{\text{Poisson}}} \equiv \frac{\Big\langle \operatorname{Tr}\left[\boldsymbol{T}\left(\boldsymbol{I}-\boldsymbol{T}\right)\right]\Big\rangle_{|E-E_0|\leqslant eV_{sd}/2}}{\Big\langle \operatorname{Tr}\boldsymbol{T}\Big\rangle_{|E-E_0|\leqslant eV_{sd}/2}}, \tag{2.10}$$

$$\mathcal{R}(V_{sd}) = \frac{\langle\langle Q^3\rangle\rangle}{\langle\langle Q^3\rangle\rangle_{\text{Poisson}}} \equiv \frac{\Big\langle \operatorname{Tr}\left[\boldsymbol{T}\left(\boldsymbol{I}-\boldsymbol{T}\right)\left(\boldsymbol{I}-2\boldsymbol{T}\right)\right]\Big\rangle_{|E-E_0|\leqslant eV_{sd}/2}}{\Big\langle \operatorname{Tr}\boldsymbol{T}\Big\rangle_{|E-E_0|\leqslant eV_{sd}/2}}, \tag{2.11}$$

where $\langle\langle Q^m\rangle\rangle_{\text{Poisson}} = e^m\langle Q\rangle$ denotes the value of $\langle\langle Q^m\rangle\rangle$ in the Poisson limit, in which all transmission probabilities are small.

2.2.2 Transfer matrix approach

Here we present a consistent way of extracting the scattering properties of a system through the mode matching. While the following description is devoted to monolayer graphene in the Corbino geometry (Appendix A in Ref. [75] describes a similar procedure for BLG), the adaptation of the method for rectangular systems is straightforward.

A generic wavefunction corresponding to a transmission channel l is given by a linear combination of two spinor functions corresponding to two independent solutions,

$$\phi^l(r) = a_1^l\phi_1^l(r) + a_2^l\phi_2^l(r), \tag{2.12}$$

where a_α^l are arbitrary amplitudes and $\phi_\alpha^l(r) = \left[\phi_{\alpha,A}^l, \phi_{\alpha,B}^l\right]^T(r)$ is a normalized spinor function with A and B corresponding to sublattice indices. The normalization has to be carried out in such a way that the total current remains constant. The current density can be written as

$$\vec{j} = ev_F \left[\phi^l(r)\right]^\dagger \mathbb{J}\phi^l(r), \tag{2.13}$$

where[2]

$$\mathbb{J} = \vec{\sigma}. \tag{2.14}$$

In principle, it is sufficient to normalize only the wavefunctions in the leads since the relation between them (the incoming, transmitted and reflected wavefunctions) ultimately defines matrices $\mathbf{r}$ and $\mathbf{t}$. Current conservation guarantees that amplitudes r_{mn} and t_{mn} preserve their probabilistic interpretation. A normalization carried out for the wavefunctions in the sample area is not necessary for successful mode matching. Although the amplitudes $\{a_\alpha^l\}$ quantifying the share of different solutions $\phi_\alpha^l(r)$ in the total wavefunction $\phi^l(r)$ lose their probability-related interpretation, one is not interested in them in the first place.

It is convenient to present a set of wavefunctions as a vector with each element corresponding to a different transmission channel. Since only a limited number of channels effectively contributes to the quantum transport, one can introduce the cutoff transmission channel M such that $l \in [-M, M]$. The cutoff is chosen large enough for the results not to be affected by M. One can write

$$\boldsymbol{\phi}(r) = \mathbb{M}(r) \begin{pmatrix} \boldsymbol{a}_1 \\ \boldsymbol{a}_2 \end{pmatrix}, \tag{2.15}$$

where $\mathbb{M}(r)$ is a $(4M+2)\times(4M+2)$ matrix, $\boldsymbol{a}_\alpha = \left[a_\alpha^{-M}, \ldots, a_\alpha^M\right]^T$. The explicit form of matrix $\mathbb{M}(r)$ will be presented later. The notation introduced in Eq. (2.15) is especially convenient in the case when we are dealing with a system with mode mixing introduced by position-dependent potential.

We are primarily interested in the relation between amplitudes $\boldsymbol{a}_\alpha$ connected with wavefunctions at different radii, say, r and R_i. The relation between wavefunctions at r and R_i can be represented by a propagator $\mathbb{U}(r, R_i)$

$$\boldsymbol{\phi}(r) \;=\; \mathbb{U}(r, R_i)\,\boldsymbol{\phi}(R_i). \tag{2.16}$$

The operator $\mathbb{U}(r, R_i)$ can be derived from an equation obtained by inserting (2.16) into the Dirac equation. The equation takes then the following form

$$\partial_r \mathbb{U}(r, R_i) = \mathbb{A}(r)\,\mathbb{U}(r, R_i), \tag{2.17}$$

with an initial condition $\mathbb{U}(R_i, R_i) = \mathbb{I}_{(4M+2)\times(4M+2)}$. Matrix $\mathbb{A}(r)$ carries the complete information about the potential and couplings in the system. If this matrix is

[2]For bilayer graphene, $\mathbb{J} = \mathbb{I}_{2\times2} \otimes \vec{\sigma}$, see [48, 76].

diagonal (for instance, in the MLG case, see [64, 65, 77]) we have $[\mathbb{A}(r), \mathbb{A}(r')] = 0$ for arbitrary r and r', and Eq. (2.17) has a simple solution

$$\mathbb{U}(r, R_i) = \exp\left[\int_{R_i}^{r} dr' \mathbb{A}(r')\right]. \tag{2.18}$$

Even if the condition $[\mathbb{A}(r), \mathbb{A}(r')] = 0$ is not met, an analytical solution is still possible as long as we can derive the wavefunctions. In such a case, the propagator is simply $\mathbb{U}(r, R_i) = [\boldsymbol{\phi}(r)]^{-1} \boldsymbol{\phi}(R_i)$. In other cases, one has to find $\mathbb{U}(r, R_i)$ numerically[3]. In the last article attached to this thesis, we have employed a fixed-step explicit Runge Kutta method of the 4th order [80–82]. Both the step as well as the angular-momentum cutoff M depend on the system size as well as on the magnetic field in an approximately linear manner (see Ref. [75]).

Once we know the propagator in the sample area, we can now translate it into a transfer matrix of the whole system by simply connecting the wavefunctions in the leads with the wavefunctions in the sample via the mode-matching

$$\begin{aligned} \boldsymbol{\phi}^L(R_o) &= \boldsymbol{\phi}^S(R_o) \\ &= \mathbb{U}(R_o, R_i)\, \boldsymbol{\phi}^S(R_i) \\ &= \mathbb{U}(R_o, R_i)\, \boldsymbol{\phi}^L(R_i), \end{aligned} \tag{2.19}$$

where $\boldsymbol{\phi}^L(R_o) = \mathbb{M}_L(r)\, \boldsymbol{a}$, and we have set doping in the leads to infinity. In such an approximation, the matrix $\mathbb{M}_L(r)$ can be presented as a Kronecker product $\mathbb{M}_L(r) = \mathbb{B}(r) \otimes \mathbb{I}_{(2M+1)\times(2M+1)}$ (we have dropped the phase constant connected with the doping in the leads as it is insignificant when calculating the transport properties), where

$$\mathbb{B}(r) = f(r) \begin{pmatrix} 1 & 1 \\ 1 & -1 \end{pmatrix}, \tag{2.20}$$

with $f(r) = 1/\sqrt{r}$ for the Corbino geometry[4]. Matrix $\mathbb{B}(r)$ is created from independent wavefunctions corresponding to two different directions of propagations (incoming and outgoing waves). The transfer matrix thus reads

$$\mathbb{T} = \mathbb{M}_L^{-1}(R_o)\, \mathbb{U}(R_o, R_i)\, \mathbb{M}_L(R_i). \tag{2.21}$$

Note that $\mathbb{M}(r)$ can be expressed through the propagator $\mathbb{U}(r, R_i)$ and $\mathbb{M}_L(R_i)$, i.e.,

$$\mathbb{M}(r) = \mathbb{U}(r, R_i)\, \mathbb{M}_L(R_i). \tag{2.22}$$

[3]The solution has a general Dyson series like form $\mathbb{U}(r, R_i) = \mathcal{T}\exp\left[\int_{R_i}^{r} dr' \mathbb{A}(r')\right]$, with $\mathcal{T}$ being a time ordering operator, see Refs. [78, 79].

[4]For a rectangular system, $f(r) = 1$.

Next, in order to obtain the transmission properties of the system, one needs to retrieve the scattering-matrix elements from $\mathbb{T}$. The transfer matrix can be expressed by blocks of the scattering matrix as follows

$$\mathbb{T} = \begin{bmatrix} \left(\mathbf{t}^{\dagger}\right)^{-1} & \mathbf{r}' \cdot (\mathbf{t}')^{-1} \\ -(\mathbf{t}')^{-1} \cdot \mathbf{r}' & (\mathbf{t}')^{-1} \end{bmatrix}, \tag{2.23}$$

with $\mathbf{t}$ ($\mathbf{r}$) being the transmission (reflection) matrix for a wavefunction incoming from the inner lead, and $\mathbf{t}'$ ($\mathbf{r}'$) being the transmission (reflection) matrix for a wavefunction incoming from the outer lead [29, 73].

Unfortunately, the transfer matrix acts as a two-edged sword. As mentioned above, the transfer matrix is directly linked with the propagator for the wave function in a system. Contrary to scattering matrices, transfer matrices can be combined with each other through a simple product, i.e., $\mathbb{T}_{1,2} \equiv \mathbb{T}_2 \cdot \mathbb{T}_1$. The problem lies within the eigenvalues of these matrices - they can be both exponentially small and large thus the multiplication of subsequent transfer matrices can be numerically unstable [65]. One can overcome this hurdle by translating the transfer matrices into scattering matrices which usually appear to be numerically stable [83–85]. The scattering matrices can be combined as follows

$$\mathbb{S}_{1,2} \equiv \mathbb{S}_1 \circ \mathbb{S}_2 = \begin{pmatrix} r_1 + t_1' \rho_1 r_2 t_1 & t_1' \rho_1 t_2' \\ t_2 \rho_2 t_1 & r_2' + t_2 \rho_2 r_1' t_2' \end{pmatrix}, \tag{2.24}$$

where $\rho_1 = (1 - r_2 r_1')^{-1}$ and $\rho_2 = (1 - r'_1 r_2)^{-1}$. Although being aware of this workaround, we have disregarded it and applied the floating-point arithmetics, setting the precision up to 300 decimal digits. This way it is sufficient to directly consider the transfer matrices.

3 Conductance scaling for ballistic bilayer graphene

3.1 Conductance of disordered systems and the scaling function

One of the core concepts behind the scaling theory of localization is the *single parameter scaling hypothesis*. It states that the so-called scaling function $\beta(g) = d\log g/d\log L$, describing the dependance of dimensionless conductance $g = G/(e^2/\hbar)$ on the system size L, is a function of conductivity only, disregarding the size of the system or the magnitude of disorder in the system [86, 87]. Introduced by Abrahams and his coworkers [88] after earlier works of Anderson, Thouless, Wegner and coauthors [89–91], the scaling function β differs from system to system based on the dimensionality as well as symmetry classes of the microscopic Hamiltonians.

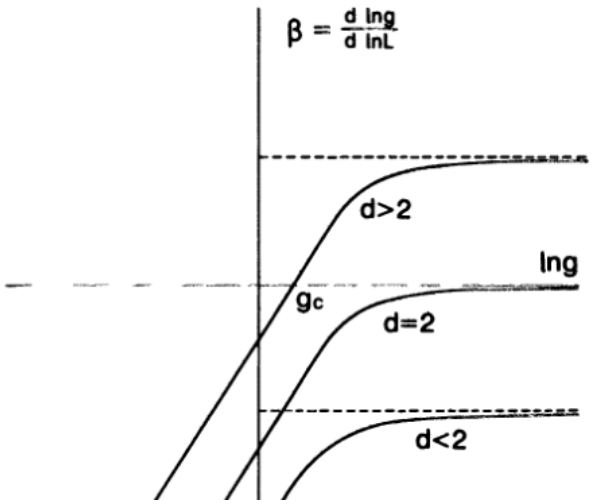

Figure 3.1: Scaling function for disordered systems of different dimensionality. Note that both 1D and 2D systems are expected to be insulating, provided no interaction is taken into account. Adapted from Ref. [87].

When dealing with a highly conducting metal, one expects an ohmic-like behavior, i.e., $g \propto L^{d-2}$ (where d is the dimension of the system). In such a case, the scaling function is constant, $\beta = d - 2$. In an opposite scenario, if the charge carriers

in a material are localized due to impurities (the so-called *Anderson localization*), conductance decreases exponentially with the system size $g = g_1 \exp(-\alpha L)$, and thus $\beta = \ln(g/g_1)$. These two limits are connected since it is assumed that β is a continuous function[1]. In general, if $\beta < 0$, the conductance decreases with increasing L, and the system is in the localization regime. If $\beta > 0$, the system is in a metallic regime (see Fig. 3.1). The metal-insulator transition takes place if $\beta = 0$ and $\beta' > 0$. For $d = 2$ the conductivity σ and the conductance G are connected through a simple relation $\sigma = GW/L$. Since we are considering the case with $W/L = const$, hereinafter we redefine $\beta \equiv \beta(\sigma)$.

In an undoped monolayer graphene, three different scenarios are expected. If there is no disorder, the conductivity $\sigma = \sigma_{MLG}$ is L-independent [22, 34]. The long range disorder[2] (responsible for the intravalley scattering) leads to $\sigma \to \infty$ for $L \to \infty$ [65, 66]. To the contrary, the short range disorder[3] introducing intervalley scattering leads to suppression of conductivity ($\sigma \to 0$) for sufficiently large systems [94, 95].

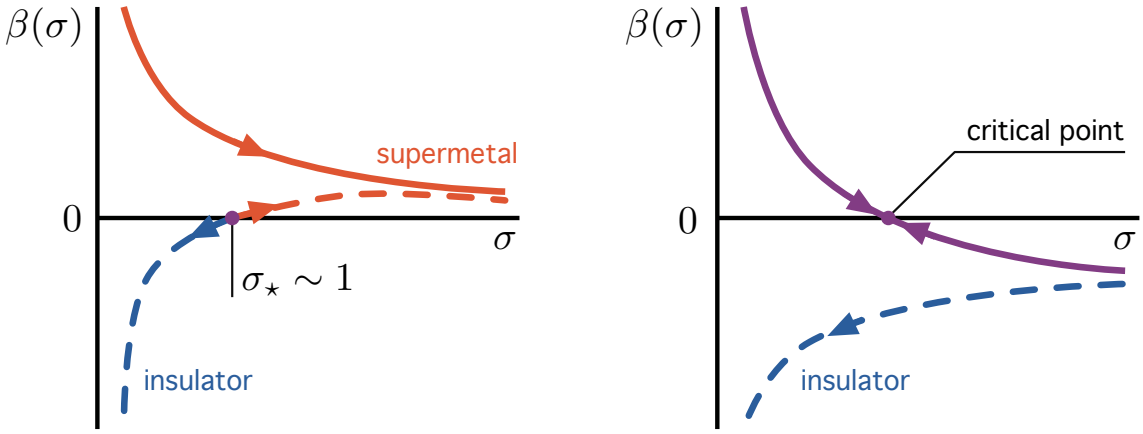

Figure 3.2: Comparison between scaling functions for Dirac and spin-orbit systems depicted with solid and dashed lines, respectively. The left (right) picture shows a system without (with) Coulomb interaction taken into account. Adapted from Ref. [96].

Coulomb interaction between the charge carriers may significantly alter the conductance scaling (see Fig. 3.2). While a noninteracting spin-orbit system has a repulsive transition point separating insulating and metallic phases, the Coulomb interaction turns it to an insulator. Similarly, a disordered system of noninteracting Dirac fermions always behaves like a metal. Coulomb repulsion affects this behavior

[1] In some particular cases the continuity of β can be lifted, for instance by the spin-orbit impurities [86].

[2] This type of disorder can describe for instance the impact of charged dopants or the influence of the ripples [67].

[3] For instance, the Anderson type of disorder modeling adatoms or charged impurities [92, 93].

introducing an attractive critical point, for which the conductivity $\sigma = \sigma_\star$ no longer depends on the system size [65, 66, 97].

A similar analysis can be carried out for bilayer graphene. As its charge carriers are both chiral and massive, it can be anticipated that conductance scaling in this system may show a new, nontrivial behavior. In particular, the skew interlayer hopping integrals introduce conductance dependence on both the orientation and the size of the sample [50]. In Refs. [75, 96] the author and Rycerz have investigated the scaling properties of the conductivity in the context of one parameter scaling hypothesis.

3.2 Conductivity dependence on the system size: single parameter scaling for BLG

The considered system is a ballistic (disorder free) sample. Following Moghaddam and Zareyan [50], we employ the four-band Hamiltonian with skew-interlayer hopping integrals (in such a picture electron-electron interactions are not taken into account) and the Landauer-Büttiker formalism. Our analysis is focused on the transition between $\sigma = \sigma_{BLG}$ for small systems ($L \ll 50$ nm) to $\sigma \to 3\sigma_{BLG} \equiv \sigma_\star$ for $L \to \infty$. The latter limit may be affected by a specific choice of crystallographic orientation since BLG conductance is not isotropic for $t' \neq 0$ (see above).

Size dependence of the conductivity has been already considered in Ref. [32] on the example of a wide, rectangular sample ($W \gg L$) with a zigzag orientation (identified by the angle $\theta = 0°$). Based on the smooth and monotonic $G(L)$ behavior for large L, we have proposed the size dependence of the conductivity $\sigma = GL/W \approx \sigma_\infty [1 - (\lambda/L)^\gamma]$ in which σ_∞, λ and γ are free parameters. These parameters have been subsequently fitted to data sets obtained numerically for different values of the skew interlayer hopping integral t'. Best fitted parameters $\gamma \approx 0.23$ and $\sigma_\infty \approx \sigma_\star$ for two different values of skew hopping integral, $t' = 0.16$ eV and $t' = 0.32$ eV, suggested a more general nature of the conductivity dependence on L.

The size-dependent conductivity may contribute to the explanation of the discrepancy between the experimental value of the minimal conductivity $\sigma = 3/2\sigma_{BLG}$ - $5/2\sigma_{BLG}$ [98–100] and theoretical predictions for ballistic samples [49, 50]. While the disorder as well as interactions may contribute to this difference, the size of the measured sample may be a crucial factor.

The analysis is expanded in Ref. [96] by numerically reproducing the scaling function β. Contrary to the previous case, we have considered an orientation for which[4] $\theta = 45^o$. Based on the fitted parameters, we have recovered the approximate scaling function $\beta = d\log\sigma/d\log L = -\gamma(1 - \sigma_\star/\sigma)$. Best fitted parameters $\gamma \approx 0.53$ and $\sigma_\star \approx 0.98$ lead to $\beta > 0$ for $\sigma < \sigma_\star$, which indicates a metallic character of bilayer graphene. Interestingly, $\sigma = \sigma_\star$ is an attractive point ($\beta'(\sigma_\star) < 0$ for $\gamma \approx 0.53$) of

[4] As mentioned in Ref. [50], conductivity for asymptotically large systems with $\theta = 0^o$ should be $\sigma \simeq 7/3\sigma_{BLG}$ while for $\theta = 45^o$ it approaches $\sigma \simeq 3\sigma_{BLG}$.

the renormalization group flow. Surprisingly, such a behavior was earlier predicted for disordered Dirac systems with Coulomb interaction [97]. The inclusion of t' in the analysis of ballistic BLG, with no interaction taken into account, thus creates a nontrivial analogy between these two systems.

3.2.1 Shot noise characteristics

Results from Ref. [96] have been supplemented by an analysis of the Corbino disk in which the influence of crystallographic orientation is eliminated [75]. Apart from investigation of the scaling function, we have considered the length dependence of the Fano factor $\mathcal{F}$, and the third charge transfer cumulant $\mathcal{R}$. We have chosen two radii ratios ($R_o/R_i = 3/2$ and $R_o/R_i = 2$) for which the system has a large number of transmission channels. At the charge-neutrality point such systems are expected to exhibit a pseudodiffusive behavior. With increasing size of the system, the conductivity strongly diverges from the pseudodiffusive value σ_{BLG}, whereas both $\mathcal{F}$ and $\mathcal{R}$ are close to pseudodiffusive average values ($\bar{\mathcal{F}} = 1/3$ and $\bar{\mathcal{R}} = 1/15$). Both these characteristics show Fabry-Perot like oscillations slowly decreasing with the system length $R_o - R_i$. These results suggest that the pseudodiffusive regime of the quantum transport perseveres the breakdown of the parabolic dispersion relation due to the trigonal warping. However, in such a case the pseudodiffusive character of the charge transport is indicated by the higher charge-transfer cumulants rather than by the universal conductivity.

3.2.2 Impact of electrostatic bias between the layers

Another problem tackled in Ref. [96] is the effect of bias between the layers V on the conductivity (discussed as a function of Fermi energy). The bias potential can emerge by applying an external, perpendicular, electric field and is responsible for opening an energy gap [20]. Some experiments suggest that the bias between the layers can spontaneously emerge in BLG samples with dopings near the charge-neutrality point due to electron-electron interactions [71, 72].

While it is possible to obtain analytically wavefunctions for $t' = 0$, the case with $t' \neq 0$ and $E \neq 0$ has no analytical solution. This is not an issue as it is sufficient to find numerical forms of wavefunctions and follow standard mode matching procedures. Notice that there is no mode mixing in case of a rectangular sample. At zero bias potential ($V = 0$), in a small vicinity of the Dirac point $|E| < E_L \simeq t_\perp \left(t'/t_0\right)^2/4$ (where E_L is the Lifshitz energy), the conductivity monotonically increases with t'. Outside this region, the conductivity gradually loses its dependence on t' with increasing Fermi energy. At $V \gg E_L$ (but still of the order of meV) the conductivity reaches a maximum close to $\sigma \approx \sigma_{BLG}$ for $E = \pm V/2$ and an arbitrary value of t'. This maximum is substantially smaller than the first peak in conductivity for $V = 0$, and seems to reproduce the behavior of a monolayer sample at the Dirac point. Again, effects of V and t' are suppressed at Fermi energies $E \gg V \gg t'$.

Results presented in this chapter are based on the following publications:

- G. Rut and A. Rycerz, *Pseudodiffusive conductance, quantum-limited shot noise, and Landau-level hierarchy in biased graphene bilayer*, **Physical Review B 89, 045421 (2014)**;
- G. Rut and A. Rycerz, *Minimal conductivity and signatures of quantum criticality in ballistic graphene bilayer*, **Europhysics Letters 107, 47005 (2014)**; and the unpublished manuscript
- G. Rut and A. Rycerz, *Trigonal warping, pseudodiffusive transport, and finite-system version of the Lifshitz transition in magnetoconductance of bilayer-graphene Corbino disks,* http://arxiv.org/abs/1511.04705.

4 Magnetoconductance of bilayer graphene

4.1 Overview

In 2006, Prada and coworkers investigated the magnetoconductance of a short and wide ($W \gg L$) ballistic graphene junction[1] [30]. Similarly as in 2DEG, the character of charge transport depends the mutual relation between the system size L and the cyclotron diameter $2r_c = 2l_B^2 E/(\hbar v_F)$, with $l_B = \sqrt{\hbar/(eB)}$ being the magnetic length. Namely, the conductance remains ballistic (if $2r_c > L$) or is field suppressed (if $2r_c < L$). Strikingly, quantum transport in close vicinity of the LLs counter-intuitively avoids the field suppression even if $2r_c \ll L$. The conductance as well as higher charge transfer cumulants $\mathcal{F}$ and $\mathcal{R}$, remain close to their pseudodiffusive values at the Dirac point (the lowest Landau level is pinned to the charge-neutrality point, in case the Zeeman splitting is neglected) and other Landau levels. In other words, the pseudodiffusive transport regime appears in the finite vicinity of any LL, the width of which decays as $\exp\left[-(L/l_B)^2/2\right]$.

The pseudodiffusive character of quantum transport on LLs in a monolayer graphene suggested that an analogous regime has to exist in bilayer graphene. A question remained, how the additional degeneracy of the two lowest LLs (0th and 1st), occurring at the charge-neutrality point [52], affects the conductance and higher charge-transfer cumulants.

4.2 Method of approach

Following Snyman and Beenakker [48], we have derived BLG magnetoconductance by applying the effective low energy Hamiltonian first without skew interlayer hopping integrals ($t' = 0$). Subsequently, we have investigated how the conductance is affected by the *trigonal warping.* Our analysis revealed that the impact of t', above a crossover magnetic field B_L, is swiftly suppressed with B, approaching the high magnetic field limit in which one can disregard the skew interlayer hopping integrals, at least for $W/L \gg 1$. Below we summarize our results for these cases in separate sections devoted to the high magnetic field limit (for $t' = 0$) and to the impact of trigonal warping (for $t' \neq 0$) .

[1] The Authors considered edge currents in the limit $W \gg L$ as negligible.

It must be noted that the applicability of an approximation neglecting trigonal warping is limited. McCann and Fal'ko have shown that the spectrum of Landau levels in bilayer graphene can be accurately described by neglecting t' as long as $\hbar l_B^{-1} > t' t_\perp / (2 v_F t_0)$ [52]. Moreover, McCann and Koshino specified the energy range $(t'/t_0)^2 t_\perp < E < t_\perp$ in which the *trigonal warping* does not have to be taken into account [101, 102]. Lastly, Moghaddam and Zareyan, through quantum transport analysis of BLG with $t' \neq 0$, have proved that for systems of length $L \ll \pi \hbar v_F t_0 / (t' t_\perp) \approx 50\text{nm}$ the transmission amplitudes for ballistic BLG have the same asymptotic form as derived by Snyman and Beenakker [48, 50].

4.3 High magnetic field limit for $t' = 0$

As in a monolayer graphene, the BLG conductance, $G \simeq \sigma_{BLG} W/L$, is not affected by magnetic field at the Dirac point. Moreover, we have shown that at higher LLs the conductance of bilayer graphene, $G \simeq \sigma_{MLG} W/L = \sigma_{BLG} W/(2L)$, turned out to be the same as in a single layer[2]. The result can be associated with the fact that, as mentioned in the previous section, the Dirac point is shared by two Landau levels while other LLs are not degenerated. This has been confirmed by further investigations for a BLG with an electrostatic bias between the layers.

An external electric field, perpendicular to the sample plane, creates a potential difference between the layer which results in an energy gap [20, 101] and lifted valley degeneracy of LLs. In effect, the lowest LL breaks into four distinct Landau resonances while each of the other LLs splits into two. The conductance at each of these resonances is equal to $G = \sigma_{BLG} W/(4L)$, that is, a half of the monolayer conductance. The second and the third charge-transfer cumulants, $\mathcal{F} = 1/3$ and $\mathcal{R} = 1/15$, remain the same as in MLG.

4.4 Finite voltage effect

While the above results have been derived supposing the linear response regime, their physical meaning may be limited, especially in high magnetic fields. Resonances with Landau levels rapidly shrink with increasing magnetic field [30] and experimental systems always have a finite source-drain voltage V_{sd}, often larger than the transmission resonance width $\mathcal{W}$, $V_{sd} \gtrsim \mathcal{W}$. Similar reasoning applies for systems with fluctuating dopings which might especially affect long-time measurements of shot noise characteristics. Both these situations can be treated with the Levitov formula [29, 68], in which the finite voltage (or the fluctuating doping) is introduced through an average over a relevant doping integral.

We have proposed an empirical model of transmission resonances $T(E, k_y)$ in the wavevector-doping parameter plane. Each resonance is modeled as a product of the Breit-Wigner distribution, describing the doping dependence, and a function

[2]The same result is expected for $t' \neq 0$ in high magnetic fields.

$1/\cosh^2(\mathcal{A}k_yL)$, where k_y is the transverse wavevector, and $\mathcal{A}$ is a free parameter close to unity. An analytical approximation for wide samples has allowed us to predict the dependence of both $\mathcal{F}(V_{sd})$ and $\mathcal{R}(V_{sd})$ on the voltage V_{sd}. Apart from restoring the pseudodiffusive values $\mathcal{F}(0) = 1/3$ and $\mathcal{R}(0) = 1/15$ for zero voltage, we have predicted $\mathcal{F}(\infty) \to 2/3$ and $\mathcal{R}(\infty) \to 2/5$ for high voltages. A numerical analysis, based on actual transmission resonances following from the mode matching, revealed that the limiting values are $\mathcal{F}(\infty) \simeq 0.7$ and $\mathcal{R}(\infty) \simeq 0.5$, respectively. These results allow us to expect that both $\mathcal{F}(V_{sd})$ and $\mathcal{R}(V_{sd})$ are still quantum-limited beyond the linear transport regime.

4.5 Effect of trigonal warping

In chapter 5, we investigate the impact of skew interlayer hopping integrals in the context of the Corbino geometry. As the Corbino geometry with $t' \neq 0$ can be approached only numerically, we first attempt to understand its properties by exploring, in this section, its resemblance with narrow rectangular samples. For moderate width-to-length ratios $W/L \lesssim 5$, such a system also shows magnetoconductance oscillations[3]. The main advantage of such a geometry over a disk is the absence of mode mixing, which allows one to derive the properties of BLG in analytical terms, at least in principle.

The magnetoconductance of BLG monotonically increases with magnetic field from, $B = 0$ up to a crossover field B_{res}, for which the effect of *trigonal warping* is maximal. Above this crossover field B_{res} the influence of t' is slowly suppressed by the magnetic field B and the conductance decreases asymptotically as B^{-1}, approaching $G \simeq \sigma_{BLG}W/L$ (for large W/L). This, in principle, means that the effective Hamiltonian with $t' = 0$ correctly describes pseudodiffusive systems in the high magnetic field limit ($B \to \infty$).

The second effect, present in systems with $W \sim L$, is the emergence of beating patterns, with the envelope period proportional to square root of magnetic field $\sqrt{B}$. In the high field limit, these beating patterns remain visible thus the interference effect predicted in Ref. [103] should not emerge for $t' \neq 0$.

During the mode matching we have discovered a peculiar effect which manifests itself both via beating patterns in magnetoconductance as well as via the average conductance. Due to a nonzero skew interlayer hopping integrals two species of quasiparticles, feeling a different system size $L_\pm$ (with the index $\pm$ related to the presence of two layers), dependent on both the magnetic field B and the hopping integral t'. These two effective sizes of the system, L_+ and L_-, lead to different conductance values originating from two distinct transmission resonances $G_\pm \simeq \sigma_{BLG}W/(2L_\pm)$ which in moderate magnetic fields are larger (as a sum) than $G \simeq \sigma_{BLG}W/L$, $G_+ + G_- > G \simeq \sigma_{BLG}W/L$. Also, L_+ and L_- lead to two different

[3]One should not expect these oscillations to appear in real life systems. Here they appear due to a simplified description with no boundary effects taken into account.

magnetic fluxes $\Phi_\pm = BWL_\pm$ piercing the system. This results in magnetoconductance oscillations with different frequencies, leading to the appearance of beating patterns.

Results referred in this chapter are based on the following publications:

- G. Rut and A. Rycerz, *Pseudodiffusive conductance, quantum-limited shot noise, and Landau-level hierarchy in biased graphene bilayer*, **Physical Review B 89, 045421 (2014)**;
- G. Rut and A. Rycerz, *Trigonal warping, pseudodiffusive transport, and finite-system version of the Lifshitz transition in magnetoconductance of bilayer-graphene Corbino disks,* http://arxiv.org/abs/1511.04705.

5 Quantum relativistic Corbino effect (QRCE)

5.1 Introduction

The Corbino disk is an experimental setup in which a ring-shaped sample, characterized by the inner radius R_i and the outer radius R_o, is surrounded from both exterior and interior sides with metallic leads (see Fig. 5.1). The Corbino geometry has been known in physics for over a century [104, 105] and has been employed in the investigation of magnetic field related properties and effects such as magnetoresistivity or classical and quantum Hall effects. Such a system is free of boundary effects, which are often difficult to cope, allowing to focus on intrinsic properties of the analyzed material.

The theoretical analysis of conductance in nano-scale Corbino disks in 2DEG was provided by George Kirczenow in 1994 [106]. Conductance of a disk with ideal contacts turned out to be quantized with steps of odd multiples of $2e^2/h$. Further analysis revealed linear suppression of conductance in the magnetic field [107, 108]. In 2009 Rycerz, Recher and Wimmer showed that, while the conductance of MLG Corbino disk exhibits a modulation with a period $\sim \pi\hbar v_F/(R_o - R_i)$, the quantization will not occur [109]. Moreover, in 2010 Rycerz and Katsnelson independently investigated the magnetoconductance of MLG disks [56, 57]. In the pseudodiffusive transport regime, conductance exhibits oscillatory dependence on magnetic field due to discrete spectrum of transmission channels. This unexpected behavior allows to coin the term: *quantum relativistic Corbino effect* (QRCE) [62].

In the pseudodiffusive regime, conductance of graphene Corbino disk oscillates periodically with magnetic flux piercing the disk area $\Phi_D = B\pi\left(R_o^2 - R_i^2\right)$. The larger the radii ratio R_o/R_i, the larger the oscillations amplitude. The amplitude exceeds 5% of the mean conductance $G = 8g_0/\log\left(R_o/R_i\right)$, where $g_0 = e^2/h$, for a system with the radii ratio $R_o/R_i \gtrsim 5$.

In 2006 Akhmerov and Beenakker considered the pseudodiffusive transport through a graphene junction with one of the contacts being a superconductor[111]. Similarly as for a system with two metallic leads, the conductance for such a setup can be expressed in terms of transmission probabilities, and reads

$$G = 8g_0 \sum_j \frac{T_j^2}{\left(2 - T_j\right)^2}. \tag{5.1}$$

Setting the superconductor as the inner lead in the Corbino disk defines the so-called

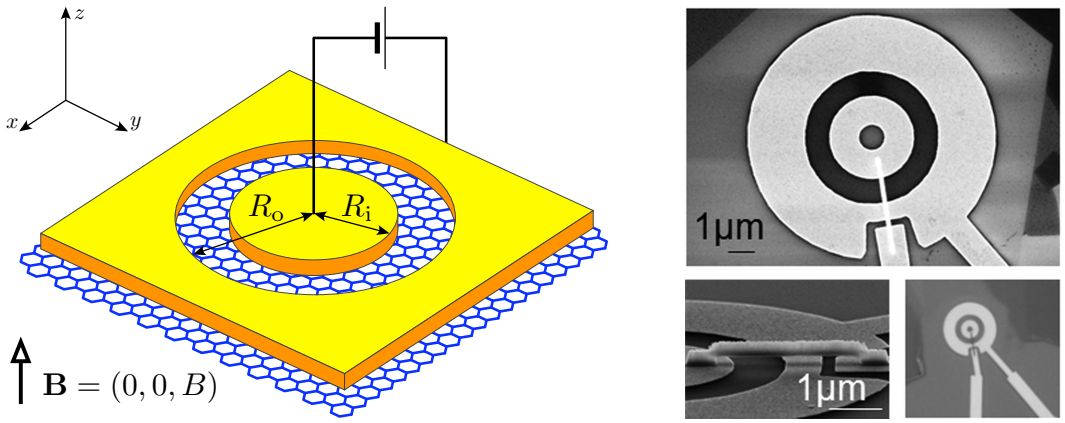

Figure 5.1: Left: Visualization of the Corbino disk in graphene in a perpendicular magnetic field B. The ring shaped sample are is characterized by inner R_i and outer R_o radii. The current is passed through the sample between metallic leads (yellow areas) which are modeled by infinitely doped graphene. Doping in the sample is controlled by a gate electrode (not shown). Right: Scanning electron micrograph of a real device. Pictures reprinted from Refs. [57] (left) and [110] (right).

Andreev-Corbino geometry. In such a setup the QRCE oscillations amplitude is magnified. For instance, amplitudes exceeding 5% of the mean conductance appear already for $R_o/R_i \gtrsim 2.2$.

Briefly speaking, the oscillations associated with QRCE emerge due to a limited number of transmission channels contributing to the transport. The transmission probabilities of passing through the disk are given by

$$T_j \equiv T\left(j + \Phi_D/\Phi_0\right) = \frac{1}{\cosh^2\left[\mathcal{L}\left(j + \Phi_D/\Phi_0\right)\right]}, \tag{5.2}$$

where $\Phi_0 = (2h/e)\,\mathcal{L}$, with $\mathcal{L} = \log\left(R_o/R_i\right)$, and $j = \pm 1/2, \pm 3/2, \ldots$ denotes an eigenvalue of the total angular momentum operator $J_z = -i\hbar\partial_\phi + \hbar\sigma_z/2$. The larger the radii ratio R_o/R_i, the narrower the transmission resonance in the space of angular momentum eigenvalues. While the spectrum of J_z eigenvalues is discrete, Φ_D/Φ_0 changes continuously with magnetic field, and thus a periodic behavior is predicted for the conductance $G = 4g_0 \sum_j T_j$. At radii ratios of the order of $R_o/R_i \gtrsim 5$, each conductance maximum ($G_{max} \overset{R_o \gg R_i}{\to} 4g_0$) corresponds to single-channel transport at $j = -\Phi_D/\Phi_0$, whereas the conductance minimum ($G_{min} \overset{R_o \gg R_i}{\simeq} 32 g_0 R_i/R_o$) originates from two equivalent transmission channels with $j_\pm = -\mathrm{int}\left(\Phi_D/\Phi_0 \mp 1/2\right) - 1/2$.

Both the conductance amplitude and the period can be extracted from the Landauer-Buttiker formula by expanding it in the Fourier series in units of Φ_D/Φ_0. Since the

period in flux units Φ_D/Φ_0 is simply 1, we can write

$$\frac{G}{4g_0} = \frac{a_0}{2} + \sum_{m=1}^{\infty} a_m \cos\left(2\pi m \Phi_D/\Phi_0\right), \tag{5.3}$$

where $a_\alpha = 2\int_0^1 \sum_j T\left(j+x\right)\cos\left(2\pi\alpha x\right)dx$. The expression for a_α can be simplified into an integral over a single transmission mode, since

$$\begin{aligned}\int_0^1 \sum_j T\left(j+x\right)\cos\left(2\pi\alpha x\right)dx &= \sum_j \int_j^{j+1} T(x)\cos\left(2\pi\alpha x\right)(-1)^\alpha dx \\ \simeq (-1)^\alpha \int_{-\infty}^{\infty} T\left(x\right)\cos\left(2\pi\alpha x\right)dx &= \frac{2\pi^2\alpha(-1)^\alpha}{\mathcal{L}^2 \sinh\left(\pi^2\alpha/\mathcal{L}\right)}.\end{aligned} \tag{5.4}$$

The conductance expressed in the Fourier series reads

$$G = \frac{8g_0}{\mathcal{L}} + \sum_{m=1}^{\infty} G_m \cos\left[2\pi m \Phi_D/\Phi_0\right], \tag{5.5}$$

in which $G_m = g_0\left(4\pi/\mathcal{L}\right)^2(-1)^m m\,\mathrm{csch}\left(\pi^2 m/\mathcal{L}\right)$. The first part of Eq. (5.5), $8g_0/\mathcal{L}$, represents the pseudodiffusive value of conductance, the latter describes the oscillations. For moderate radii ratios, say $R_o/R_i \lesssim 10$, we get $G_1 \gg G_2 \gg ...$, thus $G \approx 8g_0/\mathcal{L} + G_1\cos\left[2\pi m\Phi_D/\Phi_0\right]$ becomes a reasonable approximation. One can now easily link Φ_0 with the period and G_1 with oscillations amplitude. For the Andreev-Corbino setup, while the mean conductance remains the same, the amplitudes are transformed as $G_m\left(\mathcal{L}\right) \to G_m^{AC}\left(\mathcal{L}\right) \equiv 2G_m\left(2\mathcal{L}\right)$, which effectively leads to a significant amplification of the oscillations at given $\mathcal{L}$.

5.2 QRCE in bilayer graphene

Since coupling between the layers in BLG plays an important role in the description of transport properties of this material, it has been anticipated that its magnetoconductance oscillations would not be simply twice as large as in MLG even in the absence of trigonal warping. Skew interlayer hopping integrals t' lead to *trigonal warping* of the dispersion relation in which secondary Dirac points are created. The cylindrical symmetry, allowing one to discuss the quantum transport in analytical terms, is in this case broken making it necessary to find a workaround. On the other hand, the results of Ref. [32] allow to expect that in the high field limit it is enough to consider $t_\perp$ as the only interlayer hopping integral. For such a simplified model it was possible to obtain an analytical description of QRCE. Here we refer results for the case of $t' = 0$ (after Ref. [103] - the high magnetic field limit) and $t' \neq 0$ (after Ref. [75]).

5.2.1 High magnetic field limit; $t' = 0$

The cylindrical symmetry of the low energy Hamiltonian (applicable for $t' = 0$), which correctly describes the pseudodiffusive behavior of BLG in high magnetic field limit, allows us to analytically derive the transmission properties of the Corbino disk at the charge-neutrality point. As it was shown in Refs. [32, 48], there are two transmission resonances in the angular-momentum space[1]. While the shape of these resonances is determined only by the radii ratio R_o/R_i, the distance between them depends on the system size as well as on the coupling between the layers characterized by $t_\perp$. Regardless of $t_\perp$, pseudodiffusive conductance is simply twice as large as the conductance of MLG. On the other hand, the varying distance between the resonances leads to an interference effect modulating oscillations amplitude. If the system is large enough ($R_i \gtrsim 10l_\perp$, $R_o/R_i \gtrsim 3$), it is possible to estimate a condition for two extreme cases of this interference

$$\mathcal{L} \approx 4 \ln \left(R_i/2l_\perp \right) /p, \tag{5.6}$$

where p is an odd (even) integer for vanishing (maximal) oscillations. Generally speaking, the Corbino-Andreev setup, in which one of the contacts is a superconductor, magnifies the oscillations. Even if a system satisfies condition (5.6) with p being an odd integer, the oscillations do not vanish in the same manner as in a regular system. Instead, they still remain pronounced and their period is twice smaller than Φ_D. This is due to the ratio of Fourier amplitudes $G_1^{AC}/G_2^{AC} \not\gg 1$ for radii ratios $R_o/R_i \gtrsim 2$.

As there is only a single transmission resonance in the angular-momentum space associated with any LL other than those at the Dirac point, the BLG disk effectively behaves in the same way as in MLG. The mean conductance, as well as the oscillation amplitudes, are equal. If an electrostatic bias between the layers opens an energy gap, a similar behavior is expected for the lowest LL as well (LLs in such a case are no longer degenerated, thus interference effects originating from $t_\perp$ are lifted).

5.2.2 Impact of trigonal warping

The skew interlayer hopping integrals break the cylindrical symmetry of the effective low-energy Hamiltonian. We have overcome this problem by treating elements of the Hamiltonian proportional to t' as a perturbation potential and expressing the wavefunctions as linear combinations of angular-momentum eigenfunctions. At the cost of introducing mode mixing to our analysis, this procedure allows us to retrieve the transmission properties of the analyzed system due to a simple relation between the Dirac equation and the transfer matrix. Furthermore, we have based a qualitative description of the Corbino disk's behavior on its resemblance to a rectangular sample with periodic boundary conditions (see sec. 4.5).

[1] In the Corbino disk, these channels correspond simply to eigenvalues of the angular momentum operator J_z, while in a rectangular geometry they are connected with the transverse momentum p_y.

Most remarkably, the suppression of oscillations, predicted for some particular parameter in the $t' = 0$ case (see Eq. (5.6)), do not appear in the presence of trigonal warping. Instead, similarly as in the rectangular sample, magnetoconductance oscillations show beating patterns. Although the envelope is not as regular as in a rectangular system (presumably because of the mode mixing), their period is still proportional to $\sqrt{B/t'}$. Beating patterns appear also for other charge transfer cumulants, such as $\mathcal{F}$ and $\mathcal{R}$. Other trigonal-warping effects identified for a rectangular sample, such as the enhanced mean conductance (with a maximum near a crossover field B_{res}), reappear for the Corbino geometry as well. Since both the envelope period and the mean conductance depend on t', the QRCE can be utilized to determine the skew interlayer hopping integrals.

It is important to point out that the beating patterns appear only at the charge-neutrality point as it hosts two LLs. In the high field limit, the quantum transport at Landau levels outside the Dirac point can be correctly described with $t' = 0$.

5.3 Beyond the linear response regime

The energy range in the vicinity of a given LL, in which the pseudodiffusive transport regime occurs, decays exponentially with the magnetic field. For this reason, accessing the linear response regime may become challenging (see also sec. 4.4). With this hurdle in mind, the QRCE has been investigated in a MLG system with a finite source-drain voltage V_{sd} [112]. Following a similar procedure as in the case with a rectangular sample of BLG (see Ref. [32]), the charge transfer cumulants have been derived using the Levitov formula [29].

It turns out that the conductance vanishes in the high-field limit for any finite voltage $V_{sd} \neq 0$, yet the oscillations for $\mathcal{F}$ and $\mathcal{R}$ persevere. The magnitude, as well as the period of these oscillations are approximately independent of V_{sd}, and mean values of $\mathcal{F}$ and $\mathcal{R}$ for any $V_{sd} \neq 0$ monotonically approach limits $\bar{\mathcal{F}} \simeq 0.76$ and $\bar{\mathcal{R}} \simeq 0.55$ with increasing magnetic field. Interestingly, these asymptotic values do not depend on the size of the disk or its radii ratio and thus should reappear for other graphene-based devices with finite source drain voltages at high magnetic fields. These limits can be considered as high-fields analogs of pseudodiffusive shot noise characteristics ($\mathcal{F} = 1/3$ and $\mathcal{R} = 1/15$), relevant for ballistic graphene systems with finite voltage and high magnetic field.

5.4 QRCE in 2DEG

The QRCE appears either in BLG or MLG, two examples of systems with quasiparticles described by the Dirac equation. As a natural consequence, an investigation whether this effect has an analog in the Schrödinger system has been carried out in Ref. [103]. In principle, magnetoconductance of 2DEG Corbino disk has been already analyzed by George Kirczenow in 1994 [106], yet the particular scenario at

which QRCE may emerge has not been considered. Firstly, QRCE may appear only on LLs. The conductance at LLs has not been discussed in Ref. [106] since these energy levels depend on the magnetic field and thus it might have seem of a limited importance, also because relatively large radii ratios ($R_o/R_i \gtrsim 3$) are required. Moreover, Kirczenow has modeled ideal contacts by applying a peculiar angular-momentum dependent potential, allowing to introduce wavefunctions in form of cylindrical waves. In order to focus on the case with clear relation to Dirac systems, a system in which potential in the leads is large but constant has been considered.

At low magnetic fields, the conductance of 2DEG Corbino disk shows several distinct maxima corresponding to quantum-dot energy levels. They gradually evolve with increasing magnetic field into resonances corresponding to LLs. Away from these resonances, the conductance is suppressed provided the field exceeds the value $B > \sqrt{2mE}/\left[e\left(R_o - R_i\right)\right]$ (here m is the effective mass and $-e$ is the electron charge), which separates the ballistic and quantum-tunneling transport regimes.

The difference between BLG and 2DEG emerges in the quantum-tunneling transport regime. In the Dirac system the conductance oscillates with increasing magnetic field but its average value remains constant. In the Schrödinger system the conductance simply vanishes at strong magnetic fields. This shows that the QRCE appearing in the pseudodiffusive transport regime is a purely relativistic effect and has no analog in nonrelativistic systems.

Results presented in this chapter are based on the following publications:

- G. Rut and A. Rycerz, *Magnetoconductance of the Corbino disk in graphene: Chiral tunneling and quantum interference in the bilayer case,* **Journal of Physics: Condensed Matter 26, 485301 (2014)**;
- G. Rut and A. Rycerz, *Quantum-limited shot noise and quantum interference in graphene based Corbino disk*, **Philosophical Magazine 95, 599-608, (2015)**; and the unpublished manuscript
- G. Rut and A. Rycerz, *Trigonal warping, pseudodiffusive transport, and finite-system version of the Lifshitz transition in magnetoconductance of bilayer-graphene Corbino disks,* http://arxiv.org/abs/1511.04705.

6 Conditions for conductance quantization in graphene nanostructures

6.1 Overview

Conductance quantization visualizes the role of transmission channels in the description of quantum transport [29, 73]. The effect was observed for the first time in 1988 in GaAlAs-GaAs heterostructures [113, 114]. The 2DEG formed close to the interface of the two structures has been modeled by gate electrodes to create an effective waveguide with a constriction. The applied gate voltage allowed to control the width of the constriction and, in result, the number of transmission modes. With continuously increasing gate voltage, the conductance of the system varied in steps of $2e^2/h$ (see Fig. 6.1).

A relatively simple condition for conductance quantization can be derived for a 2DEG waveguide with an adiabatic constriction characterized by the minimal width a and the second derivative of the width as a function of the longitudinal coordinate a'' [29, 115]. The smearing of nth step is of the order $\Omega_n = [\hbar^2 n/(2m)]\sqrt{a''/a^3}$. The conductance of a system with such a constriction can be approximated by

$$G = 2g_0\left\{n - 1 + \left[1 + \exp\left(-\frac{E - W_n}{\Omega_n}\right)\right]^{-1}\right\}, \tag{6.1}$$

where $W_n = h^2 n^2/(8a^2 m)$ is an effective potential barrier the charge carriers have to pass. As long as

$$|E - W_n| \gg \Omega_n, \tag{6.2}$$

conductance steps are sharp and well pronounced.

Conductance quantization has been previously studied in both graphene nanoconstrictions [116, 117] and nanoribbons [118, 119]. Different boundary conditions in such systems allow one to expect different transport behaviors. For the armchair edges, the conductance has a quantization sequence $0, 1, 2...$ in units of $2e^2/h$, where 2 stands for spin degeneracy[1] [120]. On the other hand, for zigzag edges, conductance takes values in odd multiples $(1, 3, 5, ...)$ of $2e^2/h$, due to the spin and valley degeneracy.

[1] In a disorder free graphene sample with archair edges the valley degeneracy is lifted.

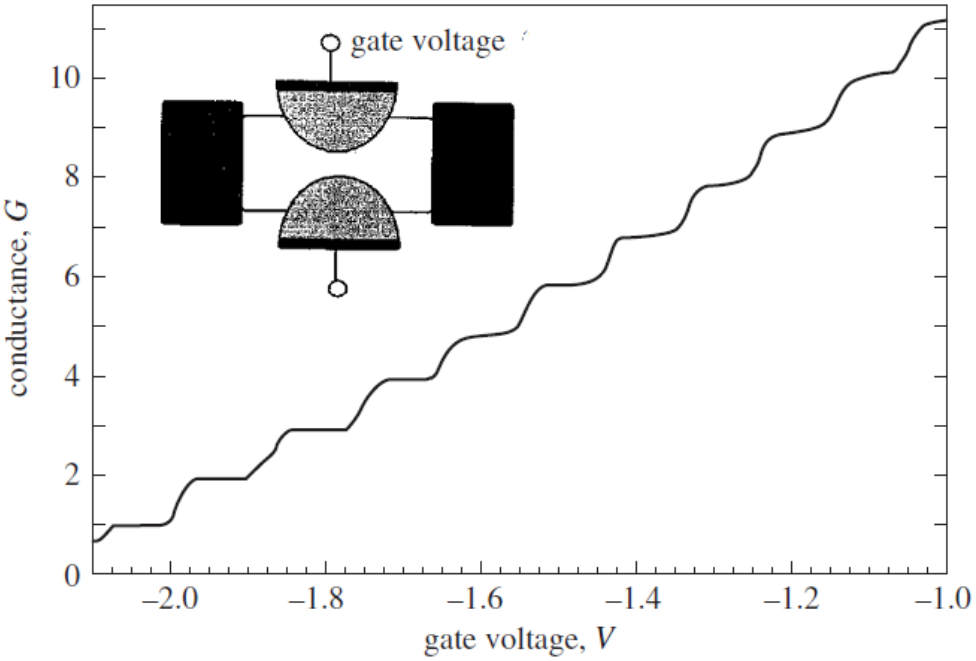

Figure 6.1: Conductance (in units of $2e^2/h$) measured for GaAlAs-GaAs heterostructure. Inset: schematic representation of the system. The shape of 2DEG is modulated by two gate electrodes on two sides of the system. Picture adapted from Refs. [29, 73].

While the conductance quantization is clearly visible in GNR [22, 119], Rycerz, Recher, and Wimmer have shown that it does not occur in graphene-based Corbino disks [109]. One can expect a section of a disk, with the opening angle θ, to interpolate between the GNR behavior (reproduced for $\theta \ll \pi$) and the disk-like behavior ($\theta \geq \pi$).

6.2 Conductance of MLG disk section

Theoretical description of the disk section starts from imposing the conditions for vanishing angular currents at the edges of the sample. Such conditions have been derived by Berry and Mondragon in their insightful 1986 work on neutrino bilards [121]. The wavefunctions have been chosen as linear combinations of angular momentum operator (J_z) eigenfunctions $a_j\psi_j + b_{-j}\psi_{-j}$, where j is the angular-momentum quantum number. Such a choice guaranteed that they carry zero angular momentum. From a physical point of view, this leads to a more radial path of the quasiparticle traveling through the sample.

By employing the condition of Berry and Mondragon, eigenvalues of J_z contributing to the transport through the disk sections with opening angles $\theta = \pi/m$, with m an odd integer, have been derived.

At small radii ratios $R_o/R_i \lesssim 2$ and relatively wide opening angles $\theta \gtrsim \pi/3$, conductance of the disk section, in the vicinity of the Dirac point, follows the formula for pseudodiffusive conductance $G_{\text{diff}} \approx 4g_0\theta/(\pi\mathcal{L})$ derived within the conformal mapping technique in Ref. [109]. For smaller opening angles and larger radii ratios, the system is in the quantum-tunneling regime, characterized by the limited number of transmission channels, and the above formula works no more.

The first step of conductance, as a function of doping, emerges already for opening angles $\theta = \pi/3$. By decreasing the angle even further, more steps become visible. Due to the interference between incoming and outgoing waves from one lead to another, a Fabry Perot like oscillations appear. These can be suppressed by increasing the radii ratio.

Surprisingly, the steepness of consecutive steps decreases. Based on the semiclassical transmission probability through a electrostatic potential barrier, we have derived a similar condition for sharpness of nth conductance step in graphene

$$\sqrt{n}\theta/\pi \ll 1. \tag{6.3}$$

This may explain why, contrary to 2DEG, only first steps in conductance are observed in graphene nanoconstrictions [120].

This chapter refers the results of the article

- G. Rut and A. Rycerz, *Conditions for conductance quantization in mesoscopic Dirac systems on the examples of graphene nanoconstrictions*, **Acta Physica Polonica A 126, A-114 (2014)**.

Conclusions and perspectives

We have discussed several topics regarding the pseudodiffusive transport regime in both monolayer (MLG) and bilayer graphene (BLG). In particular, quantum transport dependence on such factors as external electric and magnetic fields, the size, and the geometry of the system has been investigated. Our calculations, employing the effective Dirac-like Hamiltonians, have been carried out in the vicinity of the Dirac point. Our description of the conductivity and higher charge transfer cumulants is based on the Landauer-Büttiker formalism along with the Levitov formula.

We have investigated the evolution of bilayer graphene conductivity, at the charge-neutrality point, with the system size for different values of the skew-interlayer integrals t'. The scaling function $\beta(\sigma)$ is insensitive to the value of t', as long as it is nonzero. Most surprisingly, the shape of the scaling function suggests a possible analogy between disordered Dirac systems with repulsive Coulomb interaction and a perfectly clean ballistic bilayer graphene.

The enhancement of BLG conductivity in the vicinity of the charge-neutrality point, emerging for $t' \neq 0$, can be lifted by strong magnetic field. Above a crossover field B_{res} for which the conductivity is maximized, the asymptotic value $\sigma \simeq \sigma_{BLG}$ is approached and $\sigma - \sigma_{BLG} \propto t'/B$. This high magnetic field limit can be effectively described by a 4-band Hamiltonian including the interlayer coupling $t_\perp$ only. In this limit, the conductivity of bilayer graphene is twice as large as in a single layer. However, in case of higher Landau levels the conductivity is equal for both systems. Moreover, the conductivity is halved in case we apply an electric field leading to a different potential between the layers.

Quantum transport through the Corbino disk in bilayer graphene is strongly affected by the interlayer hopping integrals. In particular, the trigonal warping ($t' \neq 0$) leads to the appearance of beating patterns for all charge transfer cumulants. The envelope period is approximately proportional to $\sqrt{B/t'}$ and can be, in principle, used to estimate the value of t'. In the high field limit, the scenario derived for $t = 0'$ is reproduced at LLs outside the charge-neutrality point, as well as in case of a nonzero potential difference between the layers. The amplitudes of the oscillations are then the same or twice as small as in MLG, respectively.

In high magnetic fields, the pseudodiffusive transport regime appears in narrow intervals of chemical potential centered at the charge-neutrality point or at higher Landau levels. This applies to both monolayer and bilayer graphene. It is possible to observe several effects, indicating the presence of the pseudodiffusive transport regime, by applying a finite source-drain voltage. The voltage leads to a suppression of conductivity and to an enhancement of higher charge-transfer cumulants ($\mathcal{F}$

and $\mathcal{R}$). In the Corbino geometry, these quantities still preserve their oscillatory behavior.

Finally, we have shown that a section of graphene-based Corbino disk characterized by an opening angle close to $\theta \simeq \pi/3$ may demonstrate conductance quantization. We have derived a simple condition for the sharpness of nth conductance step $\sqrt{n}\theta/\pi \ll 1$. Contrary to standard 2DEG, each consecutive step is less pronounced.

Since we have dealt with perfect systems, a natural extension of our research would be to investigate the robustness of our results. Below we have pointed out three main topics, a further analysis of which would be particularly beneficial.

- Several factors may affect the conductivity scaling, including mechanical strains, different types of disorder (long range, short range and edge disorder) as well the Coulomb repulsion. While the Landauer-Büttiker formalism together with mode matching could in principle handle all types of disorder, inclusion of interaction between charge carries would require more advanced techniques. Natural candidates are methods based on the Green functions [73, 79, 122, 123]. Although these techniques are much more complex and numerically challenging, there are several software packages with their efficient implementation [124–126].

- The main issue related to QRCE is its missing experimental observation. It should be expected that the real-life devices based on the Corbino disk may diverge from an ideally cylindrical symmetry. There are other, more subtle difficulties such as reproduction of coaxial leads or the fragility of the bridge between them. In our analysis of the QRCE we have considered a perfect Corbino disk. It is an open question to what extent the oscillations of charge transfer cumulants depend on such details of the geometry. It may also be interesting to investigate how the system would behave, if the inner lead is removed and the charge carriers are injected through an STM tip. Such a setup, consisting of a circular quantum dot surrounded by a simple metallic lead from the exterior only, might be much simpler in realization.

- The pseudodiffusive transport regime occupies a rather narrow part of a phase diagram in the field-doping parameter plane. It would be interesting to explore the perspective of its broadening. Preliminary numerical results suggest that long-range disorder enlarges the area around LLs with nonzero conductivity. Also, a uniaxial strain seems to lead to a similar effect [31, 58].

Bibliography

[1] L. Malard, J. Nilsson, D. Elias, J. Brant, F. Plentz, E. Alves, A. C. Neto, and M. Pimenta, "Probing the electronic structure of bilayer graphene by raman scattering," Physical Review B **76**, 201401 (2007).

[2] L. Zhang, Z. Li, D. N. Basov, M. Fogler, Z. Hao, and M. C. Martin, "Determination of the electronic structure of bilayer graphene from infrared spectroscopy," Physical Review B **78**, 235408 (2008).

[3] A. Kuzmenko, I. Crassee, D. Van Der Marel, P. Blake, and K. Novoselov, "Determination of the gate-tunable band gap and tight-binding parameters in bilayer graphene using infrared spectroscopy," Physical Review B **80**, 165406 (2009).

[4] K. Fesenmaier, "Physicists uncover novel phase of matter," http://phys.org/news/2015-10-physicists-uncover-phase.html (2015).

[5] P. R. Wallace, "The band theory of graphite," Physical Review **71**, 622 (1947).

[6] K. Novoselov, A. K. Geim, S. Morozov, D. Jiang, M. Katsnelson, I. Grigorieva, S. Dubonos, and A. Firsov, "Two-dimensional gas of massless dirac fermions in graphene," Nature **438**, 197–200 (2005).

[7] R. Peierls, "Quelques propriétés typiques des corps solides," in *Annales de l'institut Henri Poincaré*, Vol. 5 (1935) pp. 177–222.

[8] L. Landau, "Zur theorie der phasenumwandlungen ii," Phys. Z. Sowjetunion **11**, 26–35 (1937).

[9] N. D. Mermin, "Crystalline order in two dimensions," Physical Review **176**, 250 (1968).

[10] A. K. Geim and K. S. Novoselov, "The rise of graphene," Nature Materials **6**, 183–191 (2007).

[11] J. Venables, G. Spiller, and M. Hanbucken, "Nucleation and growth of thin films," Reports on Progress in Physics **47**, 399 (1984).

[12] J. Evans, P. Thiel, and M. C. Bartelt, "Morphological evolution during epitaxial thin film growth: Formation of 2d islands and 3d mounds," Surface Science Reports **61**, 1–128 (2006).

[13] A. Fasolino, J. Los, and M. I. Katsnelson, "Intrinsic ripples in graphene," Nature Materials **6**, 858–861 (2007).

[14] G. Fiori, F. Bonaccorso, G. Iannaccone, T. Palacios, D. Neumaier, A. Seabaugh, S. K. Banerjee, and L. Colombo, "Electronics based on two-dimensional materials," Nature Nanotechnology **9**, 768–779 (2014).

[15] M. Katsnelson, K. Novoselov, and A. Geim, "Chiral tunnelling and the klein paradox in graphene," Nature Physics **2**, 620–625 (2006).

[16] Y. Zhang, Y.-W. Tan, H. L. Stormer, and P. Kim, "Experimental observation of the quantum hall effect and berry's phase in graphene," Nature **438**, 201–204 (2005).

[17] Y.-M. Lin, C. Dimitrakopoulos, K. A. Jenkins, D. B. Farmer, H.-Y. Chiu, A. Grill, and P. Avouris, "100-ghz transistors from wafer-scale epitaxial graphene," Science **327**, 662–662 (2010).

[18] F. Schedin, A. Geim, S. Morozov, E. Hill, P. Blake, M. Katsnelson, and K. Novoselov, "Detection of individual gas molecules adsorbed on graphene," Nature Materials **6**, 652–655 (2007).

[19] D. Cohen-Tanugi and J. C. Grossman, "Water desalination across nanoporous graphene," Nano Letters **12**, 3602–3608 (2012).

[20] E. V. Castro, K. Novoselov, S. Morozov, N. Peres, J. L. Dos Santos, J. Nilsson, F. Guinea, A. Geim, and A. C. Neto, "Biased bilayer graphene: semiconductor with a gap tunable by the electric field effect," Physical Review Letters **99**, 216802 (2007).

[21] C. Beenakker and M. Büttiker, "Suppression of shot noise in metallic diffusive conductors," Physical Review B **46**, 1889 (1992).

[22] J. Tworzydło, B. Trauzettel, M. Titov, A. Rycerz, and C. W. Beenakker, "Sub-poissonian shot noise in graphene," Physical Review Letters **96**, 246802 (2006).

[23] R. Danneau, F. Wu, M. Craciun, S. Russo, M. Tomi, J. Salmilehto, A. Morpurgo, and P. Hakonen, "Shot noise in ballistic graphene," Physical Review Letters **100**, 196802 (2008).

[24] L. DiCarlo, J. Williams, Y. Zhang, D. McClure, and C. Marcus, "Shot noise in graphene," Physical Review Letters **100**, 156801 (2008).

[25] F. Liefrink, J. Dijkhuis, M. De Jong, L. Molenkamp, and H. Van Houten, "Experimental study of reduced shot noise in a diffusive mesoscopic conductor," Physical Review B **49**, 14066 (1994).

[26] A. H. Steinbach, J. M. Martinis, and M. H. Devoret, "Observation of hot-electron shot noise in a metallic resistor," Physical Review Letters **76**, 3806 (1996).

[27] M. Henny, S. Oberholzer, C. Strunk, and C. Schönenberger, "1/3-shot-noise suppression in diffusive nanowires," Physical Review B **59**, 2871 (1999).

[28] Y. M. Blanter and M. Büttiker, "Shot noise in mesoscopic conductors," Physics Reports **336**, 1–166 (2000).

[29] Y. Nazarov and Y. Blanter, *Quantum Transport: Introduction to Nanoscience* (Cambridge University Press, Cambridge, 2009).

[30] E. Prada, P. San-Jose, B. Wunsch, and F. Guinea, "Pseudodiffusive magnetotransport in graphene," Physical Review B **75**, 113407 (2007).

[31] W.-R. Hannes and M. Titov, "Ballistic charge transport in chiral-symmetric few-layer graphene," EPL (Europhysics Letters) **89**, 47007 (2010).

[32] G. Rut and A. Rycerz, "Pseudodiffusive conductance, quantum-limited shot noise, and landau-level hierarchy in a biased graphene bilayer," Physical Review B **89**, 045421 (2014).

[33] E. Schrodinger, "Non powerful motion in the relativistic quantum mechanics," Sitzungsb. Preuss. Akad. Wiss. Phys.-Math. Kl **24**, 418–428 (1930).

[34] M. Katsnelson, "Zitterbewegung, chirality, and minimal conductivity in graphene," The European Physical Journal B-Condensed Matter and Complex Systems **51**, 157–160 (2006).

[35] M. Auslender and M. Katsnelson, "Generalized kinetic equations for charge carriers in graphene," Physical Review B **76**, 235425 (2007).

[36] T. M. Rusin and W. Zawadzki, "Transient zitterbewegung of charge carriers in mono-and bilayer graphene, and carbon nanotubes," Physical Review B **76**, 195439 (2007).

[37] W. Zawadzki and T. M. Rusin, "Zitterbewegung (trembling motion) of electrons in semiconductors: a review," Journal of Physics: Condensed Matter **23**, 143201 (2011).

[38] M. Katsnelson, *Graphene: carbon in two dimensions* (Cambridge University Press, 2012).

[39] L. D. Landau, L. P. Pitaevskii, E. M. Lifshitz, and V. B. Berestetskii, "Relativistic quantum theory," (1971).

[40] A. Davydov, *Quantum Mechanics, 2-nd ed* (Pergamon Press, Oxford, 1976).

[41] A. W. Ludwig, M. P. Fisher, R. Shankar, and G. Grinstein, "Integer quantum hall transition: An alternative approach and exact results," Physical Review B **50**, 7526 (1994).

[42] K. Ziegler, "Robust transport properties in graphene," Physical Review Letters **97**, 266802 (2006).

[43] K. Ziegler, "Minimal conductivity of graphene: Nonuniversal values from the kubo formula," Physical Review B **75**, 233407 (2007).

[44] S. Ryu, C. Mudry, A. Furusaki, and A. Ludwig, "Landauer conductance and twisted boundary conditions for dirac fermions in two space dimensions," Physical Review B **75**, 205344 (2007).

[45] F. Miao, S. Wijeratne, Y. Zhang, U. Coskun, W. Bao, and C. Lau, "Phase-coherent transport in graphene quantum billiards," Science **317**, 1530–1533 (2007).

[46] M. Katsnelson, "Minimal conductivity in bilayer graphene," The European Physical Journal B-Condensed Matter and Complex Systems **52**, 151–153 (2006).

[47] J. Cserti, "Minimal longitudinal dc conductivity of perfect bilayer graphene," Physical Review B **75**, 033405 (2007).

[48] I. Snyman and C. W. J. Beenakker, "Ballistic transmission through a graphene bilayer," Physical Review B **75**, 045322 (2007).

[49] J. Cserti, A. Csordás, and G. Dávid, "Role of the trigonal warping on the minimal conductivity of bilayer graphene," Physical Review Letters **99**, 066802 (2007).

[50] A. G. Moghaddam and M. Zareyan, "Anisotropic minimal conductivity of graphene bilayers," Physical Review B **79**, 073401 (2009).

[51] E. McCann, D. S. Abergel, and V. I. Fal'ko, "The low energy electronic band structure of bilayer graphene," The European Physical Journal Special Topics **148**, 91–103 (2007).

[52] E. McCann and V. I. Fal'ko, "Landau-level degeneracy and quantum hall effect in a graphite bilayer," Physical Review Letters **96**, 086805 (2006).

[53] J. McClure, "Diamagnetism of graphite," Physical Review **104**, 666 (1956).

[54] F. D. M. Haldane, "Model for a quantum hall effect without landau levels: Condensed-matter realization of the" parity anomaly"," Physical Review Letters **61**, 2015 (1988).

[55] Y. Zheng and T. Ando, "Hall conductivity of a two-dimensional graphite system," Physical Review B **65**, 245420 (2002).

[56] M. I. Katsnelson, "Aharonov-bohm effect in undoped graphene: Magnetotransport via evanescent waves," EPL (Europhysics Letters) **89**, 17001 (2010).

[57] A. Rycerz, "Magnetoconductance of the corbino disk in graphene," Physical Review B **81**, 121404 (2010).

[58] Z. Khatibi, H. Rostami, and R. Asgari, "Valley polarized transport in a strained graphene based corbino disc," Physical Review B **88**, 195426 (2013).

[59] W. Ehrenberg and R. Siday, "The refractive index in electron optics and the principles of dynamics," Proceedings of the Physical Society. Section B **62**, 8 (1949).

[60] Y. Aharonov and D. Bohm, "Significance of electromagnetic potentials in the quantum theory," Physical Review **115**, 485 (1959).

[61] M. Peshkin and A. Tonomura, "The aharonov-bohm effect," in *The Aharonov-Bohm Effect*, Vol. 340 (1989).

[62] A. Rycerz, "Aharonov-bohm and relativistic corbino effects in graphene: A comparative study of two quantum interference phenomena," Acta Physica Polonica A **121**, 1242–1245 (2011).

[63] P. Ostrovsky, I. Gornyi, and A. Mirlin, "Electron transport in disordered graphene," Physical Review B **74**, 235443 (2006).

[64] M. Titov, "Impurity-assisted tunneling in graphene," EPL (Europhysics Letters) **79**, 17004 (2007).

[65] J. H. Bardarson, J. Tworzydło, P. Brouwer, and C. Beenakker, "One-parameter scaling at the dirac point in graphene," Physical Review Letters **99**, 106801 (2007).

[66] K. Nomura, M. Koshino, and S. Ryu, "Topological delocalization of two-dimensional massless dirac fermions," Physical Review Letters **99**, 146806 (2007).

[67] A. Schuessler, P. Ostrovsky, I. Gornyi, and A. Mirlin, "Analytic theory of ballistic transport in disordered graphene," Physical Review B **79**, 075405 (2009).

[68] L. S. Levitov, H. Lee, and G. B. Lesovik, "Electron counting statistics and coherent states of electric current," Journal of Mathematical Physics **37**, 4845–4866 (1996).

[69] E. McCann and M. Koshino, "The electronic properties of bilayer graphene," Reports on Progress in Physics **76**, 056503 (2013).

[70] C. Beenakker, "Colloquium: Andreev reflection and klein tunneling in graphene," Reviews of Modern Physics **80**, 1337 (2008).

[71] G. M. Rutter, S. Jung, N. N. Klimov, D. B. Newell, N. B. Zhitenev, and J. A. Stroscio, "Microscopic polarization in bilayer graphene," Nature Physics **7**, 649–655 (2011).

[72] W. Bao, J. Velasco, F. Zhang, L. Jing, B. Standley, D. Smirnov, M. Bockrath, A. H. MacDonald, and C. N. Lau, "Evidence for a spontaneous gapped state in ultraclean bilayer graphene," Proceedings of the National Academy of Sciences **109**, 10802–10805 (2012).

[73] S. Datta, *Electronic transport in mesoscopic systems* (Cambridge university press, 1997).

[74] B. Reulet, J. Senzier, and D. Prober, "Environmental effects in the third moment of voltage fluctuations in a tunnel junction," Physical Review Letters **91**, 196601 (2003).

[75] G. Rut and A. Rycerz, "Trigonal warping, pseudodiffusive transport and magnetoconductance of bilayer graphene corbino disk," accepted to Physical Review B .

[76] W. Greiner, *Relativistic quantum mechanics*, Vol. 3 (Springer, 1990).

[77] P. San-Jose, E. Prada, and D. S. Golubev, "Universal scaling of current fluctuations in disordered graphene," Physical Review B **76**, 195445 (2007).

[78] A. A. Abrikosov, L. P. Gorkov, I. E. Dzyaloshinski, and I. E. Dzialoshinskiĭ, *Methods of quantum field theory in statistical physics* (Courier Corporation, 1975).

[79] G. D. Mahan, *Many-particle physics* (Springer Science & Business Media, 2013).

[80] M. Abramowitz and I. A. Stegun, *Handbook of mathematical functions: with formulas, graphs, and mathematical tables*, 55 (Courier Corporation, 1964).

[81] F. W. Olver, *NIST handbook of mathematical functions* (Cambridge University Press, 2010).

[82] E. Hairer, S. Nørsett, and G. Wanner, *Solving ordinary differential equations I. Nonstiff problems* (Springer-Verlag, Berlin, 1987).

[83] S. Datta, M. Cahay, and M. McLennan, "Scatter-matrix approach to quantum transport," Physical Review B **36**, 5655 (1987).

[84] M. Cahay, M. McLennan, and S. Datta, "Conductance of an array of elastic scatterers: A scattering-matrix approach," Physical Review B **37**, 10125 (1988).

[85] H. Tamura and T. Ando, "Conductance fluctuations in quantum wires," Physical Review B **44**, 1792 (1991).

[86] P. A. Lee and T. Ramakrishnan, "Disordered electronic systems," Reviews of Modern Physics **57**, 287 (1985).

[87] K. Efetov, *Supersymmetry in disorder and chaos* (Cambridge University Press, 1999).

[88] E. Abrahams, P. Anderson, D. Licciardello, and T. Ramakrishnan, "Scaling theory of localization: Absence of quantum diffusion in two dimensions," Physical Review Letters **42**, 673–676 (1979).

[89] P. W. Anderson, "Absence of diffusion in certain random lattices," Physical Review **109**, 1492 (1958).

[90] D. J. Thouless, "Electrons in disordered systems and the theory of localization," Physics Reports **13**, 93–142 (1974).

[91] F. J. Wegner, "Electrons in disordered systems. scaling near the mobility edge," Zeitschrift für Physik B Condensed Matter **25**, 327–337 (1976).

[92] T. Wehling, M. Katsnelson, and A. Lichtenstein, "Impurities on graphene: Midgap states and migration barriers," Physical Review B **80**, 085428 (2009).

[93] S. Gattenlöhner, W.-R. Hannes, P. Ostrovsky, I. Gornyi, A. Mirlin, and M. Titov, "Quantum hall criticality and localization in graphene with short-range impurities at the dirac point," Physical Review Letters **112**, 026802 (2014).

[94] I. Aleiner and K. Efetov, "Effect of disorder on transport in graphene," Physical Review Letters **97**, 236801 (2006).

[95] A. Altland, "Low-energy theory of disordered graphene," Physical Review Letters **97**, 236802 (2006).

[96] G. Rut and A. Rycerz, "Minimal conductivity and signatures of quantum criticality in ballistic graphene bilayer," EPL (Europhysics Letters) **107**, 47005 (2014).

[97] P. Ostrovsky, I. Gornyi, and A. Mirlin, "Interaction-induced criticality in z 2 topological insulators," Physical Review Letters **105**, 036803 (2010).

[98] K. Novoselov, E. McCann, S. Morozov, V. I. Fal'ko, M. Katsnelson, U. Zeitler, D. Jiang, F. Schedin, and A. Geim, "Unconventional quantum hall effect and berry's phase of 2π in bilayer graphene," Nature Physics **2**, 177–180 (2006).

[99] J. B. Oostinga, H. B. Heersche, X. Liu, A. F. Morpurgo, and L. M. Vandersypen, "Gate-induced insulating state in bilayer graphene devices," Nature Materials **7**, 151–157 (2008).

[100] A. Mayorov, D. Elias, M. Mucha-Kruczynski, R. Gorbachev, T. Tudorovskiy, A. Zhukov, S. Morozov, M. Katsnelson, A. Geim, and K. Novoselov, "Interaction-driven spectrum reconstruction in bilayer graphene," Science **333**, 860–863 (2011).

[101] E. McCann, "Electronic properties of monolayer and bilayer graphene," in *Graphene Nanoelectronics* (Springer, 2012) pp. 237–275.

[102] E. McCann and M. Koshino, "The electronic properties of bilayer graphene," Reports on Progress in Physics **76**, 056503 (2013).

[103] G. Rut and A. Rycerz, "Magnetoconductance of the corbino disk in graphene: chiral tunneling and quantum interference in the bilayer case," Journal of Physics: Condensed Matter **26**, 485301 (2014).

[104] L. Boltzmann, "Anz. kaiserlichen akad. wiss. wien, 23 (1886) 77," Philosophical Magazine **22**, 226 (1886).

[105] S. Galdabini and G. Giuliani, "Magnetic field effects and dualistic theory of metallic conduction in italy (1911–1926): cultural heritage, creativity, epistemological beliefs, and national scientific community," Annals of Science **48**, 21–37 (1991).

[106] G. Kirczenow, "Quantum transport in ballistic nano-scale corbino disks," Journal of Physics: Condensed Matter **6**, L583 (1994).

[107] S. Souma and A. Suzuki, "Interedge scattering in mesoscopic corbino disks near the ballistic regime," Physical Review B **60**, 15928–15936 (1999).

[108] S. Souma and A. Suzuki, "Effect of impurity scattering in nanoscale corbino disks," Physical Review B **58**, 4649–4655 (1998).

[109] A. Rycerz, P. Recher, and M. Wimmer, "Conformal mapping and shot noise in graphene," Physical Review B **80**, 125417 (2009).

[110] E. C. Peters, A. Giesbers, M. Burghard, and K. Kern, "Scaling in the quantum hall regime of graphene corbino devices," Applied Physics Letters **104**, 203109 (2014).

[111] A. Akhmerov and C. Beenakker, "Pseudodiffusive conduction at the dirac point of a normal-superconductor junction in graphene," Physical Review B **75**, 045426 (2007).

[112] G. Rut and A. Rycerz, "Quantum-limited shot noise and quantum interference in graphene-based corbino disk," Philosophical Magazine **95**, 599–608 (2015), http://dx.doi.org/10.1080/14786435.2014.974712 .

[113] B. Van Wees, H. Van Houten, C. Beenakker, J. G. Williamson, L. Kouwenhoven, D. Van der Marel, and C. Foxon, "Quantized conductance of point contacts in a two-dimensional electron gas," Physical Review Letters **60**, 848 (1988).

[114] D. Wharam, T. Thornton, R. Newbury, M. Pepper, H. Ahmed, J. Frost, D. Hasko, D. Peacock, D. Ritchie, and G. Jones, "One-dimensional transport and the quantisation of the ballistic resistance," Journal of Physics C: solid state physics **21**, L209 (1988).

[115] R. S. G. Lesovik and D. Khmelnitskii, "Reflectionless quantum transport and fundamental ballistic-resistance steps in microscopic constrictions," Jetp Letters **48**, 238–241 (1988).

[116] F. Muñoz-Rojas, J. Fernández-Rossier, L. Brey, and J. Palacios, "Performance limits of graphene-ribbon field-effect transistors," Physical Review B **77**, 045301 (2008).

[117] S. Ihnatsenka and G. Kirczenow, "Conductance quantization in graphene nanoconstrictions with mesoscopically smooth but atomically stepped boundaries," Physical Review B **85**, 121407 (2012).

[118] K. Wakabayashi, "Electronic transport properties of nanographite ribbon junctions," Physical Review B **64**, 125428 (2001).

[119] N. Peres, A. C. Neto, and F. Guinea, "Conductance quantization in mesoscopic graphene," Physical Review B **73**, 195411 (2006).

[120] N. Tombros, A. Veligura, J. Junesch, M. H. Guimarães, I. J. Vera-Marun, H. T. Jonkman, and B. J. van Wees, "Quantized conductance of a suspended graphene nanoconstriction," Nature Physics **7**, 697–700 (2011).

[121] M. V. Berry and R. Mondragon, "Neutrino billiards: time-reversal symmetry-breaking without magnetic fields," in *Proceedings of the Royal Society of London A: Mathematical, Physical and Engineering Sciences*, Vol. 412 (The Royal Society, 1987) pp. 53–74.

[122] L. P. Kadanoff and G. A. Baym, *Quantum statistical mechanics* (Benjamin, 1962).

[123] M. Wimmer, *Quantum transport in nanostructures: From computational concepts to spintronics in graphene and magnetic tunnel junctions*, Ph.D. thesis (2009).

[124] A. R. Rocha, V. Garcia-Suarez, S. Bailey, C. Lambert, J. Ferrer, and S. Sanvito, "Spin and molecular electronics in atomically generated orbital landscapes," Physical Review B **73**, 085414 (2006).

[125] J. Ferrer, C. J. Lambert, V. M. García-Suárez, D. Z. Manrique, D. Visontai, L. Oroszlany, R. Rodríguez-Ferradás, I. Grace, S. Bailey, K. Gillemot, *et al.*, "Gollum: a next-generation simulation tool for electron, thermal and spin transport," New Journal of Physics **16**, 093029 (2014).

[126] C. W. Groth, M. Wimmer, A. R. Akhmerov, and X. Waintal, "Kwant: a software package for quantum transport," New Journal of Physics **16**, 063065 (2014).

PHYSICAL REVIEW B **89**, 045421 (2014)

Pseudodiffusive conductance, quantum-limited shot noise, and Landau-level hierarchy in a biased graphene bilayer

Grzegorz Rut and Adam Rycerz
Marian Smoluchowski Institute of Physics, Jagiellonian University, Reymonta 4, PL-30059 Kraków, Poland
(Received 26 July 2013; revised manuscript received 2 January 2014; published 22 January 2014)

We discuss, by means of mode-matching analysis for the Dirac equation, how splittings of the Landau-level (LL) degeneracies associated with spin, valley, and layer degrees of freedom affect the ballistic conductance of graphene bilayer. The results show that for wide samples ($W \gg L$) the Landauer-Büttiker conductance reaches the maximum $G \simeq se^2/(\pi h) \times W/L$ at the resonance via each LL, with the prefactor varying from $s = 8$ if all three degeneracies are preserved, to $s = 1$ if all the degeneracies are split. In the absence of bias between the layers, the degeneracies associated with spin and layer degrees of freedom may be split by manipulating the doping and magnetic field; the conductance at the zeroth LL is twice as large, while the conductance at any other LL equals to the corresponding conductance of graphene monolayer. The presence of bias potential allows one also to split the valley degeneracy. Our results show that the charge transfer at each LL has pseudodiffusive character, with the second and third cumulant quantified by $\mathcal{F} = 1/3$ and $\mathcal{R} = 1/15$ (respectively). In case the electrochemical potential is allowed to slowly fluctuate in a finite vicinity of LL, the resulting charge-transfer characteristics are still quantum limited, with $\mathcal{F} \simeq 0.7$ and $\mathcal{R} \simeq 0.5$ in the limit of large fluctuations. Analogously, the above values of $\mathcal{F}$ and $\mathcal{R}$ are predicted to be approached in the limit of high source-drain voltage difference applied. The possible effects of indirect interlayer hopping integrals are also briefly discussed.

DOI: 10.1103/PhysRevB.89.045421 PACS number(s): 72.80.Vp, 73.43.Qt, 73.63.−b, 73.50.Td

I. INTRODUCTION

Several unique physical phenomena were observed in graphene or its derivatives at high magnetic fields [1–3]. These include Shubnikov-de-Haas oscillations indicating zero quasiparticle rest mass [4], room-temperature quantum Hall effect with a nonstandard (half-odd integer) sequence of Landau levels [5], signatures of a fractal energy spectrum known as Hofstadter's butterfly [6], and many others. This new subarea of condensed-matter physics emerges primarily due to the nature of effective quasiparticles, which are chiral Dirac fermions with zero (the case of graphene monolayer) or small effective masses ($m_{\rm eff} = 0.033\, m_e$ in the case of graphene bilayer, with m_e the free electron mass) coupled to the external electromagnetic field via additive terms in low-energy Hamiltonians, which are *linear* in both scalar and vector potentials [7]. A remarkable consequence of such a coupling is the quantization of the visible light absorption [8].

Among numerous phenomena which were predicted theoretically but not yet fully confirmed experimentally, we focus our attention on the so-called *pseudodiffusive* transport in ballistic graphene. For an undoped monolayer, elementary mode-matching analysis for the Dirac equation [9,10] leads to the Landauer-Büttiker conductance [11] of a rectangular sample (with the width W and the length L) scaling as $G = \sigma_0 \times W/L$ for $W \gg L$, where $\sigma_0 = (4/\pi)e^2/h$ is the universal quantum value of the conductivity. Additionally, the Fano factor is $\mathcal{F} = 1/3$, and all the other charge-transfer characteristics are indistinguishable from those of a classical diffusive conductor [12,13]. In the pseudodiffusive regime, applied magnetic field is predicted to affect neither the conductance [14,15] nor other transport characteristics [16]. Existing experiments [17–19] generally support these theoretical results, leaving some ambiguity concerning the origin of the $\mathcal{F}$ value observed [2,20]. For high dopings and magnetic fields, charge transport through a monolayer was discussed in analytical terms for the rectangular [16] and the disklike (Corbino geometry) samples [21,22]. In both cases, pseudodiffusive behavior is expected to be recovered at each resonance with the Landau level (LL) in the absence of disorder. Remarkably, recent numerical study of large disordered samples [23] reports the longitudinal conductivity $\sigma_{xx} \simeq 1.4\, e^2/h$ (which is numerically close to σ_0) appearing at each LL for wide ranges of disorder and magnetic fields. The nature of this coincidence, however, remains unclear so far.

For a bilayer, a few theoretical studies [24–26] showed that regardless *massive* Dirac fermions govern low-energy properties of the system, the pseudodiffusive conductivity of undoped ballistic samples is $(8/\pi)e^2/h = 2\sigma_0$ (twice as large as in the case of a monolayer), and the Fano factor $\mathcal{F} = 1/3$ again. Surprisingly, a role of the most desired property of graphene bilayer, which is a tunability of the energy gap related to the potential energy difference between the layers V [27–30], has been only marginally discussed in the context of pseudodiffusive transport [31]. We notice here, that for a Hall-bar setup (for which $W \lesssim L$ and the pseudodiffusive limit is usually inaccessible) it was shown both numerically and experimentally that the eightfold degeneracy of the lowest LL can be lifted by manipulating the external electromagnetic fields (see Fig. 1), and the effect was usually attributed to electron-electron interactions [32–34].

Here, transport properties of graphene bilayer in the presence of potential energy difference between the layers and external magnetic fields are discussed in analytical terms. Namely, we start from the four-band Dirac Hamiltonian [27] taking into account the inter- and intralayer nearest neighbor hopping parameters, and employ the Landauer-Büttiker formalism [11] to investigate the field-dependent conductance and other transport characteristics of a ballistic sample. The geometry considered (wide-and-short sample) is chosen in

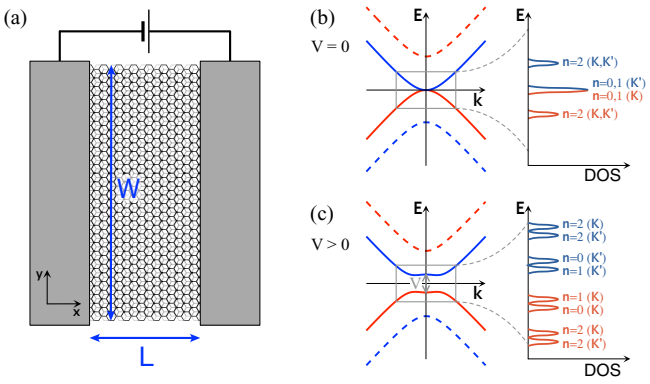

FIG. 1. (Color online) Schematics of system studied analytically in the paper and energy band structure in the quantum Hall regime. (a) A strip of graphene bilayer of width W attached to two electrodes (shaded rectangles) at a distance L. A voltage source drives a current through the sample area. Separate top and bottom gate electrodes (not shown) allow one to tune the carrier concentration and the band gap (related to the potential energy difference between the layers V). (b), (c) The formation of Landau levels in bilayer graphene with and without a band gap. Landau levels are indexed with the orbital index n and the valley pseudospin (K or K'); the twofold spin degeneracy of each level is assumed for clarity. In the absence of a band gap ($V = 0$) almost every Landau level shows the fourfold (spin and valley) degeneracy, with the exception of eightfold degenerate zero-energy level, for which the states arising from two layers (red and blue lines) coexist. Both layer and valley degeneracies are split in the presence of a band gap ($V > 0$).

such a way that the boundary conditions applied to the Dirac equation do not affect the resulting physical quantities.

The remaining part of the paper is organized as follows. In Sec. II we present the system details and find all linearly-independent solutions of the corresponding Dirac equation at finite dopings, biases, and magnetic fields. Then, in Sec. III we discuss the field-dependent transport characteristics in three different situations: at the Dirac point, in an unbiased sample ($V = 0$), and in a sample with different potentials on the layers ($V \neq 0$). In Sec. IV we analyze the influence of a finite voltage difference or doping fluctuations (in the vicinity of pseudodiffusive regions), on the shot-noise power and on the third charge-transfer cumulant. Also in Sec. IV we compare, with a help of the so-called *partial conductance*, the statistical distribution of transmission probabilities for graphene bilayer in high magnetic fields with the corresponding distribution for a generic diffusive system. In Sec. V we discuss, by solving the appropriately modified Dirac equation numerically, the possible role of indirect interlayer hopping integrals. The conclusions are given in Sec. VI.

II. THE SETUP AND MODE-MATCHING FOR THE DIRAC EQUATION

A. The effective Hamiltonian

Following Snyman and Beenakker [25], we consider a rectangular, weakly doped bilayer sample attached to two heavily-doped strips modeling contacts [see Fig. 1(a)]. It is also assumed that the magnetic field ($B \neq 0$) is present only in the sample area. Our analysis starts from the four-band Hamiltonian for the K valley [27]

$$H = \begin{pmatrix} U_1(x) & \pi_x + i\pi_y & t_\perp & 0 \\ \pi_x - i\pi_y & U_1(x) & 0 & 0 \\ t_\perp & 0 & U_2(x) & \pi_x - i\pi_y \\ 0 & 0 & \pi_x + i\pi_y & U_2(x) \end{pmatrix}, \quad (1)$$

where $t_\perp \simeq 0.4$ eV is the interlayer nearest-neighbor hopping energy, $\pi_j/v_F = (-i\hbar\partial_j + eA_j)$ is the gauge-invariant in-plane momentum operator ($j = 1,2$), the electron charge is $-e$, and $v_F \simeq 10^6$ m/s is the Fermi velocity in a single layer. $U_l(x)$ (with $l = 1,2$ the layer index) is the electrostatic potential energy chosen as

$$U_l(x) = \begin{cases} U_\infty & \text{if} \quad x < 0 \text{ or } x > L, \\ \lambda_l V - g\mu_B B\, m_s & \text{if} \quad 0 < x < L, \end{cases} \quad (2)$$

where V is the difference between potentials on the layers, $\lambda_l = \frac{1}{2}(-1)^l$, and $g\mu_B B m_s$ is the Zeeman term (the z component of spin $m_s = \pm\frac{1}{2}$). The experimental values of the Lande factor for graphene bilayer are $g \simeq 2-3$ [35–37], thus we set $g = 2$ for the numerical discussion. In order to obtain the Hamiltonian for the other valley (K'), it is sufficient to substitute $V \to -V$ and $\pi_j \to -\pi_j$ in Eq. (1).

B. The sample area

We choose the Landau gauge $\mathbf{A} \equiv (A_x, A_y) = (0, -Bx)$, with the uniform magnetic field $B \neq 0$ for $0 < x < L$ (otherwise, $B = 0$). The wave function is a four-component spinor, which can be written as $\psi = (\phi_{A_1}, i\phi_{B_1}, \phi_{B_2}, i\phi_{A_2})^T$. The Hamiltonian (1) commutes with $-i\partial_y$, and thus ψ varies in the y direction as a plane wave of a form $\propto \exp(ik_y y)$, with the transverse wave number k_y. The Dirac equation for a sample area, after a substitution $\xi = l_B^{-1}x - k_y l_B$ (with $l_B = \sqrt{\hbar/|eB|}$ the magnetic length), can be written as

$$\begin{pmatrix} -\varepsilon - \delta & \partial_\xi + \xi & t & 0 \\ \partial_\xi - \xi & \varepsilon + \delta & 0 & 0 \\ t & 0 & -\varepsilon + \delta & \partial_\xi - \xi \\ 0 & 0 & \partial_\xi + \xi & \varepsilon - \delta \end{pmatrix} \begin{pmatrix} \phi_{A_1} \\ \phi_{B_1} \\ \phi_{B_2} \\ \phi_{A_2} \end{pmatrix} = 0, \quad (3)$$

where we have defined $\varepsilon = (E - g\mu_B B m_s) l_B/(\hbar v_F)$, $\delta = -V l_B/(2\hbar v_F)$, and $t = t_\perp l_B/(\hbar v_F)$. The functions ϕ_α are given explicitly in Appendix A. Here we only mention that solutions at the Dirac point ($\varepsilon = \delta = 0$) still have a peculiar form of evanescent waves, leading to zero-field value of the pseudodiffusive conductance [25] unaltered for arbitrarily high magnetic fields. We address this issue in a detailed manner in Sec. III.

C. Contact regions

For contact regions, one can neglect the bias potential ($\delta \simeq 0$) due to a high doping. The Dirac equation can thus be written

as

$$\begin{pmatrix} -\tilde{\epsilon} & ke^{i\theta_k} & \tilde{t} & 0 \\ ke^{-i\theta_k} & -\tilde{\epsilon} & 0 & 0 \\ \tilde{t} & 0 & -\tilde{\epsilon} & ke^{-i\theta_k} \\ 0 & 0 & ke^{i\theta_k} & -\tilde{\epsilon} \end{pmatrix} \begin{pmatrix} \phi_{A_1} \\ i\phi_{B_1} \\ \phi_{B_2} \\ i\phi_{A_2} \end{pmatrix} = 0, \quad (4)$$

with $\tilde{\epsilon} = (E - U_\infty)/(\hbar v_F)$, $\tilde{t} = t_\perp/(\hbar v_F)$, $k = \sqrt{k_x^2 + k_y^2}$, and $\theta_k = \arg(k_x + i\,k_y)$. After straightforward calculations, one obtains the dispersion relation

$$\tilde{\epsilon}(k)^2 = \left(\frac{\eta}{2}\tilde{t} + \sqrt{\frac{1}{4}\tilde{t}^2 + k^2}\right)^2, \quad (5)$$

with $\eta = \pm 1$ referring to the two subbands.

The eigenfunctions in contact regions take the form of plane wave spinors, namely

$$\psi_L^\pm(x) = C(\tilde{\epsilon}, k_x^\pm)\exp(-ixk_x^\pm)\begin{pmatrix} \mp\tilde{\epsilon} \\ \pm(k_x^\pm + i\,k_y) \\ \tilde{\epsilon} \\ -k_x^\pm + i\,k_y \end{pmatrix}, \quad (6)$$

$$\psi_R^\pm(x) = C(\tilde{\epsilon}, k_x^\pm)\exp(ixk_x^\pm)\begin{pmatrix} \mp\tilde{\epsilon} \\ \mp(k_x^\pm - i\,k_y) \\ \tilde{\epsilon} \\ k_x^\pm + i\,k_y \end{pmatrix}. \quad (7)$$

The symbols $\psi_R^\pm$ and $\psi_L^\pm$ denote the solutions moving to the right and to the left (respectively), with the signs $\pm$ referring to the two subbands again. The normalization factors $C(\tilde{\epsilon}, k_x^\pm)$ are chosen such that the total current $I_{L(R)}^\pm = ev_F \int_0^W dy(\psi_{L(R)}^\pm)^\dagger \left(\begin{smallmatrix} \sigma_x & 0 \\ 0 & \sigma_x \end{smallmatrix}\right)\psi_{L(R)}^\pm$ satisfies $|I_{L(R)}^\pm| = ev_F$, implying $C(\tilde{\epsilon}, k_x^\pm) = 1/\sqrt{4W\tilde{\epsilon}k_x^\pm}$.

For instance, we can model the heavily electron-doped contacts by taking the limit $U_\infty \to -\infty$, leading to $k_x^\pm = \sqrt{\tilde{\epsilon}\,(\tilde{\epsilon} \pm \tilde{t}) - k_y^2} \simeq |\tilde{\epsilon}|$. Also, in such a limit, the wave functions $\psi_R^\pm$ (6) and $\psi_L^\pm$ (7) take asymptotic forms in which they depend on $\tilde{\epsilon}$ (and U_∞) only via phase factors. In turn, the measurable quantities become insensitive to the specific value of U_∞.

III. TRANSPORT OF DIRAC FERMIONS

In this section we present our main results concerning the conductance G, the Fano factor $\mathcal{F}$, and the factor $\mathcal{R}$ quantifying the third charge-transfer cumulant for ballistic graphene bilayer. We employ the standard Landauer-Büttiker formalism [11], namely

$$G = G_0 \mathrm{Tr}\, \boldsymbol{T}, \quad (8)$$

$$\mathcal{F} = \frac{\mathrm{Tr}[\boldsymbol{T}(\mathbf{1} - \boldsymbol{T})]}{\mathrm{Tr}\, \boldsymbol{T}}, \quad (9)$$

$$\mathcal{R} = \frac{\mathrm{Tr}[\boldsymbol{T}(\mathbf{1} - \boldsymbol{T})(\mathbf{1} - 2\boldsymbol{T})]}{\mathrm{Tr}\, \boldsymbol{T}}, \quad (10)$$

where $G_0 = e^2/h$ is the conductance quantum, $\boldsymbol{T} = \boldsymbol{t}^\dagger \boldsymbol{t}$, and $\boldsymbol{t}$ is a block-diagonal matrix with each block [of the form given by Eq. (B3) in Appendix B] corresponding to a single transmission channel, identified by the valley index (K or K'), the transverse momentum k_y, and the z component of spin m_s. Details of the mode-matching analysis are given in Appendix B.

A. Unbiased graphene bilayer

At zero doping and zero bias potential ($\varepsilon = \delta = 0$) we obtain the transmission probabilities

$$T_{k_y}^\pm(0) = \cosh^{-2}\left[\left(k_y - \frac{1}{2}l_B^{-2}L \pm k_c\right)L\right], \quad (11)$$

where $k_c = \frac{1}{L}\ln\left[\frac{Lt_\perp}{2\hbar v_F} + \sqrt{1 + (\frac{Lt_\perp}{2\hbar v_F})^2}\right]$ and the pairwise structure $\{T_{k_y}^+, T_{k_y}^-\}$ for a given k_y can be attributed to the presence of two graphene layers. [Hereinafter, the limit of heavily-doped contacts is imposed.] In comparison to the case of bilayer graphene at the Dirac point at zero magnetic field studied in Ref. [25], the wave vector is shifted by a factor $-l_B^{-2}L/2$, which is proportional to B. Provided the sample width is much larger than the length ($W \gg L$) the boundary effects do not play an important role and one can choose the periodic boundary conditions; i.e., $k_y = 2\pi n/W$ with $n = 0, \pm 1, \pm 2, \ldots$. In such a limit, each of the sums over transverse momenta in Eqs. (8–10) can be approximated by an integral according to

$$\sum_{k_y} \underset{W \gg L}{\simeq} W \int_{-\infty}^{\infty} \frac{dk_y}{2\pi}.$$

In case the Zeeman splitting can be neglected ($g \simeq 0$) this leads to the field-independent pseudodiffusive conductance twice as large as in the case of a monolayer, i.e.,

$$G_{\mathrm{diff}}^{(2)} = 2G_{\mathrm{diff}}^{(1)} = G_0 \frac{8}{\pi}\frac{W}{L}, \quad (12)$$

where the upper index denotes the number of layers. Also, the shot-noise power and the third charge-transfer cumulant are field-independent and quantified by $\mathcal{F} \simeq 1/3$ and $\mathcal{R} \simeq 1/15$, respectively.

At finite dopings and zero bias potential ($\varepsilon \neq 0$, $\delta = 0$), one can identify three distinct transport regimes: the highly-conducting ($G \gg G_{\mathrm{diff}}^{(2)}$), the field suppressed ($G \ll G_{\mathrm{diff}}^{(2)}$), and the pseudodiffusive ($G \simeq G_{\mathrm{diff}}^{(2)}$), as depicted in Fig. 2. The highly-conducting regime shows up in relatively weak fields, when the cyclotron radius $r_C = \hbar k/|eB| \gtrsim L/2$. Using the energy dispersion for the lower conductance (or the higher valence) subband given by Eq. (5), one can rewrite this condition as

$$|E| \gtrsim \frac{1}{2}\left[\sqrt{t_\perp^2 + \left(\frac{\hbar v_F L}{l_B^2}\right)^2} - t_\perp\right]. \quad (13)$$

In stronger fields, the charge transport is suppressed and a considerable conductance $G \gtrsim G_0$ emerges only in narrow energy intervals near LLs, in analogy with corresponding results for a monolayer reported in Refs. [16] and [22]. For any of these intervals, it is possible to increase B keeping the doping such that $\varepsilon^2 \pm \sqrt{(\varepsilon t)^2 + 1} \simeq 2n - 1$ (with n being the number of LL). Following such a procedure, we have numerically reproduced the pseudodiffusive transport

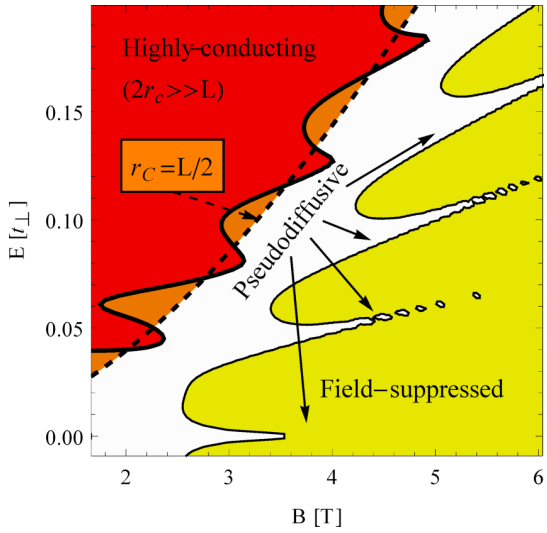

FIG. 2. (Color online) Transport regimes in unbiased graphene bilayer (Zeeman splitting is not taken into account). Two solid lines delimit the areas with $G/G_0 > 8\,W/L$ (red) and $G/G_0 < 2.4\,W/L$ (yellow), where we set $W/L = 20$ and $L = 48\,\hbar v_F/t_\perp \simeq 77$ nm. Dashed line marks a border of the highly-conducting regime following from Eq. (13).

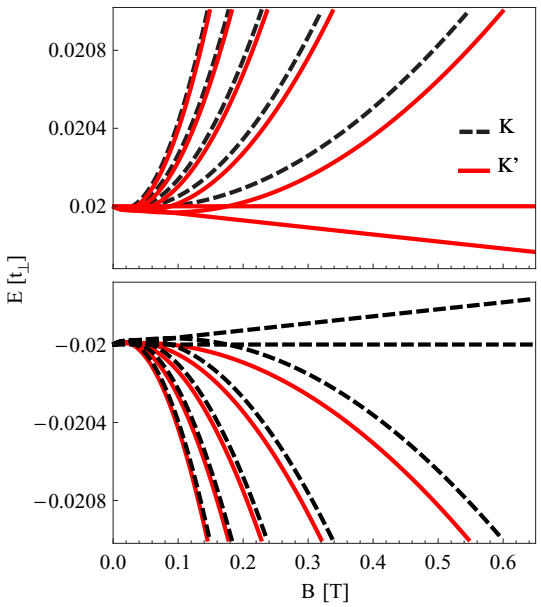

FIG. 3. (Color online) Magnetic field dependence of LL energies in graphene bilayer with a potential bias $V = 4 \times 10^{-2} t_\perp$ obtained from Eq. (14). (The Zeeman splitting is not taken into account for clarity.) Notice that the states corresponding to different valleys (K or K') are exchanged between the conductance and the valence bands (top and bottom panels).

characteristics of a monolayer, i.e., $G \simeq G^{(1)}_{\rm diff}$, $\mathcal{F} \simeq 1/3$, and $\mathcal{R} \simeq 1/15$, for any $n \geq 1$. [Notice that we have set $g = 0$ for clarity. When the Zeeman term is taken into account ($g = 2$), the conductance approaches $G^{(1)}_{\rm diff}/2 = (2/\pi) G_0 W/L$ per each direction of spin, whereas the values of $\mathcal{F}$ and $\mathcal{R}$ are not altered.]

B. Graphene bilayer with nonzero bias

We focus now on the effects appearing in the presence of a bias between the layers ($\delta \neq 0$). Analyzing normalization conditions for the wave functions, one can obtain the following equation for LL energies:

$$\varepsilon^2 + \delta^2 \pm \sqrt{(1 - 2\,\delta\,\varepsilon)^2 + t^2\,(\varepsilon^2 - \delta^2)} = 2\,n - 1, \qquad (14)$$

with $n = 0, 1, \ldots$. This supplements the results reported in the first paper of Ref. [30]. In a peculiar situation when $\varepsilon = \pm\delta$, the differential equations untangle and two additional solutions corresponding to LLs emerge, although it is not possible to find them in a closed analytic form. Numerical values of LL energies are presented in the physical units in Fig. 3.

As illustrated in Figs. 3 and 4, the bias field lifts the valley degeneracy (see Fig. 3), and thus the conductance per spin at any LL becomes two times smaller than for a monolayer, $G \simeq G^{(1)}_{\rm diff}/4 = (1/\pi) G_0 W/L$ (see Fig. 4). The second and third charge-transfer cumulants are still quantified by $\mathcal{F} \simeq 1/3$ and $\mathcal{R} \simeq 1/15$ (respectively), see Fig. 5. Also, the electron-hole symmetry is broken and the two lowest LLs ($n = 0, 1$) exist for electrons (or holes) only in the K' (or K) valley, see Fig. 3.

It is worth stressing here that each LL in biased bilayer is associated with a bunch of transmission resonances corresponding to different k_ys, similarly as in the simplest case of unbiased system at the Dirac point described by Eq. (11). Remarkably, for the energy close to any given LL, the transmission resonances merge in the momentum space. In fact, the wave number shift of $-l_B^{-2} L/2$ appears to provide a reasonable approximation of the typical resonance position, regardless $\delta = 0$ or $\delta \neq 0$. For these reasons, in the numerical discussion presented in the remaining part of the paper, we suppose the mean position of transmission resonances associated with a single LL (up to an integer multiplicity of $2\pi/W$) is given by

$$k_{\rm res} = \frac{2\pi}{W}\,{\rm nint}\left(\frac{W L}{4\pi l_B^2}\right), \qquad (15)$$

where nint (x) is the nearest integer to x.

IV. EFFECTS OF A FINITE VOLTAGE DIFFERENCE OR DOPING FLUCTUATIONS

So far, we have discussed transport properties of graphene bilayer in situations when the doping E is sharply defined and the standard Landauer-Büttiker formulas for the linear-response regime [see Eqs. (8)–(10)] can be applied. Such an approach may not be fully justified at high fields, when the nonzero transmission appears only at narrow doping intervals centered around LLs. For instance, the experimental results may deviate from our theoretical predictions even at zero temperature due to a finite source-drain potential difference V_{sd}, as we may have (at sufficiently high B) $eV_{sd} \gtrsim \mathcal{W}_0$, with $\mathcal{W}_0$ being the typical transmission resonance width. We also argue that similar effects originate from slow doping fluctuations, which may occur in nanosystems when long-time measurements of the higher charge-transfer cumulants are performed.

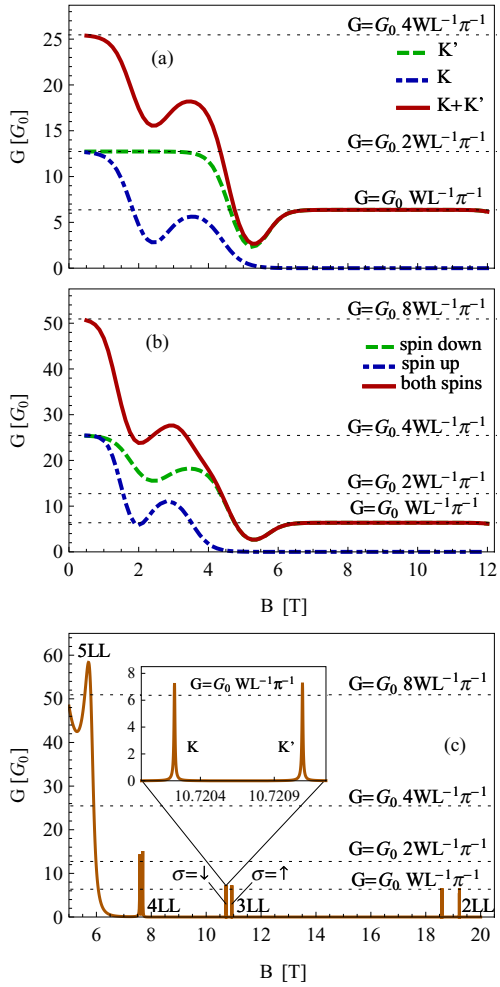

FIG. 4. (Color online) Hierarchy of Landau levels and pseudodiffusive conductance in biased graphene bilayer. (a), (b) Magnetoconductance for the field-dependent doping obtained by solving Eq. (14) for $n = 2$ and $m_s = -\frac{1}{2}$. Two panels show the contributions from the transmission channels corresponding to $m_s = -\frac{1}{2}$ and different valleys [panel (a)] and the conductance summed over the valleys for different directions of spin [panel (b)]. Notice the suppression of the contribution from K valley and $m_s = +\frac{1}{2}$. (c) Magnetoconductance for the doping fixed at $E = 0.2\,t_\perp$. Inset shows the separation of resonances corresponding to K' and K valleys for LL with $n = 3$ and $m_s = -\frac{1}{2}$. We took $V = 2 \times 10^{-4}\,t_\perp$ and $g = 2$. Remaining system parameters are the same as in Fig. 2.

We now extend our analysis in order to describe the above-mentioned effects of finite V_{sd} (or fluctuating doping) in a systematic manner. We start from presenting an empirical model describing the dependence transmission probabilities $T_{k_y}(E)$ on k_y and E (see Sec. IV A). Next, theoretical predictions for $\mathcal{F}$ and $\mathcal{R}$ as functions of V_{sd}, arising from our model, are confronted with the corresponding results of computational experiments (see Sec. IV B). The evolution of statistical distribution of transmission eigenvalues $\rho(T)$ with increasing V_{sd} is also briefly discussed (in Sec. IV C).

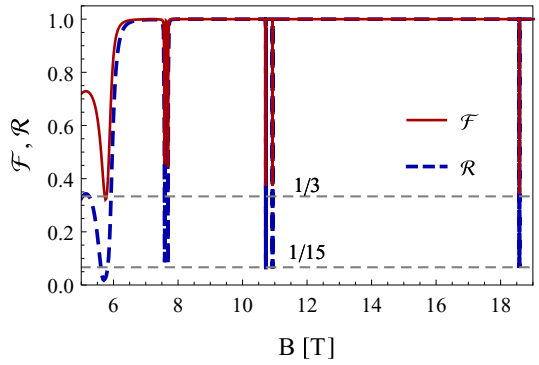

FIG. 5. (Color online) Shot-noise power and the third charge-transfer cumulant, quantified by the Fano factor $\mathcal{F}$ (9) and the $\mathcal{R}$-factor (10), as functions of the magnetic field B. Physical parameters are same as used in Fig. 4(c). Dashed horizontal lines mark the pseudodiffusive values $\mathcal{F} = 1/3$ and $\mathcal{R} = 1/15$.

A. Charge-transfer cumulants at finite V_{sd}

In the so-called shot-noise limit $eV_{sd} \gg k_B T$, electric charge Q passing a nanoscale graphene device during the time Δt is a random variable, a distribution of which can be expressed via the characteristic function

$$\Lambda(\chi) = \langle \exp(i\chi Q/e) \rangle \tag{16}$$

(with $\langle X \rangle$ denoting the expectation value of X), which is given by the Levitov formula [11]

$$\ln \Lambda(\chi) = (\Delta t/h) \times \int_{E_0 - eV_{sd}/2}^{E_0 + eV_{sd}/2} dE' \times \ln\{\det[\boldsymbol{I} + (e^{i\chi} - 1)\boldsymbol{T}(E')]\}, \tag{17}$$

where $\boldsymbol{I}$ is the identity matrix, E_0 is mean doping in the sample area, and we have assumed $V_{sd} > 0$ for simplicity. The average charge $\langle Q \rangle$, as well as higher charge-transfer cumulants $\langle\langle Q^m \rangle\rangle \equiv \langle (Q - \langle Q \rangle)^m \rangle$ may be obtained by subsequent differentiation of $\ln \Lambda(\chi)$ with respect to $i\chi$ at $\chi = 0$. In particular, the conductance

$$\begin{aligned} G(V_{sd}) &= \frac{\langle Q \rangle}{V_{sd}\Delta t} \\ &= \frac{e}{V_{sd}\Delta t} \frac{\partial \ln \Lambda}{\partial (i\chi)}\bigg|_{\chi=0} \\ &= \frac{G_0}{eV_{sd}} \int_{E_0 - eV_{sd}/2}^{E_0 + eV_{sd}/2} dE'\, \mathrm{Tr}\, \boldsymbol{T}(E') \\ &\equiv G_0 \langle \mathrm{Tr}\, \boldsymbol{T} \rangle_{|E - E_0| \le eV_{sd}/2}, \end{aligned} \tag{18}$$

where we have identified the value of $\mathrm{Tr}\, \boldsymbol{T}(E)$ averaged over the energy interval $|E - E_0| \le eV_{sd}/2$. Equation (8) gets restored for $V_{sd} \to 0$. Analogously,

$$\begin{aligned} \mathcal{F}(V_{sd}) &= \frac{\langle\langle Q^2 \rangle\rangle}{\langle\langle Q^2 \rangle\rangle_{\mathrm{Poisson}}} \\ &\equiv \frac{\langle \mathrm{Tr}\,[\boldsymbol{T}(\boldsymbol{I} - \boldsymbol{T})] \rangle_{|E - E_0| \le eV_{sd}/2}}{\langle \mathrm{Tr}\, \boldsymbol{T} \rangle_{|E - E_0| \le eV_{sd}/2}} \end{aligned} \tag{19}$$

and

$$\mathcal{R}(V_{sd}) = \frac{\langle\langle Q^3\rangle\rangle}{\langle\langle Q^3\rangle\rangle_{\text{Poisson}}} \equiv \frac{\langle \text{Tr}\,[\boldsymbol{T}(\boldsymbol{I}-\boldsymbol{T})(\boldsymbol{I}-2\boldsymbol{T})]\rangle_{|E-E_0|\le eV_{sd}/2}}{\langle \text{Tr}\,\boldsymbol{T}\rangle_{|E-E_0|\le eV_{sd}/2}}, \quad (20)$$

where $\langle\langle Q^m\rangle\rangle_{\text{Poisson}} \equiv e^m\langle Q\rangle$ denotes the value of $\langle\langle Q^m\rangle\rangle$ for the Poissonian limit, at which all transmission probabilities $T_{k_y}(E) \ll 1$. We notice that Eqs. (9) and (10) are restored for $V_{sd} \to 0$.

The structure of last expressions in Eqs. (18)–(20) allows us to expect that the results presented in this section are also relevant for a slightly different physical situation, namely, when $eV_{sd} \ll \mathcal{W}_0$, but the doping slowly fluctuates during a measurement procedure, covering uniformly the energy interval

$$|E - E_0| \le \mathcal{W}_0\Delta/2, \quad (21)$$

with Δ being the dimensionless scaling factor. For the sake of clarity, charge-transfer characteristics are hereinafter discussed as functions of Δ, and the theoretical predictions for the finite-voltage situation can be immediately obtained by setting $\Delta \equiv eV_{sd}/\mathcal{W}_0$.

Our numerical results for $T_{k_y}(E)$ in case the doping E is close to LL can be summarized as follows:

(i) The transmission probability depends on the wave vector k_y in a similar manner as for a system at zero magnetic field, i.e., $T_{k_y}(E) \propto \cosh^{-2}[\mathcal{A}(k_y - k_{\text{res}})L]$, where $\mathcal{A}$ is the momentum-independent empirical parameter close to unity, and k_{res} is given by Eq. (15).

(ii) The dependence of $T_{k_y}(E)$ on the doping E can be rationalized with the Breit-Wigner distribution, characterized by $\mathcal{W}(k_y)$, the momentum-dependent full width at half maximum (FWHM).

Subsequently,

$$T_{k_y}(E) \simeq \frac{\cosh^{-2}[\mathcal{A}(k_y - k_{\text{res}})L]}{1 + [2(E-E_0)/\mathcal{W}(k_y)]^2}, \quad (22)$$

where we have further assumed that the mean doping E_0 corresponds to the transmission maximum. Substituting the above to Eqs. [19 and 20] and taking $\mathcal{W}(k_y) \simeq \mathcal{W}_0$ at the first step, we obtain the approximating formulas for $\mathcal{F}$ and $\mathcal{R}$ in the $W \gg L$ limit

$$\overline{\mathcal{F}}(\Delta) = \frac{2}{3} - \frac{\Delta}{3(1+\Delta^2)\arctan\Delta}, \quad (23)$$

$$\overline{\mathcal{R}}(\Delta) = \frac{2}{5} - \frac{\Delta}{5(1+\Delta^2)\arctan\Delta}\left[3 - \frac{4}{3(1+\Delta^2)}\right]. \quad (24)$$

We observe that $\overline{\mathcal{F}}(\Delta)$ (23) reaches its minimum at $\Delta = 0$, restoring the linear-response value $\overline{\mathcal{F}}(0) = 1/3$. To the contrary, the minimum of $\overline{\mathcal{R}}(\Delta)$ corresponds to a nonzero voltage difference (or the amplitude of doping fluctuations), namely $\Delta_{\min} = 0.34$ and $\mathcal{R}(\Delta_{\min}) = 0.064$, which is slightly lower than the linear-response value $\overline{\mathcal{R}}(0) = 1/15$. A striking consequence of Eqs. (23) and (24) is that the second and third charge-transfer cumulants are expected to be quantum limited also for $\Delta \to \infty$, with $\mathcal{F}$ and $\mathcal{R}$ approaching the values close to $\overline{\mathcal{F}}(\infty) = 2/3$ and $\overline{\mathcal{R}}(\infty) = 2/5$, respectively, which are still significantly smaller than for the Poissonian process ($\mathcal{F}_{\text{Poisson}} = \mathcal{R}_{\text{Poisson}} = 1$).

B. Numerical results

Instead of employing the empirical expression for $T_{k_y}(E)$ (22), one can calculate the averages in Eqs. (19) and (20) numerically, for the ensemble of actual transmission matrices $\boldsymbol{T}(E)$ obtained by repeating the mode matching (as presented in Appendix B) for different values of E sampled over a desired energy interval [38]. Such a computational experiment brought us to the conclusion that $\overline{\mathcal{F}}(\Delta)$ (23) and $\overline{\mathcal{R}}(\Delta)$ (24) provide reasonable approximations of the actual $\mathcal{F}$ and $\mathcal{R}$ values for $\Delta \lesssim 2$ only.

Nevertheless, we find both the approximations are substantially improved when taking

$$\mathcal{W}(k_y) \simeq \mathcal{W}_0 + \alpha\left[\frac{W(k_y - k_{\text{res}})}{2\pi}\right]^2, \quad (25)$$

with the additional empirical parameter α. A comparison of $\mathcal{W}(k_y)$ given by Eq. (25) with the values of FWHW obtained numerically is presented in Fig. 6. Next, in Fig. 7, we compare the values of $\mathcal{F}$ and $\mathcal{R}$ obtained by means of the mode-matching analysis [solid lines], with these following from the empirical model for $T_{k_y}(E)$ constituted by Eqs. (22) and (25) [dashed lines]. $\overline{\mathcal{F}}(\Delta)$ (23) and $\overline{\mathcal{R}}(\Delta)$ (24) are also shown in Fig. 7 [dotted lines]. Our results show that the model for $T_{k_y}(E)$ as presented, generically reproduces the actual values of $\mathcal{F}$ and $\mathcal{R}$ within 1% accuracy, provided $\Delta \lesssim 20$ and the position in the doping-field plane (E_0, B) is chosen such that $\mathcal{W}_0 \lesssim 10^{-3}\,t_\perp$. Moreover, our prediction that the second and third charge-transfer cumulant are quantum limited for $\Delta \to \infty$ is now further supported, and the limiting values of $\mathcal{F}$ and $\mathcal{R}$ can be approximated by

$$\mathcal{F}_\infty \simeq 0.7 \quad \text{and} \quad \mathcal{R}_\infty \simeq 0.5. \quad (26)$$

C. Transmission statistics

For the sake of completeness, we discuss now the evolution of statistical distribution of transmission eigenvalues $\rho(T)$ with the increasing voltage difference (or the amplitude of doping fluctuations), quantified by the factor Δ again [see Eq. (21)]. For the linear-response regime ($\Delta \to 0$) such a distribution reads [12,13]

$$\rho^{(1,2)}_{\text{diff}}(T) = \frac{2G^{(1,2)}_{\text{diff}}}{\pi\sigma_0}\frac{1}{T\sqrt{1-T}}, \quad (27)$$

where $G^{(1,2)}_{\text{diff}}$ are given by Eq. (12) for graphene or its bilayer in the pseudodiffusive limit $W \ll L$. We further notice that the distribution $\rho^{(1,2)}_{\text{diff}}(T)$ (27) is normalized such that

$$\int_0^1 dT\,\rho^{(1,2)}_{\text{diff}}(T)T = G^{(1,2)}_{\text{diff}}. \quad (28)$$

In our numerical discussion, the sample aspect ratio is fixed at the large but finite value $W/L = 20$. (Such an approach is partly motivated by the existing experimental studies of pseudodiffusive graphene, see Refs. [17–19].) For

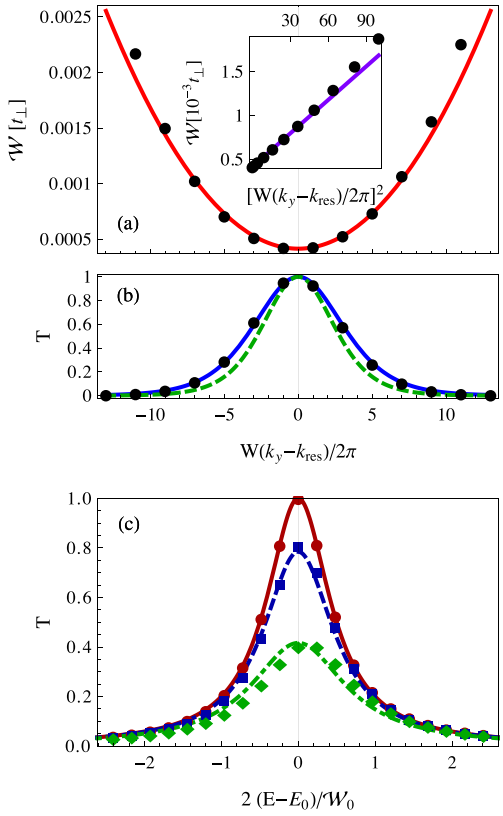

FIG. 6. (Color online) Transmission resonances for the second LL at $B = 5$ T with the remaining parameters the same as in Fig. 2. (a) The resonance width $\mathcal{W}$ as a function of k_y. Data points are derived from the mode matching analysis; solid line depicts $\mathcal{W}(k_y)$ approximated by Eq. (25) with the best-fitted parameters $\alpha \simeq 1.27 \times 10^{-5} t_\perp$ and $\mathcal{W}_0 \simeq 4.2 \times 10^{-4} t_\perp$. [The inset shows the same data as a function of $(k_y - k_{\mathrm{res}})^2$.] (b) Transmission probabilities for different k_y and the doping fixed at $E = E_0 = 0.060\,72\,t_\perp \simeq 0.024$ eV. Solid (or dashed) line corresponds to Eq. (22) with the best-fitted $\mathcal{A} \simeq 0.80$ (or the fixed $\mathcal{A} = 1$). (c) Transmission probability as a function of the doping for different k_y: Solid, dashed, and dash-dotted line depict the values obtained from Eq. (22) for $k_y - k_{\mathrm{res}} = 0, 4\pi/W$, and $-8\pi/W$ (with $\mathcal{A} \simeq 0.80$ for all three cases).

this reason, the total number of distinct nonzero transmission eigenvalues $T_{k_y}(E)$ in the energy interval (21) is relatively small, particularly for $\Delta \lesssim 1$. In effect, the corresponding histograms depicting $\rho(T)$ are sensitive to the choice of a bin size. To overcome this difficulty, we introduce the so-called *partial conductance*

$$\tilde{G}(T)/G_0 = \int_0^T dT' \rho(T') T' \equiv \int_0^T dT' \langle \mathrm{Tr}\,[\boldsymbol{T}\,\delta_{\xi\to 0}(\boldsymbol{T} - T'\boldsymbol{I})]\rangle_{|E-E_0|\le \mathcal{W}_0\Delta/2}, \tag{29}$$

where $\delta_{\xi\to 0}(\boldsymbol{M})$ is an analytic representation of the Dirac delta function with a matrix argument $\boldsymbol{M}$. [For instance, $\tilde{G}(1)$ reproduces the conductance as given by Eq. (18).] In the

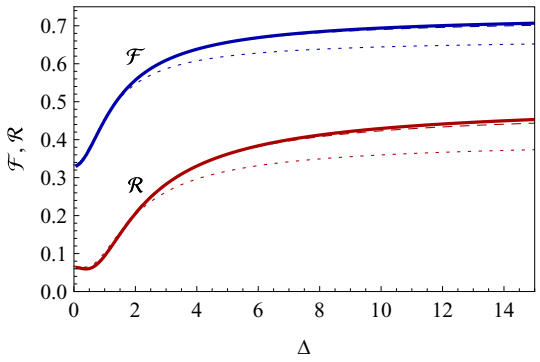

FIG. 7. (Color online) $\mathcal{F}$ and $\mathcal{R}$ as functions of the voltage difference (or the amplitude of doping fluctuations), quantified by the scaling factor Δ defined via Eq. (21). The values of E_0 and B are the same as in Fig. 6(b), the remaining parameters are the same as in Fig. 2. Solid lines depict the values obtained by calculating the averages in Eqs. [(19) and (20)] numerically, for transmission matrices derived via the mode matching, whereas dashed lines correspond to the empirical model constituted by Eqs. (22) and (25) with $\mathcal{A} = 0.80$, $\mathcal{W}_0 = 4.2 \times 10^{-4}\,t_\perp$, and $\alpha = 1.27 \times 10^{-5}\,t_\perp$. The approximating values of $\overline{\mathcal{F}}(\Delta)$ (23) and $\overline{\mathcal{R}}(\Delta)$ (24) are also shown (with dotted lines).

pseudodiffusive limit, we have

$$\tilde{G}^{(1,2)}_{\mathrm{diff}}(T) = G_0 \int_0^T dT' \rho^{(1,2)}_{\mathrm{diff}}(T') T' = G^{(1,2)}_{\mathrm{diff}}(1 - \sqrt{1-T}). \tag{30}$$

In Fig. 8, we compare $\tilde{G}(T)$ obtained from Eq. (29) utilizing three different numerical approaches, in analogy to the earlier presentation of Fig. 7. First, the average in Eq. (29) is calculated for actual transmission matrices derived via the mode matching [solid lines]. Next, the empirical model constituted by Eqs. (22) and (25) [dotted lines] and its simplified version obtained by setting $\mathcal{W}(k_y) \simeq \mathcal{W}_0$ [dashed lines] are employed. The values of $G^{(2)}_{\mathrm{diff}}(T)$ [Eq. (30)] are also shown in Fig. 8 [dot-dashed lines]. Our results show that the actual distribution of transmission eigenvalues $\rho(T)$ may follow the pseudodiffusive distribution $\rho^{(2)}_{\mathrm{diff}}(T)$ (27) only if the doping energy is adjusted rather closely to LL ($\Delta = 0.1$). When doping fluctuations get larger ($\Delta = 1$), a significant deviation of $\rho(T)$ from $\rho^{(2)}_{\mathrm{diff}}(T)$ is observed, due to the enhanced contribution of low transmission eigenvalues. In both cases, the agreement with the empirical model presented earlier [see Eqs. (22) and (25)] is excellent.

V. INFLUENCE OF INDIRECT INTERLAYER HOPPING INTEGRALS

Theoretical calculations based on the Kubo formula [39] show that the minimal conductivity of ballistic graphene bilayer may be unstable with respect to indirect interlayer hopping integrals [40], which are neglected in the Hamiltonian (1). At zero field and zero bias situation ($B = V = 0$), the minimal conductivity is predicted to be $(24/\pi)\,e^2/h = 6\sigma_0$ (i.e, *six times* larger than the conductivity of a monolayer) for arbitrarily small indirect interlayer hoppings. In the absence of

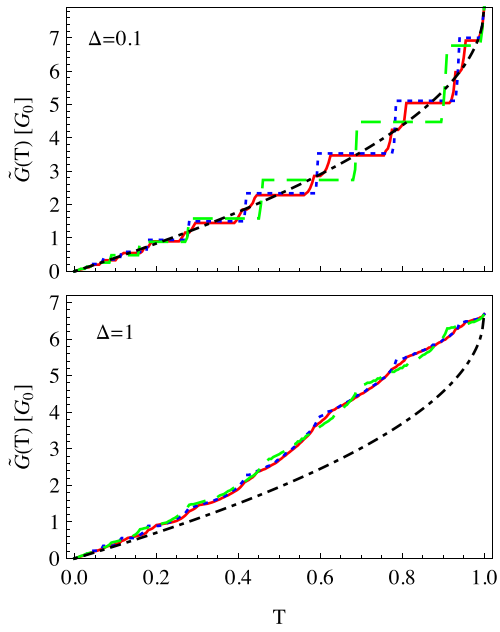

FIG. 8. (Color online) Partial conductance $\tilde{G}(T)$ [Eq. (29)] for the two values of Δ [Eq. (21)] [specified for each panel] and the physical parameters same as in Fig. 7. Solid lines mark the values obtained by calculating the average in Eq. (29) numerically for transmission matrices derived via the mode matching. Dotted lines correspond to the empirical model constituted by Eqs. (22) and (25) with $\mathcal{A} = 0.80$, $\mathcal{W}_0 = 4.2 \times 10^{-4}\, t_\perp$, and $\alpha = 1.27 \times 10^{-5}\, t_\perp$, whereas dashed lines present the values obtained by setting $\mathcal{A} = 1$, $\alpha = 0$, and leaving $\mathcal{W}_0$ same as for dotted lines. The pseudodiffusive values of $G^{(2)}_{\rm diff}(T)$ [Eq. (30)] are also shown (with dot-dashed lines).

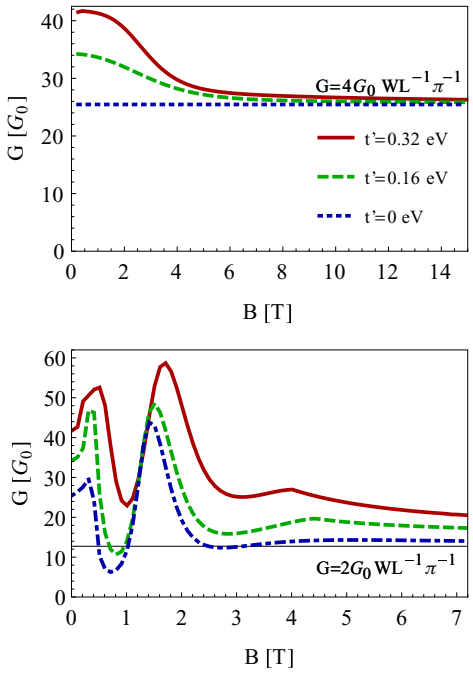

FIG. 9. (Color online) Magnetoconductance of unbiased graphene bilayer (per one direction of spin) for different values of the next-nearest neighbor interlayer hopping t'. The field-dependent doping is adjusted to follow the transmission maxima for $n = 0$ (top panel) and $n = 2$ (bottom panel) Landau levels. The system parameters are the same as used in Fig. 2.

such hoppings, the Kubo conductivity drops back to $2\sigma_0$, what is attributed to the disappearance of additional Fermi surface pockets at low energies [41,42]. (We notice here, that the effect has no high-frequency analog, which beautifully manifests itself by direct scaling of visible light absorption with the number of layers, see Ref. [8].) The experimental value of $\sigma_{xx} \simeq 5\sigma_0$ [43] is close to the prediction of Ref. [39], with a small deviation which may be related to several factors, such as a finite system size, the presence of disorder, electron-phonon coupling, or electron-electron interactions, not taken into account by existing theory in a rigorous manner. Additionally, the values following from the Kubo formula are known to be sensitive to the order in which certain limits are taken [44]. For these reasons, an independent calculation employing the Landauer-Büttiker formalism for a ballistic system of a given length L and a width W, allowing one at least to identify the possible effects of a finite system size, is desired.

The Hamiltonian for K valley [Eq. (1)] is now replaced by

$$H' = \begin{pmatrix} U_1(x) & \pi_x + i\pi_y & t_\perp & 0 \\ \pi_x - i\pi_y & U_1(x) & 0 & \pi'_x + i\pi'_y \\ t_\perp & 0 & U_2(x) & \pi_x - i\pi_y \\ 0 & \pi'_x - i\pi'_y & \pi_x + i\pi_y & U_2(x) \end{pmatrix}, \tag{31}$$

where $\pi'_j = (t'/t_0)\,\pi_j$ with $j = 1,2$, $t_0 = \frac{2}{3}\sqrt{3}\hbar v_F/a$ is the nearest neighbor hopping in a single layer defined via the Fermi velocity and the lattice spacing $a = 0.246$ nm, t' is the next-nearest-neighbor interlayer hopping [45], and the remaining symbols are the same as in Eq. (1). Next, the Dirac equation $H'\psi = E\psi$ is solved numerically for the sample area $0 < x < L$, separately for each value of the transverse wave number $k_y = 2\pi n/W$ (with $n = 0, \pm1, \pm2, \ldots$) following from the periodic boundary conditions. The mode matching analysis is then carried out as reported in Appendix B. Although the wave functions for $t' \neq 0$ can still be obtained analytically in some particular situations (and will be given elsewhere), the compact-form expressions for transmission eigenvalues $T_{k_y}(E)$, such as given by Eq. (11), are now unavailable even for the simplest $E = 0$ and $B = 0$ case. The numerical results are presented in Figs. 9 and 10, where we have further limited our discussion to the case of a zero bias between the layers ($V = 0$) and to the limit of wide samples ($W \gg L$).

In Fig. 9, we demonstrate (as a proof of principle) that indirect interlayer hoppings play no role at high magnetic fields, for which $l_B \ll L$, and the transmission resonances via individual LLs are well defined. In such a limit, the conductance per one direction of spin approaches the value of $G^{(1)}_{\rm diff} = (4/\pi)\, G_0 W/L$ for the Dirac point (see top panel) or $G^{(1)}_{\rm diff}/2$ for higher LLs (see bottom panel for $n = 2$ case) consistent with the results reported in Sec. III A for the $t' = 0$ case. In the opposite limit of $B \to 0$, the zero-energy conductance is enhanced by a factor of 1.6 for $t' = 0.32$ eV

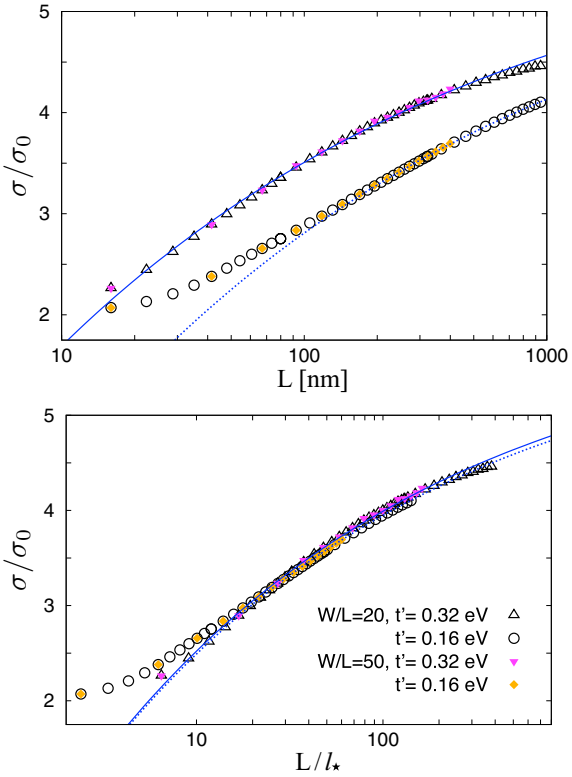

FIG. 10. (Color online) Minimal conductivity of unbiased bilayer as a function of the sample length L for $W/L = 20$ (open symbols) and $W/L = 50$ (solid symbols). The value of t' is specified for each data set. Lines show the best fitted power-law relations (32) with parameters given by Eq. (33) [solid lines] and Eq. (34) [dashed lines]. Top panel shows the raw data. In the bottom panel the data sets are shifted horizontally to demonstrate the universal behavior for $L/l_\star \gg 1$.

[or 1.3 for $t' = 0.16$ eV] above the pseudodiffusive value, which is significantly smaller than a t'-independent factor 3 predicted by Ref. [39]. The pseudodiffusive values of $\mathcal{F}$ and $\mathcal{R}$ are unaffected by t'. (We further notice that the numerical results presented in Fig. 9 correspond to $W/L = 20$ and $L = 48\,\hbar v_F/t_\perp \simeq 77$ nm.)

To further understand the nature of this clear discrepancy between the results obtained employing the Kubo formula and the Landauer-Büttiker formalism, we analyze numerically the ballistic conductivity at $E = B = 0$ as a function of L (see Fig. 10). We find that the conductivity is no longer universal for $t' > 0$, but slowly grows with L, and can be approximated (for large L) within a power law relation

$$\sigma(L) = \sigma_\infty\left[1 - \left(\frac{l_\star}{L}\right)^\gamma\right]. \tag{32}$$

Least-square fitted parameters in Eq. (32) are

$$\sigma_\infty = 6.05\sigma_0, \quad l_\star = 2.5 \text{ nm}, \quad \gamma = 0.23 \quad \text{for} \quad t' = 0.32 \text{ eV}, \tag{33}$$

and

$$\sigma_\infty = 6.0\,\sigma_0, \quad l_\star = 6.7 \text{ nm}, \quad \gamma = 0.23 \quad \text{for} \quad t' = 0.16 \text{ eV}, \tag{34}$$

with the standard deviations not exceeding 1% in all cases. We observe that only the parameter $l_\star$ significantly varies with t'. Replotting the conductivity as a function of the dimensionless variable $L/l_\star$ (see bottom panel in Fig. 10) shows the universal nature of the length dependence of the conductivity.

Although the Landauer-Büttiker conductivity approaches the value of $\sigma_\infty \simeq 6\sigma_0$ for $L \to \infty$, restoring the results of Ref. [39], the values of $\sigma(L)$ following from Eq. (32) for typical lengths of ballistic samples used in the experiments are still significantly smaller that $6\sigma_0$. In particular, using the parameters given by Eqs. [(33) and (34)] for an extrapolation, one gets $\sigma(L = 1\,\mu\text{m}) = 4.1 - 4.6\,\sigma_0$ and $\sigma(L = 10\,\mu\text{m}) = 4.9 - 5.2\,\sigma_0$, where the upper (lower) limit corresponds to $t' = 0.32$ eV ($t' = 0.16$ eV). Therefore, the fact that experimental values of the minimal conductivity [43] are noticeably smaller than the prediction of Ref. [39] may be predominantly caused by finite system sizes, with only a secondary role played by the disorder or many-body effects.

VI. CONCLUSIONS

We have calculated the conductance G, the Fano factor $\mathcal{F}$, and the factor $\mathcal{R}$ quantifying the third charge-transfer cumulant, for a ballistic strip in graphene bilayer, in the presence of bias between the layers and strong magnetic fields. Our results show that the so-called pseudodiffusive charge-transport regime appears generically for a sample with large aspect ratio ($W \gg L$) not only at the Dirac point (DP), but also in the vicinity of any Landau level (LL). However, the conductivity $\sigma = GL/W$ in the pseudodiffusive regime is not always equal to $2\sigma_0$ [with $\sigma_0 = (4/\pi)\,e^2/h$ being the conductivity of a monolayer] as predicted for a zero-field and zero-bias situation by Snyman and Beenakker [25], but takes quantized values of $s\sigma_0/2$, with the prefactor $s = 1, 2, 4$, or 8, depending whether each of spin, valley, and layer degeneracies is present or absent (see Table I).

Other charge-transfer characteristics studied are insensitive to the splittings of degeneracies, leading to $\mathcal{F} \simeq 1/3$ and $\mathcal{R} \simeq 1/15$ in any case the pseudodiffusive regime is approached. This observation is further supported with statistical analysis of the distribution of transmission eigenvalues, which follows the corresponding distribution for a diffusive wire, provided the sample doping is kept in a vicinity of DP or LL.

TABLE I. The degeneracy prefactors occurring in the expression for pseudodiffusive conductance $G = se^2/(\pi h) \times W/L$ for graphene or its bilayer in different physical situations. Indexes σ, v, and l marks the degeneracies associated with spin, valley, and layer degrees of freedom (respectively).

Degeneracy,		$B \neq 0$	
s	$B = 0$	0th LL	Other LLs
Monolayer	$4_{(\sigma,v)}$	$2_{(v)}$	$2_{(v)}$
Bilayer, $V = 0$	$8_{(\sigma,v,l)}$[a]	$4_{(v,l)}$	$2_{(v)}$
Bilayer, $V \neq 0$	$4_{(\sigma,v)}$	1	1

[a]This particular value applies in the absence of indirect interlayer hopping ($t' = 0$) only.

Additionally, the analysis is extended beyond the standard linear-response regime, i.e., we considered the effects of a finite voltage difference or slow doping fluctuations. Numerical analysis of transmission matrices obtained via the mode matching for the Dirac equation at different dopings allows us to propose an empirical model for transmission probabilities, which is then used to rationalize the dependence of charge-transfer characteristics on the voltage difference (or the amplitude of doping fluctuations). Probably, the most remarkable feature of these results is that both the shot-noise power and the third charge-transfer cumulant are predicted to be quantum limited also for large doping fluctuations, leading to $\mathcal{F}$ and $\mathcal{R}$ approaching the limiting values of $\mathcal{F}_\infty \simeq 0.5$ and $\mathcal{R}_\infty \simeq 0.7$.

Finally, we have discussed the influence of indirect interlayer hoppings (quantified by t') on the conductance and other charge-transfer characteristics. The results show that such hoppings may only affect the conductance at zero or weak magnetic fields. At stronger fields, when LLs are formed, the behavior earlier identified for $t' = 0$ is restored. Surprisingly, for $t' \neq 0$ the zero-field zero-bias conductivity at the Dirac point is neither equal to $2\sigma_0$ [25] nor $6\sigma_0$ [39], but grows monotonically with the system length, taking the values from an interval $2\sigma_0 < \sigma(L) < 6\sigma_0$. A very slow convergence to the upper conductivity limit is observed for large L and can be rationalized as $\sigma(L) \simeq 6\sigma_0[1 - (l_\star/L)^{-\gamma}]$, with a t'-independent exponent $\gamma \simeq 0.23$. The characteristic length $l_\star$ is of the order of nanometers and strongly depends on t', offering a possibility to determine the effective value of t' solely by the minimal conductivity measurement at fixed $L \ll W$.

ACKNOWLEDGMENTS

We thank to Patrik Recher for helpful comments and the correspondence. The work was supported by the National Science Centre of Poland (NCN) via Grant No. N-N202-031440, and partly by Foundation for Polish Science (FNP) under the program TEAM "*Correlations and coherence in quantum materials and structures (CCQM).*" G.R. acknowledges the support from WIKING project. Computations were partly performed using the PL-Grid infrastructure.

APPENDIX A: WAVE FUNCTIONS

In this Appendix we present the wave functions of a charge carrier in a carbon bilayer at the Dirac point as well as at finite dopings, in the presence of a uniform magnetic field.

1. The Dirac point ($\varepsilon = \delta = 0$)

A general solution of Eq. (3) for $\varepsilon = \delta = 0$ has the form of a linear combination of four independent spinors with arbitrary coefficients $C_1, \ldots, C_4$, namely

$$\begin{pmatrix} \phi_{A_1}(x) \\ \phi_{B_1}(x) \\ \phi_{B_2}(x) \\ \phi_{A_2}(x) \end{pmatrix} = C_1 \begin{pmatrix} f_{B,k_y}(x) \\ 0 \\ 0 \\ -t_\perp x f_{B,k_y}(x) \end{pmatrix} + C_2 \begin{pmatrix} 0 \\ \bar{f}_{B,k_y}(x) \\ 0 \\ 0 \end{pmatrix} + C_3 \begin{pmatrix} 0 \\ -t_\perp x \bar{f}_{B,k_y}(x) \\ \bar{f}_{B,k_y}(x) \\ 0 \end{pmatrix} + C_4 \begin{pmatrix} 0 \\ 0 \\ 0 \\ f_{B,k_y}(x) \end{pmatrix}, \tag{A1}$$

where $f_{B,k_y}(x) = \exp(l_B^{-2} x^2/2 - x\, k_y)$ and $\bar{f}_{B,k_y}(x) = 1/f_{B,k_y}(x)$.

2. Finite dopings ($\varepsilon \neq 0$ or $\delta \neq 0$)

In the case of finite dopings ($\varepsilon \neq 0$ or $\delta \neq 0$) we have two pairs of solutions, hereinafter labeled as $\phi^{\pm}_{1,\alpha}$ and $\phi^{\pm}_{2,\alpha}$ (with the signs $\pm$ related to the two subbands), which are given by

$$\begin{aligned}
\phi^{\pm}_{1,A_1}(\varepsilon,\delta;\xi) &= e^{-\xi^2/4}\,{}_1\mathrm{F}_1\left(\frac{1-2\zeta_\pm}{4};\frac{1}{2};\frac{\xi^2}{2}\right)\\
\phi^{\pm}_{2,A_1}(\varepsilon,\delta;\xi) &= \xi\, e^{-\xi^2/4}\,{}_1\mathrm{F}_1\left(\frac{3-2\zeta_\pm}{4};\frac{3}{2};\frac{\xi^2}{2}\right),\\
\phi^{\pm}_{1,B_1}(\varepsilon,\delta;\xi) &= (1+2\,\zeta_\pm)[(\delta+\varepsilon)\sqrt{2}]^{-1}\,\xi\, e^{-\xi^2/4}\,{}_1\mathrm{F}_1\left(\frac{1-2\zeta_\pm}{4};\frac{3}{2};\frac{\xi^2}{2}\right),\\
\phi^{\pm}_{2,B_1}(\varepsilon,\delta;\xi) &= [(\delta+\varepsilon)\,3\sqrt{2}]^{-1}\,e^{-\xi^2/4}\left\{(3+2\,\zeta_\pm)\,\xi^2\,{}_1\mathrm{F}_1\left(\frac{3-2\zeta_\pm}{4};\frac{5}{2};\frac{\xi^2}{2}\right)-6\,{}_1\mathrm{F}_1\left(\frac{3-2\zeta_\pm}{4};\frac{3}{2};\frac{\xi^2}{2}\right)\right\},\\
\phi^{\pm}_{1,B_2}(\varepsilon,\delta;\xi) &= (\delta+\varepsilon)^{-1}\,\alpha_\pm\, e^{-\xi^2/4}\,{}_1\mathrm{F}_1\left(\frac{1-2\zeta_\pm}{4};\frac{1}{2};\frac{\xi^2}{2}\right),\\
\phi^{\pm}_{2,B_2}(\varepsilon,\delta;\xi) &= (\delta+\varepsilon)^{-1}\,\alpha_\pm\,\xi\, e^{-\xi^2/4}\,{}_1\mathrm{F}_1\left(\frac{3-2\zeta_\pm}{4};\frac{3}{2};\frac{\xi^2}{2}\right),\\
\phi^{\pm}_{1,A_2}(\varepsilon,\delta;\xi) &= [(1-2\,\zeta_\pm)\,\alpha_\pm/\sqrt{2}]\,\xi\, e^{-\xi^2/4}\,{}_1\mathrm{F}_1\left(\frac{5-2\zeta_\pm}{4};\frac{3}{2};\frac{\xi^2}{2}\right),\\
\phi^{\pm}_{2,A_2}(\varepsilon,\delta;\xi) &= \alpha_\pm[(\delta^2-\varepsilon^2)3\sqrt{2}]^{-1}\,e^{-\xi^2/4}\left\{6\,(1+\xi^2)\,{}_1\mathrm{F}_1\left(\frac{3-2\zeta_\pm}{4};\frac{3}{2};\frac{\xi^2}{2}\right)-\xi^2\,(3+2\,\zeta_\pm)\,{}_1\mathrm{F}_1\left(\frac{3-2\zeta_\pm}{4};\frac{5}{2};\frac{\xi^2}{2}\right)\right\},
\end{aligned} \tag{A2}$$

where $\xi = \sqrt{2}(l_B^{-1}x + l_B\,k_y)$, $\alpha_\pm = [(\delta+\varepsilon)^2 - 1 - 2\,\zeta_\pm]/t$, $\zeta_\pm = \frac{1}{2}[\varepsilon^2+\delta^2 \pm \sqrt{(1-2\delta\varepsilon)^2 + t^2(\varepsilon^2-\delta^2)}]$, ${}_pF_q(a_1,\ldots,a_p;b_1,\ldots,b_q;z)$ denotes the generalized hypergeometric function [46], and the remaining symbols are the same as in Eq. (3) in the main text.

APPENDIX B: TRANSMISSION EIGENVALUES

Using wave functions of the form $\psi = (\phi_{A_1}, i\phi_{B_1}, \phi_{B_2}, i\phi_{A_2})^T$, one can write the charge-conservation conditions for a strip of width W and length L (see Fig. 1) in graphene bilayer as follows

$$\psi^\pm_{R,\mathrm{I}}(x_0) + r_p^\pm \psi^+_{L,\mathrm{I}}(x_0) + r_n^\pm \psi^-_{L,\mathrm{I}}(x_0) = \psi_{\mathrm{II}}(x_0), \quad t_p^\pm \psi^+_{R,\mathrm{III}}(x_1) + t_n^\pm \psi^-_{R,\mathrm{III}}(x_1) = \psi_{\mathrm{II}}(x_1), \tag{B1}$$

where we set $x_0 = 0$, $x_1 = L$. The lower indexes R and L refer to the solutions moving to the right or left (respectively), whereas the indexes I, II, and III refer to left contact, sample, and right contact. The upper indexes $\pm$ refer to the two subbands, and $r_p^\pm$, $r_l^\pm$ ($t_p^\pm$, $t_l^\pm$) denote the corresponding reflection (transmission) amplitudes. We further suppose that the functions $\psi_R^\pm$, $\psi_L^\pm$ in regions I and III are normalized to carry a unit current.

Taking the limit of $|U_\infty| \to \infty$ [i.e., choosing the functions $\psi_R^\pm$, $\psi_L^\pm$ for regions I and III as given by Eqs. (6) and (7) in the main text] we obtain the following system of linear equations

$$\begin{pmatrix}
1 & -1 & \phi^+_{1,A_1}(\varepsilon,\delta;\xi_0) & \phi^-_{1,A_1}(\varepsilon,\delta;\xi_0) & \phi^+_{2,A_1}(\varepsilon,\delta;\xi_0) & \phi^-_{2,A_1}(\varepsilon,\delta;\xi_0) & 0 & 0 \\
-1 & 1 & i\phi^+_{1,B_1}(\varepsilon,\delta;\xi_0) & i\phi^-_{1,B_1}(\varepsilon,\delta;\xi_0) & i\phi^+_{2,B_1}(\varepsilon,\delta;\xi_0) & i\phi^-_{2,B_1}(\varepsilon,\delta;\xi_0) & 0 & 0 \\
-1 & -1 & \phi^+_{1,B_2}(\varepsilon,\delta;\xi_0) & \phi^-_{1,B_2}(\varepsilon,\delta;\xi_0) & \phi^+_{2,B_2}(\varepsilon,\delta;\xi_0) & \phi^-_{2,B_2}(\varepsilon,\delta;\xi_0) & 0 & 0 \\
1 & 1 & i\phi^+_{1,A_2}(\varepsilon,\delta;\xi_0) & i\phi^-_{1,A_2}(\varepsilon,\delta;\xi_0) & i\phi^+_{2,A_2}(\varepsilon,\delta;\xi_0) & i\phi^-_{2,A_2}(\varepsilon,\delta;\xi_0) & 0 & 0 \\
0 & 0 & \phi^+_{1,A_1}(\varepsilon,\delta;\xi_1) & \phi^-_{1,A_1}(\varepsilon,\delta;\xi_1) & \phi^+_{2,A_1}(\varepsilon,\delta;\xi_1) & \phi^-_{2,A_1}(\varepsilon,\delta;\xi_1) & 1 & -1 \\
0 & 0 & i\phi^+_{1,B_1}(\varepsilon,\delta;\xi_1) & i\phi^-_{1,B_1}(\varepsilon,\delta;\xi_1) & i\phi^+_{2,B_1}(\varepsilon,\delta;\xi_1) & i\phi^-_{2,B_1}(\varepsilon,\delta;\xi_1) & 1 & -1 \\
0 & 0 & \phi^+_{1,B_2}(\varepsilon,\delta;\xi_1) & \phi^-_{1,B_2}(\varepsilon,\delta;\xi_1) & \phi^+_{2,B_2}(\varepsilon,\delta;\xi_1) & \phi^-_{2,B_2}(\varepsilon,\delta;\xi_1) & -1 & -1 \\
0 & 0 & i\phi^+_{1,A_2}(\varepsilon,\delta;\xi_1) & i\phi^-_{1,A_2}(\varepsilon,\delta;\xi_1) & i\phi^+_{2,A_2}(\varepsilon,\delta;\xi_1) & i\phi^-_{2,A_2}(\varepsilon,\delta;\xi_1) & -1 & -1
\end{pmatrix}
\begin{pmatrix} r_p^\pm \\ r_n^\pm \\ C_1^\pm \\ C_2^\pm \\ C_3^\pm \\ C_4^\pm \\ t_p^\pm \\ t_n^\pm \end{pmatrix}
= \begin{pmatrix} \mp 1 \\ \mp 1 \\ 1 \\ 1 \\ 0 \\ 0 \\ 0 \\ 0 \end{pmatrix}, \tag{B2}$$

where $\xi_0 = \sqrt{2}\,l_B\,k_y$, $\xi_1 = \sqrt{2}(l_B^{-1}L + l_B\,k_y)$, and the remaining symbols are the same as used in Appendix A. In turn, the transmission matrix for the K valley and the transverse momentum fixed at k_y is of the form:

$$\mathbf{t}_{K,k_y}(\varepsilon,\delta) = \begin{pmatrix} t_p^+ & t_n^+ \\ t_p^- & t_n^- \end{pmatrix}. \tag{B3}$$

[Notice that the dependence on the z component of spin m_s is incorporated in ε, see Eq. (3) in the main text.] The transmission matrix for the K' valley can be obtained from an analogous procedure, starting from the wave function $\psi' = (\phi_{A_1}, -i\phi_{B_1}, \phi_{B_2}, -i\phi_{A_2})^T$, with the components given by Eq. (A2) after the substitution $\delta \to -\delta$.

[1] A. H. Castro Neto, F. Guinea, N. M. R. Peres, K. S. Novoselov, and A. K. Geim, Rev. Mod. Phys. **81**, 109 (2009).

[2] S. Das Sarma, Sh. Adam, E. H. Hwang, and E. Rossi, Rev. Mod. Phys. **83**, 407 (2011).

[3] M. O. Goerbig, Rev. Mod. Phys. **83**, 1193 (2011).

[4] K. S. Novoselov, A. K. Geim, S. V. Morozov, D. Jiang, M. I. Katsnelson, I. V. Grigorieva, S. V. Dubonos, A. A. Firsov, and Y. Zhang, Nature (London) **438**, 197 (2005); Y. Zhang, Y.-W. Tan, H. L. Stormer, and P. Kim, *ibid.* **438**, 201 (2005).

[5] K. S. Novoselov, Z. Jiang, Y. Zhang, S. V. Morozov, H. L. Stormer, U. Zeitler, J. C. Maan, G. S. Boebinger, P. Kim, and A. K. Geim, Science **315**, 1379 (2007).

[6] C. R. Dean, L. Wang, P. Maher, C. Forsythe, F. Ghahari, Y. Gao, J. Katoch, M. Ishigami, P. Moon, M. Koshino *et al.*, Nature (London) **497**, 598 (2013); L. A. Ponomarenko, R. V. Gorbachev, G. L. Yu, D. C. Elias, R. Jalil, A. A. Patel, A. Mishchenko, A. S. Mayorov, C. R. Woods, J. R. Wallbank *et al.*, *ibid.* **497**, 594 (2013).

[7] In the case of graphene bilayer, the linear nature of the coupling gets unveiled when considering the four-band effective Hamiltonian, see Ref. [27].

[8] R. R. Nair, P. Blake, A. N. Grigorenko, K. S. Novoselov, T. J. Booth, T. Stauber, N. M. R. Peres, and A. K. Geim, Science **320**, 1308 (2008); T. Stauber, N. M. R. Peres, and A. K. Geim, Phys. Rev. B **78**, 085432 (2008).

[9] M. I. Katsnelson, Eur. Phys. J. B **51**, 157 (2006).

[10] J. Tworzydło, B. Trauzettel, M. Titov, A. Rycerz, and C. W. J. Beenakker, Phys. Rev. Lett. **96**, 246802 (2006).

[11] Yu.V. Nazarov and Ya.M. Blanter, *Quantum Transport: Introduction to Nanoscience* (Cambridge University Press, Cambridge, 2009).

[12] C. W. J. Beenakker, Rev. Mod. Phys. **80**, 1337 (2008).

[13] For a generalization of these results for other than rectangular samples, see: A. Rycerz, P. Recher, and M. Wimmer, Phys. Rev. B **80**, 125417 (2009).

[14] P. M. Ostrovsky, I. V. Gornyi, and A. D. Mirlin, Phys. Rev. B **74**, 235443 (2006).

[15] E. Louis, J. A. Verges, F. Guinea, and G. Chiappe, Phys. Rev. B **75**, 085440 (2007).

[16] E. Prada, P. San-Jose, B. Wunsch, and F. Guinea, Phys. Rev. B **75**, 113407 (2007).

[17] F. Miao, S. Wijeratne, Y. Zhang, U. C. Coscun, W. Bao, and C. N. Lau, Science **317**, 1530 (2007).

[18] L. DiCarlo, J. R. Williams, Y. Zhang, D. T. McClure, and C. M. Marcus, Phys. Rev. Lett. **100**, 156801 (2008).

[19] R. Danneau, F. Wu, M. F. Craciun, S. Russo, M. Y. Tomi, J. Salmilehto, A. F. Morpurgo, and P. J. Hakonen, Phys. Rev. Lett. **100**, 196802 (2008).

[20] A. D. Wiener and M. Kindermann, Phys. Rev. B **84**, 245420 (2011).

[21] V. V. Cheianov and V. I. Fal'ko, Phys. Rev. B **74**, 041403(R) (2006).

[22] A. Rycerz, Phys. Rev. B **81**, 121404(R) (2010); M. I. Katsnelson, Europhys. Lett. **89**, 17001 (2010).

[23] F. Ortmann and S. Roche, Phys. Rev. Lett. **110**, 086602 (2013).

[24] M. I. Katsnelson, Eur. Phys. J. B **52**, 151 (2006).

[25] I. Snyman and C. W. J. Beenakker, Phys. Rev. B **75**, 045322 (2007).

[26] J. Cserti, Phys. Rev. B **75**, 033405 (2007).

[27] E. McCann and V. I. Fal'ko, Phys. Rev. Lett. **96**, 086805 (2006); E. McCann, Phys. Rev. B **74**, 161403(R) (2006).

[28] E. V. Castro, K. S. Novoselov, S. V. Morozov, N. M. R. Peres, J. M. B. Lopes, Dos Santos, J. Nilsson, F. Guinea, A. K. Geim, and A. H. Castro Neto, Phys. Rev. Lett. **99**, 216802 (2007); J. B. Oostinga, H. B. Heersche, X. Liu, A. F. Morpurgo, and L. M. K. Vandersypen, Nat. Mater. **7**, 151 (2007).

[29] J. Nilsson, A. H. Castro Neto, F. Guinea, and N. M. R. Peres, Phys. Rev. B **76**, 165416 (2007).

[30] J. M. Pereira, F. M. Peeters, and P. Vasilopoulos, Phys. Rev. B **76**, 115419 (2007); M. Zarenia, Ph.D. Thesis, Universiteit Antwerpen, Belgium (Antwerpen, 2013), http://www.cmt.ua.ac.be/ua/Zarenia.pdf.

[31] A. Ferreira, J. Viana-Gomes, J. Nilsson, E. R. Mucciolo, N. M. R. Peres, and A. H. Castro Neto, Phys. Rev. B **83**, 165402 (2011).

[32] R. T. Weitz, M. T. Allen, B. E. Feldman, J. Martin, and A. Yacoby, Science **330**, 812 (2010).

[33] Y. H. Lai, J. H. Ho, C. P. Chang, and M. F. Lin, Phys. Rev. B **77**, 085426 (2008).

[34] Y.-T. Zhang, X. C. Xie, and Q.-f. Sun, Phys. Rev. B **86**, 035447 (2012).

[35] Z. Jiang, Y. Zhang, Y.-W. Tana, H. L. Stormer, and P. Kim, Solid State Commun. **143**, 14 (2007).

[36] E. V. Kurganova, H. J. van Elferen, A. McCollam, L. A. Ponomarenko, K. S. Novoselov, A. Veligura, B. J. van Wees, J. C. Maan, and U. Zeitler, Phys. Rev. B **84**, 121407(R) (2011).

[37] A. V. Volkov, A. A. Shylau, and I. V. Zozoulenko, Phys. Rev. B **86**, 155440 (2012).

[38] Typically, we took $10^2\Delta - 10^3\Delta$ different values of the doping E uniformly distributed over the energy interval $|E - E_0| \leq \mathcal{W}_0\Delta/2$, with the scaling factor varied from $\Delta = 0.1$ to 100 with the steps of 0.1.

[39] J. Cserti, A. Csordás, and G. Dávid, Phys. Rev. Lett. **99**, 066802 (2007); M. Koshino and T. Ando, Phys. Rev. B **73**, 245403 (2006).

[40] A. B. Kuzmenko, I. Crassee, D. van der Marel, P. Blake, and K. S. Novoselov, Phys. Rev. B **80**, 165406 (2009).

[41] E. McCann and M. Koshino, Rep. Prog. Phys. **76**, 056503 (2013).

[42] B. Wang, C. Zhang, and Z. Ma, J. Phys.: Condens. Matter **24**, 485303 (2012); **24**, 035303 (2012).

[43] A. S. Mayorov, D. C. Elias, M. Mucha-Kruczyński, R. V. Gorbachev, T. Tudorovskiy, A. Zhukov, S. V. Morozov, M. I. Katsnelson, V. I. Falko, A. K. Geim, and K. S. Novoselov, Science **333**, 860 (2011).

[44] K. Ziegler, Phys. Rev. B **75**, 233407 (2007).

[45] For the numerical calculations, we took $t_0 = 3.16$ eV and $t_\perp = 0.38$ eV after Ref. [40]. Two different values of $t' = 0.16$ eV and 0.32 eV are considered to cover the range of results reported in different works, see Ref. [41].

[46] F. W. J. Olver, D. W. Lozier, R. F. Boisvert, and C. W. Clark, *NIST Handbook of Mathematical Functions* (Cambridge University Press, Cambridge, 2010), Chap. 16.

Proceedings of the XVI National Conference on Superconductivity and Strongly Correlated Systems, Zakopane 2013

Conditions for Conductance Quantization in Mesoscopic Dirac Systems on the Examples of Graphene Nanoconstrictions

G. Rut and A. Rycerz

Marian Smoluchowski Institute of Physics, Jagiellonian University, W.S. Reymonta 4, PL-30-059 Kraków, Poland

Ballistic transport through an impurity-free section of the Corbino disk in graphene is investigated by means of the Landauer–Büttiker formalism in the mesoscopic limit. In the linear-response regime the conductance is quantized in steps close to integer multiples of $4e^2/h$, yet Fabry–Perot oscillations are strongly suppressed. The quantization arises for small opening angles $\theta \lesssim \pi/3$ and large radii ratios $R_2/R_1 \gtrsim 10$. We find that the condition for emergence of the n-th conductance step can be written as $\sqrt{n}\theta/\pi \ll 1$. A brief comparison with the conductance spectra of graphene nanoribbons with parallel edges is also provided.

DOI: 10.12693/APhysPolA.126.A-114

PACS: 73.63.–b, 72.80.Vp, 81.07.Vb

1. Introduction

Conductance quantization was observed a quarter-century ago in heterostructures with two-dimensional electron gas (2DEG) [1]. The emergence of quantization steps as multiples of $2e^2/h$ was swiftly associated to finite number of transmission modes. Further theoretical investigation revealed the generic conditions under which conductance quantization appears in systems with constrictions [2, 3]. It is predicted that conductance of the Corbino disks in 2DEG is also quantized, yet in odd-integer multiples of $2e^2/h$ [4]. Unfortunately, the experimental confirmation of this result is missing so far.

In the case of graphene, theoretical calculations predict the emergence of conductance quantization in multiples of $4e^2/h$ for nanoribbons (GNRs) as well as for systems with modulated width [5–8]. Experimental demonstration of these phenomena is challenging, mainly due to the role of disorder and boundary effects [9]. These issues encourage us to study other systems exhibiting conductance quantization which may be more resistant to the above-mentioned factors.

Transport properties of the full Corbino disk in graphene were discussed by numerous authors [10–12]. In contrast to a similar disk in 2DEG [4], conductance of the graphene-based system is not quantized. In the case of finite disk sections, systems with wide opening angles θ (see Fig. 1) should exhibit a behavior similar to complete disks as currents at the edges play a minor role. On the other hand, narrow section strongly resemble GNR, thus one could raise a question: *At which opening angle the quantization will emerge?* In this paper we show that conductance steps may appear for disk sections, provided that the ratio of outer to inner radius R_2/R_1 is large, and the opening angle is narrow.

The paper is organized as follows. In Sect. 2 we discuss solutions of the Dirac equation for a system with cylindrical symmetry. Following Berry and Mondragon [13], we then impose the so-called infinite-mass boundary conditions [14]. In Sect. 3 we discuss the exact results of mode-matching for various radii ratios and opening angles. In Sect. 4, the semiclassical approximation for transmission probability is used to determine the conditions for conductance quantization in mesoscopic Dirac systems. For such systems, the step width is $\propto \sqrt{n}$ (where n is the channel index), thus steps corresponding to large n are smeared out. Also in Sect. 4, the conductance spectra a disk section GNR are compared.

2. Model

Our system is a section of the Corbino disk in graphene characterized by the opening angle θ and the inner (outer) radius R_1 (R_2) (see Fig. 1). The leads are modelled with heavily-doped graphene areas [5]. Mode-matching analysis (see Appendices A and B) gives the transmission amplitudes for quasiparticles passing through the sample area. The conductance is obtained by summing the transmission probabilities over the modes in the Landauer–Büttiker formula

$$G = G_0 \sum_j |t_j|^2 , \tag{1}$$

with $G_0 = 4e^2/h$ due to spin and valley degeneracies.

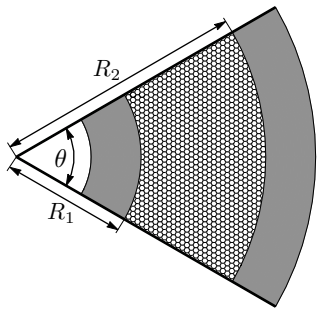

Fig. 1. A section of the Corbino disk in graphene attached to two metal contacts (shaded areas). Tick lines at the system edges depict infinite-mass boundary conditions. The opening angle $\theta = \pi/3$ and the radii ratio $R_2/R_1 = 2$ are set for an illustration only.

As the wave functions should in general possess cylindrical symmetry, we start from the analysis of the full disk. The Dirac equation in polar coordinates (r, ϕ) can be written as

$$\begin{bmatrix} \epsilon & \mathrm{e}^{-\mathrm{i}\phi}\left(\mathrm{i}\partial_r + \dfrac{\partial_\phi}{r}\right) \\ \mathrm{e}^{\mathrm{i}\phi}\left(\mathrm{i}\partial_r - \dfrac{\partial_\phi}{r}\right) & \epsilon \end{bmatrix} \begin{pmatrix} \psi_A \\ \psi_B \end{pmatrix} = 0, \quad (2)$$

where $\epsilon = (E - V)/\hbar v_\mathrm{F}$, $v_\mathrm{F} \approx c/300$ is the Fermi velocity, and the electrostatic potential energy is

$$V(r) = \begin{cases} -V_\infty & \text{if } r < R_1 \text{ or } r > R_2, \\ 0 & \text{if } R_1 < r < R_2. \end{cases} \quad (3)$$

Since the Hamiltonian commutes with the total angular momentum operator $J_z = -\mathrm{i}\hbar\partial_\phi + \hbar\sigma_z/2$, the wave function reads

$$\psi_j(r, \phi) = \exp(\mathrm{i}\phi(j - 1/2)) \begin{pmatrix} \varphi_A(r) \\ \exp(\mathrm{i}\phi)\varphi_B(r) \end{pmatrix}, \quad (4)$$

where $j = \pm\frac{1}{2}, \pm\frac{3}{2}, \ldots$ is the angular momentum quantum number. Substituting ψ_j into Eq. (2) we can derive

$$\varphi_j(r) \equiv \begin{pmatrix} \varphi_A(r) \\ \varphi_B(r) \end{pmatrix} = \begin{pmatrix} H^{(\zeta)}_{j-1/2}(\epsilon r) \\ \mathrm{i}H^{(\zeta)}_{j+1/2}(\epsilon r) \end{pmatrix}, \quad (5)$$

where $H^{(\zeta)}_\nu$, with $\zeta = 2$ (1) for the incoming (outgoing) waves, is the Hankel function of the second (first) kind [15]. The momentum-independent radial current density is $(\boldsymbol{j})_r = -ev_F\psi_j^\dagger(\sigma_x\cos\phi + \sigma_y\sin\phi)\psi_j = 4\lambda_\zeta ev_\mathrm{F}/(\pi\epsilon r)$, with $\lambda_\zeta = (-1)^\zeta$. In the high-doping limit $\varphi_j(r)$ (5) simplifies to

$$\varphi_j(r) \overset{|\epsilon|\to\infty}{\simeq} \sqrt{\frac{2}{\pi\epsilon r}} \exp(-\mathrm{i}\lambda_\zeta(\epsilon r - \pi j/2)) \begin{pmatrix} 1 \\ -\lambda_\zeta \end{pmatrix}. \quad (6)$$

Now, the sample edges are introduced to our analysis via the infinite-mass boundary conditions. Following Ref. [13], we demand that the angular current vanishes at the sample edges; i.e., $(\boldsymbol{j})_n = \hat{\boldsymbol{n}}\cdot\left[\psi_j^\dagger(\hat{x}\sigma_x + \hat{y}\sigma_y)\psi_j\right] = 0$, where $\hat{\boldsymbol{n}}$ denotes the unit vector normal to the boundary. This leads to

$$\psi_B/\psi_A = \mathrm{i}\exp(\gamma), \quad (7)$$

where $\gamma = 0$ for $\phi = \pi/2$ or $\gamma = \theta + \pi$ for $\phi = \theta + \pi/2$ (without loss of generality we set the boarders at $\phi = \pi/2$ and $\phi = \theta + \pi/2$). In particular, for $\theta = \pi/(2k+1)$ with $k = 0, 1, 2, \ldots$, the solutions can be found as linear combinations of the form $a_j\psi_j + b_j\psi_{-j}$ and are given explicitly in Appendix A. Due to Eq. (7), the values of j contributing to the sum in Eq. (1) are further restricted to

$$j = -\frac{\pi(2n-1)}{2\theta}, \quad n = 1, 2, 3\ldots \quad (8)$$

3. Conductance quantization

The numerical results for disk sections with different geometric parameters are presented in Fig. 2. For small radii ratios $R_2/R_1 \lesssim 2$ and large opening angles $\theta \gtrsim \pi/3$, the approximating formula for the pseudodiffusive limit [10]

$$G_\mathrm{diff} \approx \frac{4e^2}{\pi h}\frac{\theta}{\ln(R_2/R_1)} \quad (9)$$

reproduces the exact values obtained via Eq. (1) for $\epsilon \to 0$. In other cases, the conductance near the Dirac point is highly suppressed due to the limited number of transmission modes. At higher dopings and for $R_2/R_1 \lesssim 10$, we notice the Fabry–Perot oscillations arising from strong interference between the incoming and outgoing waves in the sample area. The conductance quantization is clearly visible for $\theta \lesssim \pi/3$. Decreasing θ, one can systematically increase the number of sharp conductance steps (see Fig. 2a).

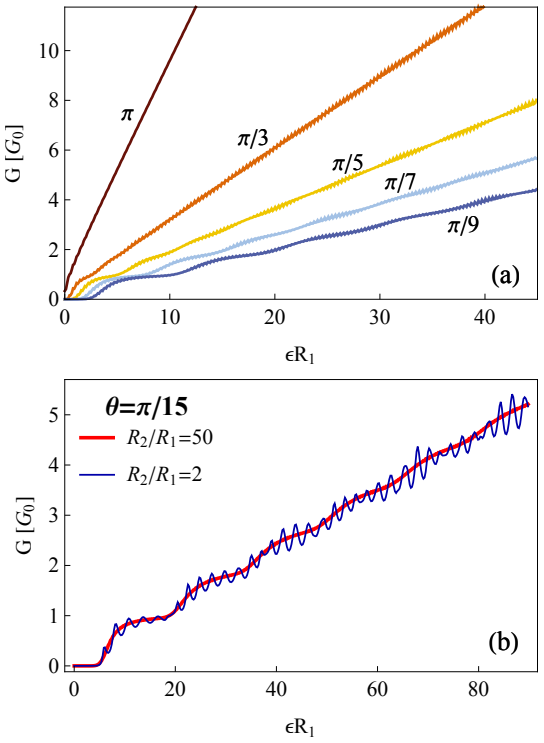

Fig. 2. (a) Conductance of the disk section as a function of doping for the opening angle varying from $\theta = \pi$ down to $\pi/9$ (specified for each curve) and the radii ratio fixed at $R_2/R_1 = 10$. (b) Same as (a) but for $\theta = \pi/15$ and two values of R_2/R_1. Notice the suppression of the Fabry–Perot oscillations for $R_2/R_1 = 50$.

To describe the above-mentioned effect in a quantitative manner, we plotted (in Fig. 3) the squared step width $\Delta\mu^2$ of several consecutive conductance steps ($1 \leqslant n \leqslant 7$) for $R_2/R_1 = 10$ and different angles θ. The n-th step width is quantified by the inverse slope of the straight line least-square fitted to the exact conductance-doping dependence; i.e.,

$$G/G_0 \approx \frac{1}{\sqrt{\Delta\mu^2}}\epsilon R_1 + \mathrm{const}, \quad (10)$$

where the fitting is performed near the inflection point corresponding to the n-th conductance step. Remark-

ably, $\Delta\mu^2$ increases systematically with n. This observation can be rationalized by calculating the transmission probability for electrostatic potential barrier within the semiclassical approximation [16]. For the classically forbidden regime, $R_1 < r < j/\epsilon$, one can write

$$T_j \approx \exp\left(-2\int_{R_1}^{j/\epsilon} \mathrm{d}r \sqrt{\left(\frac{j}{r}\right)^2 - \epsilon^2}\right), \tag{11}$$

where j/r [with j given by Eq. (8)] plays a role of the transverse wave number and we have further supposed that $R_2 \gg R_1$. Each individual step, associated with the inflection point on the conductance-doping plot, corresponds to $T_j \approx 1/2$ for a given j. A clear step becomes visible when T_j rises fast enough with ϵ, such that the step width is significantly smaller than distances to the neighboring steps. These lead to

$$\sqrt{n}\,\theta/\pi \ll 1. \tag{12}$$

In turn, for any finite θ only a limited number of the conductance steps near zero doping ($n \leqslant n_{\max}$) is visible, whereas the higher steps get smeared out. This effect has no direct analogue in similar Schrödinger systems.

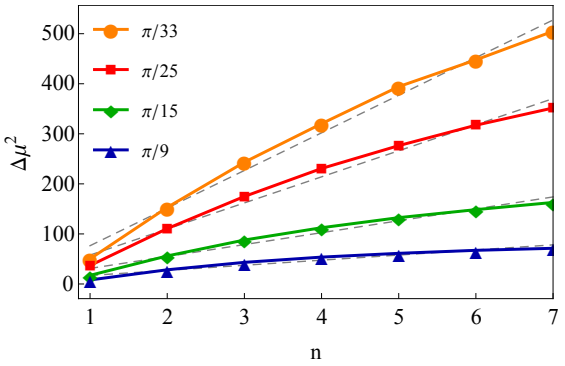

Fig. 3. Squared width $\Delta\mu^2$ versus the step index n for $R_2/R_1 = 10$ and different values of θ. Solid lines are guides for the eye only; dashed lines depict best-fitted linear dependence of $\Delta\mu^2$ on n.

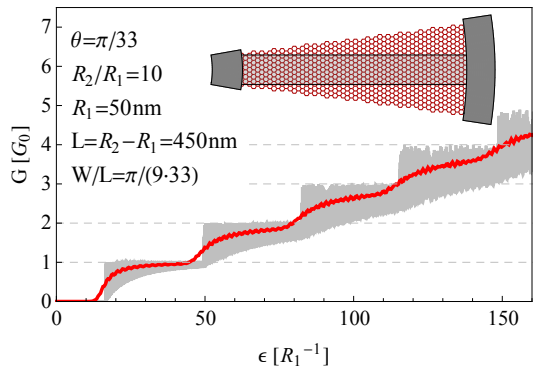

Fig. 4. Conductance as a function of doping for graphene nanoribbon (thin gray line) narrow disk section (thick red line). Inset: schematics of the two systems considered.

We compare now our results with more familiar conductance quantization appearing for GNRs, using the analytic formula for a strip with infinite-mass boundary conditions derived by Tworzydło et al. [5]. In fact, a rectangular sample of the width $W = \theta R_1$ and the length $L = R_2 - R_1$ essentially reproduces a geometric quantization appearing in a disk section for small opening angles. As shown in Fig. 4, the conductance-doping curves for the two systems closely follow each other, except from the Fabry–Perot oscillations present in GNR and strongly suppressed in the disk section with nonparallel borders.

4. Conclusion

We have investigated ballistic charge transport through a finite section of the Corbino disk in graphene with the infinite-mass boundaries. The system conductance as a function of doping shows sharp quantization steps for opening angles $\theta \lesssim \pi/3$. In comparison to the situation in graphene nanoribbons, the Fabry–Perot oscillations are strongly suppressed, particularly for large radii ratios $R_2/R_1 \gtrsim 10$. For these reasons, our theoretical study suggests that a narrow section of the disk, or a triangle, may be the most suitable sample geometry for experimental demonstration of the conductance quantization in graphene or other Dirac system.

Additionally, a special feature of the conductance-doping dependence for the Dirac systems has been identified. Namely, the quantization steps are blurred such that the step width is proportional to $\sqrt{n}$, with n being the step number. This observation helps to understand why only a very limited number of sharp conductance steps were identified so far in both experimental [9] and numerical studies [8].

Acknowledgments

The work was supported by the National Science Centre of Poland (NCN) via grant No. N-N202-031440, and partly by Foundation for Polish Science (FNP) under the program TEAM. Some computations were performed using the PL-Grid infrastructure.

Appendix A: Wave functions

In this Appendix we give explicitly the pairs of linearly-independent solutions $[f_{A,j}, f_{B,j}]^{\mathrm{T}}$ and $[g_{A,j}, g_{B,j}]^{\mathrm{T}}$ of Eq. (2) with the boundary conditions (7). For the leads ($r < R_1$ or $r > R_2$) we define the dimensionless variable $\rho = \epsilon_\infty r$ and get

$$f^L_{\alpha,j}(\rho,\phi) = \sqrt{\frac{8}{\pi\rho}}\exp\left(\mathrm{i}\,(\rho \mp \phi/2)\right) \times \cos\left(j\left(\phi - \frac{\pi}{2}\right)\right), \tag{13}$$

$$g^L_{\alpha,j}(\rho,\phi) = \pm\sqrt{\frac{8}{\pi\rho}}\exp\left(-\mathrm{i}\,(\rho \pm \phi/2)\right)$$

$$\times \cos\left(j\left(\phi+\frac{\pi}{2}\right)\right), \tag{14}$$

where the upper (lower) signs correspond to the sublattice index $\alpha = A$ ($\alpha = B$). Similarly, for the sample area ($R_1 < r < R_2$) $\rho = \epsilon r$, and the wave functions read

$$f^S_{A,j}(\rho,\phi) = \exp\left(\mathrm{i}(j+1/2)(\pi-\phi)\right) H^{(1)}_{j+1/2}(\rho) + \exp\left(\mathrm{i}\,(j-1/2)\,\phi\right) H^{(1)}_{j-1/2}(\rho), \tag{15}$$

$$f^S_{B,j}(\rho,\phi) = \mathrm{i}\left\{\exp\left(\mathrm{i}\,(j+1/2)\,\phi\right) H^{(1)}_{j+1/2}(\rho) + \exp\left(\mathrm{i}(j-1/2)(\pi-\phi)\right) H^{(1)}_{j-1/2}(\rho)\right\}, \tag{16}$$

$$g^S_{A,j}(\rho,\phi) = \exp\left(-\mathrm{i}(j+1/2)(\phi+\pi)\right) H^{(2)}_{j+1/2}(\rho) + \exp\left(\mathrm{i}\,(j-1/2)\,\phi\right) H^{(2)}_{j-1/2}(\rho), \tag{17}$$

$$g^S_{B,j}(\rho,\phi) = \mathrm{i}\left\{\exp\left(\mathrm{i}\,(j+1/2)\,\phi\right) H^{(2)}_{j+1/2}(\rho) + \exp\left(-\mathrm{i}(j-1/2)(\phi+\pi)\right) H^{(2)}_{j-1/2}(\rho)\right\}. \tag{18}$$

Appendix B: Mode-matching

The current conservation conditions at $r = R_1$ and $r = R_2$ lead to the system of linear equations

$$\begin{pmatrix} 0 & -f^L_{A,j}(\epsilon_\infty R_1,\phi) & f^S_{A,j}(\epsilon R_1,\phi) & g^S_{A,j}(\epsilon R_1,\phi) \\ 0 & -f^L_{B,j}(\epsilon_\infty R_1,\phi) & f^S_{B,j}(\epsilon R_1,\phi) & g^S_{B,j}(\epsilon R_1,\phi) \\ -g^L_{A,j}(\epsilon_\infty R_2,\phi) & 0 & f^S_{A,j}(\epsilon R_2,\phi) & g^S_{A,j}(\epsilon R_2,\phi) \\ -g^L_{B,j}(\epsilon_\infty R_2,\phi) & 0 & f^S_{B,j}(\epsilon R_2,\phi) & g^S_{B,j}(\epsilon R_2,\phi) \end{pmatrix} \begin{pmatrix} t_j \\ r_j \\ a_j \\ b_j \end{pmatrix} = \begin{pmatrix} g^L_{A,j}(\epsilon_\infty R_1,\phi) \\ g^L_{B,j}(\epsilon_\infty R_1,\phi) \\ 0 \\ 0 \end{pmatrix}, \tag{19}$$

where we have supposed that the wave is incident from the inner lead. We further notice that the transmission probability $|t_j|^2$ is insensitive to the specific value of ϵ_∞, as it only affects the phases of wave functions $f^L_{\alpha,j}$ (13) and $g^L_{\alpha,j}$ (14).

References

[1] B.J. van Wees, H. van Houten, C.W.J. Beenakker, J.G. Williamson, L.P. Kouwenhoven, D. van der Marel, C.T. Foxon, *Phys. Rev. Lett.* **60**, 848 (1988); D.A. Wharam, T.J. Thornton, R. Newbury, M. Pepper, H. Ahmed, J.E.F. Frost, D.G. Hasko, D.C. Peacock, D.A. Ritchie, G.A.C. Jones, *J. Phys. C Solid State Phys.* **21**, L209 (1988).

[2] L.I. Glazman, G.B. Lesovik, D.E. Khmel'nitskii, R.I. Shekhter, Pis'ma Zh., *Eksp. Teor. Fiz.* **48**, 218 (1988).

[3] Yu.V. Nazarov, Ya.M. Blanter, *Quantum Transport: Introduction to Nanoscience*, Cambridge University Press, Cambridge 2009, Ch. 1.

[4] G. Kirczenow, *J. Phys. Condens. Matter* **6**, L583 (1994); S. Souma, A. Suzuki, *Phys. Rev. B* **58**, 4649 (1998).

[5] J. Tworzydło, B. Trauzettel, M. Titov, A. Rycerz, C.W.J. Beenakker, *Phys. Rev. Lett.* **96**, 246802 (2006).

[6] A. Rycerz, J. Tworzydło, C.W.J. Beenakker, *Nature Phys.* **3**, 172 (2007); A. Rycerz, *Phys. Status Solidi A* **205**, 1281 (2008).

[7] J. Wurm, M. Wimmer, I. Adagideli, K. Richter, H.U. Baranger, *New J. Phys.* **11**, 095022 (2009); A. Rycerz, *Acta Phys. Pol. A* **118**, 238 (2010).

[8] S. Ihnatsenka, G. Kirczenow, *Phys. Rev. B* **85**, 121407 (2012).

[9] N. Tombros, A. Veligura, J. Junesch, M.H.D. Guimaraes, I.J. Vera-Marun, H.T. Jonkman, B.J. van Wees, *Nature Phys.* **7**, 697 (2011); B. Özyilmaz, P. Jarillo-Herrero, D. Efetov, P. Kim, *Appl. Phys. Lett.* **91**, 192107 (2007).

[10] A. Rycerz, P. Recher, M. Wimmer, *Phys. Rev. B* **80**, 125417 (2009).

[11] A. Rycerz, *Phys. Rev. B* **81**, 121404(R) (2010); M.I. Katsnelson, *Europhys. Lett.* **89**, 17001 (2010).

[12] Z. Khatibi, H. Rostami, R. Asgari, *Phys. Rev. B* **88**, 195426 (2013).

[13] M.V. Berry, R.I. Mondragon, *Proc. R. Soc. A* **41**, 53 (1987).

[14] A.R. Akhmerov, C.W.J. Beenakker, *Phys. Rev. B* **77**, 085423 (2008); C.G. Beneventano, E.M. Santangelo, *Int. J. Mod. Phys. Conf. Ser.* **14**, 240 (2012).

[15] *Handbook of Mathematical Functions*, Eds. M. Abramowitz, I.A. Stegun, Dover Publ., New York 1965, Ch. 9.

[16] V.V. Cheianov, V.I. Fal'ko, *Phys. Rev. B* **74**, 041403(R) (2006); K.J.A. Reijnders, T. Tudorovskiy, M.I. Katsnelson, *Ann. Phys.* **333**, 155 (2013).

epl A Letters Journal Exploring the Frontiers of Physics

August 2014

EPL, **107** (2014) 47005
doi: 10.1209/0295-5075/107/47005

www.epljournal.org

Minimal conductivity and signatures of quantum criticality in ballistic graphene bilayer

Grzegorz Rut and Adam Rycerz

Marian Smoluchowski Institute of Physics, Jagiellonian University - Reymonta 4, PL-30059 Kraków, Poland

received on 7 July 2014; accepted by M. Polini on 29 July 2014
published online 8 August 2014

PACS 72.80.Vp – Electronic transport in graphene
PACS 73.43.Nq – Quantum phase transitions
PACS 73.63.-b – Electronic transport in nanoscale materials and structures

Abstract – We study the ballistic conductivity of graphene bilayer in the presence of next-nearest neighbor hoppings between the layers. An undoped and unbiased system was found in Rut G. and Rycerz A., *Phys. Rev. B*, **89** (2014) 045421, to show a nonuniversal (length-dependent) conductivity $\sigma(L)$, approaching the value of $\sigma_\star = 3/\pi \simeq 0.95$ for large L. Here we demonstrate one-parameter scaling and determine the scaling function $\beta(\sigma) = \mathrm{d}\ln\sigma/\mathrm{d}\ln L$. The scaling flow has an attractive fixed point ($\beta(\sigma_\star) = 0$, $\beta'(\sigma_\star) < 0$) reproducing the scenario predicted for random impurity scattering of Dirac fermions with Coulomb repulsion, albeit the system considered is perfectly ballistic and interactions are not taken into account. The role of electrostatic bias between the layers is also briefly discussed.

Introduction. – One of the most unexpected properties of graphene —a two-dimensional form of carbon discovered in 2005 [1]— is the pseudodiffusive nature of charge transport via undoped ballistic samples, manifesting itself by the fact that dc conductance obeys Ohm's law for classical conductors characterized by the universal quantum value of the conductivity [2–5], namely

$$G = \sigma_0 \frac{W}{L}, \qquad \sigma_0 = \frac{1}{\pi} \quad \left[\frac{se^2}{h}\right], \tag{1}$$

where W is the sample width, L is the length [6], and the units of se^2/h with $s = 4$ are chosen to account the spin and valley degeneracies. Such a macroscopic quantum phenomenon has a remarkable high-frequency analog, *i.e.*, the visible light opacity of graphene also takes quantized values [7]. Although the opacity directly scales with the number of graphene layers, such an additive property usually does not apply for dc conductance [8].

Early theoretical works on ballistic graphene bilayers [9,10] showed that the minimal conductivity at zero bias situation changes abruptly as a function of the next-nearest neighbor interlayer hopping integral t', taking the value of $\sigma_0 = 1/\pi$ for $t' = 0$, or $\sigma_\star = 3\sigma_0$ for any $t' \neq 0$ [11], provided that $s = 8$ in eq. (1) due to the additional layer degeneracy. The appearance of such a quantum-critical behavior was attributed to the topological transition of the Fermi surface at low energies [8]. Experimental values of the minimal conductivity are generally lower than $\sigma_\star$, covering the range from $\sim \sigma_0$ [12] up to $2.5\,\sigma_0$ [13]. We have recently shown, employing the Landauer-Büttiker formalism, that the minimal conductivity of finite, ballistic samples is not universal but length dependent [14], and can be rationalized, for large L, as

$$\sigma(L) \simeq \overline{\sigma}(L) = \sigma_\star \left[1 - (\lambda/L)^\gamma\right], \tag{2}$$

where the characteristic length $\lambda = \lambda(t')$, and $\gamma < 1$ is the parameter-independent exponent. In turn, the predictions of refs. [9,10] are restored for $L \to \infty$, whereas in the opposite limit ($L \to 0$) one gets $\sigma(L) \to \sigma_0$ regardless of $t' = 0$ or $t' \neq 0$. It is also shown in ref. [14] that the universal conductivity is restored for resonances with the Landau levels at high magnetic fields [15].

In this paper, we point out that the scaling function

$$\beta(\sigma) = \frac{\mathrm{d}\ln\sigma}{\mathrm{d}\ln L}, \tag{3}$$

which plays a central role in the conceptual understanding of the metal insulator transition [16] and is widely considered in the context of disordered Dirac or spin-orbit systems [17–19] (see fig. 1), also unveils an intriguing analogy between interaction-induced quantum criticality in disordered Dirac systems [19] and transport properties of

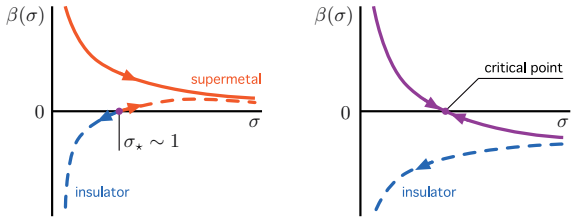

Fig. 1: (Colour on-line) Schematic scaling functions $\beta(\sigma)$ (3) for two-dimensional disordered Dirac (solid lines) and spin-orbit (dashed lined) systems. Left: noninteracting case [17]; right: Coulomb interaction included [19]. Arrows indicate the flows of the dimensionless conductivity σ with increasing L. (Adapted from ref. [19].)

ballistic graphene bilayer with skew interlayer hoppings. The paper is organized as follows: In the next section we present the mode-matching analysis for transport of Dirac fermions via finite samples of ballistic bilayer. In the third section we discuss the functions $\sigma(L)$ for different values of t' and demonstrate one-parameter scaling. Possible effects of nonzero bias between the layers are summarized in the fourth section. A brief overview of the results given in the last section.

Mode-matching for Dirac fermions. – The analysis starts from the four-band effective Hamiltonian for low-energy excitations [8], which can be written as

$$H = \xi \begin{pmatrix} -V/2 & e^{-i\theta}\pi & \xi t_\perp & 0 \\ e^{i\theta}\pi^\dagger & -V/2 & 0 & \nu e^{-i\theta}\pi \\ \xi t_\perp & 0 & V/2 & e^{i\theta}\pi^\dagger \\ 0 & \nu e^{i\theta}\pi^\dagger & e^{-i\theta}\pi & V/2 \end{pmatrix}, \qquad (4)$$

where the valley index $\xi = 1$ (-1) for the K (K') valley, θ denotes the angle between the x-axis and the armchair direction (see fig. 2), $\pi = \hbar v_F(-i\partial_x + \partial_y)$ with $v_F = \sqrt{3}\, t_0 a/2 \simeq 10^6\,\mathrm{m/s}$ being the Fermi velocity (in a monolayer) defined via the interlayer hopping $t_0 = 3.16\,\mathrm{eV}$ [20] and the lattice parameter $a = 0.246\,\mathrm{nm}$, the nearest-neighbor interlayer hopping $t_\perp = 0.38\,\mathrm{eV}$, $\nu = t'/t_0$ with t' being the next-nearest neighbor interlayer hopping, and V is the electrostatic bias between the layers. We further consider solutions of the Dirac equation $H\Psi = E\Psi$ in the form

$$\Psi(x,y) = \begin{pmatrix} \phi_1(x) \\ \phi_2(x) \\ \phi_3(x) \\ \phi_4(x) \end{pmatrix} \exp(ik_y y) \qquad (5)$$

due to the translational invariance in the y-direction.

We focus here on a zero bias case $V = 0$ (for the discussion of $V \neq 0$ case see the fourth section), for which a general solution for $E = 0$ (the sample area) and the K valley reads

$$\begin{pmatrix} \phi_1(x) \\ \phi_2(x) \\ \phi_3(x) \\ \phi_4(x) \end{pmatrix} = c_1 \begin{pmatrix} -\alpha_1^+ f_1^+ \\ 0 \\ 0 \\ e^{i\theta} f_1^+ \end{pmatrix} + c_2 \begin{pmatrix} -\alpha_{-1}^+ f_{-1}^+ \\ 0 \\ 0 \\ e^{i\theta} f_{-1}^+ \end{pmatrix} + c_3 \begin{pmatrix} 0 \\ e^{-i\theta} f_{-1}^- \\ -\alpha_{-1}^- f_{-1}^- \\ 0 \end{pmatrix} + c_4 \begin{pmatrix} 0 \\ e^{-i\theta} f_1^- \\ -\alpha_1^- f_1^- \\ 0 \end{pmatrix}, \qquad (6)$$

where $\alpha_\zeta^\pm = \nu \exp(\pm 3i\theta)\left[i + \zeta\sqrt{\pm 8ik_y/\left[\exp(\pm 3i\theta)\,\tilde{t}\nu\right] + 1}\right]$, $f_\zeta^\pm = \exp[(\pm k_y + \alpha_\zeta^\pm \tilde{t})x]$, $\tilde{t} = t_\perp/(\hbar v_F)$, and the coefficients $c_1, \ldots, c_4$ are to be determined later. In the opposite limit of $E \to \infty$ (heavily doped leads) we obtain

$$\begin{pmatrix} \phi_{1,s}^\pm(x) \\ \phi_{2,s}^\pm(x) \\ \phi_{3,s}^\pm(x) \\ \phi_{4,s}^\pm(x) \end{pmatrix} = \mathcal{N}_\pm(\nu) \times \exp(ik_x x) \begin{pmatrix} -(\mu_\mp/2)\exp(-2i\theta) \\ s\eta_\pm\left(\mu_\pm/\sqrt{2}\right)\exp(-i\theta) \\ s\sqrt{2}\eta_\pm \exp(i\theta) \\ 1 \end{pmatrix}, \qquad (7)$$

where $s = \mathrm{sgn}(k_x)$, $\mu_\pm = \nu \pm \sqrt{\nu^2+4}$, $\eta_\pm = 1/\sqrt{2 + \nu\mu_\pm}$, and the factors $\mathcal{N}_\pm(\nu) = \sqrt{\mu_\pm/\left[2\left(\mu_\pm + 2\right)\right]}$ are chosen to normalize the current. Matching the solutions given by

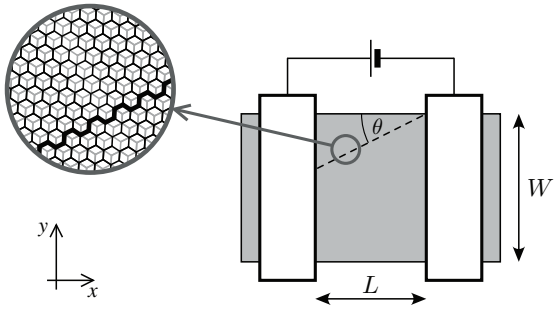

Fig. 2: A strip of bilayer graphene (shaded area) of width W, contacted by two electrodes (white rectangles) at a distance L. A voltage source drives the electric current through the device. Separate top- and bottom-gate electrodes (not shown) allow both the Fermi energy E and the bias between the layers V to be controlled electrostatically. A magnified view exhibits the crystallographic orientation, with the angle θ between an armchair direction (dashed line in the main plot) and x-axis of the coordinate system (see bottom left).

$$\begin{pmatrix} \phi^+_{1,-1} & \phi^-_{1,-1} & \alpha^+_1 & \alpha^+_{-1} & 0 & 0 & 0 & 0 \\ \phi^+_{2,-1} & \phi^-_{2,-1} & 0 & 0 & -e^{-i\theta} & -e^{-i\theta} & 0 & 0 \\ \phi^+_{3,-1} & \phi^-_{3,-1} & 0 & 0 & \alpha^-_{-1} & \alpha^-_1 & 0 & 0 \\ \phi^+_{4,-1} & \phi^-_{4,-1} & -e^{-i\theta} & -e^{-i\theta} & 0 & 0 & 0 & 0 \\ 0 & 0 & \alpha^+_1 f^+_1 & \alpha^+_{-1} f^+_{-1} & 0 & 0 & \phi^+_{1,1} & \phi^-_{1,1} \\ 0 & 0 & 0 & 0 & -e^{-i\theta} f^-_{-1} & -e^{-i\theta} f^-_1 & \phi^+_{2,1} & \phi^-_{2,1} \\ 0 & 0 & 0 & 0 & \alpha^-_{-1} f^-_{-1} & \alpha^-_1 f^-_1 & \phi^+_{3,1} & \phi^-_{3,1} \\ 0 & 0 & -e^{i\theta} f^+_1 & -e^{i\theta} f^+_{-1} & 0 & 0 & \phi^+_{4,1} & \phi^-_{4,1} \end{pmatrix} \begin{pmatrix} r^\pm_p \\ r^\pm_n \\ c^\pm_1 \\ c^\pm_2 \\ c^\pm_3 \\ c^\pm_4 \\ t^\pm_p \\ t^\pm_n \end{pmatrix} = \begin{pmatrix} -\phi^\pm_{1,1} \\ -\phi^\pm_{2,1} \\ -\phi^\pm_{3,1} \\ -\phi^\pm_{4,1} \\ 0 \\ 0 \\ 0 \\ 0 \end{pmatrix}, \tag{8}$$

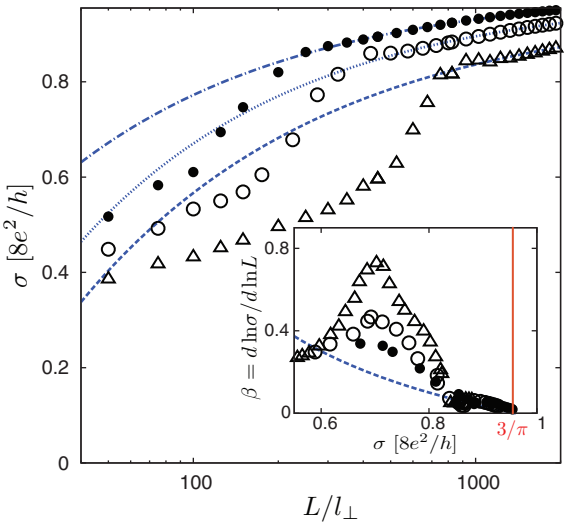

Fig. 3: (Colour on-line) Minimal conductivity of an unbiased graphene bilayer as a function of the sample length L (specified in units of $l_\perp = \hbar v_F/t_\perp \simeq 1.60\,\mathrm{nm}$). Different datapoints correspond to different values of the next-nearest neighbor interlayer hopping: $t' = 0.1\,\mathrm{eV}$ (△), $0.2\,\mathrm{eV}$ (◯), and $0.3\,\mathrm{eV}$ (●). Lines depict best-fitted approximating functions $\overline{\sigma}(L)$ (2) (see table 1 for further details). The inset shows the scaling function $\beta(\sigma)$ (3) obtained by numerical differentiation of the data. (Notice that the approximating function is replotted for $t' = 0.1\,\mathrm{eV}$ only, as the three lines overlap for the variables used in the inset.) The sample aspect ratio is fixed at $W/L = 20$; the crystallographic orientation is $\theta = \pi/4$.

eqs. (6), (7) at $x = 0$ and $x = L$ leads to

see eq. (8) above

where we have further defined $\phi^\pm_{j,s} \equiv \phi^\pm_{j,s}(0)$, $f^\pm_q = f^\pm_q(L)$. Solving the linear system of equations (8) one obtains the transmission and reflection matrices for a given transverse wave number

$$\mathbf{t}(k_y) = \begin{pmatrix} t^+_p & t^+_n \\ t^-_p & t^-_n \end{pmatrix}, \quad \mathbf{r}(k_y) = \begin{pmatrix} r^+_p & r^+_n \\ r^-_p & r^-_n \end{pmatrix}, \tag{9}$$

where the internal structure arises from the presence of two subbands in the dispersion relation. At zero magnetic field, time-reversal symmetry coupling the valleys K and K' is preserved, and each transmission eigenvalue from one valley has a copy in the other valley [21].

Table 1: Least-square fitted parameters $\sigma_\star$, λ, and γ of the function $\overline{\sigma}(L)$, defined by eq. (2), corresponding to the lines in fig. 3. The values of $L_{0.01}$, such that for $L \geqslant L_{0.01}$ the function $\overline{\sigma}(L)$ matches the actual conductivity with accuracy better that 1%, are given in the last column.

t' (eV)	$\sigma_\star\ (8e^2/h)$	$\lambda/l_\perp$	γ	$L_{0.01}/l_\perp$
0.1	0.96	16.8	0.50	935
0.2	0.98	12.6	0.55	457
0.3	0.99	6.1	0.53	278

Conductivity and one-parameter scaling. – Next, the dimensionless conductivity is determined from the Landauer-Büttiker formula [22]

$$\sigma(L) = \frac{L}{W} \sum_{\{k_y\}} \mathrm{Tr}\left[\mathbf{t}(k_y)\,\mathbf{t}^\dagger(k_y)\right], \tag{10}$$

where we have assumed periodic boundary conditions at y-direction, leading to the quantization of the transverse wave number $k_y = 0, \pm 2\pi/W, \pm 4\pi/W, \ldots$. Our numerical results for $E = V = 0$ are summarized in fig. 3 and table 1. For demonstrative purposes, we have chosen $W/L = 20$ and $\theta = \pi/4$. For any $t' \neq 0$, the conductivity given by eq. (10) slowly grows with L, taking the values from the interval $1/\pi \leqslant \sigma(L) \leqslant 3/\pi$, with the upper (lower) bound approached for $L \to 0$ ($L \to \infty$). The best-fitted approximating functions $\overline{\sigma}(L)$ of the form given by eq. (2) (lines in fig. 3) rationalize the numerical results for large L (datapoints). The least-square fitted parameters $\sigma_\star$ and γ (see table 1) weakly depend on t', taking the values close to $\sigma_\star \simeq 3/\pi$ and $\gamma \simeq 1/2$ for small t'. These scaling characteristics appear generically for other crystallographic orientations θ, except for $\theta = \pi/6 + n\pi/3$ (with integer n), corresponding to the propagation along a zigzag direction, for which a lower value of $\gamma \simeq 1/4$ was found (see also ref. [14]).

The scaling function $\beta(\sigma)$ (3) can be obtained by numerical differentiation of $\sigma(L)$ given by eq. (10) (see inset in fig. 3). For the asymptotic range, eq. (2) leads to

$$\beta(\sigma) \simeq -\gamma\,(1 - \sigma_\star/\sigma), \tag{11}$$

with $\sigma = \sigma_\star \simeq 3/\pi$ being an attractive fixed point ($\beta'(\sigma_\star) < 0$ for $\gamma \simeq 1/2 > 0$) of the renormalization group flow. Such a scenario, earlier predicted for disordered Dirac systems with Coulomb interaction [19], is reproduced by our results for graphene bilayer. The values of $\beta(\sigma)$ obtained numerically become t'-independent and follow eq. (11) for $\sigma \gtrsim 0.8$.

This surprising coincidence (it is worth stressing here that the system we consider is ballistic and no interactions are taken into account) seems difficult to understand in terms of the existing symmetry-based theory of localization [18,19]. Particular features of the results suggest that next-nearest neighbor interlayer hoppings, apart from breaking the rotational symmetry of the Hamiltonian in a single valley (a phenomenon known as *trigonal warping* [8]), may also induce corrections to $\beta(\sigma)$ of the Altshuler-Aronov type [23], destroying the supermetallic phase in graphene. A further clarification of the above-mentioned issue requires a numerical study of charge transport through the disordered graphene bilayer, which is beyond the scope of this paper.

Effects of finite bias between the layers. – Probably, the most intriguing property of a graphene bilayer is the possibility to convert it from semimetal to narrow-gap semiconductor by applying a perpendicular electrostatic field [24–28], leading to a finite bias between the layers V in the effective Hamiltonian H (4). Also, some experimental works showed that the energy gap may also appear spontaneously, due to electron-electron interactions, for bilayer samples close to the charge-neutrality point [29,30]. For these reasons, the extension of our discussion on the $V \neq 0$ case is desirable.

In such a case, the effective Dirac equation $H\Psi = E\Psi$, with $\Psi(x, y)$ in the form given by eq. (5), is integrated numerically for the sample area ($0 < x < L$), separately for each value of the transverse wave number k_y. The obtained solutions are then matched with wave functions in the leads (see eq. (7)), in analogy with the procedure presented in the second section.

The resulting conductivity spectra, for selected values of V and t', are displayed in figs. 4(a)–(d). For demonstrating purposes the sample dimensions are fixed at $W/L = 20$, $L = 48\,\hbar v_F/t_\perp$. For the unbiased sample case (see fig. 4(a)) the conductivity systematically grows with increasing t' in the small vicinity of the Dirac point, the width of which can be roughly approximated by $|E| \lesssim E_\mathrm{L}$, with

$$E_\mathrm{L} = \frac{1}{4}\, t_\perp \left(t'/t_0\right)^2 \qquad (12)$$

being the Lifshitz energy [8], reaching the value of $E_\mathrm{L} \simeq 1\,\mathrm{meV}$ for $t' = 0.32\,\mathrm{eV}$. For $V = 0$ and higher Fermi energies, σ is weakly affected by t'. For $V > 0$, the conductivity is strongly suppressed in the range of $|E| < V/2$ for any t' (see figs. 4(b)–(d)), provided that $V \gg E_\mathrm{L}$. Again, for sufficiently high energies the conductivity is almost unaffected by either the value of V or t'.

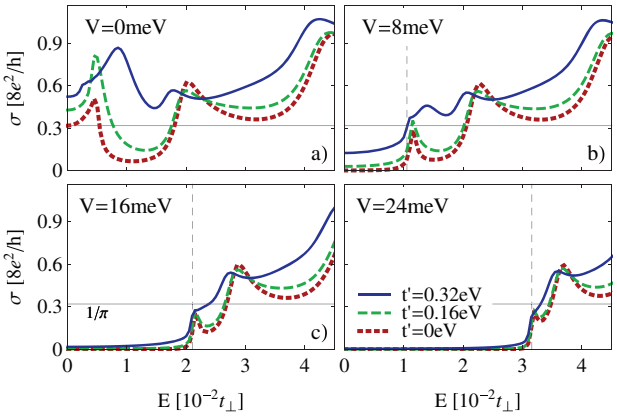

Fig. 4: (Colour on-line) Conductivity of a graphene bilayer as a function of the Fermi energy. The value of bias between the layers V is varied between the panels. Different lines at each panel depict the data obtained numerically for different values of the next-nearest neighbor interlayer hopping: $t' = 0$ (red dashed line), $t' = 0.16\,\mathrm{eV}$ (green dash-dotted line), and $t' = 0.32\,\mathrm{eV}$ (blue solid line). The vertical dashed line marks the value of $E = V/2$, the horizontal solid line corresponds to $\sigma_0 = 1/\pi$. The sample length is fixed at $L = 48\,l_\perp \simeq 77\,\mathrm{nm}$; the remaining system parameters are the same as in fig. 3.

Probably, the most interesting feature of the results presented in fig. 4 is that the dimensionless conductivity at its first maximum as a function of E reaches the value close to $\sigma \simeq 1/\pi$ for $V \gg E_\mathrm{L}$ and arbitrary t', while it is significantly higher for $V = 0$. For this reason, the measurements of the conductivity spectra of ballistic samples at zero magnetic field, and different biases between the layers, may constitute an alternative experimental method for detecting the Lifshitz transition in a graphene bilayer, supplementing the recent study focusing on the anomalies in the sequence of Landau levels [31], at least in principle.

A brief overview. – We have investigated, by means of analytical mode-matching for the effective Dirac equation, the length-dependent minimal conductivity $\sigma(L)$ of *unbiased* graphene bilayer with the nearest ($t_\perp$) and the next-nearest neighbor (t') interlayer hoppings included. The scaling function $\beta(\sigma) = \mathrm{d}\ln\sigma/\mathrm{d}\ln L$ was found i) to be insensitive to the precise value of t' and to the crystallographic orientation of the sample, provided that the physical dimensions are in the asymptotic range, *i.e.*, that $W \gg L \gg \hbar v_F/t_\perp$ (with v_F being the energy-independent Fermi velocity in a monolayer), and ii) to have an attractive fixed point at $\sigma_\star \simeq 3/\pi$. These features closely resemble the quantum-critical behavior predicted theoretically for disordered Dirac systems with Coulomb interaction [19], although the system we consider is ballistic and interactions are not taken into account. Our results show that the well-known correspondence between charge-transfer characteristics of a classical diffusive conductor and perfectly clean monolayer graphene [3,32] is accompanied by another, probably more surprising, analogy between chaotic impurity scattering of interacting Dirac

fermions and ballistic transport via bilayer samples, which gets unveiled when one-parameter scaling is demonstrated.

The actual effects of electron-electron interaction in bilayer graphene are generally beyond the scope of this paper. Nevertheless, it is worth pointing out that possible effects primarily include the gap opening due to spontaneous breaking of the symmetry between the layers [29,30]. We show, by numerically analysing the transport through a *biased* bilayer, that opening a few meV gap V (*i.e.*, larger than the Lifshitz energy) leads to the appearance of conductivity peaks at Fermi energies $E \simeq \pm V/2$, where $\sigma \simeq 1/\pi$, reproducing the dimensionless conductivity of a ballistic monolayer. These are the reasons for which an extensive experimental study of size-dependent conductance for clean bilayer samples (with their lengths $L > 1\,\mu$m and widths $W \gg L$), which is missing so far, seems crucial to determine the significance of the factors such as the trigonal warping and the electron-electron interaction in the effective description of bilayer-based graphene nanodevices[1].

* * *

The work was supported by the National Science Centre of Poland (NCN) via Grant No. N-N202-031440, and partly by Foundation for Polish Science (FNP) under the program TEAM "*Correlations and coherence in quantum materials and structures (CCQM)*". Computations were partly performed using the PL-Grid infrastructure.

REFERENCES

[1] Novoselov K. S., Geim A. K., Morozov S. V. *et al.*, *Nature*, **438** (2005) 197; Zhang Y., Tan Y.-W., Stormer H. L. and Kim P., *Nature*, **438** (2005) 201.
[2] Katsnelson M. I., *Eur. Phys. J. B*, **51** (2006) 157.
[3] Tworzydło J., Trauzettel B., Titov M., Rycerz A. and Beenakker C. W. J., *Phys. Rev. Lett.*, **96** (2006) 246802.
[4] Miao F., Wijeratne S., Zhang Y., Coscun U. C., Bao W. and Lau C. N., *Science*, **317** (2007) 1530.
[5] Danneau R., Wu F., Craciun M. F., Russo S. *et al.*, *Phys. Rev. Lett.*, **100** (2008) 196802.
[6] The rectangular sample geometry is assumed for simplicity. For a generalization, see: Rycerz A., Recher P. and Wimmer M., *Phys. Rev. B*, **80** (2009) 125417.
[7] Nair R. R., Blake P., Grigorenko A. N. *et al.*, *Science*, **320** (1308) 2008; Stauber T., Peres N. M. R. and Geim A. K., *Phys. Rev. B*, **78** (2008) 085432.
[8] McCann E. and Koshino M., *Rep. Prog. Phys.*, **76** (2013) 056503.
[9] Snyman I. and Beenakker C. W. J., *Phys. Rev. B*, **75** (2007) 045322.
[10] Cserti J., Csordás A. and Dávid G., *Phys. Rev. Lett.*, **99** (2007) 066802; Koshino M. and Ando T., *Phys. Rev. B*, **73** (2006) 245403.
[11] Minimal conductivity $\sigma_\star = 3\sigma_0$ appears for a generic crystallographic orientation of a sample. In a particular case, when the current passes precisely along a zigzag direction, the lower value of $(7/3)\,\sigma_0$ is predicted; see: Moghaddam A. G. and Zareyan M., *Phys. Rev. B*, **79** (2009) 073401.
[12] Feldman B., Martin J. and Yacoby A., *Nat. Phys.*, **5** (2009) 889.
[13] Mayorov A. S., Elias D. C., Mucha-Kruczyński M. *et al.*, *Science*, **333** (2011) 860.
[14] Rut G. and Rycerz A., *Phys. Rev. B*, **89** (2014) 045421.
[15] Remarkably, some numerical studies of *disordered* monolayer samples report the longitudinal conductivity close to σ_0, appearing at each Landau level for wide ranges of disorder and magnetic fields, see: Ortmann F. and Roche S., *Phys. Rev. Lett.*, **110** (2013) 086602.
[16] Efetov K., *Supersymmetry in Disorder and Chaos* (Cambridge University, Cambridge) 1997.
[17] Bardarson J. H., Tworzydło J., Brouwer P. W. and Beenakker C. W. J., *Phys. Rev. Lett.*, **99** (2007) 106801; Nomura K., Koshino M. and Ryu S., *Phys. Rev. Lett.*, **99** (2007) 146806.
[18] Evers F. and Mirlin A. D., *Rev. Mod. Phys.*, **80** (2008) 1355.
[19] Ostrovsky P. M., Gornyi I. V. and Mirlin A. D., *Phys. Rev. Lett.*, **105** (2010) 036803.
[20] Tight-binding parameters are taken from: Kuzmenko A. B., Crassee I., van der Marel D., Blake P. and Novoselov K. S., *Phys. Rev. B*, **80** (2009) 165406.
[21] Bardarson J. H., *J. Phys. A: Math. Theor.*, **41** (2008) 405203.
[22] Landauer R., *Philos. Mag.*, **21** (1970) 863; Büttiker M., *Phys. Rev. B*, **46** (1992) 12485.
[23] Altshuler B. L. and Aronov A. G., in *Electron-Electron Interactions in Disordered Conductors*, edited by Efros A. L. and Pollak M. (Elsevier, New York) 1985, p. 1.
[24] McCann E., *Phys. Rev. B*, **74** (2006) 161403(R).
[25] Ohta T., Bostwick A., Seyller T., Horn K. and Rotenberg E., *Science*, **313** (2006) 951.
[26] Oostinga J. B., Heersche H. B., Liu X., Morpurgo A. F. and Vandersypen L. M. K., *Nat. Mater.*, **7** (2007) 151.
[27] Castro E. V., Novoselov K. S., Morozov S. V., Peres N. M. R., Lopes Dos Santos J. M. B., Nilsson J., Guinea F., Geim A. K. and Castro Neto A. H., *Phys. Rev. Lett.*, **99** (2007) 216802.
[28] Zhang Y., Tang T.-T., Girit C., Hao Z., Martin M. C., Zettl A., Crommie M. F., Shen Y. R. and Wang F., *Nature*, **459** (2009) 820.
[29] Rutter G. M., Jung S., Klimov N. N., Newell D. B., Zhitenev N. B. and Stroscio J. A., *Nat. Phys.*, **7** (2011) 649.
[30] Bao W., Velasco J. jr., Zhang F., Jing L., Standley B., Smirnov D., Bockrath M., MacDonald A. H. and Lau C. N., *Proc. Natl. Acad. Sci. U.S.A.*, **109** (2012) 10802.
[31] Varlet A., Bischoff D., Simonet P., Watanabe K., Taniguchi T., Ihn T., Ensslin K., Mucha-Kruczynski M. and Fal'ko V. I., arXiv:1403.3244 (unpublished).
[32] Beenakker C. W. J., *Rev. Mod. Phys.*, **80** (2008) 1337.

[1] We further note that the result of ref. [14], reporting the conductivity quite close to $\sigma_\star$, suggests that the influence of electron-electron interactions on charge transport in large ballistic bilayer samples may be negligible.

IOP Publishing Journal of Physics: Condensed Matter
J. Phys.: Condens. Matter **26** (2014) 485301 (12pp) doi:10.1088/0953-8984/26/48/485301

Magnetoconductance of the Corbino disk in graphene: chiral tunneling and quantum interference in the bilayer case

Grzegorz Rut and Adam Rycerz

Marian Smoluchowski Institute of Physics, Jagiellonian University, Reymonta 4, PL-30059 Kraków, Poland

E-mail: Grzegorz.Rut@uj.edu.pl and adam.rycerz@uj.edu.pl

Received 27 July 2014, revised 6 October 2014
Accepted for publication 8 October 2014
Published 4 November 2014

Abstract

Quantum transport through an impurity-free Corbino disk in bilayer graphene is investigated analytically, using the mode-matching method to give an effective Dirac equation, in the presence of uniform magnetic fields. Similarly as in the monolayer case (see Rycerz 2010 *Phys. Rev.* B **81** 121404; Katsnelson 2010 *Europhys. Lett.* **89** 17001), conductance at the Dirac point shows oscillations with the flux piercing the disk area Φ_D characterized by the period $\Phi_0 = 2\,(h/e)\ln(R_o/R_i)$, where R_o (R_i) is the outer (inner) disk radius. The oscillation magnitude depends either on the radii ratio or on the physical disk size, with the condition for maximal oscillations being $R_o/R_i \simeq [\,R_i t_\perp/(2\hbar v_F)\,]^{4/p}$ (for $R_o/R_i \gg 1$), where $t_\perp$ is the interlayer hopping integral, v_F is the Fermi velocity in graphene, and p is an *even* integer. *Odd*-integer values of p correspond to vanishing oscillations for the normal Corbino setup, or to oscillation frequency doubling for the Andreev–Corbino setup. At higher Landau levels, magnetoconductance behaves almost identically in the monolayer and bilayer cases. A brief comparison with the Corbino disk in a two-dimensional electron gas is also provided in order to illustrate the role of chiral tunneling in graphene.

Keywords: graphene, graphene bilayer, magnetoconductance, Corbino geometry, quantum transport

(Some figures may appear in colour only in the online journal)

1. Introduction

The potential of bilayer graphene (BLG) for carbon-based electronics rests on the possibility for controlling its transport properties using external electromagnetic fields employing the mechanisms that have no analogs in monolayer graphene (MLG) or in semiconducting heterostructures containing two-dimensional electron gas (2DEG) (for a recent review of the topic, see [3]). BLG with an AB stacking order can be converted from a semimetal to a narrow gap semiconductor by applying a perpendicular electrostatic field [4–8]. This is possible, because: (i) the interlayer hoppings break the sublattice symmetry in a single layer, leading to the formation of two parabolic chiral bands touching themselves at the so-called Dirac points [4][1], and (ii) the perpendicular electric field further breaks the inversion symmetry, opening a gap between conduction and valence bands. Several experiments on dual-gated devices in ultraclean BLG have pursued the possibility of exploiting such a field-tunable energy gap [9–15]. Yan and Fuhrer [11] used the Corbino geometry, proposed over a century ago, to measure the magnetoresistance without generating the Hall voltage (for a historical introduction, see [16]). In such a geometry (see figure 1), the current is passed through a disk-shaped sample surrounded on both its exterior and interior sides with metallic leads, which suppress the influence of boundary modes [17] on various dynamical properties of nanosystems in both BLG and MLG [18–21].

[1] Skew-interlayer hoppings may lead to the appearance of secondary Dirac points affecting the transport properties of unbiased samples, but a gap still opens when applying the electrostatic field; see [3].

From a more fundamental point of view, several relativistic quantum effects, observed for MLG and resulting from the chiral nature of effective quasiparticles, are predicted to manifest themselves in BLG in slightly modified versions, mainly due to the presence of a new characteristic length scale for low-energy excitations [22]

$$l_\perp = \hbar v_\mathrm{F}/t_\perp \simeq 11\, d_0, \tag{1}$$

where $v_\mathrm{F} \simeq 10^6\,\mathrm{m\,s^{-1}}$ is the energy-independent Fermi velocity in MLG, $t_\perp \simeq 0.4\,\mathrm{eV}$ is the nearest-neighbor interlayer hopping integral, and $d_0 = 0.142\,\mathrm{nm}$ is a C–C bond length. For instance, the universal ballistic conductivity of MLG $\sigma_0 = (4/\pi)\,e^2/h$, characterizing the so-called *pseudodiffusive* transport regime [23–27], is replaced by the length-dependent value $\sigma(L)$, which varies from σ_0 to $3\sigma_0$ per layer [28–30], with the upper limit approached for the system size $L \to \infty$. In the quantum-Hall regime, the zero-energy Landau level (LL) shows the eightfold degeneracy for BLG (instead of the fourfold degeneracy for MLG), which can be lifted by manipulating the external electromagnetic fields, partly due to electron–electron interactions [10, 13, 20]. Also, the quantum interference in graphene Aharonov–Bohm rings (for a review, see [31]) may result in different oscillation patterns appearing for MLG and BLG [32–34].

An intriguing quantum-interference phenomenon was predicted theoretically for impurity-free Corbino disks in MLG [1, 2, 35–38]. In brief, periodic (approximately sinusoidal) magnetoconductance oscillations are followed, for an *undoped* sample, by similar oscillations of the shot-noise power [2] and the third charge-transfer cumulant [35, 38]. The effect has a direct analog for strain-induced pseudomagnetic fields [36], allowing consideration of a fully mesoscopic counterpart to the earlier proposed valley filters in MLG [39–41] or carbon nanotubes [42]. At higher dopings, the oscillations reappear provided the magnetic field is adjusted to the positions of the n-th LLs in the field-doping parameter plane [1]. Also very recently, LL splittings due to a possible substrate-induced spin–orbit interaction in Corbino devices were discussed as an alternative mechanism [43] for graphene-based spintronics [44].

Most remarkably, the disk conductance averaged over a single period restores the pseudodiffusive value [27]

$$G^{\mathrm{MLG}}_{\mathrm{diff}} = \frac{2\pi\sigma_0}{\ln(R_\mathrm{o}/R_\mathrm{i})}. \tag{2}$$

Analogous behavior is predicted for higher charge-transfer cumulants[2], showing that the effect is another manifestation of the chiral nature of Dirac fermions in graphene. For these reasons, we have coined the term of *quantum-relativistic Corbino effect* (QRCE).

In this paper, magnetoconductance of the Corbino disk in BLG is discussed in analytical terms, starting from the four-band effective Hamiltonian [4] and employing the Landauer–Büttiker formalism [45] for the linear-response regime. The paper is organized as follows. In section 2 we present the system details and discuss the solutions of the corresponding Dirac equation for arbitrary dopings and magnetic fields. Then, in section 3, magnetotransport signatures of QRCE are demonstrated for the normal Corbino and for the Andreev–Corbino setups. Section 4 provides a quantitative comparison with the magnetoconductance spectra for the Corbino disk in 2DEG. The conclusions are given in section 5.

[2] In the linear-response regime, the average Fano factor quantifying the shot-noise power $\overline{\mathcal{F}} = \mathcal{F}_{\mathrm{diff}} = 1/3$, and the average $\mathcal{R}$-factor quantifying the third charge-transfer cumulant $\overline{\mathcal{R}} = \mathcal{R}_{\mathrm{diff}} = 1/15$. For a discussion of a finite-voltage situation, see [38].

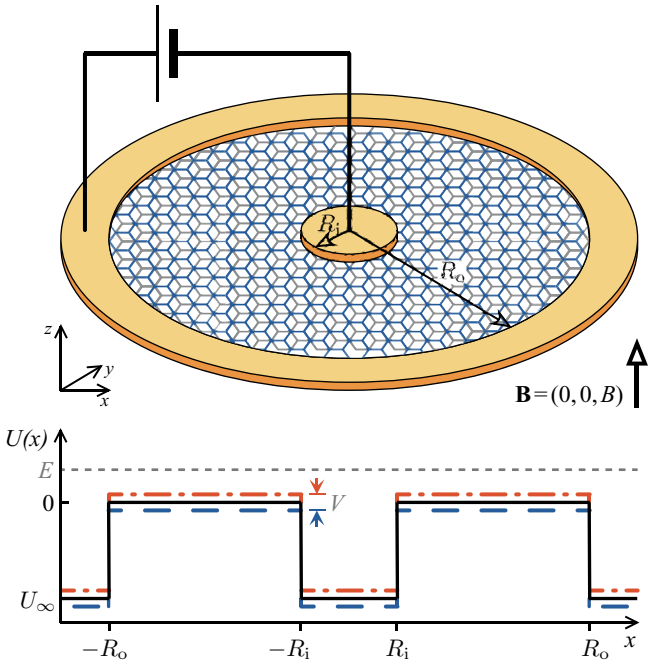

Figure 1. The Corbino disk in AB stacked bilayer graphene. Top: device schematics. The current is passed through the disk-shaped area with inner radius R_i and outer radius R_o in a perpendicular magnetic field $\mathbf{B} = (0, 0, B)$. Bottom: the electrostatic potential cross section along the x-axis $U(x)$ following from equation (4) (black solid line). The leads (yellow areas) are modeled as infinitely doped graphene regions ($|U_\infty| \to \infty$). The additional top- and bottom-gate electrodes (not shown) are used to tune the Fermi energy (E) (grey dotted line) and to induce the electrostatic bias between the layers (V), leading to the local potential energies $U(x) + V/2$ (red dash–dot line) and $U(x) - V/2$ (blue dashed line).

2. Mode-matching for the effective Dirac equation

2.1. The Hamiltonian and envelope wavefunctions

The analysis starts from the four-band effective Hamiltonian for K valley [4], which is given by

$$H = \begin{pmatrix} V/2 & \pi & t_\perp & 0 \\ \pi^\dagger & V/2 & 0 & 0 \\ t_\perp & 0 & -V/2 & \pi^\dagger \\ 0 & 0 & \pi & -V/2 \end{pmatrix} + U(r)\,\mathbb{I}, \tag{3}$$

where V is the electrostatic bias between the layers, $\pi = \pi_x + \mathrm{i}\pi_y$ and $\pi^\dagger = \pi_x - \mathrm{i}\pi_y$, with $\pi_j/v_\mathrm{F} = (-\mathrm{i}\hbar\,\partial_j + eA_j)$ being a component of the gauge-invariant momentum operator ($j = 1, 2$). The electron charge is $-e$, the potential energy term $U(r)\,\mathbb{I}$ depends only on $r = \sqrt{x^2 + y^2}$ (with $\mathbb{I}$ the identity matrix), and the remaining symbols are the same

as in equation (1). We choose the symmetric gauge $\mathbf{A} \equiv (A_x, A_y) = (B/2)(-y, x)$, with the uniform magnetic field $B \neq 0$ in the disk area ($R_\mathrm{i} < r < R_\mathrm{o}$) and $B = 0$ otherwise. The inner and outer contacts are modeled with heavily doped BLG areas; that is, we set the potential energy profile in equation (3) as follows

$$U(r) = \begin{cases} U_\infty & \text{if } r < R_\mathrm{i} \text{ or } r > R_\mathrm{o}, \\ 0 & \text{if } R_\mathrm{i} < r < R_\mathrm{o}, \end{cases} \tag{4}$$

and focus on the limit of $|U_\infty| \to \infty$. In order to obtain the Hamiltonian for the other valley (K'), it is sufficient to substitute $V \to -V$ and $\pi \to -\pi$ in equation (3).

Since our model system possesses a cylindrical symmetry, the Hamiltonian (3) commutes with the total angular-momentum operator [46]

$$J_z = -\mathrm{i}\hbar\partial_\varphi + \frac{\hbar}{2}\begin{pmatrix}\sigma_0 & 0\\ 0 & -\sigma_0\end{pmatrix} + \frac{\hbar}{2}\begin{pmatrix}-\sigma_z & 0\\ 0 & \sigma_z\end{pmatrix}, \tag{5}$$

where σ_0 is the 2×2 identity matrix, σ_z is one of the Pauli matrices, and we have used the polar coordinates (r, φ). In turn, the wavefunctions can be written as products of angular and radial parts (the so-called *envelope wavefunctions*), namely

$$\psi(r, \varphi) = \mathrm{e}^{\mathrm{i}m\varphi}\begin{pmatrix}\phi_1(r)\\ \mathrm{i}\mathrm{e}^{-\mathrm{i}\varphi}\phi_2(r)\\ \phi_3(r)\\ \mathrm{i}\mathrm{e}^{\mathrm{i}\varphi}\phi_4(r)\end{pmatrix} \tag{6}$$

where $m = 0, \pm1, \pm2, \ldots$. Notice that the angular momentum quantum number in the BLG case is an integer m, in contrast to the half-odd integer the j in MLG case [47].

2.2. The contact regions

For the contact regions ($r < R_\mathrm{i}$ or $r > R_\mathrm{o}$), we have $B = 0$ and thus the four-band Dirac equation $H\psi = E\psi$, with H given by equation (3) and E being the Fermi energy, can be written as

$$\begin{pmatrix}\tilde{\epsilon}+\Delta & \kappa_+ & -l_\perp^{-1} & 0\\ \kappa_- & \tilde{\epsilon}+\Delta & 0 & 0\\ -l_\perp^{-1} & 0 & \tilde{\epsilon}-\Delta & \kappa_-\\ 0 & 0 & \kappa_+ & \tilde{\epsilon}-\Delta\end{pmatrix}\psi(r, \phi) = 0 \tag{7}$$

where $\tilde{\epsilon} = (E - U_\infty)/(\hbar v_\mathrm{F})$, $\kappa_\pm = \mathrm{i}\mathrm{e}^{\pm\mathrm{i}\varphi}\left(\partial_r \pm \mathrm{i}r^{-1}\partial_\varphi\right)$ and $\Delta = -V/(2\hbar v_\mathrm{F})$. Substituting $\psi(r, \varphi)$ (6) into equation (7) and decoupling the equation for $\phi_1^\pm(r)$ one gets

$$\left(\partial_r^2 + \frac{1}{r}\partial_r - \frac{m^2}{r^2} + \eta_\pm\right)\phi_1^\pm(r) = 0, \tag{8}$$

where $\eta_\pm = \left(\Delta^2 + \tilde{\epsilon}^2\right) \pm \sqrt{\tilde{\epsilon}^2\left(4\Delta^2 + 1/l_\perp^2\right) - \Delta^2/l_\perp^2}$. Next, using the differential relations following from equation (7), one can obtain the remaining components of the wavefunction $\phi^\pm(r) = \left[\phi_1^\pm(r), \phi_2^\pm(r), \phi_3^\pm(r), \phi_4^\pm(r)\right]^T$, which are given explicitly in appendix A.

2.3. The disk area

For the disk area ($R_\mathrm{i} < r < R_\mathrm{o}$), we have $B \neq 0$ and it is convenient to define the dimensionless variable $\rho = r/l_B$, with the magnetic length $l_B = \sqrt{\hbar/|eB|}$. In turn, equation (7) is replaced by

$$\begin{pmatrix}\varepsilon+\delta & \xi_+ & -t & 0\\ \xi_- & \varepsilon+\delta & 0 & 0\\ -t & 0 & \varepsilon-\delta & \xi_-\\ 0 & 0 & \xi_+ & \varepsilon-\delta\end{pmatrix}\psi(\rho, \phi) = 0, \tag{9}$$

where $t = l_B/l_\perp$, $\varepsilon = El_B/(\hbar v_\mathrm{F})$, $\delta = -Vl_B/(2\hbar v_\mathrm{F})$ and $\xi_\pm = \mathrm{i}\exp(\pm\mathrm{i}\varphi)\left(\partial_\rho \pm \mathrm{i}\rho^{-1}\partial_\varphi \mp \rho/2\right)$. Eliminating the angle-dependent part of the wavefunction, we obtain

$$\left(\partial_\rho^2 + \frac{1}{\rho}\partial_\rho - \frac{\rho^2}{4} - \frac{m^2}{\rho^2} - m - 1 + \gamma_\pm\right)\phi_1^\pm(\rho) = 0, \tag{10}$$

where $\gamma_\pm = \left(\delta^2 + \varepsilon^2\right) \pm \sqrt{\varepsilon^2\left(4\delta^2 + t^2\right) - \delta^2 t^2}$. The complete solution of equation (9) is presented in appendix A. It can be shown that the normalization condition for the wavefunction leads to the energies of LLs [8]

$$\gamma_\pm = n + \frac{|m| + m + 1}{2}, \tag{11}$$

where $n = 0, 1, 2, \ldots$.

2.4. Reflection and transmission coefficients

Next, we consider the scattering problem for the radial wave functions, assuming that the initial wave is incoming from the inner lead. The solutions of equation (7) for the inner and outer leads can be presented as follows

$$\phi_\mathrm{i}^\pm(r) = \phi_\mathrm{in}^\pm(r) + r_p^\pm\phi_\mathrm{out}^+(r) + r_n^\pm\phi_\mathrm{out}^-(r), \tag{12}$$

$$\phi_\mathrm{o}^\pm(r) = t_p^\pm\phi_\mathrm{in}^+(r) + t_n^\pm\phi_\mathrm{in}^-(r), \tag{13}$$

where $\phi_\mathrm{in}^\pm(r)$ and $\phi_\mathrm{out}^\pm(r)$ denote the wavefunctions propagating from $r = 0$ and $r = \infty$ (respectively) and carrying the unit current. In analogy, a general solution of equation (9) for the disk area corresponds to the linear combination of four eigenspinors, namely

$$\phi_\mathrm{d}^\pm(r) = \sum_{\mu=1}^{4}\alpha_\mu^\pm\phi_\mu(r), \tag{14}$$

where $\{\alpha_\mu^\pm\}_{\mu=1,\ldots,4}$ are arbitrary complex coefficients. Matching the wavefunctions $\phi_\mathrm{i}^\pm(r)$ (12) and $\phi_\mathrm{d}^\pm(r)$ (14) at $r = R_\mathrm{i}$, as well as $\phi_\mathrm{d}^\pm(r)$ (14) and $\phi_\mathrm{o}^\pm(r)$ (13) at $r = R_\mathrm{o}$, we obtain the reflection and transmission coefficients corresponding to the K valley and the angular momentum quantum number m, which can be arranged in 2×2 matrices, namely

$$\mathbf{r}_{K,m} = \begin{pmatrix}r_p^+ & r_n^+\\ r_p^- & r_n^-\end{pmatrix}, \quad \mathbf{t}_{K,m} = \begin{pmatrix}t_p^+ & t_n^+\\ t_p^- & t_n^-\end{pmatrix}. \tag{15}$$

The remaining details of the mode-matching procedure are given in appendix B.

It is worth mentioning here that skew-interlayer hoppings [3], neglected in the Hamiltonian H (3), are predicted theoretically to enhance, typically by a factor of 3, the zero-magnetic field conductivity of large bilayer samples at the Dirac point [3, 28, 48]. The experimental values reported by [12] are close, but noticeably smaller than the theoretical prediction, which can be attributed to several factors, including the finite system size [30]. Nevertheless, it is also shown in [30] that the conductance of finite bilayer samples (with length $L \lesssim 100$ nm) becomes insensitive to skew-interlayer hoppings at high magnetic fields $B \gtrsim 5$ T, and thus the scattering approach constituted by the four-band Hamiltonian (3) is sufficient to discuss basic magnetotransport characteristics of nanoscale devices in BLG.

3. Quantum relativistic Corbino effect in BLG

In this section, we present our main results concerning the magnetoconductance of the Corbino disk in BLG. In the linear-response regime, the conductance is given by the Landauer–Büttiker formula [49]

$$G = 2_s 2_v g_0 \mathrm{Tr}\, \boldsymbol{T}, \tag{16}$$

where $g_0 = e^2/h$ is the conductance quantum, $2_{s(v)}$ is the spin (valley) degeneracy, $\boldsymbol{T} = \boldsymbol{t}^\dagger \boldsymbol{t}$ and $\boldsymbol{t}$ is a block-diagonal matrix with each block given by the second equality in equation (15). The Zeeman splitting is neglected for clarity. As the first step, we have also assumed the unbiased sample case ($V = 0$), for which the twofold valley degeneracy occurs. The $V \neq 0$ case is discussed separately later in this section.

3.1. Magnetoconductance at the Dirac point

For $E = V = 0$ and $|U_\infty| \to \infty$, transmission eigenvalues can be found analytically, and read

$$T_m^{\pm} = \frac{1}{\cosh^2\left[\mathcal{L}(m \pm \mathcal{A} + \Phi_D/\Phi_0)\right]}, \tag{17}$$

where $\Phi_D = \pi\left(R_\mathrm{o}^2 - R_\mathrm{i}^2\right) B$ is the flux piercing the disk area, $\mathcal{L} = \ln\left(R_\mathrm{o}/R_\mathrm{i}\right)$ and $\Phi_0 = 2\,(h/e)\,\mathcal{L}$. The parameter

$$\mathcal{A} = -\frac{\ln\left(\Upsilon - \sqrt{\Upsilon^2 - 1}\right)}{2\mathcal{L}}, \tag{18}$$

with $\Upsilon = \cosh(\mathcal{L}) + \Lambda \sinh(\mathcal{L})$ and $\Lambda = (R_\mathrm{o}^2 - R_\mathrm{i}^2)/(4l_\perp^2)$, takes values from the range $1/2 < \mathcal{A} < \infty$. Summing over the normal modes labeled by integer m, one immediately finds that G (16) shows periodic oscillations as a function of Φ_D, with a period equal to Φ_0 (see figure 2), closely resembling the magnetoconductance behavior predicted for the Corbino disk in MLG [1, 2]. However, for any fixed Φ_D, equation (17) describes the two transmission maxima separated by a distance of $2\mathcal{A}\hbar$ in the angular-momentum space. In turn, the corresponding contributions to the magnetoconductance may interfere constructively or destructively with each other.

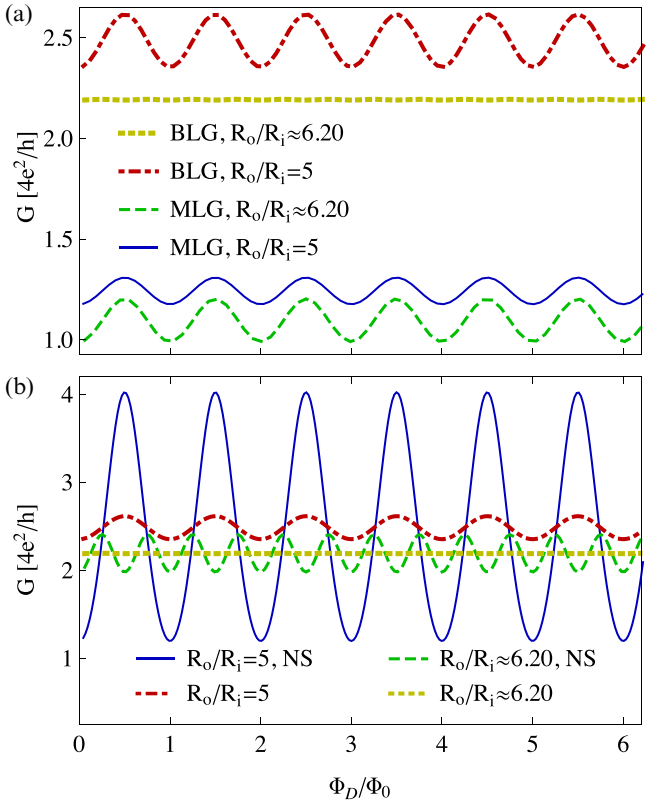

Figure 2. Conductance of different graphene-based Corbino devices with inner radius $R_\mathrm{i} = 50\,l_\perp \simeq 80$ nm as a function of the magnetic field. (*a*) Magnetoconductance oscillations in mono- and bilayer disks at the Dirac point for the two values of the radii ratio, for which the oscillation magnitude is close to the maximal ($R_\mathrm{o}/R_\mathrm{i} = 5$) and to the minimal values ($R_\mathrm{o}/R_\mathrm{i} = 6.2$) in the bilayer case. (*b*) Magnetoconductance of bilayer disks in normal Corbino and Andreev–Corbino (NS) setups. Notice the oscillation frequency doubling for the Andreev–Corbino setup and $R_\mathrm{o}/R_\mathrm{i} = 6.2$.

The nature of the interference depends both on the sample size and on the interlayer hopping integral $t_\perp$[3].

For a clear overview of the effect, we represent G following from equations (16) and (17) by a Fourier series

$$G = \frac{16 g_0}{\mathcal{L}} + \sum_{q=1}^{\infty} G_q \cos\left(\frac{2\pi q\, \Phi_D}{\Phi_0}\right), \tag{19}$$

where

$$G_q = \frac{32\pi^2 q\, g_0 \cos\left(2\pi q \mathcal{A}\right)}{\mathcal{L}^2 \sinh\left(\pi^2 q/\mathcal{L}\right)} \equiv 2(-)^q G_q^{\mathrm{MLG}} \cos\left(2\pi q \mathcal{A}\right), \quad q = 1, 2, 3, \ldots. \tag{20}$$

The constant term in equation (19), $16 g_0/\mathcal{L} \equiv 2G_\mathrm{diff}^{\mathrm{MLG}}$ (see equation (2)), gives the average conductance, which is simply twice as large as in the monolayer case [1, 2]. Such a sum rule does not generically apply to the Fourier amplitudes G_q, which are related to the corresponding amplitudes for MLG (G_q^{MLG}) via the second equality in equation (20). A special case of $G_q = 2G_q^{\mathrm{MLG}}$ occurs for $\mathcal{A} = 1/2$. For sufficiently large

[3] In the limit $t_\perp \to 0$, corresponding to the separation of two layers, we have $l_\perp \to \infty$ and $\mathcal{A} \to 1/2$, leading to the same conductance per layer as in the monolayer case.

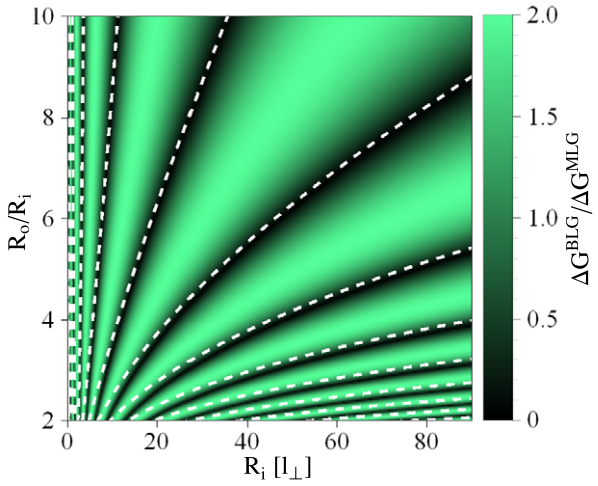

Figure 3. Oscillation magnitudes ratio for bilayer and monolayer disks, $\Delta G^{\mathrm{BLG}}/\Delta G^{\mathrm{MLG}}$ (where $\Delta G \equiv G_{\max} - G_{\min}$). Dashed lines mark the parameter values obtained from the approximating equation (21) for $p = 1, 3, 5, \ldots$.

systems, we have $|G_1| \gg |G_2| \gg \ldots$, and it is possible to find approximate conditions for maximal and minimal oscillation magnitudes $\Delta G \equiv G_{\max} - G_{\min} \simeq 2|G_1|$, namely

$$p\mathcal{L} \simeq 4 \ln\left(\frac{R_i}{2l_\perp}\right), \tag{21}$$

where p are even (odd) integers for maximal (minimal) oscillation magnitudes. As illustrated in figure 3, the parameter values following from equation (21) for odd p (white dashed lines) coincide with the actual regions where the oscillation magnitude vanishes (black areas), provided that $R_o/R_i \gtrsim 3$ and $R_i/l_\perp \gtrsim 10$.

For the sake of completeness, we discuss now the magnetoconductance in the Andreev–Corbino setup, in which the disk-shaped sample is attached to one normal and one superconducting lead. In such a situation, the conductance is given by [50]

$$G^{\mathrm{NS}} = 2_s 2_v g_0 \mathrm{Tr}\left[2\boldsymbol{T}^2(2-\boldsymbol{T})^{-2}\right]. \tag{22}$$

For a BLG disk at the Dirac point, this leads to

$$G^{\mathrm{NS}} = 8g_0 \sum_{m=-\infty}^{\infty} \left\{ \frac{1}{\cosh^2\left[2\mathcal{L}(\overline{m}+\mathcal{A})\right]} + \frac{1}{\cosh^2\left[2\mathcal{L}(\overline{m}-\mathcal{A})\right]} \right\}, \tag{23}$$

where we have defined $\overline{m} = m + \Phi_D/\Phi_0$. G^{NS} (23) can be represented by a Fourier series of the form given by equation (19) with the same average conductance ($2G^{\mathrm{MLG}}_{\mathrm{diff}}$), and the amplitudes G_q (20) replaced by

$$G_q^{\mathrm{NS}} = \frac{16\pi^2 q\, g_0 \cos(2\pi q\mathcal{A})}{\mathcal{L}^2 \sinh\left[\pi^2 q/(2\mathcal{L})\right]}. \tag{24}$$

Strictly speaking, the scaling rule earlier found for the disk in MLG, namely $G_q^{\mathrm{MLG,NS}}(\mathcal{L}) = 2G_q^{\mathrm{MLG}}(2\mathcal{L})$ [1], does not apply in the bilayer case due to the interlayer coupling manifesting itself via the $\mathcal{A}$-dependent factor in equation (24). However, we still have $G_q^{\mathrm{NS}}/G_q \to 1$ for $R_o/R_i \to \infty$ (and arbitrary q). Also, magnetoconductance oscillations for bilayer disks with moderate radii ratios are noticeably amplified in the Andreev–Corbino setup in comparison to the normal Corbino setup (see figures 2(*a*) and (*b*)).

The approximate conditions for maximal and minimal oscillations, given by equation (21), are essentially valid for both the normal Corbino and the Andreev–Corbino setups. The relation $|G_1^{\mathrm{NS}}| \gg |G_2^{\mathrm{NS}}| \gg |G_3^{\mathrm{NS}}| \gg \ldots$ is satisfied, for moderate radii ratios, near the oscillation maxima (even p in equation (21)), whereas close to the minima one typically gets $G_1^{\mathrm{NS}} \simeq 0$ and $|G_2^{\mathrm{NS}}| \gg |G_3^{\mathrm{NS}}| \gg \ldots$, leading to the visible oscillation frequency doubling (see figure 2(*b*)). In the normal Corbino setup, with the radii fixed at $R_i = 50\, l_\perp$ and $R_o = 6.2\, R_i$, the magnetoconductance is almost constant (yellow dotted line). On the other hand, if one of the leads is superconducting, the frequency of conductance oscillations is doubled in comparison to Φ_0^{-1} (green dashed line).

3.2. Finite-doping effects

We now extend our analysis to situations where the Fermi energy is close but not precisely adjusted to the Dirac point, keeping the zero bias between the layers ($E \neq 0$ and $V = 0$). (Hereinafter, the normal Corbino setup is considered.) The corresponding magnetoconductance spectra are presented in figure 4. In the monolayer case, the disk conductance at weak dopings follows the zero-doping curve for first few oscillation periods, and then starts to decrease rapidly with increasing field [1] (see blue dashed lines in all panels of figure 4). For BLG (see red solid lines) we have a relatively wide crossover field interval, separating the oscillating and the field-suppressed conductance ranges. Typically, the conductance in the crossover interval does not decay monotonically with the field. Instead, a well-defined magnetoconductance peak appears, with $G \simeq G^{\mathrm{MLG}}_{\mathrm{diff}}$ near the maximum. Below, we link these features to the presence—in the vicinity of the Dirac point—of the two independent transmission channels for any angular momentum quantum number m, characterized by the transmission probabilities, which are numerically close to $T_m^{\pm}$ (17).

The contribution to the disk conductance originating from evanescent waves, for either MLG or BLG close to the Dirac point, can be roughly estimated by

$$\sum_{l,\,\mathrm{eva}} T_l \sim \left(\frac{R_i}{R_o}\right)^{2|l_{\max}|} \quad (\text{for } R_i \ll R_o), \tag{25}$$

where $l_{\max}$ denotes the angular momentum corresponding to the maximal transmission at $E = 0$, namely $l_{\max} = \eta\mathcal{A} - \Phi_D/\Phi_0$, where $\eta = 0$ for MLG or $\eta = \pm 1$ for BLG. The contribution from the propagating waves appearing for $E \neq 0$ is of the order of

$$\sum_{l,\,\mathrm{pro}} T_l \sim (k_0 R_i)^2 \quad (\text{for } k_0 R_i \ll 1), \tag{26}$$

where we have defined the wavevector $k_0 = |E|/(\hbar v_F)$. Quasiperiodic magnetoconductance oscillations can be

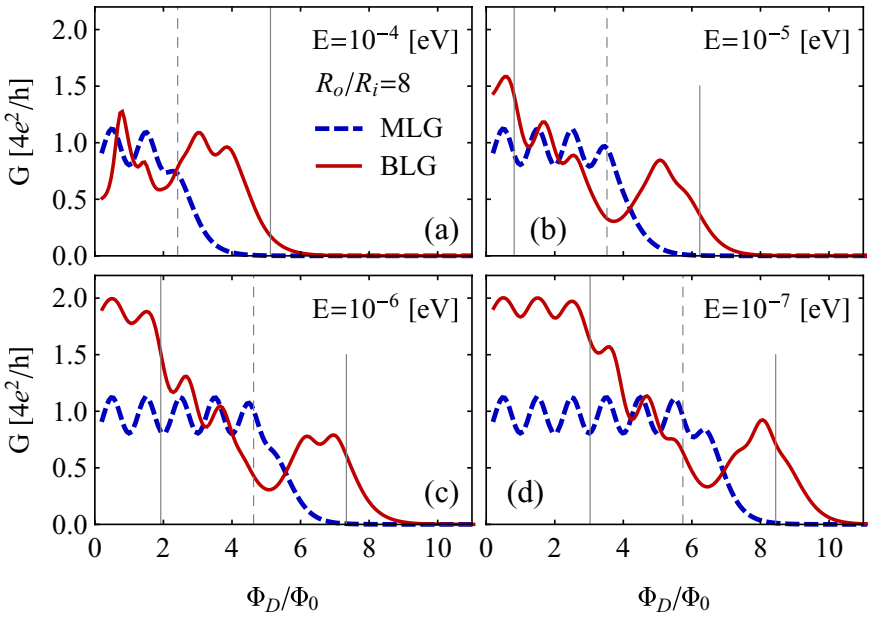

Figure 4. Same as figure 2, but for the Fermi energy $E > 0$ (specified for each panel). The radii ratio is fixed at $R_o/R_i = 8$. Blue dashed and red solid lines correspond to the mono- and bilayer cases (respectively); zero bias ($V = 0$) is supposed for BLG. Vertical lines mark the values of $\Phi_D^{\max,\eta}$ (27) for $\eta = 0$ (grey dashed lines) and $\eta = \pm 1$ (grey solid lines).

observed as long as $\sum_{l,\,\mathrm{eva}} T_l \gtrsim \sum_{l,\,\mathrm{pro}} T_l$, directly leading to the limits for magnetic fluxes

$$|\Phi_D| \lesssim \Phi_D^{\max,\eta} = \frac{2h}{e}\Big[\,\eta\mathcal{A}\mathcal{L} - \ln(k_0 R_i)\,\Big]. \qquad (27)$$

The values of $\Phi_D^{\max,\eta}$, for $\eta = 0, \pm 1$, are also depicted in figure 4 (see vertical lines), showing that the flux range defined as $\Phi_D^{\max,-1} \leqslant \Phi_D \leqslant \Phi_D^{\max,+1}$ coincides with the crossover field interval for a BLG disk with $R_i = 50\,l_\perp$, $R_o/R_i = 8$ and $|E| \leqslant 10^{-6}$ eV. For larger R_o, such a coincidence can also be observed at higher E, provided that $\Phi_D^{\max,-1} \gtrsim 2\Phi_0$.

3.3. The biased sample case ($V \neq 0$)

We focus now on the effect of a nonzero electrostatic bias between the layers in the normal Corbino geometry. The corresponding magnetoconductance spectra for the two selected radii ratios $R_o/R_i = 5$ and $R_o/R_i = 6.2$ (with $R_i = 50\,l_\perp$) are presented in figure 5, where we have fixed the Fermi energy at $E = V/2 = 0.1$ eV. The disk conductance first shows rather irregular behavior with increasing field, varying in the range $0 < G \lesssim G_{\mathrm{diff}}^{\mathrm{MLG}}$ (the corresponding magnetoconductance spectra for $E = V = 0$, and for undoped MLG disks, are also shown in figure 5). For $\Phi_D \gtrsim 10\,\Phi_0$, periodic oscillations are restored, but the average conductance is $4g_0/\mathcal{L} = G_{\mathrm{diff}}^{\mathrm{MLG}}/2$. Also, the oscillation magnitude $\Delta G = \Delta G^{\mathrm{MLG}}$. (Notice that we have selected the disk radii such that ΔG^{BLG} is close to the maximal and to the minimal value in the $E = V = 0$ case, see green dashed lines.) These features can be attributed to the splittings of layer and valley degeneracies of the lowest LL in the presence of a band gap and magnetic field (see [30]).

Also for higher LLs, the disk conductance oscillates periodically with Φ_D, qualitatively reproducing the behavior

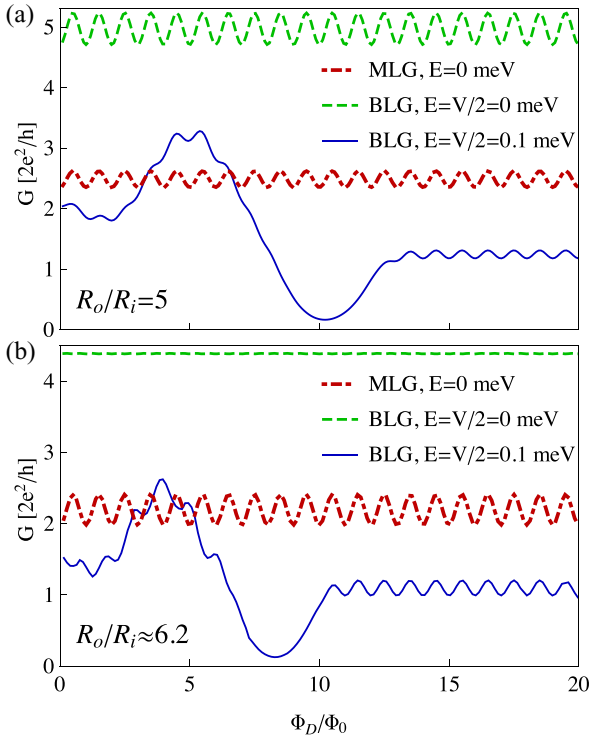

Figure 5. Same as figures 2 and 4, but for the electrostatic bias between the layers $V/2 = E = 0.1$ meV (blue solid lines). Remaining lines show the magnetoconductance spectra for the Corbino disk in unbiased and undoped BLG ($V/2 = E = 0$) (green dashed lines), as well as in undoped MLG (red dash-dot lines). The values of the radii ratios are $R_o/R_i = 5$ (top panel) and $R_o/R_i = 6.2$ (bottom panel).

predicted for the monolayer case in [1]. This is because finite doping eliminated the level degeneracy associated with the two layers, even in the absence of the electrostatic bias ($V = 0$). For $V \neq 0$, the valley degeneracy no longer applies, and

the conductance further drops by a factor of 2. A complete overview of different transport regimes on the field-doping parameter plane is given in section 4, where we compare (in a quantitative manner) the magnetoconductance of the Corbino disks in BLG and in 2DEG.

4. Magnetoconductance of the Corbino disk in 2DEG

For both BLG and 2DEG systems, parabolic bands appear in the low-energy dispersion relation, and the effective masses are in the range $m_\star/m_e = 10^{-2}$ to 10^{-1} (where m_e denotes the free electron mass). Therefore, a detailed comparison of the magnetic field effects described in section 3, with analogous effects for the Corbino disk in 2DEG, is desired to identify the role of chiral tunneling of Dirac fermions in BLG. Below, we extend the mode-matching analysis presented in [27] for the nonzero field situation.

The effective Schrödinger equation for electrons in a 2DEG system reads

$$\left[\frac{1}{2m_\star}\left(\frac{\hbar}{\mathrm{i}}\boldsymbol{\nabla}+e\mathbf{A}\right)^2+U(r)\right]\psi = E\psi, \tag{28}$$

where $\psi(\mathbf{r})$ is the complex-scalar wavefunction, the vector potential $\mathbf{A}$ is same as in equation (3) and the Zeeman term is neglected again. The electrostatic potential energy $U(r)$ is still given by equation (4), but we no longer assume infinite doping in the leads, as the mismatch in Fermi velocities results in zero transmission in such a limit [51–53][4]. Instead, U_∞ can be adjusted such that $\pi R_\mathrm{i}\sqrt{m_\star(E-U_\infty)/\hbar^2} \gtrsim 10$, entering the multimode leads regime, in which the conductance only weakly depends on U_∞.

Since the Hamiltonian in equation (28) commutes with the orbital momentum operator $L_z = -\mathrm{i}\hbar\partial_\phi$, we choose wavefunctions of the form $\psi(r,\phi) = \varphi(r)\exp(\mathrm{i}l\phi)$, with l integer. This bring us to solving the effective one-dimensional scattering problem, with the Schödinger equation

$$\left[-\partial_r^2-\frac{1}{r}\partial_r+\frac{l^2}{r^2}+\frac{r^2}{4l_B^4}\right]\varphi(r) = \zeta_l\varphi(r), \tag{29}$$

where $\zeta_l = 2m_\star[E-U(r)]/\hbar^2 - l/l_B^2$. For the contact regions we have $l_B^{-1}=0$, and the solutions are given by the Hankel functions [54], namely

$$\begin{aligned}\varphi_l^{(\mathrm{i})}(r) &= H_l^{(1)}(Kr)+r_l H_l^{(2)}(Kr),\\ \varphi_l^{(\mathrm{o})}(r) &= t_l H_l^{(1)}(Kr),\end{aligned} \tag{30}$$

where $K = \sqrt{2m_\star(E-U_\infty)/\hbar^2}$, r_l (t_l) is the reflection (transmission) coefficient, and we have assumed scattering from the inner lead.

[4] We further notice that the early theoretical works on the Corbino disks in 2DEG [51, 52] utilized a particular form of the effective radial potential, leading to conductance quantization. The quantization steps are smeared out when employing the direct mode-matching technique (see [27]), leading to yet another surprise when discussing the applicability of the adiabatic expansion to scattering problems in physics [53].

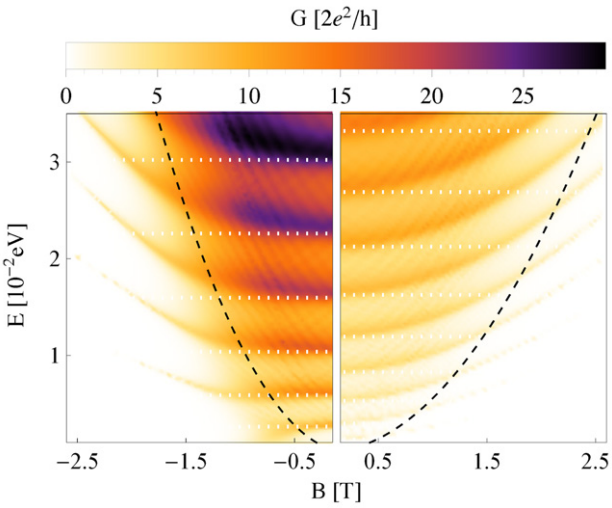

Figure 6. Conductance as a function of doping and magnetic field for the Corbino disks in unbiased BLG (left) and in 2DEG (right). The radii are fixed at $R_\mathrm{i} = 25\,l_\perp \simeq 40$ nm and $R_\mathrm{o} = 4R_\mathrm{i}$ for both cases. Black dashed lines mark the condition for cyclotronic diameters $2r_\mathrm{C} = R_\mathrm{o} - R_\mathrm{i}$. White dotted lines depict the energy levels given by equation (33).

For the disk area, we get

$$\begin{aligned}\varphi_l^{(\mathrm{d})}(r) &= (C_l/r)\,\mathrm{W}_{\Omega_l,\,l/2}\left(-\tfrac{1}{2}r^2/l_B^2\right)\\ &\quad+(D_l/r)\,\mathrm{W}_{-\Omega_l,\,l/2}\left(\tfrac{1}{2}r^2/l_B^2\right),\end{aligned} \tag{31}$$

where $\Omega_l = \left(l-k^2l_B^2\right)/2$ with $k=\sqrt{2m_\star E/\hbar^2}$, $W_{\kappa,\mu}(x)$ is the Whittaker function [55], and C_l, D_l are arbitrary constants. In particular, imposing the normalization of $\varphi_l^{(\mathrm{d})}$, one can obtain the well-known energy quantization

$$E_n = \hbar\omega_c\,(n+1/2), \tag{32}$$

with $\omega_c = eB/\hbar$ and $n = 0, 1, 2, \ldots$. For the open system studied here, the normalization condition for wavefunctions does not apply, but the LL energies E_n (32) coincide with the transmission maxima of $T_l = |t_l|^2$.

Carrying out the mode-matching procedure for each value of l separately (see appendix C for the details), we get the Landauer–Büttiker conductance $G = 2_s g_0 \sum_l T_l$ for arbitrary dopings and magnetic fields. For the numerical analysis, we set the effective mass to be the same as in GaAs systems $m_\star = 0.067m_e$, the inner radius is $R_\mathrm{i} = 25\,l_\perp \simeq 40$ nm and the doping on the leads is such that $E - U_\infty = 0.4$ eV.

The results are displayed in figures 6 and 7. Both for BLG and 2DEG disks (see figure 6) we observe, at low magnetic fields, well-defined conductance maxima corresponding to the quantum-dot energy levels

$$E_q = \begin{cases}\dfrac{1}{2}\left[-t_\perp+\sqrt{t_\perp^2+\left(\frac{\hbar v_\mathrm{F}}{L}\right)^2 q^2}\right] & \text{for BLG,}\\ h^2q^2/\,(8m_\star L) & \text{for 2DEG,}\end{cases} \tag{33}$$

with $L \equiv R_\mathrm{o} - R_\mathrm{i}$ and q an integer. These maxima gradually evolve, with increasing field, towards narrow peaks corresponding to the resonances with LLs, at energies given by equation (11) for BLG or equation (32) for 2DEG. Away from the maxima, some background conductance $G \gtrsim g_0$

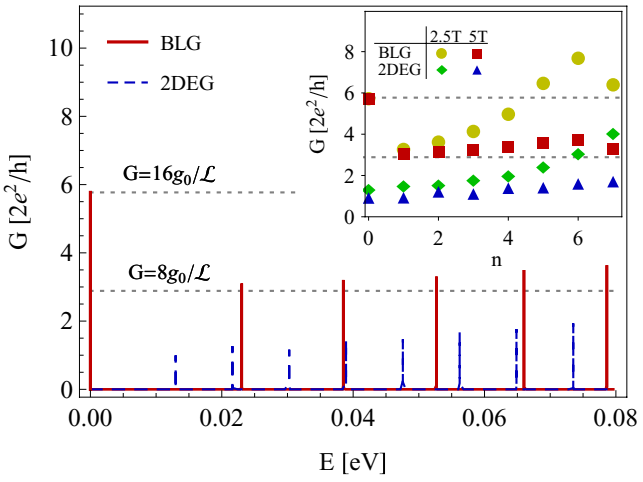

Figure 7. Conductance as a function of doping at fixed $B = 5$ T. The parameters are the same as in figure 6. The inset shows the maximal conductance at the resonance with the n-th LL, for two different values of the magnetic field ($B = 2.5$ and 5 T).

appears when the cyclotronic diameter $2r_C \gtrsim L$. (Otherwise, $G \ll g_0$.) In turn, the ballistic and the quantum-tunneling transport regimes can be identified for both the systems considered.

The key difference in charge transport via Corbino disks in BLG and in 2DEG appears in the quantum-tunneling regime, and is visualized in figure 7. For BLG, the conductance at the local maximum corresponding to the resonance with the n-th LL is $G_{\max} \simeq 2G_{\rm diff}^{\rm MLG}$ for $n = 0$, or $G_{\max} \simeq G_{\rm diff}^{\rm MLG}$ for $n \neq 0$. When increasing the magnetic field, every single resonance gets narrow in the energy scale, but the peak conductance is almost unaffected[5].

In contrast, transmission resonances for the disk in 2DEG simply vanish with increasing field (see inset in figure 7), as the pseudodiffusive charge transport regime does not occur in this case.

5. Conclusions

We have investigated, by means of analytical mode matching for the effective Dirac equation, the effects of the interlayer hopping and the electrostatic bias on magnetoconductance of a Corbino disk in bilayer graphene. Most remarkably, the disk conductance still shows periodic (approximately sinusoidal) oscillations with the applied field, typically with the same period as in the monolayer case [1, 2], both when the system is at the Dirac point, or when the values of electrochemical doping follow the field-dependent position of any higher LL at a given bias. In any case, the average conductance coincides with the pseudodiffusive value for a disk-shaped bilayer sample, provided the degeneracies associated with valley and layer degrees of freedom are correctly taken into account [30]. A quantitative comparison with a similar system in 2DEG, for which the conductance gradually decays with increasing field, makes it clear that the chiral tunneling of Dirac fermions governs the charge transport through the Corbino disk in bilayer graphene.

A special feature of the magnetoconductance spectra, directly linked to the presence of the hopping between the layers, may be observed for an unbiased disk at the Dirac point. In such a case, the two periodic contributions to the disk conductance may interfere constructively or destructively, depending on the geometric parameters (i.e. the radii $R_{\rm i}$ and $R_{\rm o}$) and on the interlayer hopping integral ($t_\perp$). For particular combinations of these variables, obeying the approximation equation (21), which can be rewritten as

$$\frac{R_{\rm o}}{R_{\rm i}} \simeq \left(\frac{R_{\rm i}\, t_\perp}{2\hbar v_{\rm F}}\right)^{4/p} \quad \text{with } p = 1, 3, 5, \ldots, \tag{34}$$

the interference is maximally destructive, leading to the approximately field-independent conductance (twice as large as the pseudodiffusive value for the disk setup in a monolayer [27]) for moderate radii ratios $R_{\rm o}/R_{\rm i} \lesssim 10$ in the normal Corbino setup, or to the oscillation frequency doubling for the Andreev–Corbino setup. We notice that the effect that we described offers, at least in principle, an independent way of determining the basic microscopic parameters of bilayer graphene.

Quite remarkably, the energy-gap opening from applying the external electrostatic bias affects the transport properties of the Corbino disk in bilayer graphene in a rather unexpected manner. New features, mentioned above and absent in the monolayer, appear for unbiased disks at the Dirac point, whereas the gap opening essentially reduces the variety of magnetotransport behavior to that earlier described for monolayer disks. This observation seems particularly significant, as some experimental works showed that the energy gap may also appear spontaneously, due to electron–electron interactions, for bilayer samples close to the charge-neutrality point [13, 14]. It must be noticed, however, that the results of other conductance measurements [12] coincide with theoretical predictions for an unbiased bilayer, leaving an ambiguity concerning the role of interactions in the system.

The effects of disorder [3], lattice defects [56] or magnetic impurities [57, 58], which may modify the transport properties of graphene-based devices, are beyond the scope of this paper as we have focused on perfectly clean ballistic systems. Certain features of the results, including the fact that unit transmission appears periodically (for consecutive normal modes) with increasing field, and that the oscillation period is proportional to the ratio of fundamental constants h/e, allow us to believe that symmetry-protected quantum channels [59] would lead to magnetoconductance oscillations appearing in a more general situation as well.

Acknowledgments

We thank M Burkhard and E Moomivand for their correspondence. The work was supported by the National Science Centre of Poland (NCN) via Grant No. N–N202–031440, and partly by the Foundation for Polish Science (FNP)

[5] The system parameters $R_{\rm i} = 25\, l_\perp$ and $R_{\rm o} = 4R_{\rm i}$ are adjusted such that the oscillation magnitude at the Dirac point $\Delta G^{\rm BLG} \simeq 0$. At higher LLs, the relative magnitude is given by $\Delta G^{\rm MLG}/G_{\rm diff}^{\rm MLG} \simeq 0.05$, defining the range in which the peak conductance may vary with increasing field, namely: $|G_{\max}^{n\neq 0} - G_{\rm diff}^{\rm MLG}| \lesssim \Delta G^{\rm MLG}/2$.

under the program TEAM 'Correlations and coherence in quantum materials and structures (CCQM)'. GR acknowledges support from the WIKING project. Computations were partly performed using the PL-Grid infrastructure.

Appendix A. Wavefunctions

In this appendix, we present the wavefunctions of a charge carrier in bilayer graphene, having the form of eigenspinors of the total angular-momentum operator J_z (5), and thus adjusted for a scattering problem with cylindrical symmetry. The cases of zero and nonzero magnetic fields, relevant for the leads and the sample area in the system of figure 1, are discussed separately.

A.1. Zero magnetic field

Four linearly independent solutions of the Dirac equation $H\psi = E\psi$ with the Hamiltonian given by equation (3), corresponding to the angular-momentum quantum number m, have forms of envelope wavefunctions given by equation (6). For $B = 0$, the radial parts of these functions can be written as

$$\phi^{\pm}_{\mathrm{in}}(r) = \begin{pmatrix} H^{(1)}_m(s_\pm r) \\ -s_\pm \epsilon_u^{-1} H^{(1)}_{m-1}(s_\pm r) \\ (\epsilon_u^2 - \eta_\pm) l_\perp \epsilon_u^{-1} H^{(1)}_m(s_\pm r) \\ s_\pm (\epsilon_u^2 - \eta_\pm) l_\perp (\epsilon_u \epsilon_d)^{-1} H^{(1)}_{m+1}(s_\pm r) \end{pmatrix} \tag{A1}$$

for the waves propagating from $r = 0$ (the index $\pm$ refers to the two subbands), or

$$\phi^{\pm}_{\mathrm{out}}(r) = \begin{pmatrix} H^{(2)}_m(s_\pm r) \\ -s_\pm \epsilon_u^{-1} H^{(2)}_{m-1}(s_\pm r) \\ (\epsilon_u^2 - \eta_\pm) l_\perp \epsilon_u^{-1} H^{(2)}_m(s_\pm r) \\ s_\pm (\epsilon_u^2 - \eta_\pm) l_\perp (\epsilon_u \epsilon_d)^{-1} H^{(2)}_{m+1}(s_\pm r) \end{pmatrix} \tag{A2}$$

for the waves propagating from $r = \infty$, with $s_\pm = \sqrt{\eta_\pm}$, $\eta_\pm = \left(\Delta^2 + \tilde{\epsilon}^2\right) \pm \sqrt{\tilde{\epsilon}^2\left(4\Delta^2 + 1/l_\perp^2\right) - \Delta^2/l_\perp^2}$, $\epsilon_u = \tilde{\epsilon} + \Delta$, $\epsilon_d = \tilde{\epsilon} - \Delta$, $H^{(1)}_m(x)$ ($H^{(2)}_m(x)$) being the Hankel function of the first (second) kind [54], and the remaining symbols are the same as in equation (7). For $\tilde{\epsilon} \to \infty$, the asymptotic forms of the radial wavefunctions are[6]

$$\phi^{\pm}_{\mathrm{in}}(r) \simeq \sqrt{\frac{2}{\pi \tilde{\epsilon} r}} \exp\left[\mathrm{i}\left(\tilde{\epsilon} r - \frac{1}{2}\pi m - \frac{1}{4}\right)\right] \begin{pmatrix} 1 \\ -i \\ \mp 1 \\ \pm i \end{pmatrix} \tag{A3}$$

and

$$\phi^{\pm}_{\mathrm{out}}(r) \simeq \sqrt{\frac{2}{\pi \tilde{\epsilon} r}} \exp\left[-\mathrm{i}\left(\tilde{\epsilon} r - \frac{1}{2}\pi m - \frac{1}{4}\right)\right] \begin{pmatrix} 1 \\ i \\ \mp 1 \\ \mp i \end{pmatrix}. \tag{A4}$$

[6] We use $H^{(1)}_\nu(\rho) \approx \sqrt{2/(\pi\rho)} \exp[\mathrm{i}(\rho - \nu\pi/2 - \pi/4)]$ for $\rho \gg 1$, and $H^{(2)}_\nu(\rho) = [H^{(1)}_\nu(\rho)]^\star$.

A.2. Nonzero magnetic field

At the Dirac point ($\varepsilon = \delta = 0$), the radial part of the wavefunction, being a general solution of equation (9), reads

$$\phi_{\mathrm{d}}(r) = \alpha_1 \begin{pmatrix} f_m(\rho) \\ 0 \\ 0 \\ t\rho f_m(\rho)/2 \end{pmatrix} + \alpha_2 \begin{pmatrix} 0 \\ \rho^{-1} \bar{f}_m(\rho) \\ 0 \\ 0 \end{pmatrix} + \alpha_3 \begin{pmatrix} 0 \\ t\rho \bar{f}_m(\rho)/2 \\ \bar{f}_m(\rho) \\ 0 \end{pmatrix} + \alpha_4 \begin{pmatrix} 0 \\ 0 \\ 0 \\ \rho^{-1} f_m(\rho) \end{pmatrix}, \tag{A5}$$

where $f_m(\rho) = \exp\left(-m \ln\rho - \rho^2/4\right)$, $\bar{f}_m(\rho) = 1/f_m(\rho)$, α_j are arbitrary complex coefficients (taking different values depending whether the mode-matching analysis is carried out for the wave incoming from $r = 0$ given by $\phi^{+}_{\mathrm{in}}(r)$ or $\phi^{-}_{\mathrm{in}}(r)$; see appendix B), and the remaining symbols are the same as in equation (9).

At finite dopings ($\varepsilon \neq 0$ or $\delta \neq 0$), the radial wavefunctions are given by

$$\phi^{\pm}_l(r) = \begin{pmatrix} a^{\pm}_{m,l}(\varepsilon, \delta;\ \rho) \\ b^{\pm}_{m,l}(\varepsilon, \delta;\ \rho) \\ c^{\pm}_{m,l}(\varepsilon, \delta;\ \rho) \\ d^{\pm}_{m,l}(\varepsilon, \delta;\ \rho) \end{pmatrix} \quad (l = 1, 2), \tag{A6}$$

where the spinor components can be written as

$$\begin{aligned}
a^{\pm}_{m,1}(\varepsilon, \delta;\ \rho) &= 2^{(m+1)/2} \mathrm{e}^{\rho^2/4} \rho^m\, \mathrm{U}\left(\frac{\gamma_\pm}{2}, m+1, -\frac{\rho^2}{2}\right), \\
b^{\pm}_{m,1}(\varepsilon, \delta;\ \rho) &= -(\delta+\varepsilon)^{-1}\, 2^{(m+1)/2}\, \mathrm{e}^{\rho^2/4}\, \rho^{m-1} \\
&\quad \times \left[\left(2m + \rho^2\right) \mathrm{U}\left(\frac{\gamma_\pm}{2}, m+1, -\frac{\rho^2}{2}\right) \right. \\
&\quad \left. + \frac{\rho^2}{2} \gamma_\pm \mathrm{U}\left(\frac{\gamma_\pm}{2}+1, m+2, -\frac{\rho^2}{2}\right) \right], \\
c^{\pm}_{m,1}(\varepsilon, \delta;\ \rho) &= (\delta+\varepsilon)^{-1}\, 2^{(m+1)/2} \mathrm{e}^{\rho^2/4}\, \rho^m\, t^{-1} \\
&\quad \times \left[-\gamma_\pm + (\delta+\varepsilon)^2 + 2\right] \mathrm{U}\left(\frac{\gamma_\pm}{2}, m+1, -\frac{\rho^2}{2}\right), \\
d^{\pm}_{m,1}(\varepsilon, \delta;\ \rho) &= (\delta^2 - \varepsilon^2)^{-1}\, 2^{(m-1)/2} \mathrm{e}^{\rho^2/4}\, \rho^{m+1}\, t^{-1} \gamma_\pm \\
&\quad \times \left[-\gamma_\pm + (\delta+\varepsilon)^2 + 2\right] \mathrm{U}\left(\frac{\gamma_\pm}{2}+1, m+2, -\frac{\rho^2}{2}\right),
\end{aligned} \tag{A7}$$

and

$$\begin{aligned}
a^{\pm}_{m,2}(\varepsilon, \delta;\ \rho) &= 2^{(m+1)/2} \mathrm{e}^{\rho^2/4} \rho^m\, \mathrm{L}^m_{-\gamma_\pm/2}\left(-\frac{\rho^2}{2}\right), \\
b^{\pm}_{m,2}(\varepsilon, \delta;\ \rho) &= -(\delta+\varepsilon)^{-1}\, 2^{(m+1)/2}\, \mathrm{e}^{\rho^2/4}\, \rho^{m-1} \\
&\quad \times \left[\rho^2\, \mathrm{L}^{m+1}_{-\gamma_\pm/2-1}\left(-\frac{\rho^2}{2}\right) + \left(2m + \rho^2\right) \mathrm{L}^m_{-\gamma_\pm/2}\left(-\frac{\rho^2}{2}\right) \right], \\
c^{\pm}_{m,2}(\varepsilon, \delta;\ \rho) &= (\delta+\varepsilon)^{-1}\, 2^{(m+1)/2}\, \mathrm{e}^{\rho^2/4}\, \rho^m\, t^{-1} \\
&\quad \times \left[-\gamma_\pm + (\delta+\varepsilon)^2 + 2\right] \frac{\Gamma\left(m - \gamma_\pm/2 + 1\right)}{\Gamma\left(1 - \gamma_\pm/2\right)} \\
&\quad \times \mathcal{F}\left(\frac{\gamma_\pm}{2}; m+1; -\frac{\rho^2}{2}\right),
\end{aligned}$$

$$d^{\pm}_{m,2}(\varepsilon,\delta;\,\rho) = (\delta^2-\varepsilon^2)^{-1}\,2^{(m+1)/2}\,\mathrm{e}^{\rho^2/4}\,\rho^{m+1}\,t^{-1} \times\left[-\gamma_\pm+(\delta+\varepsilon)^2+2\right]\frac{\Gamma\left(m-\gamma_\pm/2+1\right)}{\Gamma\left(-\gamma_\pm/2\right)} \times\mathcal{F}\left(\frac{\gamma_\pm}{2}+1;\,m+2;\,-\frac{\rho^2}{2}\right). \tag{A8}$$

We have further defined $\gamma_\pm = \left(\delta^2+\varepsilon^2\right)\pm\sqrt{\varepsilon^2\left(4\delta^2+t^2\right)-\delta^2t^2}$. $\mathrm{L}^a_b(x)$ is the generalized Laguerre polynomial (see [54], Chapter 22), $\mathrm{U}(a,b,x)$ denotes the confluent hypergeometric function [55], $\Gamma(z)=\int_0^\infty x^{z-1}\mathrm{e}^{-x}\mathrm{d}x$ is the Euler gamma function, $\mathcal{F}(a;b;z)\equiv{}_1\mathrm{F}_1(a;b;z)\,\Gamma(b)$ with ${}_pF_q(a_1,\ldots,a_p;b_1,\ldots,b_q;z)$ denoting the generalized hypergeometric function [60], and the remaining symbols are the same as in equation (9) in the main text.

Appendix B. Transmission eigenvalues

The charge conservation conditions for the interfaces between the disk area and the leads ($r=R_\mathrm{i}$ and $r=R_\mathrm{o}$; see also figure 1) can be written, in terms of the radial wavefunctions presented in appendix A, as

$$\phi^{\pm}_{\mathrm{in}}(R_\mathrm{i})+r^{\pm}_p\phi^{+}_{\mathrm{out}}(R_\mathrm{i})+r^{\pm}_n\phi^{-}_{\mathrm{out}}(R_\mathrm{i})=\phi_\mathrm{d}(R_\mathrm{i}),\qquad \phi_\mathrm{d}(R_\mathrm{o})=t^{\pm}_p\phi^{+}_{\mathrm{in}}(R_\mathrm{o})+t^{\pm}_n\phi^{-}_{\mathrm{in}}(R_\mathrm{o}), \tag{B1}$$

where we have represented wavefunctions in the leads following equations (12) and (13) in the main text. If the disk area is undoped and unbiased ($\varepsilon=\delta=0$), the function $\phi_\mathrm{d}(r)$ is given by equation (A5). Taking the limit of $|U_\infty|\to\infty$ for the leads (i.e. choosing the functions $\phi^{\pm}_{\mathrm{in}}(r)$ and $\phi^{\pm}_{\mathrm{out}}(r)$ as given by equations (A3) and (A4)) and solving the system of linear equations following from equation (B1), one gets the closed-form expression for $T^{\pm}_m$ transmission eigenvalues for a given angular momentum quantum number m (see equation (17) in the main text).

For a more general case of finite dopings in the disk area ($\varepsilon\neq0$ or $\delta\neq0$), the limit $|U_\infty|\to\infty$ for the leads, combined with radial wavefunctions of the form $\phi^{\pm}_1(r)$ and $\phi^{\pm}_2(r)$ (see equations (A6)–(A8)) for the disk area, bring us to the system of linear equations

$$\begin{pmatrix}
-1 & -1 & a^+_{m,1}(\varepsilon,\delta;\rho_0) & a^+_{m,2}(\varepsilon,\delta;\rho_0) & a^-_{m,1}(\varepsilon,\delta;\rho_0) & a^-_{m,2}(\varepsilon,\delta;\rho_0) & 0 & 0\\
-i & -i & b^+_{m,1}(\varepsilon,\delta;\rho_0) & b^+_{m,2}(\varepsilon,\delta;\rho_0) & b^-_{m,1}(\varepsilon,\delta;\rho_0) & b^-_{m,2}(\varepsilon,\delta;\rho_0) & 0 & 0\\
1 & -1 & c^+_{m,1}(\varepsilon,\delta;\rho_0) & c^+_{m,2}(\varepsilon,\delta;\rho_0) & c^-_{m,1}(\varepsilon,\delta;\rho_0) & c^-_{m,2}(\varepsilon,\delta;\rho_0) & 0 & 0\\
i & -i & d^+_{m,1}c(\varepsilon,\delta;\rho_0) & d^+_{m,2}(\varepsilon,\delta;\rho_0) & d^-_{m,1}(\varepsilon,\delta;\rho_0) & d^-_{m,2}(\varepsilon,\delta;\rho_0) & 0 & 0\\
0 & 0 & a^+_{m,1}(\varepsilon,\delta;\rho_1) & a^+_{m,2}(\varepsilon,\delta;\rho_1) & a^-_{m,1}(\varepsilon,\delta;\rho_1) & a^-_{m,2}(\varepsilon,\delta;\rho_1) & -\mathcal{R} & -\mathcal{R}\\
0 & 0 & b^+_{m,1}(\varepsilon,\delta;\rho_1) & b^+_{m,2}(\varepsilon,\delta;\rho_1) & b^-_{m,1}(\varepsilon,\delta;\rho_1) & b^-_{m,2}(\varepsilon,\delta;\rho_1) & \mathrm{i}\mathcal{R} & \mathrm{i}\mathcal{R}\\
0 & 0 & c^+_{m,1}(\varepsilon,\delta;\rho_1) & c^+_{m,2}(\varepsilon,\delta;\rho_1) & c^-_{m,1}(\varepsilon,\delta;\rho_1) & c^-_{m,2}(\varepsilon,\delta;\rho_1) & \mathcal{R} & -\mathcal{R}\\
0 & 0 & d^+_{m,1}(\varepsilon,\delta;\rho_1) & d^+_{m,2}(\varepsilon,\delta;\rho_1) & d^-_{m,1}(\varepsilon,\delta;\rho_1) & d^-_{m,2}(\varepsilon,\delta;\rho_1) & -\mathrm{i}\mathcal{R} & \mathrm{i}\mathcal{R}
\end{pmatrix} \times\begin{pmatrix} r^\pm_p\\ r^\pm_n\\ \alpha^\pm_1\\ \alpha^\pm_2\\ \alpha^\pm_3\\ \alpha^\pm_4\\ t^\pm_p\\ t^\pm_n\end{pmatrix} = \begin{pmatrix}1\\ -i\\ \mp1\\ \pm i\\ 0\\ 0\\ 0\\ 0\end{pmatrix}, \tag{B2}$$

with $\rho_0=R_\mathrm{i}/l_B$, $\rho_1=R_\mathrm{o}/l_B$ and $\mathcal{R}=\sqrt{R_\mathrm{i}/R_\mathrm{o}}$. The elements of the reflection and transmission matrices $\tilde{\mathbf{r}}_{K,m}$ and $\tilde{\mathbf{t}}_{K,m}$ occurring in equation (B2) differ from the corresponding elements of $\mathbf{r}_{K,m}$ and $\mathbf{t}_{K,m}$ (see also equation (15) in the main text) only via phase factors, which are insignificant when calculating transmission eigenvalues. Solving equation (B2), one obtains the matrices $\tilde{\mathbf{r}}_{K,m}$ and $\tilde{\mathbf{t}}_{K,m}$ for the K valley and the angular momentum quantum number m. The reflection and transmission matrices for the K' valley can be obtained from an analogous procedure, starting from radial wavefunctions modified according to $(\phi_1,\phi_2,\phi_3,\phi_4)^T\to(\phi_1,-\phi_2,\phi_3,-\phi_4)^T$, with a substitution $\delta\to-\delta$.

Appendix C. Mode matching for a disk in 2DEG

For Schrödinger electrons in the Corbino setup, current conservation at $r=R_\mathrm{i}$ and $r=R_\mathrm{o}$ leads to four independent matching conditions

$$\varphi^{(\mathrm{i})}_l(R_\mathrm{i})=\varphi^{(\mathrm{d})}_l(R_\mathrm{i}),\quad \varphi^{(\mathrm{d})}_l(R_\mathrm{o})=\varphi^{(\mathrm{o})}_l(R_\mathrm{o}),\qquad \left.\frac{\mathrm{d}\varphi^{(\mathrm{i})}_l}{\mathrm{d}r}\right|_{R_\mathrm{i}}=\left.\frac{\mathrm{d}\varphi^{(\mathrm{d})}_l}{\mathrm{d}r}\right|_{R_\mathrm{i}},\quad \left.\frac{\mathrm{d}\varphi^{(\mathrm{d})}_l}{\mathrm{d}r}\right|_{R_\mathrm{o}}=\left.\frac{\mathrm{d}\varphi^{(\mathrm{o})}_l}{\mathrm{d}r}\right|_{R_\mathrm{o}}, \tag{C1}$$

determining the coefficients r_l, t_l, C_l and D_l, defined via equations (30) and (31) in the main text. Let us further define the wavefunctions in the disk area

$$\varphi^{(\mathrm{d})}_{1,l}(r)=\frac{1}{r}\,\mathrm{W}_{\Omega_l,l/2}\left(-\frac{r^2}{2l_B^2}\right)\quad\text{and}\quad \varphi^{(\mathrm{d})}_{2,l}(r) =\frac{1}{r}\,\mathrm{W}_{-\Omega_l,l/2}\left(\frac{r^2}{2l_B^2}\right), \tag{C2}$$

where $\Omega_l=\left(l-k^2l_B^2\right)/2$, $k=\sqrt{2m_\star E/\hbar^2}$ and $W_{\kappa,\mu}(x)$ is the Whittaker function [55]. (In turn, $\varphi^{(\mathrm{d})}_l(r)\equiv C_l\varphi^{(\mathrm{d})}_{1,l}(r)+D_l\varphi^{(\mathrm{d})}_{1,l}(r)$.) The transmission probability for the angular momentum quantum number l can now be written as

$$T_l=|t_l|^2=\frac{1}{|\mathcal{M}_l|^2}\left(\frac{4}{\pi l_B^2R_\mathrm{i}R_\mathrm{o}}\right)^2, \tag{C3}$$

where

$$\begin{aligned}\mathcal{M}_l=&\,\mathrm{H}^{(1)}_l(KR_\mathrm{i})\,\mathrm{H}^{(2)}_l(KR_\mathrm{o})\\ &\times\left[\partial_r\varphi^{(\mathrm{d})}_{1,l}(R_\mathrm{o})\,\partial_r\varphi^{(\mathrm{d})}_{2,l}(R_\mathrm{i})-\partial_r\varphi^{(\mathrm{d})}_{1,l}(R_\mathrm{i})\,\partial_r\varphi^{(\mathrm{d})}_{2,l}(R_\mathrm{o})\right]\\ &+K^2\left[\partial_\rho\mathrm{H}^{(1)}_l(KR_\mathrm{i})\right]\left[\partial_\rho\mathrm{H}^{(2)}_l(KR_\mathrm{o})\right]\\ &\times\left[\varphi^{(\mathrm{d})}_{1,l}(R_\mathrm{o})\,\varphi^{(\mathrm{d})}_{2,l}(R_\mathrm{i})-\varphi^{(\mathrm{d})}_{1,l}(R_\mathrm{i})\,\varphi^{(\mathrm{d})}_{2,l}(R_\mathrm{o})\right]\\ &+K\mathrm{H}^{(1)}_l(KR_\mathrm{i})\left[\partial_\rho\mathrm{H}^{(2)}_l(KR_\mathrm{o})\right]\end{aligned}$$

$$\times\left[\partial_r\varphi^{(\mathrm{d})}_{1,l}\left(R_\mathrm{i}\right)\varphi^{(\mathrm{d})}_{2,l}\left(R_\mathrm{o}\right)-\varphi^{(\mathrm{d})}_{1,l}\left(R_\mathrm{o}\right)\partial_r\varphi^{(\mathrm{d})}_{2,l}\left(R_\mathrm{i}\right)\right]$$
$$+K\left[\partial_\rho \mathrm{H}^{(1)}_l\left(K R_\mathrm{i}\right)\right]\mathrm{H}^{(2)}_l\left(K R_\mathrm{o}\right)$$
$$\times\left[\varphi^{(\mathrm{d})}_{1,l}\left(R_\mathrm{i}\right)\partial_r\varphi^{(\mathrm{d})}_{2,l}\left(R_\mathrm{o}\right)-\partial_r\varphi^{(\mathrm{d})}_{1,l}\left(R_\mathrm{o}\right)\varphi^{(\mathrm{d})}_{2,l}\left(R_\mathrm{i}\right)\right], \quad \text{(C4)}$$

and the derivatives are given by

$$\partial_\rho \mathrm{H}^{(\alpha)}_l(\rho) = \mathrm{H}^{(\alpha)}_{l-1}(\rho) - \frac{l}{\rho}\mathrm{H}^{(\alpha)}_l(\rho), \quad \text{(C5)}$$

$$\partial_r\varphi^{(\mathrm{d})}_{\alpha,l}(r) = -\frac{1}{r^2}\left[\left(2\lambda_\alpha\Omega_l+1+\frac{\lambda_\alpha r^2}{2l_B^2}\right)\mathrm{W}_{\lambda_\alpha\Omega_l,\,l/2}\left(-\frac{\lambda_\alpha r^2}{2l_B^2}\right)\right.$$
$$\left.+2\mathrm{W}_{1+\lambda_\alpha\Omega_l,\,l/2}\left(-\frac{\lambda_\alpha r^2}{2l_B^2}\right)\right], \quad \text{(C6)}$$

for $\alpha = 1, 2$, and $\lambda_\alpha = -(-1)^\alpha$.

References

[1] Rycerz A 2010 *Phys. Rev.* B **81** 121404
[2] Katsnelson M I 2010 *Europhys. Lett.* **89** 17001
[3] McCann E and Koshino M 2013 *Rep. Prog. Phys.* **76** 056503
[4] McCann E and Fal'ko V I 2006 *Phys. Rev. Lett.* **96** 086805
McCann E 2006 *Phys. Rev.* B **74** 161403
[5] Ohta T, Bostwick A, Seyller T, Horn K and Rotenberg E 2006 *Science* **313** 951
[6] Oostinga J B, Heersche H B, Liu X, Morpurgo A F and Vandersypen L M K 2007 *Nat. Mater.* **7** 151
[7] Castro E V, Novoselov K S, Morozov S V, Peres N M R, Lopes Dos Santos J M B, Nilsson J, Guinea F, Geim A K and Castro Neto A H 2007 *Phys. Rev. Lett.* **99** 216802
[8] Pereira J M Jr, Peeters F M and Vasilopoulos P 2007 *Phys. Rev.* B **76** 115419
[9] Feldman B E, Martin J and Yacoby A 2009 *Nat. Phys.* **5** 889
[10] Weitz R T, Allen M T, Feldman B E, Martin J and Yacoby A 2010 *Science* **330** 812
[11] Yan J and Fuhrer M S 2010 *Nano Lett.* **10** 4521
[12] Mayorov A S 2011 *Science* **333** 860
[13] Rutter G M, Jung S, Klimov N N, Newell D B, Zhitenev N B and Stroscio J A 2011 *Nat. Phys.* **7** 649
[14] Bao W, Velasco J Jr, Zhang F, Jing L, Standley B, Smirnov D, Bockrath M, MacDonald A H and Lau C N 2012 *Proc. Natl Acad. Sci. USA* **109** 10802
[15] Velasco J Jr *et al* 2012 *Nat. Nanotechnol.* **7** 156
[16] Galdabini S and Giuliani G 1991 *Ann. Sci.* **48** 21
[17] Zhang F, MacDonald A H and Mele E J 2013 *Proc. Natl Acad. Sci. USA* **110** 10546
[18] Faugeras C, Faugeras B, Orlita M, Potemski M, Nair R R and Geim A K 2010 *ACS Nano* **4** 1889
[19] Liu W, Valdés R, Hao Y, Ruoff R S and Armitage N P 2011 *J. Appl. Phys.* **110** 083510
[20] Zhao Y, Cadden-Zimansky P, Ghahari F and Kim P 2012 *Phys. Rev. Lett.* **108** 106804
[21] Peters E C 2012 *Appl. Phys. Lett.* **104** 203109
[22] Snyman I and Beenakker C W J 2007 *Phys. Rev.* B **75** 045322
[23] Katsnelson M I 2006 *Eur. Phys. J.* B **51** 157
[24] Tworzydło J, Trauzettel B, Titov M, Rycerz A and Beenakker C W J 2006 *Phys. Rev. Lett.* **96** 246802
[25] Miao F, Wijeratne S, Zhang Y, Coscun U C, Bao W and Lau C N 2007 *Science* **317** 1530
[26] Danneau R, Wu F, Craciun M F, Russo S, Tomi M Y, Salmilehto J, Morpurgo A F and Hakonen P J 2008 *Phys. Rev. Lett.* **100** 196802
[27] Rycerz A, Recher P and Wimmer M 2009 *Phys. Rev.* B **80** 125417
[28] Moghaddam A G and Zareyan M 2009 *Phys. Rev.* B **79** 073401
[29] Nilsson J, Castro Neto A H, Guinea F and Peres N M R 2008 *Phys. Rev.* B **78** 045405
[30] Rut G and Rycerz A 2014 *Phys. Rev.* B **89** 045421
[31] Schelter J, Recher P and Trauzettel B 2012 *Solid State Commun.* **152** 1411
[32] Zarenia M, Pereira J M, Chaves A, Peeters F M and Farias G A 2010 *Phys. Rev.* B **81** 045431
[33] Xavier L J P, Pereira Jr J M, Chaves A, Farias G A and Peeters F M 2010 *Appl. Phys. Lett.* **96** 212108
[34] Romanovsky I, Yannouleas C and Landman U 2012 *Phys. Rev.* B **85** 165434
[35] Rycerz A 2012 *Acta Phys. Pol.* A **121** 1242
[36] Khatibi Z, Rostami H and Asgari R 2013 *Phys. Rev.* B **88** 195426
[37] Bahamon D A, Castro Neto A H and Pereira V M 2013 *Phys. Rev.* B **88** 235433
[38] Rut G and Rycerz A 2014 *Phil. Mag.* accepted (arXiv:1401.7247)
[39] Rycerz A, Tworzydło J and Beenakker C W J 2007 *Nat. Phys.* **3** 172
Rycerz A 2008 *Phys. Status Solidi* **205** 1281
[40] Akhmerov A R, Bardarson J H, Rycerz A and Beenakker C W J 2008 *Phys. Rev.* B **77** 205416
[41] Gunlycke D and White C T 2011 *Phys. Rev. Lett.* **106** 136806
[42] Pályi A and Burkard G 2011 *Phys. Rev. Lett.* **106** 086801
[43] Villegas-Lelovsky L, Correa J L H and Qu F 2014 *Phys. Status Solidi* **251** 1451
[44] Wimmer M, Adagideli I, Berber S, Tomanek D and Richter K 2008 *Phys. Rev. Lett.* **100** 177207
Yazyev O V and Katsnelson M I 2008 *Phys. Rev. Lett.* **100** 047209
Zeng M, Shen L, Zhou M, Zhang Ch and Feng Y 2011 *Phys. Rev.* B **83** 115427
[45] Nazarov Yu V and Blanter Ya M 2009 *Quantum Transport: Introduction to Nanoscience* (Cambridge: Cambridge University Press)
[46] Pereira J M Jr, Vasilopoulos P and Peeters F M 2007 *Nano Lett.* **7** 946
Pereira J M Jr, Vasilopoulos P, Peeters F M and Farias G A 2009 *Phys. Rev.* B **79** 195403
[47] Recher P, Nilsson J, Burkard G and Trauzettel B 2009 *Phys. Rev.* B **79** 085407
[48] Cserti J, Csordás A and Dávid G 2007 *Phys. Rev. Lett.* **99** 066802
Koshino M and Ando T 2006 *Phys. Rev.* B **73** 245403
[49] Landauer R 1970 *Phil. Mag.* **21** 863
Büttiker M 1992 *Phys. Rev.* B **46** 12485
[50] Akhmerov A R and Beenakker C W J 2007 *Phys. Rev.* B **75** 045426
[51] Kirczenow G 1994 *J. Phys.: Condens. Matter* **6** L583
[52] Souma S and Suzuki A 1998 *Phys. Rev.* B **58** 4649
Souma S and Suzuki A 1999 *Phys. Rev.* B **60** 15928
[53] Peierls R 1979 *Surprises in Theoretical Physics* (New York: Princeton) chapter 1
[54] Abramowitz M and Stegun I A (ed) 1965 *Handbook of Mathematical Functions* (New York: Dover) chapter 9
[55] Abramowitz M and Stegun I A (ed) 1965 *Handbook of Mathematical Functions* (New York: Dover) chapter 13
[56] Dresselhaus M S, Jorio A, Souza Filho A G and Saito R 2010 *Phil. Trans. R. Soc.* A **368** 5355
[57] Cornaglia P S, Usaj G and Balseiro C A 2009 *Phys. Rev. Lett.* **102** 046801
Uchoa B, Rappoport T G and Castro Neto A H 2011 *Phys. Rev. Lett.* **106** 016801

[58] Sun J H, Hu F M, Tang H K and Lin H Q 2013 *Int. J. Mod. Phys.* B **27** 1362039
[59] Wakabayashi K, Takane Y and Sigrist M 2007 *Phys. Rev. Lett.* **99** 036601
Kawarabayashi T, Hatsugai Y and Aoki H 2012 *Phys. Rev.* B **85** 165410
de Gail R, Goerbig M O, Guinea F, Montambaux G and Castro Neto A H 2011 *Phys. Rev.* B **84** 045436
[60] Olver F W J, Lozier D W, Boisvert R F and Clark C W 2010 *NIST Handbook of Mathematical Functions* (Cambridge: Cambridge University Press) chapter 16

Philosophical Magazine, 2015
Vol. 95, Nos. 5–6, 599–608, http://dx.doi.org/10.1080/14786435.2014.974712

Quantum-limited shot noise and quantum interference in graphene-based Corbino disk

Grzegorz Rut and Adam Rycerz*

Marian Smoluchowski Institute of Physics, Jagiellonian University, Reymonta 4, PL–30059 Kraków, Poland

(*Received 20 July 2014; accepted 3 October 2014*)

This is a theoretical study of finite voltage effects on the conductance, the shot-noise power and the third, charge-transfer cumulant for graphene-based Corbino disk in the presence of external magnetic fields. Periodic magnetoconductance oscillations, predicted in earlier works, become invisible for relatively small source–drain voltages, as the current decays rapidly with magnetic field. Quantum interference still governs the behaviour of higher charge-transfer cumulants.

Keywords: graphene; shot noise; Corbino disk; quantum interference

1. Introduction

The Corbino geometry, in which electric current is passed through a disk-shaped sample area attached to two circular leads [see Figure 1(a), the inset] was proposed over a century ago [1,2] to measure the magnetoresistance without generating the Hall voltage, making a significant step towards understanding the nature of charge transport in ordinary solids [3]. An interest in such a geometry has reappeared due to the fabrication of GaAs/AlGaAs heterostructures [4,5]. Also, after the discovery of high-temperature superconductivity, Corbino measurements have provided a valuable insight into the vortex dynamics, as the influence of sample edges was eliminated [6].

In the context of graphene, various transport properties of Corbino disks were recently studied experimentally [7–10] and theoretically [11–15]. Next to the case of a rectangular strip geometry [16,17], the Corbino geometry provides another situation when transport properties of a graphene nanodevice can be investigated analytically [11], by solving the scattering problem for Dirac fermions, at arbitrary dopings and magnetic fields. In particular, mode-matching analysis for the effective Dirac equation gives transmission probabilities for *undoped* disk in graphene monolayer [11,12]

$$T_j^{(0)} = \frac{1}{\cosh^2\left[(j+\Phi/\Phi_0)\ln(R_\mathrm{o}/R_\mathrm{i})\right]}, \tag{1}$$

where $j = \pm\frac{1}{2}, \pm\frac{3}{2}, \ldots$ is the angular momentum quantum number labelling normal modes in the leads, $\Phi = \pi(R_\mathrm{o}^2 - R_\mathrm{i}^2)B$ is the flux piercing the disk in the uniform magnetic field

*Corresponding author. Email: adam.rycerz@uj.edu.pl

(B), R_i is the inner radius , R_o is the outer radius and $\Phi_0 = 2\,(h/e)\ln(R_\mathrm{o}/R_\mathrm{i})$. Moreover, in the derivation of Equation (1), the limit of heavily doped graphene leads [16] is imposed. Summing T_j-s over the normal modes in the leads, one finds that the Landauer–Büttiker conductance, in the linear-response regime, shows periodic (approximately sinusoidal) oscillations with the flux Φ, with Φ_0 being the oscillations period. Additionally, the disk conductance averaged over a single period restores the pseudo-diffusive value [18]

$$G_\mathrm{diff} = \frac{2\pi\sigma_0}{\ln(R_\mathrm{o}/R_\mathrm{i})}, \tag{2}$$

with $\sigma_0 = (4/\pi)\,e^2/h$ being the universal conductivity of graphene. Analogous behaviour is predicted for higher charge-transfer cumulants [12,19].

In this paper, we extend the analysis beyond the linear-response regime by calculating the conductance, the Fano factor $\mathcal{F}$ quantifying the shot-noise power, and $\mathcal{R}$-factor quantifying the third charge-transfer cumulant, in a situation when finite source–drain voltage is applied to graphene-based Corbino disk in the shot-noise limit. Our results show that albeit the conductance oscillations vanish rapidly with the voltage and magnetic field, $\mathcal{F}$ and $\mathcal{R}$ still oscillate periodically and their mean values approach $\overline{\mathcal{F}}_\infty \simeq 0.76$ and $\overline{\mathcal{R}}_\infty \simeq 0.55$ (respectively) in the high-field limit. In the remaining parts of the paper, we first (in Section 2) recall briefly the formula allowing one to determine the conductance and other charge-transfer characteristics of graphene-based Corbino disk at arbitrary voltages and magnetic fields. Next, in Section 3, our numerical results are presented in details. The conclusions are given in Section 4.

2. Charge-transfer cumulants

In the shot-noise limit $eV_\mathrm{eff} \gg k_B T$, with V_eff being the effective source–drain voltage (We assume the inner (or the outer) lead is characterized by the electrochemical potential $\mu_0 - eV_\mathrm{eff}/2$ (or $\mu_0 + eV_\mathrm{eff}/2$); the actual source–drain voltage may differ from V_eff due to charge-screening effects.), the charge Q passing a nanoscale device in a time interval Δt is A random variable, with the characteristic function $\Lambda(\chi)$ given by the Levitov formula [20]

$$\begin{aligned}\ln\Lambda(\chi) &\equiv \ln\langle\exp(i\chi Q/e)\rangle \\ &= 4_{(\sigma,v)}\frac{\Delta t}{h}\int\limits_{\mu_0-\frac{eV_\mathrm{eff}}{2}}^{\mu_0+\frac{eV_\mathrm{eff}}{2}} d\epsilon\,\sum_j \ln\left[1+\left(e^{i\chi}-1\right)T_j(\epsilon)\right],\end{aligned} \tag{3}$$

where $\langle X\rangle$ denotes the expectation value of X, the factor $4_{(\sigma,v)}$ accounts for spin and valley degeneracies, and we have assumed $V_\mathrm{eff} > 0$ without loss of a generality. The average charge $\langle Q\rangle$, as well as any charge-transfer cumulant $\langle\langle Q^m\rangle\rangle \equiv \langle\,(Q-\langle Q\rangle)^m\,\rangle$, may be obtained by subsequent differentiation of $\ln\Lambda(\chi)$ with respect to $i\chi$ at $\chi = 0$. In particular, the conductance

$$G(V_{\rm eff}) = \frac{\langle Q\rangle}{V_{\rm eff}\,\Delta t} = \frac{e}{V_{\rm eff}\,\Delta t}\left.\frac{\partial \ln \Lambda}{\partial (i\chi)}\right|_{\chi=0}$$
$$\equiv \frac{4_{(\sigma,v)}e^2}{h}\sum_j \left\langle T_j\right\rangle_{|\epsilon-\mu_0|\leqslant \frac{eV_{\rm eff}}{2}}, \tag{4}$$

where transmission probabilities $T_j(\epsilon)$ are averaged over the energy interval $|\epsilon - \mu_0| \leqslant eV_{\rm eff}/2$. Analogously,

$$\mathcal{F}(V_{\rm eff}) = \langle\langle Q^2\rangle\rangle \big/ \langle\langle Q^2\rangle\rangle_{\rm Poisson}$$
$$= \frac{\sum_j \left\langle T_j\left(1-T_j\right)\right\rangle_{|\epsilon-\mu_0|\leqslant \frac{eV_{\rm eff}}{2}}}{\sum_j \left\langle T_j\right\rangle_{|\epsilon-\mu_0|\leqslant \frac{eV_{\rm eff}}{2}}} \tag{5}$$

and

$$\mathcal{R}(V_{\rm eff}) = \langle\langle Q^3\rangle\rangle \big/ \langle\langle Q^3\rangle\rangle_{\rm Poisson}$$
$$= \frac{\sum_j \left\langle T\left(1-T_j\right)\left(1-2T_j\right)\right\rangle_{|\epsilon-\mu_0|\leqslant \frac{eV_{\rm eff}}{2}}}{\sum_j \left\langle T_j\right\rangle_{|\epsilon-\mu_0|\leqslant \frac{eV_{\rm eff}}{2}}}, \tag{6}$$

with $\langle\langle Q^m\rangle\rangle_{\rm Poisson}$ the value of mth cumulant for the Poissonian limit ($T_j(\epsilon) \ll 1$), given by a generalized Schottky formula $\langle\langle Q^m\rangle\rangle_{\rm Poisson} = e^{m-1}\langle Q\rangle$.

In the case of graphene-based Corbino disk, the energy-dependent transmission probabilities are given by [11]

$$T_j(\epsilon) = \frac{16\,(\tilde{\epsilon}^2/\beta)^{|2j-1|}}{\tilde{\epsilon}^2 R_{\rm i} R_{\rm o}\,(X_j^2+Y_j^2)}\left[\frac{\Gamma(\gamma_{j\uparrow})}{\Gamma(\alpha_{j\uparrow})}\right]^2, \tag{7}$$

where $\tilde{\epsilon} = \epsilon/(\hbar v_F)$ with $v_F \simeq 10^6$ m/s the energy-independent Fermi velocity, $\beta = eB/(2\hbar)$, $\Gamma(z)$ is the Euler Gamma function and

$$\alpha_{js} = \frac{1}{4}\left[2(j+m_s+|j-m_s|+1) - \frac{\tilde{\epsilon}^2}{\beta}\right],$$
$$\gamma_{js} = |j-m_s|+1, \tag{8}$$

with $m_s = \pm\frac{1}{2}$ for the lattice pseudospin $s = \uparrow, \downarrow$. The remaining symbols in Equation (7) are defined as:

$$X_j = w^-_{j\uparrow\uparrow} + z_{j,1}z_{j,2}w^-_{j\downarrow\downarrow},$$
$$Y_j = z_{j,2}w^+_{j\uparrow\downarrow} - z_{j,1}w^+_{j\downarrow\uparrow}, \tag{9}$$

where

$$w^{\pm}_{jss'} = \xi^{(1)}_{js}(R_{\rm i})\xi^{(2)}_{js'}(R_{\rm o}) \pm \xi^{(1)}_{js}(R_{\rm o})\xi^{(2)}_{js'}(R_{\rm i}),$$
$$z_{j,1} = [2(j+s_j)]^{-2s_j},$$
$$z_{j,2} = 2(\beta/\tilde{\epsilon}^2)^{s_j+1/2}, \tag{10}$$

with $s_j \equiv \frac{1}{2}\mathrm{sgn}(j)$. The functions $\xi_{js}^{(1)}(r)$ and $\xi_{js}^{(2)}(r)$ in the first line of Equation (10) are given by:

$$\xi_{js}^{(\nu)}(r) = (\tilde{\epsilon}r)^{|j-m_s|}\exp(-\beta r^2/2) \times \begin{cases} M(\alpha_{js},\gamma_{js},\beta r^2), & \text{if } \nu=1, \\ U(\alpha_{js},\gamma_{js},\beta r^2), & \text{it } \nu=2, \end{cases} \tag{11}$$

where $M(a,b,z)$ and $U(a,b,z)$ are the confluent hypergeometric functions [21] (Without loss of generality, we choose $B > 0$. For $B < 0$ one gets $T_j(B) = T_{-j}(-B)$.).

It can be shown that in the zero-energy limit ($\epsilon \to 0$) Equation (7) simplifies to Equation (1). Similarly, in case the energy is adjusted to a higher Landau level (LL), namely, $\tilde{\epsilon}^2/(4\beta) = n = 1, 2, \ldots$, the transmission probability for j-th normal mode (in the high-field limit) is $T_j^{(n)} = T_{j-2n}^{(0)}$ [11]. In effect, periodic magnetoconductance oscillations in the linear-response regime are followed by similar oscillations of $\mathcal{F}$ and $\mathcal{R}$ (for analytic Fourier decompositions, see Ref. [19]), with the mean values

$$\mathcal{F}_{\mathrm{diff}} = 1/3 \quad \text{and} \quad \mathcal{R}_{\mathrm{diff}} = 1/15, \tag{12}$$

provided the disk is undoped or the doping is adjusted to any higher LL. These are the basic features of a nonstandard quantum interference phenomenon, which may appear when charge transport in graphene (or other Dirac system) is primarily carried by evanescent modes [22].

3. Results and discussion

Several factors, not taken into account in the above analysis, may make it difficult to confirm experimentally the effects which are described in Refs. [11,12]. These include the influence of disorder, electron-phonon coupling or electron-electron interactions, i.e. the factors which are absent (or suppressed) in several analogues of graphene [23–25], and which are beyond the scope of this paper. Another potential obstacle is related to the fact that resonances with distinct LLs shrink rapidly with increasing field, making the linear-response regime hard to access. Here, we point out that theoretical discussion of charge transport through graphene-based Corbino disk still can be carried out, in a rigorous manner, beyond the linear-response regime.

For the purpose of numerical demonstration, we choose $R_\mathrm{o}/R_\mathrm{i} = 5$, and focus on the vicinity of the Dirac point by setting $\mu_0 = 0$ (We notice that this supposition does not affect the universality of the results. For any $eV_{\mathrm{eff}} > 2|\mu_0|$, in the high-field limit, the leading contributions to averages in Equations (5) and (6) originate from a small vicinity of the Dirac point. The same reasoning applies to higher LLs). The corresponding oscillation magnitudes, in the linear-response limit, are [19]

$$\Delta G(V_{\mathrm{eff}} \to 0) = 0.11\, G_{\mathrm{diff}}, \qquad \Delta\mathcal{F}(V_{\mathrm{eff}} \to 0) = 0.27, \quad \Delta\mathcal{R}(V_{\mathrm{eff}} \to 0) = 0.14. \tag{13}$$

For any finite V_{eff} and any flux Φ, the averages in Equations (4), (5) and (6) can be calculated numerically after substituting $T_j(\epsilon)$ given by Equation (7). Our main results are presented in Figures 1–3.

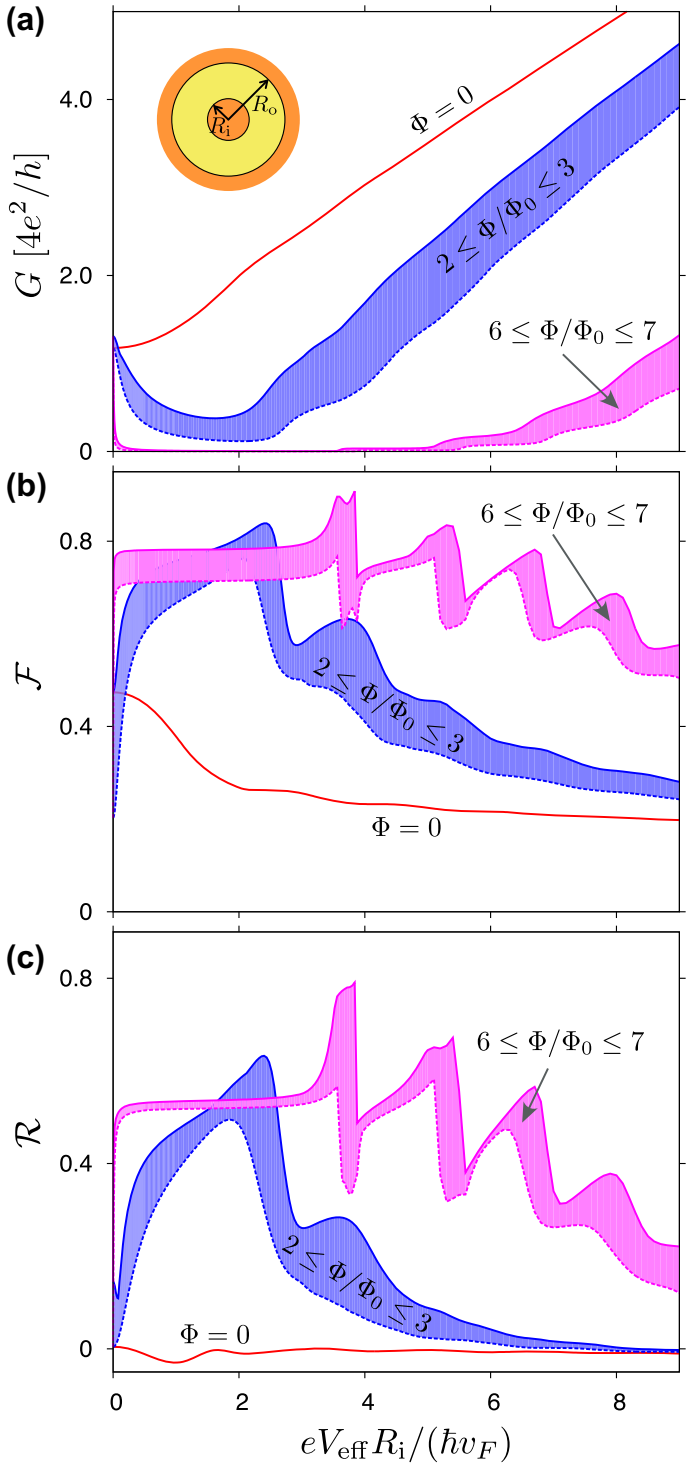

Figure 1. (colour online) Variation ranges for the finite-voltage conductance (a), Fano factor (b), and $\mathcal{R}$-factor (c) in cases the magnetic flux Φ piercing the disk area $R_\mathrm{i} < r < R_\mathrm{o}$ [see inset in panel (a)] is varied in the limits given by Equation (14) with $m_\Phi = 3$ and $m_\Phi = 7$. The values for $\Phi = 0$ are also shown.

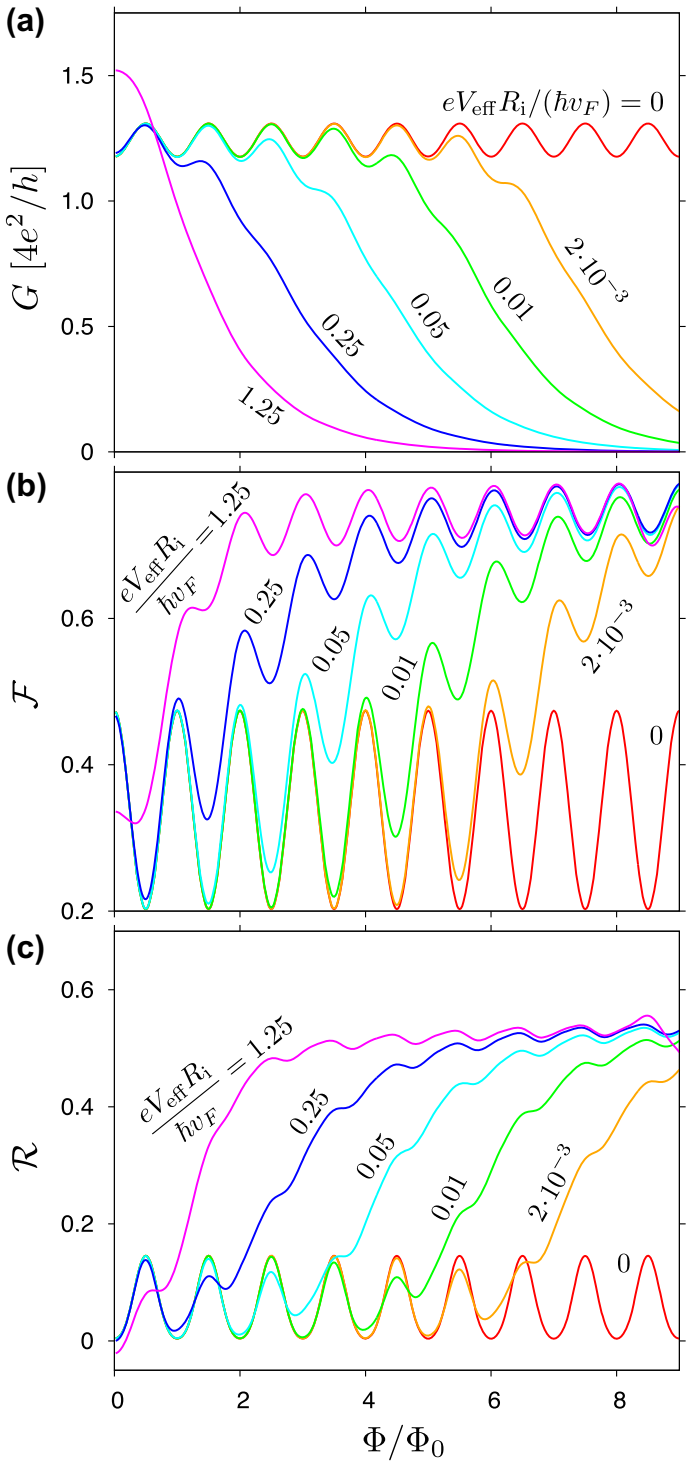

Figure 2. (colour online) Magnetic flux effect on the finite-voltage conductance (a), Fano factor (b), and $\mathcal{R}$-factor (c). The effective source–drain voltage $V_{\rm eff}$ is specified for each curve.

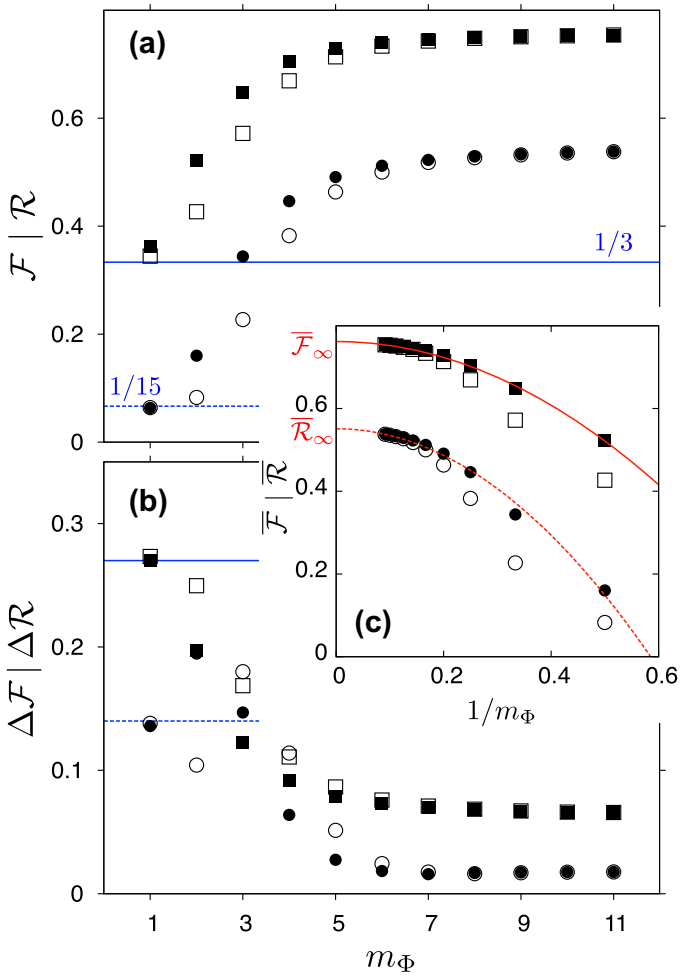

Figure 3. (colour online) Average values $\overline{X}$ (a) and oscillation magnitudes $\Delta X = \max(X) - \min(X)$ (b), with $X = \mathcal{F}$ (squares) and $X = \mathcal{R}$ (circles), calculated for several consecutive flux intervals defined by Equation (14). Open (or closed) symbols at each panel correspond to $eV_{\rm eff}R_{\rm i}/(\hbar v_F) = 0.25$ (or 0.5). Lines in panels (a) and (b) depict the linear-response values given by Equations (12) and (13). Panel (c) illustrates the scaling of $\overline{\mathcal{F}}$ and $\overline{\mathcal{R}}$ with $1/m_\Phi \to 0$ (see the main text for details).

First, in Figure 1(a)–(c), we have depicted the values taken by $G(V_{\rm eff})$, $\mathcal{F}(V_{\rm eff})$ and $\mathcal{R}(V_{\rm eff})$, when the flux is varied in separate intervals, each of which having Φ_0 width, namely,

$$(m_\Phi - 1)\,\Phi_0 \le \Phi \le m_\Phi \Phi_0, \quad m_\Phi = 1, 2, \ldots. \tag{14}$$

The two shaded areas are for $m_\Phi = 3$ and $m_\Phi = 7$; distinct solid line (at each panel) depicts the corresponding charge-transfer characteristic at $\Phi = 0$. It is clear from Figure 1 that $G(V_{\rm eff})$ is strongly suppresed by the magnetic field provided that $eV_{\rm eff} \lesssim \hbar v_F/R_{\rm i}$. For higher $V_{\rm eff}$, the ballistic transport regime is entered, leading to $G(V_{\rm eff}) \propto V_{\rm eff}$, $\mathcal{F}(V_{\rm eff}) \lesssim 0.2$ and $\mathcal{R}(V_{\rm eff}) \simeq 0$ in the $eV_{\rm eff} \gg \hbar v_F/R_{\rm i}$ limit. Most remarkably, for $0 < eV_{\rm eff} \lesssim \hbar v_F/R_{\rm i}$ and the highest discussed flux interval ($m_\Phi = 7$), $\mathcal{F}(V_{\rm eff})$ and $\mathcal{R}(V_{\rm eff})$ take the values from narrow ranges around $\mathcal{F} \simeq 0.7$ and $\mathcal{R} \simeq 0.5$ [see Figure 1(b) and (c)], coinciding with recent findings for transport near LLs in graphene bilayer [26].

These observations are further supported with the data presented in Figure 2, where the conductance and other charge-transfer characteristics are plotted directly as functions

Table 1. Limiting values of period-averaged $\overline{\mathcal{F}}$, $\overline{\mathcal{R}}$ and oscillation magnitudes $\Delta\mathcal{F}$, $\Delta\mathcal{R}$ obtained by least-squares fitting of the parameters in Equation (15). Numbers in parentheses are standard deviations for the last digit (see also Ref. (We have fixed the voltage at $eV_{\rm eff}R_{\rm i}/(\hbar v_F) = 0.5$ for the data presented. No statistically signifficant effects were detected for other $V_{\rm eff}$-s in the $1/m_\Phi \to 0$ limit.)).

$R_{\rm o}/R_{\rm i}$	$\overline{\mathcal{F}}_\infty$	$\Delta\mathcal{F}_\infty$	$\overline{\mathcal{R}}_\infty$	$\Delta\mathcal{R}_\infty$
2.5	0.761(1)	0.0014(1)	0.552(3)	0.0064(2)
5.0	0.763(1)	0.061(1)	0.555(2)	0.017(1)
10	0.771(5)	0.191(2)	0.56(1)	0.170(2)

of Φ, for selected values of $V_{\rm eff}$. Although $G(V_{\rm eff})$ decays relatively fast with Φ for any $V_{\rm eff} \neq 0$, such that magnetoconductance oscillations are visible for $eV_{\rm eff} \ll \hbar v_F/R_{\rm i}$ only [see Figure 2(a)], $\mathcal{F}(V_{\rm eff})$ and $\mathcal{R}(V_{\rm eff})$ show periodic oscillations at high fields for arbitrary $V_{\rm eff}$ [see Figure 2(b) and (c)]. In order to describe these oscillations in a quantitative manner, we have calculated numerically the average values of $\mathcal{F}(V_{\rm eff})$ and $\mathcal{R}(V_{\rm eff})$, as well as the corresponding oscillation magnitudes, for several consecutive flux intervals defined by Equation (14), and depicted them as functions of the interval number (m_Φ) in Figure 3(a) and (b). Next, the scaling with $1/m_\Phi \to 0$ is performed by least-squares fitting of the approximating formula

$$Y\,[m_\Phi] \simeq Y_\infty + A_Y \left(\frac{1}{m_\Phi}\right)^2, \tag{15}$$

for $Y = \overline{\mathcal{F}}$, $\overline{\mathcal{R}}$, $\Delta\mathcal{F}$, and $\Delta\mathcal{R}$. The examples of $\overline{\mathcal{F}}[m_\Phi]$ and $\overline{\mathcal{R}}[m_\Phi]$ are presented in Figure 3(a); the values of Y_∞ for different ratios $R_{\rm o}/R_{\rm i}$ are listed in Table 1 (We have fixed the voltage at $eV_{\rm eff}R_{\rm i}/(\hbar v_F) = 0.5$ for the data presented. No statistically signifficant effects were detected for other $V_{\rm eff}$-s in the $1/m_\Phi \to 0$ limit.).

A striking feature of the results presented in Table 1 is the total lack of effects of both the radii ratio $R_{\rm o}/R_{\rm i}$ and the source–drain voltage $V_{\rm eff}$ on limiting values of $\overline{\mathcal{F}}_\infty$ and $\overline{\mathcal{R}}_\infty$. (In contrast, $\Delta\mathcal{F}_\infty$ and $\Delta\mathcal{R}_\infty$ strongly depends on $R_{\rm o}/R_{\rm i}$.) This fact allows us to expect the quantum-limited shot noise, characterized by

$$\overline{\mathcal{F}}_\infty \simeq 0.76 \quad \text{and} \quad \overline{\mathcal{R}}_\infty \simeq 0.55, \tag{16}$$

to appear generically in graphene-based nanosystems at high magnetic fields and for finite source–drain voltages, similarly as pseudo-diffusive shot noise (with $\mathcal{F}_{\rm diff} = 1/3$ and $\mathcal{R}_{\rm diff} = 1/15$) appears generically at the Dirac point in the linear-response limit.

4. Conclusions

We have investigated the finite-voltage effects on the magnetoconductance, as well as the magnetic field dependence of the shot-noise power and the third charge-transfer cumulant, for the Corbino disk in ballistic graphene. Periodic magnetoconductance oscillations, earlier discussed theoretically in the linear-response limit [11,12], are found to decay rapidly with increasing field at finite voltages. To the contrary, the $\mathcal{F}$ and $\mathcal{R}$-factors, quantifying the higher charge-transfer cumulants, show periodic oscillations for arbitrary high fields, for

both the linear-response limit and the finite-voltage case. Although such oscillations must be regarded as signatures of a nonstandard quantum interference phenomena, specific for graphene-based disks near zero doping (and having counterparts for higher Landau levels), the parameter-independent mean values of $\overline{\mathcal{F}}_\infty \simeq 0.76$ and $\overline{\mathcal{R}}_\infty \simeq 0.55$ suggest the existence of a generic, finite-voltage and high-field analogue of a familiar pseudo-diffusive charge-transport regime in ballistic graphene.

We hope our findings will motivate some experimental attempts to understand the peculiar nature of quantum transport via evanescent waves in graphene, which manifests itself not only in the well-elaborated multimode case of wide rectangular samples [16–18], but also when a very limited number of normal modes contribute to the system conductance and other charge-transfer characteristics, as in the case of Corbino disks with large radii ratios $R_o/R_i \gg 1$. Albeit the discussion is, in principle, limited to the system with a perfect circular symmetry and the uniform magnetic field, special features of the results, in particular, the fact that mean values of the $\mathcal{F}$ and $\mathcal{R}$-factors are insensitive to the radii ratio and to the voltage, allow us to believe that quantum-limited shot noise as well as the signatures of quantum interference should appear in more general situations as well.

Funding

The work was supported by the National Science Centre of Poland (NCN) via [grant number N–N202–031440] and partly by Foundation for Polish Science (FNP) under the program TEAM. The computations were partly performed using the PL-Grid infrastructure.

References

[1] L. Boltzmann, Phil. Mag. 22 (1886) p.226.
[2] E.P. Adams, Proc. Am. Phil. Soc. 54 (1915) p.47.
[3] For a comprehensive review of early-stage researches, see: S. Galdamini and G. Giuliani, Ann. Sci. 48 (1991) p.21.
[4] G. Kirczenow, J. Phys.: Condens. Matter. 6 (1994) p.L583; S. Souma and A. Suzuki, Phys. Rev. B 58 (1998) p.4649.
[5] R.G. Mani, Europhys. Lett. 36 (1996) p.203.
[6] S.F.W.R. Rycroft, R.A. Doyle, D.T. Fuchs, E. Zeldov, R.J. Drost, P.H. Kes, T. Tamegai, S. Ooi, and D.T. Foord, Phys. Rev. B 60 (1999) p.757(R).
[7] J. Yan and M.S. Fuhrer, Nano Lett. 10 (2010) p.4521.
[8] C. Faugeras, B. Faugeras, M. Orlita, M. Potemski, R.R. Nair, and A.K. Geim. ACS Nano 4 (2010) p.1889.
[9] Y. Zhao, P. Cadden-Zimansky, F. Ghahari, and P. Kim. Phys. Rev. Lett. 108 (2012) p.106804.
[10] E.C. Peters, A.J.M. Giesbers, M. Burghard, and K. Kern. Appl. Phys. Lett. 104 (2014) p.203109.
[11] A. Rycerz. Phys. Rev. B 81 (2010) p.121404(R).
[12] M.I. Katsnelson, Europhys. Lett. 89 (2010) p.17001.
[13] M.I. Katsnelson, *Graphene: Carbon in Two Dimensions*, Cambridge University Press, Cambridge, 2012, Ch 3.
[14] Z. Khatibi, H. Rostami and R. Asgari, Phys. Rev. B 88 (2013) p.195426.
[15] L. Villegas-Lelovsky, J.L.H. Correa and F. Qu, Phys. Stat. Sol. (b) 251 (2014) p.1451
[16] J. Tworzydło, B. Trauzettel, M. Titov, A. Rycerz, and C.W.J. Beenakker. Phys. Rev. Lett. 96 (2006) p.246802.
[17] E. Prada, P. San-Jose, B. Wunsch, and F. Guinea. Phys. Rev. B 75 (2007) p.113407.
[18] A. Rycerz, P. Recher and M. Wimmer, Phys. Rev. B 80 (2009) p.125417.
[19] A. Rycerz, Acta Phys. Polon. A 121 (2012) p.1242.

[20] Y.u.V. Nazarov and Y.a.M. Blanter, *Quantum Transport: Introduction to Nanoscience*, Cambridge University Press, Cambridge, 2009.
[21] M. Abramowitz and I.A. Stegun (eds.), *Handbook of Mathematical Functions*, Dover Publications, New York, 1965, Ch 13.
[22] E.B. Kolomeisky, H. Zaidi and J.P. Straley, Phys. Rev. B 85 (2012) p.073404.
[23] A. Singha, M. Gibertini, B. Karmakar, S. Yuan, M. Polin, G. Vignale, M.I. Katsnelson, A. Pinczuk, L.N. Pfeiffer, K.W. West, and V. Pellegrini. Science 332 (2011) p.1176.
[24] Z.K. Liu, B. Zhou, Y. Zhang, Z.J. Wang, H.M. Weng, D. Prabhakaran, S.-K. Mo, Z.X. Shen, Z. Fang, X. Dai, Z. Hussain, and Y.L. Chen, Science 343 (2014) p.864.
[25] S. Borisenko, Q. Gibson, D. Evtushinsky, V. Zabolotnyy, B. Büchner, and R.J. Cava. Phys. Rev. Lett. 113 (2014) p.027603.
[26] G. Rut and A. Rycerz, Phys. Rev. B 89 (2014) p.045421.

Trigonal warping, pseudodiffusive transport, and finite-system version of the Lifshitz transition in magnetoconductance of bilayer-graphene Corbino disks

Grzegorz Rut and Adam Rycerz
Marian Smoluchowski Institute of Physics, Jagiellonian University, Łojasiewicza 11, PL–30348 Kraków, Poland
(Dated: January 21, 2015)

Using the transfer matrix in the angular-momentum space we investigate the impact of trigonal warping on magnetotransport and scaling properties of a ballistic bilayer graphene in the Corbino geometry. Although the conductivity at the charge-neutrality point and zero magnetic field exhibits a one-parameter scaling, the shot-noise characteristics, quantified by the Fano factor $\mathcal{F}$ and the third charge-transfer cumulant $\mathcal{R}$, remain pseudodiffusive. This shows that the pseudodiffusive transport regime in bilayer graphene is not related to the universal value of the conductivity but can be identified by higher charge-transfer cumulants. For Corbino disks with larger radii ratios the conductivity is suppressed by the trigonal warping, mainly because the symmetry reduction amplifies backscattering for normal modes corresponding to angular-momentum eigenvalues $\pm 2\hbar$. Weak magnetic fields enhance the conductivity, reaching the maximal value near the crossover field $B_L = \frac{4}{3}\sqrt{3}\,(\hbar/e)\,t' t_\perp \left[t_0^2 a (R_\mathrm{o} - R_\mathrm{i})\right]^{-1}$, where t_0 ($t_\perp$) is the nearest-neighbor intra- (inter-) layer hopping integral, t' is the skew-interlayer hopping integral, and R_o (R_i) is the outer (inner) disk radius. For magnetic fields $B \gtrsim B_L$ we observe quasiperiodic conductance oscillations characterized by the decreasing mean value $\langle\sigma\rangle - \sigma_0 \propto B_L/B$, where $\sigma_0 = (8/\pi)\,e^2/h$. The conductivity, as well as higher charge-transfer cumulants, show beating patterns with an envelope period proportional to $\sqrt{B/B_L}$. This constitutes a qualitative difference between the high-field ($B \gg B_L$) magnetotransport in the $t' = 0$ case (earlier discussed in Ref. [1]) and in the $t' \neq 0$ case, providing a finite-system analog of the Lifshitz transition.

PACS numbers: 72.80.Vp, 73.43.Qt, 73.63.-b

I. INTRODUCTION

Bilayer graphene (BLG) rises as a top-tier candidate material for the upcoming carbon-based electronics [2–4] either due to a tunable band gap [5] or due to topologically-protected quantum channels along domain walls [6–8], recently proposed to host nonlocal Einstein-Podolsky-Rosen pairs [9]. Low-energy physics of BLG is mainly governed by microscopic parameters describing the coupling between the two layers [5], some of which are still far from being precisely determined.

In the most common Bernal stacking, the leading tight-binding parameters: the intralayer hopping integral between nearest neighbors $t_0 = 3.16\,\mathrm{eV}$, and the nearest neighbor interlayer hopping integral $t_\perp = 0.38\,\mathrm{eV}$, are both link to the basic BLG band-structure characteristics, which are the Fermi velocity

$$v_F = \frac{\sqrt{3}\,t_0 a}{2\hbar} \approx 10^6\,\mathrm{m/s} \tag{1}$$

and the electron effective mass

$$m_\mathrm{eff} = \frac{t_\perp}{2 v_F^2} \approx 0.033\,m_e, \tag{2}$$

where $a = 0.246\,\mathrm{nm}$ is the lattice constant in a single layer and m_e is the free electron mass. For the next-nearest neighbor (or *skew*) interlayer hopping integral t', the corresponding characteristic is the Lifshitz energy

$$E_L = \frac{1}{4}\,t_\perp \left(t'/t_0\right)^2, \tag{3}$$

which can be defined as a value of the electrochemical potential below which the Fermi surface splits into a four-element manifold. E_L is difficult to be directly determined in the experiment; values of t' obtained from the infrared spectroscopy covers the range from $0.10\,\mathrm{eV}$ [10] up to $0.38\,\mathrm{eV}$ [11].

On the other hand, in BLG even a tiny band structure modification near the Dirac point due to $t' \neq 0$ may have a significant impact on the minimal conductivity [12]. For $t' = 0$, both the mode-matching analysis [13] and the Kubo formalism [14] lead to

$$\sigma_0 = 2\sigma_\mathrm{MLG} = \frac{8e^2}{\pi h}, \tag{4}$$

where σ_MLG denotes the universal conductivity of a monolayer [15–17]. For $t' \neq 0$, similar theoretical considerations show the conductivity $\sigma(L)$ is no longer universal but size-dependent, and monotonically grows with the system size L. Depending on the crystallographic orientation of a sample, the conductivity approaches $(7/3)\,\sigma_0 \leqslant \sigma(\infty) \leqslant 3\,\sigma_0$ [18]. The transport anisotropy appears as the secondary Dirac cones, present for $t' \neq 0$, break the rotational invariance of the dispersion relation [19]. In principle, the experimental study of $\sigma(L)$ for clean bilayer samples should be sufficient to determine t' [20], also in the presence of small interaction-induced energy gap [21–23]. (For instance, the value of $\sigma \approx 2.5\,\sigma_0$ reported by Mayorov *et al.* [24] coincides with the above-mentioned large-L predictions.) Unfortunately, device-to-device conductance fluctuations in real disordered systems may put the effectiveness of such a procedure in question. For this reason, new phenomena,

unveiling the influence of t' on transport characteristics which can be measured in a single-device setup, are desired.

In this paper, we consider the Corbino geometry, in which a disk-shaped sample is surrounded from both interior and exterior sides with metallic leads [see Fig. 1(a)]. Such a choice is motivated by the absence of boundary effects, and irrelevance of the sample crystallographic orientation. It is worth to stress that anisotropic aspects of quantum transport are still present in such a system as the rotational symmetry is intrinsically broken due to trigonal warping. In effect, the total angular momentum is not conserved, and the standard mode-matching method cannot be applied as in simpler systems studied earlier (namely, the monolayer disk [25, 26] and the BLG disk with $t' = 0$ [1]). Here, we overcome this difficulty by developing a numerical transfer-matrix approach in the angular momentum space. Contrary to real-space discretization applied in some related works [27–29], our approach takes benefit from the sparsity of transfer matrix in such a representation allowing highly-efficient (albeit conceptually simple) transport calculations for physical disk diameters exceeding $10\,\mu$m. Recently developed linear-scaling approach employing the time evolution scheme [30] seems to be a possible counterpart but its efficient adaptation for calculating higher charge-transfer cumulants might be difficult.

The paper is organized as follows. In Sec. II we present details of the system considered, the effective Dirac equation for low-energy excitations, and provide a description of our numerical procedure. Sec. III focuses on the size dependence of the conductivity σ, the Fano factor $\mathcal{F}$, and the third charge-transfer cumulant for BLG Corbino disk at zero magnetic field. In Sec. IV, the effects of perpendicular magnetic field on the above-mentioned transport characteristics are discussed. Also in Sec. IV, the numerical results for the disk are compared with analytical ones, obtained for an artificial system [a rectangular device with periodic boundary conditions, see Fig. 1(b)], for which the mode-matching analysis is possible, and the universal magnetoconductance characteristics, relevant for large system sizes and high magnetic fields, are identified. The conclusions are given in Sec. V.

II. THE MODEL AND THE NUMERICAL APPROACH

A. Effective Dirac equation

The Corbino disk in Bernal-stacked BLG is depicted schematically in Fig. 1(a). We start our analysis from the four-band low-energy Hamiltonian for K valley [5],

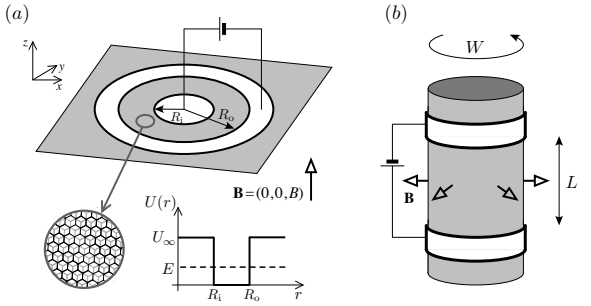

FIG. 1: Systems discussed in the paper (schematic). (a) The Corbino disk in Bernal-stacked bilayer graphene. The current flows through the disk-shaped area with the inner radius R_i and the outer radius R_o in a perpendicular magnetic field $\mathbf{B} = (0, 0, B)$. The coordinate system and the electrostatic potential $U(r)$ (with $r = \sqrt{x^2 + y^2}$) are also shown. The leads (white areas) are modeled as infinitely-doped graphene regions ($|U_\infty| \to \infty$). (b) An artificial (nanotube-like) system formed of a BLG strip of the width W, contacted by two electrodes at a distance L in uniform field B, upon applying periodic boundary conditions.

which is given by

$$H = \begin{pmatrix} 0 & \pi & t_\perp & 0 \\ \pi^\dagger & 0 & 0 & \nu\pi \\ t_\perp & 0 & 0 & \pi^\dagger \\ 0 & \nu\pi^\dagger & \pi & 0 \end{pmatrix} + U(r), \tag{5}$$

where $\pi = v_F\,(p_x + ip_y) = -i\hbar v_F e^{i\varphi}\left(\partial_r + i\frac{\partial_\varphi}{r} - \frac{eB}{2\hbar}r\right)$, with the gauge-invariant momenta $p_j = (-i\hbar\partial_j + eA_j)$ $(j = 1, 2)$ and the symmetric gauge $(A_x, A_y) = (B/2)(-y, x)$ corresponding to the uniform magnetic field parallel to z-axis. We have further defined the dimensionless parameter $\nu = t'/t_0$, and introduced the polar coordinates (r, φ). The potential energy $U(r)$ depends only on $r = \sqrt{x^2 + y^2}$, and the remaining symbols are the same as in Eqs. (1–3). As mentioned earlier, the available values of t' following from different experimental [10, 11, 31] and computational [32] approaches are far from being consistent. Magnetotransport through BLG disk with $t' = 0$ were discussed in analytical terms in Ref. [1]. In this paper we take the values of t' varying from 0.1 eV up to 0.3 eV in order to investigate numerically how it affects the system behavior.

For the disk area, $R_\mathrm{i} < r < R_\mathrm{o}$, we set $U(r) = 0$ and the effective Dirac equation $H\psi = E\psi$ (with E the Fermi energy) can be written as

$$\begin{pmatrix} \epsilon & -f & -it & 0 \\ -f^* & \epsilon & 0 & -\nu f \\ -it & 0 & \epsilon & -f^* \\ 0 & -\nu f^* & -f & \epsilon \end{pmatrix} \psi\,(r, \phi) = 0, \tag{6}$$

where $t = t_\perp/(\hbar v_F) \equiv l_\perp^{-1}$, $f = e^{i\varphi}\left(\partial_r + i\frac{\partial_\varphi}{r} - \frac{1}{2l_B^2}r\right)$, $\epsilon = E/(\hbar v_F)$, and the magnetic length $l_B = \sqrt{\hbar/(e|B|)}$.

In the absence of trigonal warping ($\nu = 0$) the system possesses a cylindrical symmetry and the effective Hamiltonian (5) commutes with the total angular momentum operator [33]

$$J_z = -i\hbar\partial_\varphi + \frac{\hbar}{2}\begin{pmatrix} \sigma_0 & 0 \\ 0 & -\sigma_0 \end{pmatrix} + \frac{\hbar}{2}\begin{pmatrix} -\sigma_z & 0 \\ 0 & \sigma_z \end{pmatrix}, \quad (7)$$

where σ_0 is the 2×2 identity matrix, and σ_z is one of the Pauli matrices. In such a case, the wavefunctions are products of angular and radial parts $\phi^m(r,\varphi) = e^{im\varphi}\left[\phi_1^m, e^{-i\varphi}\phi_2^m, \phi_3^m, e^{i\varphi}\phi_4^m\right]^T(r)$ with m being an integer angular-momentum quantum number.

B. Outline of the approach

In the presence of trigonal warping ($\nu \neq 0$) the cylindrical symmetry is broken, and the wavefunctions do not correspond directly to eigenstates of J_z. A generic workaround has been developed for systems with symmetry-breaking potentials (or impurities), where one can still express wavefunctions as linear combinations of eigenfunctions of an ideal system [34–36]. Souma and Suzuki [35] considered quantum transport through Corbino disks in two-dimensional electron gas and showed that the effects of impurities can be studied numerically, starting from truncated wavefunctions in the basis of angular-momentum eigenstates. Here we adapt this method for BLG Corbino disk, as the term proportional to ν in the Hamiltonian (5) can be regarded as a peculiar type of a symmetry-breaking potential.

A general solution of the Dirac equation (6) can be written as an infinite linear combination of angular momentum eigenfunctions, namely

$$\psi(r,\phi) = \sum_m a_m \phi^m(r,\varphi), \quad (8)$$

with arbitrary amplitudes a_m, $m = 0, \pm1, \pm2, \ldots$. Multiplying the Dirac equation (6) by the factor $e^{-il\varphi}$ (with l an arbitrary integer) and integrating over the polar angle φ, we obtain the system of equations

$$\begin{aligned}
\partial_r\phi_1^l &= -g(l,r)\,\phi_1^l + i\epsilon\phi_2^l + i\nu t\phi_1^{l-3} \\
&\quad -i\nu\epsilon\phi_3^{l-3} + 2\nu g(l-2,r)\,\phi_4^{l-3}, \\
\partial_r\phi_2^l &= i\epsilon\phi_1^l + g(l-1,r)\,\phi_2^l - it\phi_3^l, \\
\partial_r\phi_3^l &= g(l,r)\,\phi_3^l + i\epsilon\phi_4^l + i\nu t\phi_3^{l+3} \\
&\quad -i\nu\epsilon\phi_1^{l+3} - 2\nu g(l+2,r)\,\phi_2^{l+3}, \\
\partial_r\phi_4^l &= -it\phi_1^l + i\epsilon\phi_3^l - g(l+1,r)\,\phi_4^l, \quad (9)
\end{aligned}$$

where

$$g(l,r) = \frac{l}{r} + \frac{r}{2l_B^2}. \quad (10)$$

Notice that the terms proportional to ν correspond to the mode mixing due to trigonal warping. The D_{3d} dihedral symmetry of these terms (coinciding with the BLG lattice symmetry) results in the fact that equation for ϕ^l is coupled only to ϕ^{l-3} and ϕ^{l+3}, which tremendously simplifies the numerical integration.

Eqs. (9) and (10), along with the mode-matching conditions for $r = R_\mathrm{i}$ and $r = R_\mathrm{o}$ (we model the leads as heavily-doped BLG areas), allows us to construct a transfer matrix (see Appendix A for details) which can be utilized in the Landauer-Büttiker formalism in order to calculate the conductivity and other charge-transfer characteristics. Typically, the convergence is reached for the wavefunction truncated by taking $|l| \lesssim M$ in Eq. (9), with $M = 25 - 500$ depending on the system size, the strength of the trigonal warping, and the applied field (with the upper value corresponding to $R_\mathrm{o} \approx 5\,\mu$m, $t' = 0.3\,$eV, and $B \approx 80\,$T). Other computational aspects are also described in Appendix A.

III. QUANTUM TRANSPORT DEPENDENCE ON THE SYSTEM SIZE

A. One-parameter scaling

A particularly intriguing property, arising from the earlier theoretical study of ballistic transport in BLG with skew interlayer hoppings ($t' \neq 0$), is the one-parameter scaling [23]. In the absence of disorder and electron-electron interactions the scaling function

$$\beta(\sigma) = \frac{d\ln\sigma}{d\ln L}, \quad (11)$$

which plays a central role in conceptual understanding of the metal insulator transition [37], reproduces the scenario predicted for disordered Dirac systems with Coulomb interaction [38]. Here, the discussion is complemented by calculating the Fano factor $\mathcal{F}$ quantifying the shot-noise power, and the factor $\mathcal{R}$ quantifying the third charge transfer cumulant.

Employing the Landauer-Büttiker formula for the linear-response regime one can write [39]

$$\sigma = g_0\Theta_\alpha \mathrm{Tr}\,\mathbf{T}, \quad (12)$$

$$\mathcal{F} = \frac{\mathrm{Tr}\left[\,\mathbf{T}(\mathbf{1}-\mathbf{T})\,\right]}{\mathrm{Tr}\,\mathbf{T}}, \quad (13)$$

$$\mathcal{R} = \frac{\mathrm{Tr}\left[\,\mathbf{T}(\mathbf{1}-\mathbf{T})(\mathbf{1}-2\mathbf{T})\,\right]}{\mathrm{Tr}\,\mathbf{T}}, \quad (14)$$

where $g_0 = 4e^2/h$ is the conductance quantum (with the factor 4 following from the spin and valley degeneracies), the dimensionless prefactor (Θ_α) in Eq. (12) is equal to $\Theta_\mathrm{Cor} = \ln(R_\mathrm{o}/R_\mathrm{i})/(2\pi)$ for the Corbino geometry of Fig. 1(a) or $\Theta_\mathrm{rec} = L/W$ for the rectangular geometry [40], and $\mathbf{T} = \mathbf{t}^\dagger\mathbf{t}$, with $\mathbf{t}$ the transmission matrix determined via the transfer matrix (see Appendix A). It was shown in Refs. [20] and [23] that the conductivity of ballistic BLG with $t' \neq 0$ scales with the system size. For a rectangular geometry, we still get $\sigma \approx \sigma_0$ for small systems, while

for the larger ones ($L \gtrsim 500\,\mathrm{nm}$) the conductivity can be rationalized as

$$\sigma(L) \simeq \sigma_\star \left[\, 1 - (\lambda/L)^\gamma \,\right], \tag{15}$$

with typical parameters

$$\sigma_\star \approx 3\,\sigma_0, \qquad \gamma \approx 0.5, \tag{16}$$

and λ depending both on t' and the sample orientation [23]. The approximating formula given by Eqs. (15) and (16) applies for generic crystallographic orientation of the sample. However, for some particular orientations one obtains different asymptotic behaviors, including a slower power-law convergence to $\sigma_\star$ with the exponent $\gamma \approx 0.25$ if the current is passed precisely along an armchair direction [20], or the oscillating conductivity with the lower bound of $\sigma \lesssim (7/3)\,\sigma_0$ if the current is passed precisely along a zigzag direction [18]. Such issues are absent in the Corbino geometry, allowing one to focus on the universal scaling properties of the material.

TABLE I: Least-squares fitted parameters in Eq. (15) corresponding to the lines in Fig. 2. The last column gives the values of $L_{0.01}/\ell$, such that the function given by Eq. (15) matches the actual conductivity with 1% accuracy.

t' (eV)	ℓ (nm)	$\sigma_\star\,(8e^2/h)$	λ (nm)	γ	$L_{0.01}/\ell$
0.1	352	0.97	97	0.47	6.21
0.2	176	0.97	40	0.49	5.19
0.3	117	0.98	21	0.48	4.44

TABLE II: Least-squares fitted parameters in Eq. (15) corresponding to the lines in Fig. 3. The last column is same as in Table I, but for $R_\mathrm{o}/R_\mathrm{i} = 1.5$.

t' (eV)	ℓ (nm)	$\sigma_\star\,(8e^2/h)$	λ (nm)	γ	$L_{0.01}/\ell$
0.1	352	1.01	110	0.48	4.79
0.2	176	1.00	38	0.49	4.29
0.3	117	1.02	23	0.49	3.79

In the numerical calculations presented in this section, we chose radii ratios $R_\mathrm{o}/R_\mathrm{i} = 2$ and $R_\mathrm{o}/R_\mathrm{i} = 1.5$, for which the number of nonzero transmission eigenvalues T_l is relatively large even at the charge-neutrality point, allowing one to expect some remainders of the pseudodiffusive behavior known for a monolayer [16, 40]. It is also worth to mention that such radii ratios are close to that of real Corbino device in a monolayer [41]. A multimode character of the charge transport, combined with a mode mixing due to the trigonal warping, and with a necessity to study large systems in attempt to demonstrate a one-parameter scaling, provides us with an excellent test case to investigate computational aspects of the numerical approach presented in Section IIB. (For the details, see Appendix A.)

Zero-magnetic field results are presented in Figs. 2, 3, 4, and 5. In order to present the data for different t' on a single plot, we have defined the length ℓ, related to the distance between primary and secondary Dirac points in quasimomentum space

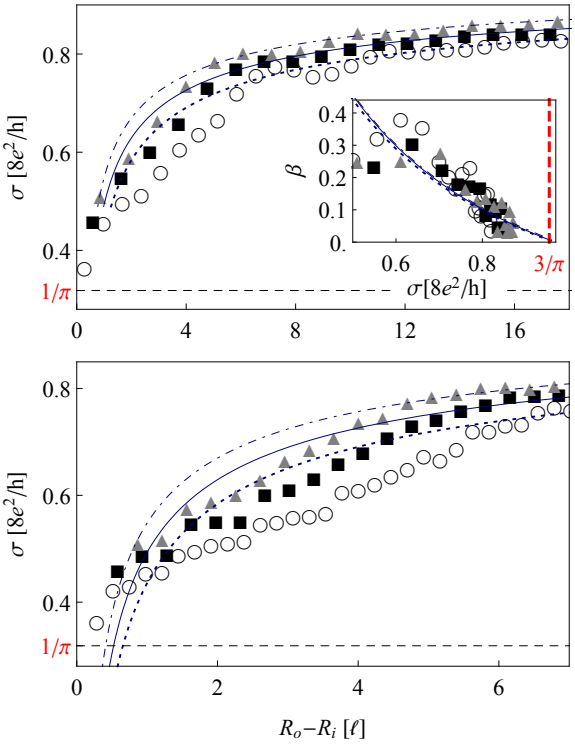

FIG. 2: Minimal conductivity of unbiased BLG Corbino disk with the radii ratio $R_\mathrm{o}/R_\mathrm{i} = 2$ as a function of the radii difference $R_\mathrm{o}-R_\mathrm{i}$, specified in the units of ℓ [see Eqs. (17,18) in the main text], for different values of t'. Triangles, squares and circles represent the data obtained numerically for $t' = 0.3\,\mathrm{eV}$, $t' = 0.2\,\mathrm{eV}$, and $t' = 0.1\,\mathrm{eV}$ (respectively), with the lines (dot-dashed, solid and dotted) depicting the approximating Eq. (15) with best-fitted parameters listed in Table I. The inset in the top panel presents the scaling function $\beta(\sigma)$ [see Eq. (11)], with $L \equiv R_\mathrm{o} - R_\mathrm{i}$, extracted numerically from $\sigma\,(R_i)$ datasets. (Notice that the best-fitted lines almost overlap each other.) The bottom panel is a zoom in, for smaller radii differences, which allows to depict the region where the actual value of the conductivity may deviate from Eq. (15). We further notice that only selected datapoints from the bottom panel are shown in the top panel for clarity.

$$\frac{2\pi}{\ell} \equiv k_\ell = \frac{\nu}{l_\perp} = \frac{2}{3}\sqrt{3}\,\frac{t' t_\perp}{t_0^2 a}, \tag{17}$$

leading to

$$\ell\, t' = 35.2\ \mathrm{nm{\cdot}eV}. \tag{18}$$

Briefly speaking, the actual conductivity reaches a close-to-asymptotic behavior, described by Eq. (15) with $L \equiv R_\mathrm{o} - R_\mathrm{i}$, for radii differences lying in a relatively narrow interval of $4 \lesssim L/\ell \lesssim 6$ (notice that varying the skew-interlayer hopping from $t' = 0.1\,\mathrm{eV}$ to $t' = 0.3\,\mathrm{eV}$ is equivalent to changing the parameter ℓ by a factor of 3

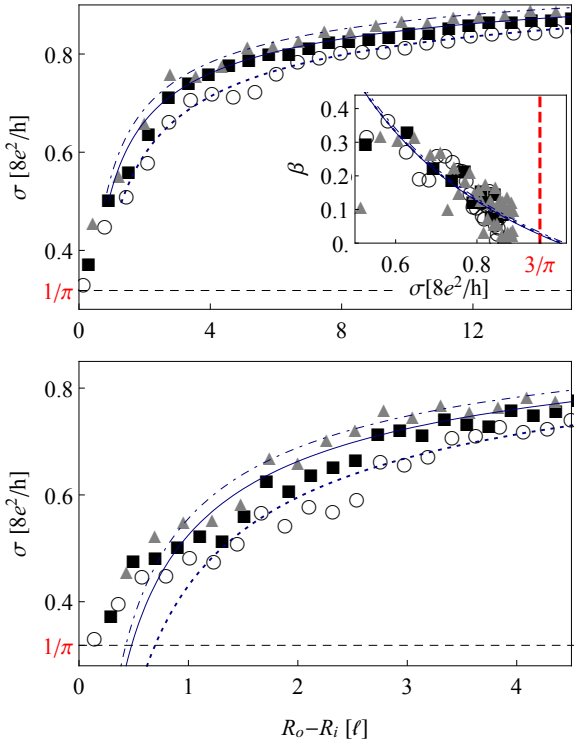

FIG. 3: Same as Fig. 2 but for the radii ratio $R_o/R_i = 1.5$. For the parameters in Eq. (15) corresponding to the lines depicted, see Table II.

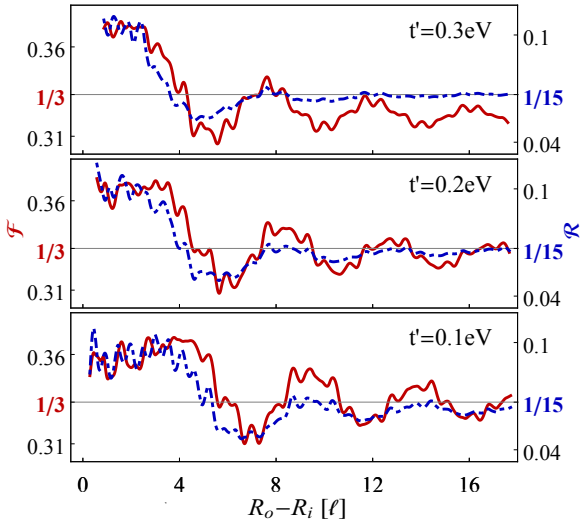

FIG. 4: The Fano factor $\mathcal{F}$ [red solid lines] and the third charge transfer cumulant $\mathcal{R}$ [blue dashed lines] for the Corbino disk with $R_o/R_i = 2$ as functions of $R_o - R_i$. Skew-interlayer hopping t' is varied between the panels. For large system size, where the Fabry-Perot oscillations become negligible, the numerical results obtained in the presence of trigonal warping approach the pseudodiffusive values of $\mathcal{F} = 1/3$ and $\mathcal{R} = 1/15$ [horizontal lines].

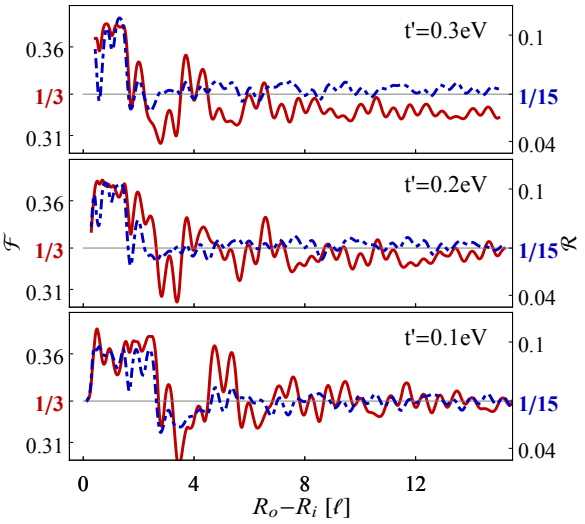

FIG. 5: Same as Fig. 4 but for $R_o/R_i = 1.5$.

between the datasets). For larger L, lines in Figs. 2 and 3, corresponding to Eq. (15) with the least-squares fitted parameters $\sigma_\star$, λ, and γ listed in Tables I and II, are closely followed by the datapoints obtained numerically for $t' = 0.1\,\mathrm{eV}$, $0.2\,\mathrm{eV}$, and $0.3\,\mathrm{eV}$. For each case, the specific value of $L_{0.01}$; i.e, the radii difference above which the approximating Eq. (15) matches the actual conductivity with an accuracy better than 1%; is also given in Table I or II. For smaller L, in particular for $L/\ell \sim 1$ [see bottom panels in Figs. 2 and 3], the conductivity becomes nonuniversal (both parameter- and geometry-dependent [42]) approaching σ_0 for $L \ll \ell$.

Although the conductivity strongly deviates from the pseudodiffusive value σ_0 (even for the lowest considered value of $t' = 0.1\,\mathrm{eV}$), the shot-noise power and the third charge-transfer cumulant are close to their pseudodiffusive values, i.e., $\mathcal{F} \approx 1/3$ and $\mathcal{R} \approx 1/15$, which are usually approached for $4 \lesssim L/\ell \lesssim 6$ (see Figs. 4 and 5).

The approximating Eq. (15) leads, via Eq. (11), to the scaling function of the form

$$\beta(\sigma) \simeq -\gamma\,(1 - \sigma_\star/\sigma)\,. \tag{19}$$

In turn, the parametres γ and $\sigma_\star$ defines the position and the slope coefficient at the attractive fixed point ($\beta(\sigma_\star) = 0$, $\beta'(\sigma_\star) > 0$) of the renormalization group flow [23]. The scaling functions $\beta(\sigma)$ [see Eq. (11)], calculated numerically for the Corbino disks with $R_o/R_i = 2$ and $R_o/R_i = 1.5$ (see insets in Figs. 2 and 3, respectively), $t' = 0.1\,\mathrm{eV}$, $0.2\,\mathrm{eV}$, and $0.3\,\mathrm{eV}$, suggest that one-parameter scaling is universal with respect to the strength of the trigonal warping. These numerical results coincide with the corresponding analysis of Ref. [23] for a rectangular sample.

B. Crossover to a quantum-tunneling regime

It was pointed out that generic MLG billiard with (at least) one narrow opening shows a crossover to the so-called *quantum-tunneling* transport regime [40], in which charge-transfer characteristics are governed by a limited number of quantum channels, with transmission probabilities showing a power-law decay with the system size. In particular, for an *undoped* Corbino disk the conductance $G = 2\pi\sigma/\ln(R_\mathrm{o}/R_\mathrm{i})$ at zero field reads

$$\frac{G_\mathrm{MLG}}{g_0} = \sum_{j=\pm\frac{1}{2},\pm\frac{3}{2},\ldots} \frac{1}{\cosh^2\left[\, j\ln(R_\mathrm{o}/R_\mathrm{i})\,\right]} \simeq \frac{8R_\mathrm{i}}{R_\mathrm{o}}, \quad (20)$$

where the asymptotic form applies for $R_\mathrm{o} \gg R_\mathrm{i}$, and represents contributions from the two channels with angular-momentum quantum numbers $j = -1/2$ and $1/2$.

For BLG billiards, the conformal mapping technique employed in Ref. [40] cannot be utilized even in the absence of trigonal warping, and the existence of a quantum-tunneling regime is not obvious. For BLG Corbino disk the conductance, for $t' = 0$ and at the charge-neutrality point, can be written as [1]

$$\frac{G_\mathrm{BLG}(t'=0)}{g_0} = \sum_m \left(T_m^+ + T_m^- \right), \quad (21)$$

$$T_m^\pm = \frac{1}{\cosh^2\left[\,(m \pm \mathcal{A})\ln\left(R_\mathrm{o}/R_\mathrm{i}\right)\right]}, \quad (22)$$

where the transmission probabilities $T_m^\pm$ (with $m = 0, \pm1, \pm2, \ldots$ being the angular-momentum quantum number) correspond to eigenvalues of the matrix $\mathbf{T} = \mathbf{t}^\dagger\mathbf{t}$ in Eqs. (12–14), and we have further defined

$$\mathcal{A} = -\frac{\ln\left(\Upsilon - \sqrt{\Upsilon^2 - 1}\right)}{2\ln\left(R_\mathrm{o}/R_\mathrm{i}\right)}, \quad (23)$$

$$\Upsilon = \cosh\left[\ln\left(\frac{R_\mathrm{o}}{R_\mathrm{i}}\right)\right] + \frac{R_\mathrm{o}^2 - R_\mathrm{i}^2}{4l_\perp^2}\sinh\left[\ln\left(\frac{R_\mathrm{o}}{R_\mathrm{i}}\right)\right]. \quad (24)$$

We focus now on the system behavior for $R_\mathrm{o} \gg R_\mathrm{i} \gg l_\perp$ [43]. In such a parameter range, Eqs. (23, 24) lead to

$$\mathcal{A} \approx \frac{3}{2} + \frac{\ln\left[\,R_\mathrm{i}/\left(2l_\perp\right)\right]}{\ln\left(R_\mathrm{o}/R_\mathrm{i}\right)}. \quad (25)$$

For any integer $\mathcal{A} = q \geqslant 2$ the conductance, analyzed as a function of $R_\mathrm{o}/R_\mathrm{i}$, reaches a local maximum with $G_\mathrm{BLG} \approx 2g_0$, following from the presence of two ballistic channels with $T_q^- = T_{-q}^+ = 1$ [see Eqs. (21) and (22)], occurring at

$$\frac{R_\mathrm{o}}{R_\mathrm{i}} \approx \left(\frac{R_\mathrm{i}}{2l_\perp}\right)^{2/(2q-3)}. \quad (26)$$

Similarly, Eq. (26) with half-odd integer $q \geqslant 5/2$ approximates a local conductance minimum (as $\mathcal{A} \approx q$) with $G_\mathrm{BLG} \approx 16g_0R_\mathrm{i}/R_\mathrm{o}$; i.e., *twice* as large as the MLG disk conductance, see Eq. (20); and four dominant channels characterized by $T_{q+1/2}^- = T_{-q-1/2}^+ \approx T_{q-1/2}^- = T_{-q+1/2}^+ \approx 4R_\mathrm{i}/R_\mathrm{o}$. In turn, a quantum-tunneling regime reappears periodically when varying $R_\mathrm{o}/R_\mathrm{i}$, near any local conductance minimum. The number of well-pronounced minima can roughly be estimated as $0.72 \times \ln[\,R_\mathrm{i}/(2l_\perp)\,]$, as for $R_\mathrm{o}/R_\mathrm{i} \lesssim 4$ the system enters a multimode pseudodiffusive transport regime. On the other hand, for $R_\mathrm{o}/R_\mathrm{i} \gtrsim R_\mathrm{i}^2/(4l_\perp^2)$, where the threshold value corresponds to the last conductance maximum following from Eq. (26) with $q = 2$, charge transport is governed by two equivalent channels, with angular momenta $\pm2\hbar$ and $T_2^- = T_{-2}^+$ monotonically decaying with increasing $R_\mathrm{o}/R_\mathrm{i}$. This suggests the system may re-enter a quantum-tunneling limit for $R_\mathrm{o}/R_\mathrm{i} \gg R_\mathrm{i}^2/(4l_\perp^2)$.

In fact, for a fixed $R_\mathrm{i} \gg l_\perp$ and $R_\mathrm{o} \to \infty$ we have $\mathcal{A} \to 3/2$, and such a limit can be regarded as an additional conductance minimum. The asymptotic form of Eq. (21) then reads

$$\frac{G_\mathrm{BLG}(t'=0)}{g_0} \simeq \frac{2R_\mathrm{i}^3}{l_\perp^2 R_\mathrm{o}} \quad (R_\mathrm{i} \gg l_\perp, R_\mathrm{o} \to \infty). \quad (27)$$

Although qualitative features of the quantum-tunneling regime for the Corbino geometry are reproduced [in particular, $G_\mathrm{BLG}(t'=0) \propto R_\mathrm{o}^{-1}$], the asymptotic conductance is elevated by a large factor of $R_\mathrm{i}^2/(4l_\perp^2)$ in comparison to the MLG disk case [44].

In Fig. 6, we compare the conductance (in the top panel) and the effective number of transmission channels (in the bottom panel)

$$N_\mathrm{ch} = \frac{G}{g_0\left(1-\mathcal{F}\right)} = \frac{\left(\sum_l T_l\right)^2}{\sum_l T_l^2}, \quad (28)$$

with the index $l \equiv (m, \pm)$ accounting for angular-momenta and layer degrees of freedom, following from Eqs. (21–24) [red lines] for $t' = 0$; as well as for the case of decoupled MLG disks ($t_\perp = t' = 0$) [blue lines]; with the numerical results obtained from Eqs. (12) and (13) for $t' = 0.1\,\mathrm{eV}$, $0.2\,\mathrm{eV}$, and $0.3\,\mathrm{eV}$ [remaining lines]. The inner radius is fixed at $R_\mathrm{i} = 15\,l_\perp$, and the outer radius is varied in the range of $1.5 < R_\mathrm{o}/R_\mathrm{i} < 80$. The effects of trigonal warping are visible for all radii ratios considered, and become particularly significant when approaching $R_\mathrm{o}/R_\mathrm{i} = R_\mathrm{i}^2/(4l_\perp^2) \approx 56$, corresponding to $\mathcal{A} \approx 2$ [following from Eq. (25)]. In such a parameter range, G systematically decreases, whereas N_ch systematically increases when enlarging t'. We also notice that Fabry-Perot resonances, corresponding to integer $k_\ell(R_\mathrm{o} - R_\mathrm{i})$, are visible for $t' \neq 0$, indicating the contribution from secondary Dirac points.

For smaller radii ratios, including $R_\mathrm{o}/R_\mathrm{i} = 7.5$ (corresponding to $\mathcal{A} \approx 5/2$) and $R_\mathrm{o}/R_\mathrm{i} = 3.83$ (corresponding to $\mathcal{A} \approx 3$) [see vertical lines in Fig. 6], the system is close to the pseudodiffusive charge-transport regime. In the $t' = 0$ case, the conductance minimum is shifted from $R_\mathrm{o}/R_\mathrm{i} = 7.5$ to $R_\mathrm{o}/R_\mathrm{i} \approx 10$ due to the influence of transmission channels with higher angular momenta.

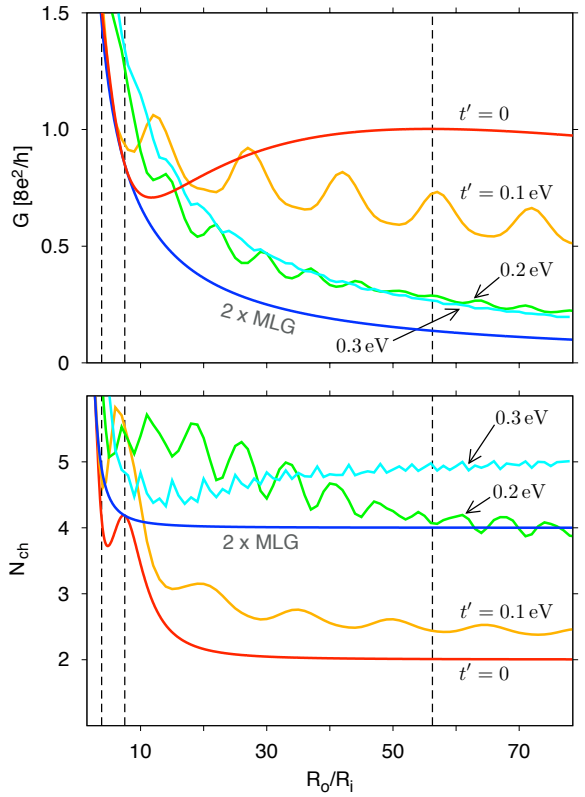

FIG. 6: Radii-ratio dependence of the conductance $G = 2\pi\sigma/\ln(R_o/R_i)$ (top panel) and the effective number of transmission channels (bottom panel) at a fixed $R_i = 15\,l_\perp \approx 24\,\mathrm{nm}$ and varying t' (specified for each line). Vertical lines mark the values of $\mathcal{A} \approx 3$ (left), $\mathcal{A} \approx 5/2$ (middle), and $\mathcal{A} \approx 2$ (right) following from Eq. (25). The corresponding results for two decoupled MLG disks ($t_\perp = t' = 0$) are also shown.

(We further notice that the effective number of channels has a local maximum $N_{\mathrm{ch}} \approx 4.2$ at $R_o/R_i \approx 7.5$, where it also precisely matches the value for two decoupled MLG disks, in good agreement with predictions for a quantum-tunneling regime reported earlier in this subsection.) The trigonal warping noticeably enhances the conductance for $R_o/R_i \lesssim 10$; i.e., the effect is opposite then for larger R_o/R_i; with some exception for the smallest considered $t' = 0.1\,\mathrm{eV}$ and $R_o/R_i \lesssim 7$, as the disk diameter $2R_o \lesssim \ell$ in such a case.

The evolution of G and N_{ch} with the trigonal warping strength, illustrated in Fig. 6, clearly shows that the role of two transmission channels with angular momenta $\pm 2\hbar$, prominent for $t' = 0$ and large R_o/R_i, is strongly suppressed for $t' \neq 0$, indicating the gradual crossover to a quantum tunneling regime characterized by $G \propto R_o^{-1}$. We attribute it to the fact that a d-wave symmetry of normal modes in leads with $m = \pm 2$ does not match the D_{3d} dihedral symmetry of the low-energy Hamiltonian for $t' \neq 0$. Moreover, for the two largest considered values of $t' = 0.2\,\mathrm{eV}$ and $0.3\,\mathrm{eV}$, both G and N_{ch} are noticeably amplified in comparison to the relevant characteristics for two decoupled MLG disks, signalling the role of quantum states close to the secondary Dirac points is important when the crossover to a quantum-tunneling regime occurs.

IV. MAGNETOTRANSPORT CHARACTERISTICS

A. Analytically soluble disk-shaped systems

Our discussion of the magnetotransport characteristics starts from pointing out that the influence of a uniform magnetic field B [45] on analytical results given by Eqs. (20) and (21) can be expressed in a very compact form: Namely, it is sufficient to replace j and m in arguments of hyperbolic cosine by [1, 25, 26]

$$\overline{j} = j + \frac{\Phi_D}{\Phi_0} \quad \text{and} \quad \overline{m} = m + \frac{\Phi_D}{\Phi_0}, \tag{29}$$

with

$$\Phi_D = \pi B(R_o^2 - R_i^2) \tag{30}$$

$$\text{and} \quad \Phi_0 = \frac{2h}{e}\ln(R_o/R_i), \tag{31}$$

denoting the flux piercing the disk area (Φ_D) and the basic period of magnetoconductance oscillations (Φ_0).

All the considered charge-transfer characteristics σ (12), $\mathcal{F}$ (13), and $\mathcal{R}$ (14), are predicted theoretically to show periodic oscillations with the magnetic flux Φ_D [see Eq. (30)] piercing a graphene-based Corbino disk [1, 25, 26, 46], provided the Fermi energy corresponds to the Dirac point or to any other Landau level (LL). The oscillations appear due to a limited number of transmission channels for $R_o \gg R_i$, and show a formal analogy with similar effects discussed for a nanotube in a magnetic field applied along the axis [47]. One should notice, however, that the oscillation period Φ_0 [see Eq. (31)] for a disk in a uniform, perpendicular field, corresponds to a physical field of 18 mT for a typical 1 μm disk ($R_o = 5R_i = 500\,\mathrm{nm}$), while for a 1 nm diameter nanotube in axial field the period, given by the standard Aharonov-Bohm flux quantum $\Phi_{\mathrm{AB}} = h/e$, corresponds to $B \approx 5300\,\mathrm{T}$.

Similar effects were also considered for graphene disks with strain-induced pseudomagnetic fields [48] and with the spin-orbit coupling [49], extending the list of different theoretical proposals for producing a valley polarization with graphene-based nanostructures [50–55] and related systems [56–59].

For MLG disks, the oscillations magnitude depends only on the radii ratio R_o/R_i. For the conductivity, we have $\Delta\sigma_{\mathrm{MLG}} \gtrsim 0.1\sigma_{\mathrm{MLG}}$ if $R_o/R_i \geqslant 5$. For BLG disks, the mode-matching analysis for the $t' = 0$ case [1] unveils an interference between the two transmission channels for each angular momentum eigenvalue, following from the coupling between the layers quantified by $t_\perp$. In turn,

the oscillations magnitude depends also on the physical system size. For instance, conductivity oscillations are predicted to vanish ($\Delta\sigma = 0$) for

$$\frac{R_\mathrm{o}}{R_\mathrm{i}} \simeq \left(\frac{R_\mathrm{i} t_\perp}{2\hbar v_F}\right)^{4/p} \qquad (\text{for } R_\mathrm{o} \gg R_\mathrm{i}), \tag{32}$$

where $p = 1, 2, 3, \ldots$. Eq. (32) with *even* p [equivalent to half-odd integer q in Eq. (26)] gives the condition for maximal oscillations, with the magnitude $\Delta\sigma = 2\Delta\sigma_\mathrm{MLG}$, same in the limit of decoupled layers ($t_\perp \to 0$).

If the Fermi energy E is close but not precisely adjusted to the Dirac point, the oscillations in both MLG and BLG disks are still predicted to appear in the limited range of magnetic fluxes, namely

$$|\Phi_D| \leqslant \Phi_D^\mathrm{max} \simeq -\frac{2h}{e}\ln(k_F R_\mathrm{i}), \quad (\text{for } k_F R_\mathrm{i} \ll 1), \tag{33}$$

with $k_F = |E|/(\hbar v_F)$, away from which the conductivity is strongly suppressed. Eq. (33) can be rewritten to obtain the corresponding energy range for a given field

$$|E| \lesssim \frac{\hbar v_F}{R_\mathrm{i}} \exp\left(-\frac{R_\mathrm{o}^2 - R_\mathrm{i}^2}{l_B^2}\right). \tag{34}$$

The limits given by Eqs. (33) and (34) essentially applies to higher charge-transfer cumulants as well, albeit the dimensionless characteristics $\mathcal{F}$ and $\mathcal{R}$ were recently found to show stable, quasiperiodic oscillations in the high source-drain voltage limit [46].

Later this Section, we employ the numerical procedure described in Section II in order to find out how the magnetotransport characteristics of BLG disks are affected by the trigonal warping ($t' \neq 0$).

B. Rectangular BLG device with periodic boundary conditions

Before discussing magnetotransport of the Corbino disk, it is instructive to consider a simpler artificial system depicted schematically in Fig. 1(b). A BLG strip of width W, contacted by the electrodes at a distance L, in a uniform field B, and with periodic boundary conditions in the transverse direction, was earlier discussed in the $W \gg L$ limit [20], in which the pseudodiffusive charge transport is predicted to appear near LLs. Here we primarily focus on the $W \lesssim \pi L$ range (a nanotube-like geometry) which do not seem to have a direct physical analogue, but can be treated in analytical terms and possesses a discrete spectrum of transmission channels closely resembling the situation in the Corbino disk.

The wavefunctions for a rectangular sample are presented in Appendix B. Each spinor component can be written as a product of the exponential function and the Airy function, with their arguments scaling as $l_B^{-2} \propto B$ for high fields; see Eq. (B2). In turn, taking the asymptotic form of the Airy function $\mathrm{Ai}\,(z) \simeq \exp\left(-2z^{3/2}/3\right) / \left(2z^{1/4}\sqrt{\pi}\right)$, we find the conductivity in the high-field limit can roughly be approximated by

$$\sigma_{L\gg l_B} \approx \frac{g_0 L}{W} \sum_{k,\pm} \cosh^{-2}\left\{ L\left(k - \frac{L}{2l_B^2}\right) \pm \frac{1}{24}\Re\left[\gamma_k(L) - \gamma_k(0)\right]\right\}, \tag{35}$$

where $k = 0, \pm 2\pi/W, \pm 4\pi/W, \ldots$,

$$\gamma_k(x) = \sqrt{-\frac{i\nu l_B}{l_\perp}}\left(\frac{8x}{l_B} - 8kl_B - \frac{i\nu l_B}{l_\perp}\right)^{3/2}, \tag{36}$$

and $\Re(z)$ denotes the real part of z. In the absence of trigonal warping, Eq. (35) is replaced by exact expression for the conductivity, namely

$$\frac{\sigma_\mathrm{rec}(t'=0)}{\sigma_0} = 1 + \sum_{n=1}^{\infty}\left\{\left(\frac{\pi n W}{L}\right)\cos(nk_c W) \times \left[\sinh\left(\frac{\pi n W}{2L}\right)\right]^{-1}\cos\left(\frac{\pi n e}{h} LWB\right)\right\}, \tag{37}$$

where $k_c = (1/L)\,\mathrm{arsinh}\,[\,Lt_\perp/(2\hbar v_F)\,]$. A Fourier series on the right-hand side represents periodic (approximately sinusoidal for moderate aspect ratios $W/L \gtrsim 2$) magnetoconductance oscillations with the period $\mathcal{T}_0 = (2h/e)(LW)^{-1}$ [60].

For $t' \neq 0$, the approximating expression given by Eqs. (35,36) is particularly convenient when extracting the beating frequency which governs high-field magnetotransport characteristics of the system. It can be shown that the presence of two relevant transmission eigenvalues for each momentum k in Eq. (35) follows directly from the fact that the lowest LL in BLG has an additional twofold degeneracy absent for higher LLs [20]. We define the two field-dependent effective system sizes determining transmission probabilities in Eq. (35), namely

$$L_\pm = L\mu_\pm, \tag{38}$$

and the corresponding momentum-quantization shifts

$$\Delta k_\pm = \frac{L}{2l_B^2\mu_\pm}, \tag{39}$$

where

$$\mu_\pm = 1 \pm \sqrt{\frac{8\nu l_B^2}{9Ll_\perp}}. \tag{40}$$

The above reasoning holds true for high magnetic fields and arbitrary W/L ratio. For instance, the conductivity in the $W \gg L$ limit can be approximated by

$$\sigma_{W\gg L\gg l_B} \approx \frac{2g_0}{\pi}\left(\frac{1}{\mu_+} + \frac{1}{\mu_-}\right) = \sigma_0\left(1 - \frac{8\nu l_B^2}{9Ll_\perp}\right)^{-1}, \tag{41}$$

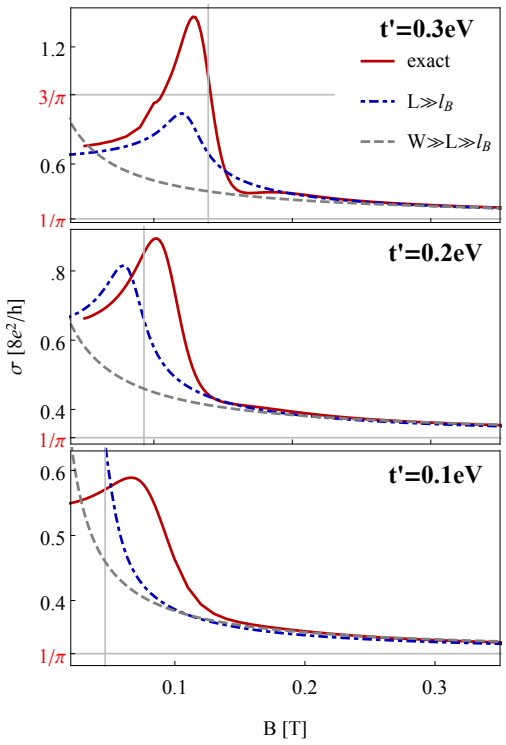

FIG. 7: Conductivity of the rectangular BLG sample at the charge-neutrality point as a function of the magnetic field B. The sample length is fixed at $L = 300\, l_\perp \simeq 480\,\text{nm}$, the width is $W = 10L$, and the skew-interlayer hopping integral t' is varied between the panels. Red solid lines: exact numerical results obtained from the mode-matching analysis via Eq. (12). Blue solid lines: results from Eqs. (35,36) for $L \gg l_B$. Dashed lines: results from Eq. (41) for $W \gg L \gg l_B$.

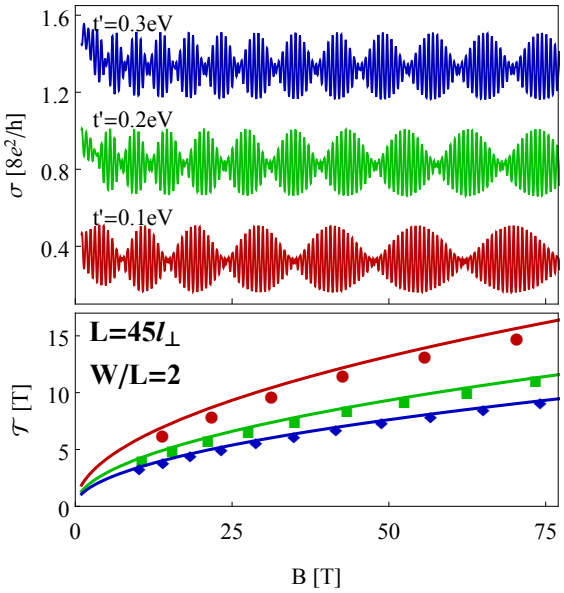

FIG. 8: Magnetoconductance oscillations for the rectangular BLG sample of the length $L = 45\, l_\perp \simeq 72\,\text{nm}$ and the width $W = 2L$ at the charge-neutrality point. Top panel: The conductivity as a function of magnetic field for three values of the skew-interlayer hopping integral t' (specified for each line). The lines for $t' = 0.3\,\text{eV}$ and $t' = 0.2\,\text{eV}$ are shifted by 1 and 1/2 for clarity. Bottom panel: Consecutive periods of the beating envelope extracted from the data shown in the top panel, for $t' = 0.1\,\text{eV}$ (circles), $t' = 0.2\,\text{eV}$ (squares), and $t' = 0.3\,\text{eV}$ (diamonds). Solid lines correspond to the approximating Eq. (44).

restoring the $t' = 0$ value ($\sigma \to \sigma_0$) for $l_B \to 0$.

In Fig. 7 we compare exact numerical results obtained from Eq. (12) for $W = 10L = 3000\, l_\perp$ and different values of skew-interlayer hopping t' [red solid lines] with corresponding results following from the approximating Eqs. (35,36) [blue solid lines] and Eq. (41) [dashed lines]. For low magnetic fields, the conductivity monotonically grows with increasing B (for any $t' \neq 0$), up to the maximal value (at $B = B_{\text{peak}}$) which may exceed $3\sigma_0$ for larger t'-s. For $B > B_{\text{peak}}$, the effect of trigonal warping on the conductivity is gradually suppressed, leading to $\sigma - \sigma_0 \propto t'/B$, in agreement with the approximating Eq. (41).

The value of B_{peak} is related to the quasimomentum shifts given by Eq. (39). For a finite aspect ratio W/L, maximal conductivity appears when the average shift is of the same order of magnitude as the distance between primary and secondary Dirac points [given by Eq. (17)], namely

$$\left(\frac{\Delta k_+ + \Delta k_-}{2}\right)_{\text{peak}} \sim k_\ell, \tag{42}$$

what can be rewritten as

$$B_{\text{peak}} \sim \frac{2h}{e}\frac{1}{L\ell} \equiv B_L, \tag{43}$$

where we have defined the crossover *Lifshitz field* B_L. It is also visible in the top panel of Fig. 7 that the approximating Eqs. (35,36) [blue dashed lines] reproduces the peak position (albeit not the maximal conductivity) with a good accuracy for $t' = 0.3\,\text{eV}$.

The conductivity maximum at $B_{\text{peak}} \sim B_L \neq 0$ can be regarded as the first effect of the trigonal warping, appearing for samples with finite aspect ratios, but still well-visible for $W/L = 10$.

The second effect, present in systems with $W \lesssim \pi L$, is the emergence of beating patterns. In the top panel of Fig. 8 we display the conductivity, as a function of magnetic field, for $W = 2L = 90\, l_\perp$. Quasiperiodic beatings are characterized by the field-dependent envelope period, which can be approximated by

$$\mathcal{T}(B) \approx \frac{4h}{eLW}\frac{\mu_+\mu_-}{\mu_+ - \mu_-} \simeq \frac{3h}{e}\frac{1}{LW}\left(\frac{B}{B_L}\right)^{1/2}, \tag{44}$$

while the period of internal oscillations remains the same as in Eq. (37). The comparison between the actual envelope periods refined from the numerical data [datapoints]

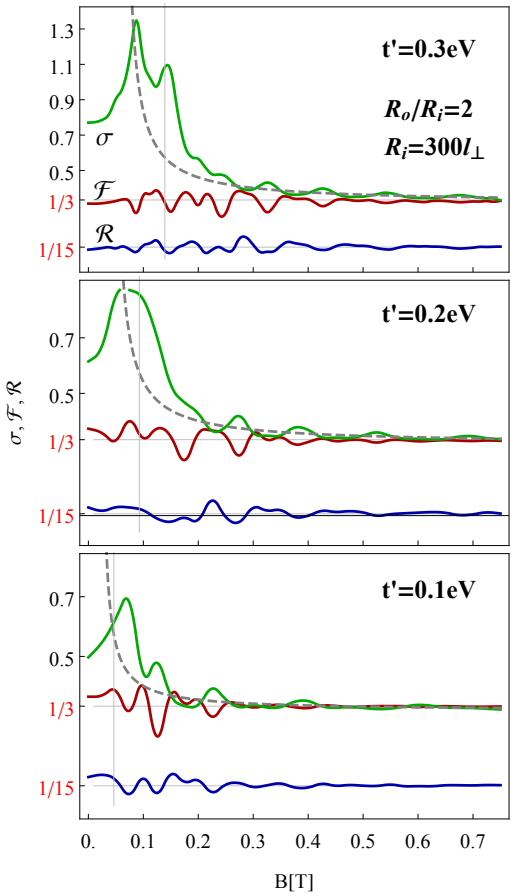

FIG. 9: Conductivity σ [specified in the units of $8e^2/h$], the Fano factor $\mathcal{F}$, and the $\mathcal{R}$ factor for BLG Corbino disk with $R_\mathrm{i} = 300\,l_\perp$, $R_\mathrm{o} = 2R_\mathrm{i}$, and different skew-interlayer hopping integrals t' (specified for each panel). Vertical lines correspond to $B = B_L$ [see Eq. (45)], the horizontal lines mark the pseudodiffusive values $\mathcal{F} = 1/3$ and $\mathcal{R} = 1/15$, the dashed lines represent the approximating Eq. (46).

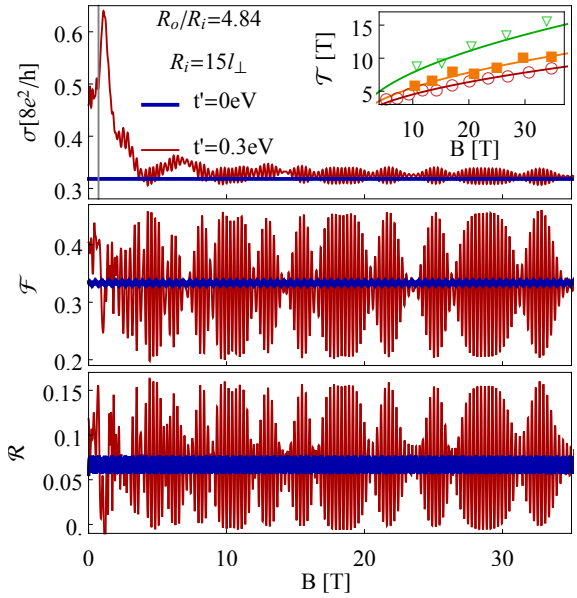

FIG. 10: Charge-transfer characteristics σ, $\mathcal{F}$, and $\mathcal{R}$ for BLG disk with $R_\mathrm{i} = 15\,l_\perp$, $R_\mathrm{o} = 4.84\,R_\mathrm{i}$. Each of the main panels compares the numerical results for $t' = 0$ (blue line) and $t' = 0.3\,\mathrm{eV}$ (red line). The vertical grey line in the top panel marks the value of B_L obtained from Eq. (45) for $t' = 0.3\,\mathrm{eV}$. The inset: Period of the beating envelope for three different values of $t' = 0.3\,\mathrm{eV}$ (circles), $0.2\,\mathrm{eV}$ (orange squares), $0.1\,\mathrm{eV}$ (triangles). Solid lines correspond to Eq. (47).

and the values following from Eq. (44) [lines] is provided in the bottom panel of Fig. 8.

For high magnetic fields, Eq. (44) leads to $\mathcal{T}(B) \propto \sqrt{B}$. In turn, the $t' = 0$ behavior characterized by single-frequency, sinusoidal magnetoconductance oscillations with a size-dependent amplitude [see Eq. (37)] cannot be restored for any $t' \neq 0$ in the high-field limit. We interpret this effect as a finite-system analog of the zero-temperature conductance instability (the parameter-driven Lifshitz transition) in bulk BLG samples [12].

C. BLG Corbino disks

Our numerical study of magnetotransport through BLG Corbino disks focuses on two different systems: First one, characterized by $R_\mathrm{i} = 300\,l_\perp$ and $R_\mathrm{o} = 2R_\mathrm{i}$ is in the pseudodiffusive charge-transport regime, whereas the second one, with $R_\mathrm{i} = 15\,l_\perp$ and $R_\mathrm{o} = 4.84\,R_\mathrm{i}$, shows the beating patterns. In the latter case, the parameters are chosen such that the magnetoconductance oscillations vanish for $t' = 0$ (see Ref. [1]), in order to illustrate the role of trigonal warping more clearly.

The numerical results for σ, $\mathcal{F}$, and $\mathcal{R}$ are presented, as functions of magnetic field B, in Figs. 9 and 10.

In the pseudodiffusive transport regime (see Fig. 9) some irregular fluctuations, visible for all the discussed charge-transfer characteristics (and all three values of t'), are suppressed for magnetic fields $B \gtrsim 0.5\,\mathrm{T}$. We attribute these fluctuations rather to a Fabry-Perot interference than to the angular momentum quantization. A striking feature of the data presented in Fig. 9 is that a distinct conductance peak appears at each panel near the field

$$B_L = \frac{4}{3}\sqrt{3}\,\frac{\hbar\, t' t_\perp}{e\, t_0^2 a\,(R_\mathrm{o} - R_\mathrm{i})}, \tag{45}$$

closely resembling the phenomena described above for a rectangular sample. [Notice that the rightmost equality in Eq. (43) and Eq. (45) are equivalent provided that $L \equiv R_\mathrm{o} - R_\mathrm{i}$]. Above the crossover field B_L, the conductivity can be approximated by the formula

$$\sigma_{B \gg B_L} \approx \sigma_0 \left(1 - 0.5\,\frac{B_L}{B}\right)^{-1}, \tag{46}$$

which is visualized with dashed lines in Fig. 9, and can be regarded as a version of Eq. (41) for BLG disk.

For the disk with larger radii ratio (see Fig. 10) all three magnetotransport characteristics exhibit quasiperiodic beating patterns for $t' = 0.3\,\mathrm{eV}$. This is not the case for $t' = 0$, when each characteristic shows approximately sinusoidal, single-frequency, oscillations with a constant amplitude. As the system no longer possesses a rotational symmetry in the presence of trigonal warping, the magnetotransport cannot be simply rationalized by defining two effective system sizes in analogy to Eq. (38). Comparing to the rectangular system case (which can be regarded, due to the periodic boundary conditions, as a nanotube-like, i.e., possessing the rotational symmetry also for $t' \neq 0$) illustrated in Fig. 8, the beatings are slightly less regular now, clustering in the groups of three. This certain feature of the data displayed in Fig. 10 suggests the presence of four, rather than two, quasiperiodic components determining the transmission probabilities.

It is worth to stress here that the main features of the magnetotransport characteristics still resemble the rectangular (or a nanotube-like) system case. In particular, we found that the beating-envelope period can now be approximated by

$$\mathcal{T}(B) \approx \frac{6.9}{\pi(R_\mathrm{o}^2 - R_\mathrm{i}^2)} \frac{h}{e} \left(\frac{B}{B_L}\right)^{1/2}, \tag{47}$$

see the inset in Fig. 10. On the other hand, the period of the internal oscillations, $\mathcal{T}_0 = \Phi_0 / \left[\pi({R_\mathrm{o}}^2 - {R_\mathrm{i}}^2)\right]$, remains the same as the basic period for MLG disks or BLG disks with $t' = 0$ [1, 25, 26]. Also, a high-field behavior of the conductivity averaged over consecutive intervals, each one of the $\mathcal{T}_0$ width, can be approximated by Eq. (46).

V. CONCLUSIONS

We have investigated, by means of numerical transfer-matrix approach in the angular-momentum space, the effects of the skew-interlayer hopping integrals (the trigonal warping) on selected transport characteristics of bilayer-graphene (BLG) Corbino disks. Additionally, the analytical mode-matching for an artificial (nanotube-like) system, formed of a BLG strip upon applying the periodic boundary conditions, was briefly presented and the analogies between these two systems were put forward.

If the Fermi energy is close to the charge-neutrality point, both the scaling behavior at zero magnetic field (which would require a comparison between devices of different sizes in an experimental study) and the single-device magnetotransport discussion unveils several phenomena, in which transport characteristics, such as the conductivity, the Fano factor, and the third charge-transfer cumulant, are noticeably affected by the trigonal warping.

In the pseudodiffusive transport regime, corresponding to the disk radii ratios $R_\mathrm{o}/R_\mathrm{i} \lesssim 2$, the conductivity shows a one-parameter scaling, in agreement with predictions of Ref. [23] for a rectangular sample. In the Corbino geometry, however, the role a crystallographic orientation is eliminated, and the zero-field minimal conductivity can be approximated by

$$\sigma_\mathrm{min} \approx 3\sigma_0 \left[1 - \left(\frac{\lambda}{R_\mathrm{o} - R_\mathrm{i}}\right)^{0.5}\right], \tag{48}$$

where $\lambda = \lambda(t')$ depends only on the skew-interlayer hopping t', and varies from $\lambda \approx 20\,\mathrm{nm}$ for $t' = 0.3\,\mathrm{eV}$ to $\lambda \approx 100\,\mathrm{nm}$ for $t' = 0.1\,\mathrm{eV}$. In the uniform magnetic field B, the conductivity increases reaching the maximal value $\sigma_\mathrm{max} \gtrsim 3\sigma_0$ near the so-called Lifshitz field B_L, for which the magnetic length follows the relation

$$(R_\mathrm{o} - R_\mathrm{i})\,\ell = 4\pi l_B^2, \tag{49}$$

where $\ell = \sqrt{3}\,\pi a t_0^2/(t_\perp t')$ is defined by t' and other microscopic parameters: the lattice spacing a as well as the nearest-neighbor intra- and interlayer hoppings t_0 and $t_\perp$. Above B_L, the conductivity gradually decreases showing the asymptotic behavior $\sigma - \sigma_0 \propto B_L/B$ [see Eq. (46)]. The second and third charge transfer cumulants stay close to their pseudodiffusive values ($\mathcal{F} = 1/3$, $\mathcal{R} = 1/15$) when varying the system size or the magnetic field.

In the opposite, quantum-tunneling regime (corresponding to $R_\mathrm{o}/R_\mathrm{i} \gtrsim 4$), the charge-transfer characteristics are also sensitive to t'. At zero field and $t' = 0$, the transport is governed by two quantum channels with angular momenta $\pm 2\hbar$. For $t' \neq 0$, the backscattering is enhanced for these channels, as the related wavefunctions no longer match the symmetry of the low-energy Hamiltonian. At high magnetic fields, all the charge-transfer characteristics show quasiperiodic beating patterns, with the envelope period $\mathcal{T}(B) \propto \sqrt{B/B_L}$ [see Eq. (47)]. Most remarkably, the beating patterns, triggered by the trigonal-warping ($t' \neq 0$), remain well-pronounced in the Landau quantization regime. (Unlike the average conductivity enhancement, which is usually eliminated by a few Tesla field.) It seems this finite-system version of the Lifshitz transition can be related to numerous phenomena appearing in different branches of physics, starting from semiconducting heterostructures [61], via strongly-correlated electron systems [62], to neutrino physics [63], in which scattering the particles between quantum states with different effective masses leads to oscillations in relevant counting statistics, although this time the interference occurs between the evanescent waves.

We stress here that finding the Lifshitz field B_L, via the asymptotic behavior of the conductivity, or via the beating period, may allow one – at least in principle – to determine the value of t' from a single-device magnetotransport measurement.

Apart from the possible verification of tight-binding parameters in BLG Hamiltonian, we believe the effects we describe, when confirmed experimentally, will provide a thorough insight into the interplay between massless- and massive-chiral states ruling the quantum transport through BLG devices near the charge-neutrality point. For instance, the conductivity enhancement for $B \sim B_L$ may dominate the signatures of interaction-related magnetic catalysis phenomenon [64] (particularly in finite-size systems), and one should precisely distinguish single- and many-body aspects when searching for this intriguing phenomenon in BLG.

As we have focused on clean ballistic systems, several factors which may modify the transport properties of graphene-based devices, including the disorder [5], lattice defects [65], or magnetic impurities [66–68], are beyond the scope of this work. Some experimental [17, 24] and numerical [30, 69] findings suggest that charge-transfer characteristics in the pseudodiffusive transport regime are quite robust against such factors. For the opposite, quantum-tunneling regime, we put forward the following reasoning: In the presence of trigonal warping, the rotational symmetry supposed in earlier studies of MLG [25, 26] or BLG [1] disks, no longer applies. In spite of this fact, the basic oscillation period [$\Phi_0 = 2\,(h/e)\ln(R_\mathrm{o}/R_\mathrm{i})$, in terms of magnetic flux piercing the disk area] remains unaltered, allowing one to believe that oscillations and beating patterns would appear in a more general situation as well.

Acknowledgements

We thank Stephan Roche for the correspondence. The work was supported by the National Science Centre of Poland (NCN) via Grant Nos. 2014/14/E/ST3/00256 (AR) and 2014/15/N/ST3/03761 (GR). Computations were partly performed using the PL-Grid infrastructure.

Appendix A: Transfer-matrix approach in the angular momentum space

A version of the transfer-matrix approach utilized in this paper is chosen such that the differential equation for transfer matrix can be directly derived from Eqs. (9) and (10) [see Section IIB] for the wavefunctions, and solved analytically in the absence of trigonal warping ($\nu \equiv t'/t_0 = 0$). The numerical procedure for $\nu \neq 0$ is described below.

First, a basis set for the transfer matrix is constructed starting from a general angular-momentum eigenstate in the disk area ($R_\mathrm{i} < R_\mathrm{o}$), corresponding to a given angular-momentum quantum number $l = 0, \pm1, \pm2, \ldots$, a radial part of which can be written as a linear combination of four spinor functions $\phi^l(r) = \sum_{\alpha=1}^{4} a^l_\alpha \phi^l_\alpha(r)$. The coefficients $\{a^l_\alpha\}$ are arbitrary amplitudes and $\phi^l_\alpha(r) = \left(\phi_1^{\alpha,l}, \phi_2^{\alpha,l}, \phi_3^{\alpha,l}, \phi_4^{\alpha,l}\right)^T(r)$ is a normalized spinor function. (The normalization is carried out in such a way that the total radial current remains constant.) The wavefunction $\phi^l(r)$ can be represented as

$$\phi^l(r) = \mathbb{W}^l(r)\,\boldsymbol{a}^l, \tag{A1}$$

where $\mathbb{W}^l(r)$ is the 4×4 matrix with elements $\left[\mathbb{W}^l(r)\right]_{m,n} = \phi_m^{n,l}(r)$, and $\boldsymbol{a}^l = \left(\, a_1^l,\ a_2^l,\ a_3^l,\ a_4^l \,\right)^T$.

Next, the radial part of the actual wavefunction [see Eq. (8) in the main text], describing the system in the presence of trigonal warping, is truncated by the linear combination of limited number $(2M+1)$ of basis functions, each given by Eq. (A1), corresponding to angular-momentum quantum numbers $l = -M, \ldots, M$. Namely, we define

$$\boldsymbol{\phi}(r) = \left[\boldsymbol{\phi}_1(r), \boldsymbol{\phi}_2(r), \boldsymbol{\phi}_3(r), \boldsymbol{\phi}_4(r)\right]^T, \tag{A2}$$

with

$$\boldsymbol{\phi}_i(r) = \sum_{j=1}^{4} \mathbb{M}(i,j;r)\,\boldsymbol{a}_j, \qquad (i = 1, \ldots, 4), \tag{A3}$$

where $\boldsymbol{a}_j = \left[a_j^{-M}, \ldots, a_j^{M}\right]^T$, and the $(2M+1)\times(2M+1)$ matrix $\mathbb{M}(i,j;r)$ is to be specified later in this Appendix. The relation between wavefunctions at different radii, say r and R_i, can be expressed within the propagator $\mathbb{U}(r, R_i)$ as follows

$$\boldsymbol{\phi}(r) \;=\; \mathbb{U}(r, R_i)\,\boldsymbol{\phi}(R_i)\,. \tag{A4}$$

Substituting Eq. (A4) into Eq. (9) in the main text, we obtain

$$\partial_r \mathbb{U}(r, R_i) = \mathbb{A}(r)\,\mathbb{U}(r, R_\mathrm{i})\,, \tag{A5}$$

with the boundary condition

$$\mathbb{U}(R_\mathrm{i}, R_\mathrm{i}) = \mathbb{I}_{(8M+4)\times(8M+4)}, \tag{A6}$$

where $\mathbb{I}_{N\times N}$ denotes the $N \times N$ identity matrix. The sparse matrix $\mathbb{A}(r)$ in Eq. (A5) has nonzero elements $\left[\mathbb{A}(r)\right]_{m,n}$ directly following from Eq. (9). Defining

$$\begin{aligned} l_m &= M - \left[(m-1) \bmod (2M+1)\right], \\ \alpha_m &= \left\lfloor (m-1)\,/\,(2M+1) \right\rfloor, \end{aligned} \tag{A7}$$

where $\lfloor x \rfloor$ denotes the largest integer smaller or equal to x, one can write down

$$[\,\mathbb{A}(r)\,]_{m,n} = [-g(l_m,r)\delta_{m,n} + i\nu t\delta_{m,n-3} + 2\nu g(l_m-2,r)\delta_{m,n-6M-6}]\,\delta_{\alpha_m,0} + [g(l_m-1,r)\delta_{m,n} - it\delta_{m,n-2M-1}]\,\delta_{\alpha_m,1} + [g(l_m,r)\delta_{m,n} + i\nu t\delta_{m,n+3} - 2\nu g(l_m+2,r)\delta_{m,n+2M+4}]\,\delta_{\alpha_m,2} - [g(l_m+1,r)\delta_{m,n} + it\delta_{m,n+6M+3}]\,\delta_{\alpha_m,3}, \tag{A8}$$

where $1 \leqslant m,n \leqslant 8M+4$, the symbol $\delta_{\alpha,\beta}$ denotes the Kronecker delta of α and β, $t = t_\perp/(\hbar v_F)$, and $g(l,r)$ is given by Eq. (10) in the main text.

The angular-momentum cutoff M is chosen to be large enough to reach the convergence of the charge-transfer characteristics. We observe that the desired relative precision of 10^{-4} requires M growing approximately linearly with the system size $R_\mathrm{o} - R_\mathrm{i}$, the magnetic field B, and the skew-interlayer hopping t'. For instance, in our numerical examples with $t' = 0.3\,\mathrm{eV}$, the number of modes varies from $2M+1 = 50$ for $R_\mathrm{o} - R_\mathrm{i} = 90\,\mathrm{nm}$ and $B = 0$, up to $2M+1 = 1000$ for $R_\mathrm{o} - R_\mathrm{i} = 5\,\mu\mathrm{m}$ and $B = 80\,\mathrm{T}$. It is also worth to mention, that in the magnetic field $B > 0$ efficient computation requires the angular momentum quantum numbers are varied in a range

$$l = -M - \lfloor \Phi_D/\Phi_0 \rfloor, \ldots, M - \lfloor \Phi_D/\Phi_0 \rfloor, \tag{A9}$$

where $\Phi_D = \pi(R_\mathrm{o}^2 - R_\mathrm{i}^2)B$.

The numerical integration of Eq. (A5), with the boundary condition given by Eq. (A6) and the matrix $\mathbb{A}(r)$ given by Eqs. (A7,A8), was carried out by employing the 4-th order explicit Runge-Kutta method with a fixed step size [70, 71]. Floating-point arithmetic, with up to 300 decimal digits, was used to guarantee the numerical stability when inverting the blocks of the resulting transfer matrix for the whole system (see below).

A procedure, described in the above, brings us to the propagator for the disk area $\mathbb{U}(R_\mathrm{o}, R_\mathrm{i})$. Writing down the standard mode-matching conditions for wavefunctions in the leads and in the disk area

$$\begin{aligned} \boldsymbol{\phi}^{\mathrm{lead}}(R_\mathrm{o}) &= \boldsymbol{\phi}^{\mathrm{sample}}(R_\mathrm{o}), \\ \boldsymbol{\phi}^{\mathrm{sample}}(R_\mathrm{i}) &= \boldsymbol{\phi}^{\mathrm{lead}}(R_\mathrm{i}), \end{aligned} \tag{A10}$$

together with Eq. (A4) for $r = R_\mathrm{o}$, gives us

$$\boldsymbol{\phi}^{\mathrm{lead}}(R_\mathrm{o}) = \mathbb{U}(R_\mathrm{o}, R_\mathrm{i})\,\boldsymbol{\phi}^{\mathrm{lead}}(R_\mathrm{i}). \tag{A11}$$

In order to find the transfer matrix for the whole system, we choose the wavefunctions in the leads such that

$$\begin{aligned} \boldsymbol{\phi}^{\mathrm{lead}}(R_\mathrm{o}) &= \mathbb{M}_{\mathrm{lead}}(R_\mathrm{o})\,\boldsymbol{a}, \\ \boldsymbol{\phi}^{\mathrm{lead}}(R_\mathrm{i}) &= \mathbb{M}_{\mathrm{lead}}(R_\mathrm{i})\,\boldsymbol{b}, \end{aligned} \tag{A12}$$

where the vector $\boldsymbol{a}$ ($\boldsymbol{b}$) contains $8M+4$ amplitudes for normal modes in the outer (inner) lead. Taking the limit of infinite doping in the leads one can disregard the parameter ν, and write down

$$\mathbb{M}_{\mathrm{lead}}(r) = \mathbb{B}(r) \otimes \mathbb{I}_{(2M+1)\times(2M+1)}, \tag{A13}$$

for $r < R_\mathrm{i}$ or $r > R_\mathrm{o}$, where

$$\mathbb{B}(r) = \frac{1}{\sqrt{r}} \begin{pmatrix} 1 & 1 & 1 & 1 \\ 1 & 1 & -1 & -1 \\ -1 & 1 & -1 & 1 \\ -1 & 1 & 1 & -1 \end{pmatrix}, \tag{A14}$$

$\mathbb{A} \otimes \mathbb{B}$ denotes the Kronecker product of the matrices $\mathbb{A}$ and $\mathbb{B}$, and we have further skipped the physically-irrelevant constant phase. In turn, the matrices $\mathbb{M}(i,j;r)$ defining the wavefunction via Eqs. (A2) and (A3) can be found as blocks of the matrix $\mathbb{U}(r, R_\mathrm{i})\mathbb{M}_{\mathrm{lead}}(R_\mathrm{i})$.

The transfer matrix thus reads

$$\begin{aligned} \mathbb{T} &= \mathbb{M}_{\mathrm{lead}}^{-1}(R_\mathrm{o})\,\mathbb{U}(R_\mathrm{o}, R_\mathrm{i})\,\mathbb{M}_{\mathrm{lead}}(R_\mathrm{i}) \\ &= \begin{pmatrix} (\mathbf{t}^\dagger)^{-1} & \mathbf{r}' \cdot (\mathbf{t}')^{-1} \\ -(\mathbf{t}')^{-1} \cdot \mathbf{r}' & (\mathbf{t}')^{-1} \end{pmatrix}, \end{aligned} \tag{A15}$$

where the rightmost equality maps the matrix blocks of $\mathbb{T}$ onto the elements of the scattering matrix: $\mathbf{t}$, $\mathbf{r}$ – the transmission and reflection matrices for a wavefunction incoming from the inner lead, and $\mathbf{t}'$, $\mathbf{r}'$ – the transmission and reflection matrices for a wavefunction incoming from the outer lead [39].

Appendix B: Wavefunctions for a rectangular sample in uniform magnetic field

In this Appendix we present the wavefunctions utilized in Sec. IVB to discuss the magnetotransport through a rectangular BLG sample at the charge-neutrality point. The low-energy Hamiltonian has a general form as given by Eq. (5) in the main text, but the potential energy now depends only on the x-coordinate

$$U(x) = \begin{cases} U_\infty, & \text{if } x < 0 \text{ or } x > L, \\ 0, & \text{if } 0 < x < L, \end{cases} \tag{B1}$$

and we choose the Landau gauge $(A_x, A_y) = (0, Bx)$. Subsequently, the solution of the Dirac equation $H\psi = E\psi$, corresponding to a given transverse wavenumber k, can be written as $\psi(x,y) = \phi_k(x)\exp(iky)$. (For the sample width W and the periodic boundary conditions along y-direction, we have $k = 0, \pm 2\pi/W, \pm 4\pi/W, \ldots$)

Using the compact notation: $\psi_\beta^\alpha(x) \equiv \psi_\beta^\alpha$, $\gamma \equiv [\,\gamma_k(x)/16\,]^{2/3}$ [see Eq. (36) in the main text], and $\chi = x\left[k + it\nu/2 - x/\left(2l_B^2\right)\right]$, one can write down a zero-energy wavefunction for the sample area $(0 < x < L)$ as

a combination of four linearly-independent spinors

$$\phi_k^{\rm sample}(x) = C_1^k \begin{pmatrix} \psi_1^1 \\ 0 \\ 0 \\ \psi_1^4 \end{pmatrix} + C_2^k \begin{pmatrix} \psi_2^1 \\ 0 \\ 0 \\ \psi_2^4 \end{pmatrix} + C_3^k \begin{pmatrix} 0 \\ \psi_1^2 \\ \psi_1^3 \\ 0 \end{pmatrix} + C_4^k \begin{pmatrix} \psi_2^2 \\ 0 \\ \psi_2^3 \\ 0 \end{pmatrix}, \quad \text{(B2)}$$

with $C_1^k, \ldots, C_4^k$ being arbitrary coefficients. The spinor components in Eq. (B2) are given by

$$\begin{aligned}
\psi_1^1 &= e^{\chi}\left[\, i\tau \mathrm{Ai}'(\gamma) - (\nu/2)\mathrm{Ai}(\gamma)\,\right], \\
\psi_2^1 &= e^{\chi}\left[\, i\tau \mathrm{Bi}'(\gamma) - (\nu/2)\mathrm{Bi}(\gamma)\,\right], \\
\psi_1^2 &= e^{-\chi^*}\mathrm{Ai}(\gamma^*), \\
\psi_2^2 &= e^{-\chi^*}\mathrm{Bi}(\gamma^*), \\
\psi_1^3 &= e^{-\chi^*}\left[\, i\tau^* \mathrm{Ai}'(\gamma^*) - (\nu/2)\mathrm{Ai}(\gamma^*)\,\right], \\
\psi_2^3 &= e^{-\chi^*}\left[\, i\tau^* \mathrm{Bi}'(\gamma^*) - (\nu/2)\mathrm{Bi}(\gamma^*)\,\right], \\
\psi_1^4 &= e^{\chi}\mathrm{Ai}(\gamma), \\
\psi_2^4 &= e^{\chi}\mathrm{Bi}(\gamma), \qquad \text{(B3)}
\end{aligned}$$

where $\mathrm{Ai}(z)$ and $\mathrm{Bi}(z)$ are the Airy functions [72], and we have further defined $\tau = \sqrt[3]{-2i\nu t^{-2}}$.

Remaining details of the mode-matching analysis are same as in Refs. [13, 20].

[1] G. Rut and A. Rycerz, J. Phys.: Condens. Matter **26**, 485301 (2014).

[2] P. Avouris, Z. Chen, and V. Perebeinos, Nature Nanotechnol. **2**, 605 (2007); G. Fiori, F. Bonaccorso, G. Iannaccone, T. Palacios, D. Neumaier, A. Seabaugh, S.K. Banerjee, and L. Colombo, *ibid.* **9**, 768 (2014).

[3] K. S. Novoselov, V. I. Falko, L. Colombo, P. R. Gellert, M. G. Schwab, and K. Kim, Nature **490**, 192 (2012).

[4] L. Britnell, R. V. Gorbachev, R. Jalil, B. D. Belle, F. Schedin, A. Mishchenko, T. Georgiou, M. I. Katsnelson, L. Eaves, S. V. Morozov *et al.*, Science **335**, 947 (2012).

[5] E. McCann and M. Koshino, Rep. Prog. Phys. **76**, 056503 (2013).

[6] I. Martin, Y. M. Blanter, and A. F. Morpurgo, Phys. Rev. Lett. **100**, 036804 (2008).

[7] F. Zhang, A. H. MacDonald, and E. J. Mele, Proc. Natl. Acad. Sci. USA **110**, 10546 (2013).

[8] L. Ju, Z. Shi, N. Nair, Y. Lv, C. Jin, J. Velasco Jr, C. Ojeda-Aristizabal, H. A. Bechtel, M. C. Martin, A. Zettl, J. Analytis, and F. Wang, Nature (London) **520**, 650 (2015).

[9] A. Schroer, P.G. Silvestrov, and P. Recher, Phys. Rev. B **92**, 241404 (2015).

[10] L. M. Malard, J. Nilsson, D. C. Elias, J. C. Brant, F. Plentz, E. S. Alves, A. H. Castro Neto, and M. A. Pimenta, Phys. Rev. B 76 201401(R) (2007).

[11] A. B. Kuzmenko, I. Crassee, D. van der Marel, P. Blake, and K.S. Novoselov, Phys. Rev. B 80, 165406 (2009).

[12] J. Cserti, A. Csordás, and G. Dávid, Phys. Rev. Lett. **99**, 066802 (2007); M. Koshino and T. Ando, Phys. Rev. B **73**, 245403 (2006).

[13] I. Snyman and C.W.J. Beenakker, Phys. Rev. B **75**, 045322 (2007).

[14] J. Cserti, Phys. Rev. B **75**, 033405 (2007).

[15] M.I. Katsnelson, Eur. Phys. J. B **51**, 157 (2006).

[16] J. Tworzydło, B. Trauzettel, M. Titov, A. Rycerz, and C.W.J. Beenakker, Phys. Rev. Lett. **96**, 246802 (2006).

[17] F. Miao, S. Wijeratne, Y. Zhang, U.C. Coscun, W. Bao, and C.N. Lau, Science **317**, 1530 (2007).

[18] A.G. Moghaddam and M. Zareyan, Phys. Rev. B **79**, 073401 (2009).

[19] E. McCann and V.I. Fal'ko, Phys. Rev. Lett. **96**, 086805 (2006).

[20] G. Rut and A. Rycerz, Phys. Rev. B **89**, 045421 (2014).

[21] G.M. Rutter, S. Jung, N.N. Klimov, D.B. Newell, N.B. Zhitenev, and J.A. Stroscio, Nat. Phys. **7**, 649 (2011).

[22] W. Bao, J. Velasco, Jr., F. Zhang, L. Jing, B. Standley, D. Smirnov, M. Bockrath, A.H. MacDonald, and C.N. Lau, Proc. Natl. Acad. Sci. USA **109**, 10802 (2012).

[23] G. Rut and A. Rycerz, Europhys. Lett. **107**, 47005 (2014).

[24] A.S. Mayorov, D.C. Elias, M. Mucha-Kruczyński *et al.*, Science **333**, 860 (2011).

[25] A. Rycerz, Phys. Rev. B **81**, 121404(R) (2010).

[26] M.I. Katsnelson, Europhys. Lett. **89**, 17001 (2010).

[27] J. Tworzydło, C. W. Groth, and C. W. J. Beenakker, Phys. Rev. B **78**, 235438 (2008); A. R. Hernández and C. H. Lewenkopf, Phys. Rev. B **86**, 155439 (2012).

[28] S. Ihnatsenka and G. Kirczenow, Phys. Rev. B **85**, 121407 (2012).

[29] D. A. Bahamon, A. H. Castro Neto, and V. M. Pereira,

Phys. Rev. B **88**, 235433 (2013).
[30] F. Ortmann and S. Roche, Phys. Rev. Lett. **110**, 086602 (2013); F. Ortmann, N. Leconte, and S. Roche, Phys. Rev. B **91**, 165117 (2015).
[31] Z. Q. Li, E. A. Henriksen, Z. Jiang, Z. Hao, M. C. Martin, P. Kim, H. L. Stormer, and D. N. Basov, Phys. Rev. Lett. **102**, 037403 (2009).
[32] H. Min, B. Sahu, S. K. Banerjee, and A. H. MacDonald, Phys. Rev. B **75**, 155115 (2007); J. C. Charlier, X. Gonze, and J. P. Michenaud, Phys. Rev. B **43**, 4579 (1991).
[33] J.M. Pereira Jr., P. Vasilopoulos, and F.M. Peeters, Nano Lett. **7**, 946, (2007); J.M. Pereira Jr., P. Vasilopoulos, F.M. Peeters, and G.A. Farias, Phys. Rev. B **79**, 195403 (2009).
[34] S. Datta, M. Cahay, and M. McLennan, Phys. Rev. B **36**, 5655(R) (1985); M. Cahay, M. McLennan, and S. Datta, Phys. Rev. B **37**, 10125 (1985).
[35] S. Souma and A. Suzuki, Phys Rev. B **58**, 4649 (1998); S. Souma and A. Suzuki, Phys. Rev. B **60**, 15928 (1999).
[36] M. Titov, Europhys. Lett. **79**, 17004 (2007); J.H. Bardarson, J. Tworzydło, P.W. Brouwer, and C.W.J. Beenakker, Phys. Rev. Lett. **99**, 106801 (2007); P. San-Jose, E. Prada, and D.S. Golubev, Phys. Rev. B **76**, 195445 (2007).
[37] K. Efetov, *Supersymmetry in Disorder and Chaos* Cambridge University Press (Cambridge, 1997).
[38] P.M. Ostrovsky, I.V. Gornyi, and A.D. Mirlin, Phys. Rev. Lett. **105**, 036803 (2010).
[39] Yu.V. Nazarov and Ya.M. Blanter, *Quantum Transport: Introduction to Nanoscience*, Cambridge University Press (Cambridge, 2009), Chapters 1.3 and 1.6.
[40] A. Rycerz, P. Recher, and M. Wimmer, Phys. Rev. B 80, 125417 (2009).
[41] E.C. Peters, A.J.M. Giesbers, M. Burghard, and K. Kern, Appl. Phys. Lett. **104**, 203109 (2014).
[42] Similar behavior occurs for rectangular samples, where the conductivity (in the L/ℓ range) strongly depends on the aspect ratio and the crystallographic orientation, see Refs. [18, 20, 23].
[43] The opposite limit of $R_\mathrm{i}, R_\mathrm{o} \ll l_\perp \to \infty$ corresponds to the separation of two layers, leading to $\mathcal{A} \to 1/2$ and $G_\mathrm{BLG}(t'=0) \simeq 2G_\mathrm{MLG}$ (regardless the ratio $R_\mathrm{o}/R_\mathrm{i}$).
[44] We further notice a very slow convergence of the actual $G_\mathrm{BLG}(t'=0)$ obtained from Eqs. (21–24) to the asymptotic form in Eq. (27). In particular, for $R_\mathrm{i} = 10\, l_\perp$ a 5% deviation is still observed for $R_\mathrm{o}/R_\mathrm{i} \approx 1000$. In comparison, for G_MLG a better agreement with the asymptotic form in Eq. (20) occurs for $R_\mathrm{o}/R_\mathrm{i} \geqslant 38$.
[45] For a bit more general discussion of centrosymmetric fields, see Ref. [26].
[46] G. Rut and A. Rycerz, Philos. Mag. **95**, 599 (2015).
[47] B. Kolomeisky, H. Zaidi, and J. P. Straley, Phys. Rev. B **85**, 073404 (2012).
[48] Z. Khatibi, H. Rostami, and R. Asgari, Phys. Rev. B **88**, 195426 (2013).
[49] L. Villegas-Lelovsky, J.L. Huamani Correa, and F. Qu, phys. stat. sol. (b) **251**, 1451 (2014).
[50] P. Recher, B. Trauzettel, A. Rycerz, Ya.M. Blanter, C.W.J. Beenakker, and A.F. Morpurgo, Phys. Rev. B **76**, 235404 (2007); P. Recher, J. Nilsson, G. Burkard, and Björn Trauzettel, *ibid.* **79**, 085407 (2009).
[51] A. Rycerz, J. Tworzydło, and C. W. J. Beenakker, Nature Phys. **3**, 172 (2007); A. Rycerz, phys. stat. sol. (a) **205**, 1281 (2008).
[52] A. R. Akhmerov, J. H. Bardarson, A. Rycerz, and C. W. J. Beenakker, Phys. Rev. B **77**, 205416 (2008).
[53] T. Fujita, M. B. A. Jalil, and S. G. Tan, Appl. Phys. Lett. 97, 043508 (2010).
[54] D. Gunlycke and C. T. White, Phys. Rev. Lett. **106**, 136806 (2011).
[55] M. M. Grujić, M. Ž. Tadić, and F. M. Peeters, Phys. Rev. Lett. **113**, 046601 (2014).
[56] E. A. Laird, F. Pei, and L. P. Kouwenhoven, Nature Nanotechnol. **8**, 565 (2013); A. Pályi and G. Burkard, Phys. Rev. Lett. **106**, 086801 (2011).
[57] D. Culcer, A. L. Saraiva, B. Koiller, X. Hu, and S. Das Sarma, Phys. Rev. Lett. **108**, 126804 (2012).
[58] Z. Gong, G.-B. Liu, H. Yu, D. Xiao, X. Cui, X. Xu, and W. Yao, Nature Commun. **4**, 2053 (2013).
[59] H. Xu, L. Huang, Y.-C. Lai and C. Grebogi, Sci. Rep. **5**, 8963 (2015).
[60] Notice that the conductivity given by Eq. (37) oscillates as a function of magnetic flux $\Phi = LWB$ with an unusual period of $2h/e$, signalling the fractional carrier charge $e/2$; see: R. Jackiw, Phys. Rev. D **29**, 2375 (1984); C.-Y. Hou, C. Chamon, and M. Mudry, Phys. Rev. Lett. **98**, 186809 (2007).
[61] Y. S. Gui, C. R. Becker, J. Liu, V. Daumer, V. Hock, H. Buhmann, and L. W. Molenkamp, Europhys. Lett. **65**, 393 (2004); F. Nichele, A. N. Pal, R. Winkler, C. Gerl, W. Wegscheider, T. Ihn, and K. Ensslin, Phys. Rev. B **89**, 081306(R) (2014).
[62] P. Korbel, J. Spałek, W. Wójcik, and M. Acquarone, Phys. Rev. B **52**, 2213(R) (1995); J. Spałek, W. Wójcik, and P. Korbel, Acta Phys. Polon. A **92**, 277 (1997).
[63] B. Pontecorvo, Zh. Eksp. Teor. Fiz. **53**, 1717 (1967) [Sov. Phys. JETP **26** 984 (1968)]; M.C. Gonzalez-Garcia and M. Maltoni, Phys. Rep. **460**, 1 (2008).
[64] V. P. Gusynin, V. A. Miransky, and I. A. Shovkovy, Phys. Rev. Lett. **73**, 3499 (1994); T. Paananen and R. Egger, Phys. Rev. B 84, 155456 (2011).
[65] M.S. Dresselhaus, A. Jorio, A.G. Souza Filho, and R. Saito, Phil. Trans. R. Soc. A **368**, 5355 (2010).
[66] K. Szałowski, Phys. Rev. B **84**, 205409 (2011); K. Szałowski, *ibid.* **90**, 085410 (2014).
[67] P.S. Cornaglia, G. Usaj, and C.A. Balseiro, Phys. Rev. Lett. **102**, 046801 (2009); B. Uchoa, T.G. Rappoport, and A.H. Castro Neto, *ibid.* **106**, 016801 (2011).
[68] J. Hong, E. Bekyarova, W. A. de Heer, R. C. Haddon, and S. Khizroev, ACS Nano, **7** 10011 (2013).
[69] S. Gattenlöhner, W.-R. Hannes, P. M. Ostrovsky, I. V. Gornyi, A. D. Mirlin, and M. Titov, Phys. Rev. Lett. **112**, 026802 (2014).
[70] W.H. Press, S.A. Teukolsky, W.T. Vetterling, and B.P. Flannery, *Numerical Recipes in C. The Art of Scientific Computing* (Cambridge University Press, Cambridge, 2002), Chapter 16.
[71] The integration step needs to be shrunken approximately linearly with the system size and magnetic field, in order to reach the desired relative precision (10^{-4}) for the output charge-transfer cumulants. For instance, if $R_\mathrm{o} - R_\mathrm{i} = 90\,\mathrm{nm}$, the step varies from $\Delta r = 10^{-10}\,\mathrm{m}$ ($B = 0$) down to $\Delta r = 10^{-11}\,\mathrm{m}$ ($B = 80\,\mathrm{T}$); for $R_\mathrm{o} - R_\mathrm{i} = 5\,\mu\mathrm{m}$ and $B = 0$ the desired precision is achieved at $\Delta r = 10^{-8}\,\mathrm{m}$.
[72] F.W.J. Olver, D.W. Lozier, R.F. Boisvert, and C.W. Clark, eds., *NIST Handbook of Mathematical Functions* (Cambridge University Press, Cambridge, 2010), Chapter 9.

UNIWERSYTET JAGIELLOŃSKI W KRAKOWIE

INSTYTUT FIZYKI IM. MARIANA SMOLUCHOWSKIEGO
Zakład Teorii Materii Skondensowanej i Nanofizyki

dr hab. Adam Rycerz

E-mail: rycerz@th.uj.edu.pl
WWW: http://th.if.uj.edu.pl/~adamr/

Coauthor's statement concerning the articles included in the PhD thesis by Mr. Grzegorz Rut, M. Sc.

To whom in may concern

This is to certify that my own contribution to the six papers authored by Grzegorz Rut and myself was as follows:

Pseudodiffusive conductance, quantum-limited shot noise, and Landau-level hierarchy in biased graphene bilayer, published as Phys. Rev. B 89, 045421 (2014). My contribution to the article was the proposal of general expressions describing the effects of finite-voltage differences on counting statistics (Sec. IVA) supplemented with the derivation of analytical expressions for simplified situations, Eqs. (24,25). I have also identified the power-law relation given by Eq. (32) approximating the numerical results obtained solely by Grzegorz Rut. Both authors contributed equally to the data analysis and the manuscript preparation. In overall, I estimate my contribution to this work as 20%.

Minimal conductivity and signatures of quantum criticality in ballistic graphene bilayer, published as Europhys. Lett. 107, 47005 (2014). My contribution was the observation that the power-law relation identified in the preceding paper is equivalent to the particular form of the scaling function $\beta(\sigma)$, supplemented with preparing some of the plots (Figs. 2 and 3); I have also written most of the article's text. G.R. performed the numerical calculations. Both authors contributed equally to the data analysis. I estimate my contribution to this work as 40%.

Conditions for Conductance Quantization in Mesoscopic Dirac Systems on the Examples of Graphene Nanoconstrictions, published as Acta Phys. Polon. A 126, A114–A117 (2014). My contribution was a general suggestion that particular linear combinations of angular-momentum eigenfunctions may satisfy the infinite-mass boundary conditions in selected constrictions; I have also taken part in the manuscript preparation, while the illustrations were prepared solely by G.R., who also performed the calculations. I estimate my contribution to this work as 20%.

Magnetoconductance of the Corbino disk in graphene: Chiral tunneling and quantum interference in the bilayer case, published as J. Phys.: Condens. Matter 26, 485301 (2014). I have derived a compact form expression for minimal magnetoconductance oscillations, Eqs. (21,34), and put forward the role of an interplay between propagating and evanescent modes at finite dopings (Sec. 3.2). Both authors contributed equally to the manuscript preparation; G.R. performed most of the analytical calculations and prepared the illustrations. I estimate my contribution to this work as 20%.

Quantum-limited shot noise and quantum interference in graphene based Corbino disk, published as Philos. Mag. 95, 599–608 (2015). Both authors have contributed equally to all elements of the work, including the numerical calculations, selection of the data for presentation, and preparation of the manuscript with illustrations. I estimate my contribution to this work as 50%.

Trigonal warping, pseudodiffusive transport, and finite-system version of the Lifshitz transition in magnetoconductance of bilayer-graphene Corbino disks, available as arXiv:1511.04705, accepted for publication in Physical Review B. My contribution to this article was the analytical discussion of the disk conductance in the quantum tunneling regime (Sec. IIIB), I have also derived compact forms of some formulas, such as Eq. (48) for the so-called Lifshitz field. The numerical calculations were performed by G.R., who also prepared most of the illustrations. Both authors contributed equally to the manuscript preparation. I estimate my contribution to this work as 30%.

Adam Rycerz

Kraków, February 3, 2016